Stability and Control of Supercritical Water Reactor System: A Study into Concepts and Applications

This dissertation is submitted to the University of Ghana, Legon, in fulfillment of the requirements for the Award of Doctor of Philosophy in

Nuclear Engineering

By

Emmanuel Ampomah-Amoako, 10235603

June, 2013

DECLARATION

This dissertation is the result of research work undertaken by Emmanuel Ampomah-Amoako in the Department of Nuclear Engineering, School of Nuclear and Allied Sciences, University of Ghana, under the supervision of Emeritus Prof. E. H. K. Akaho, Prof. B. J. B. Nyarko and Prof. Walter Ambrosini, University of Pisa, Italy.

……

Emmanuel Ampomah-Amoako

Date: February 20th, 2014

…….....

Emeritus Prof. Edward H. K. Akaho

Date: February 20th, 2014

……

Prof. Benjamin J. B. Nyarko

Date: February 20th, 2014

……

Prof. Walter Ambrosini

Date: February 20th, 2014

DEDICATION

I dedicate this dissertation to my supervisors, family and Sunday School children of Trinity Society of Methodist Church Ghana.

ACKNOWLEDGEMENT

I thank the Lord God Almighty for the grace and good health given me to undertake this study.

I acknowledge the assistance received from the International Atomic Energy Agency (IAEA) to undertake an eighteen-month fellowship at the University of Pisa during the course of my studies under the supervision of Prof. Walter Ambrosini. I appreciate the assistance I received from the students and staff of the then Dipartimento di Ingegneria Meccanica, Nucleare e della Produzione, now Dipartimento di Ingegneria Civile e Industriale of Università di Pisa. I say thank you to Prof. Nicola Forgione, Danielle Martelli, Ignazio, Alessio and Jeane Lucca. I thank Dr. Mauro Mazzotta of the Welcome Point of the University of Pisa for his kind assistance during my stay in Pisa. I appreciate Miss Giulia Morresi and Miss Gemma Damaini for their contributions in the turbulence model analysis and rod sensitivity analysis undertaken during the course of my research work.

I appreciate the support received from my Supervisors, Emeritus Prof. E. H. K. Akaho, Prof. B. J. B. Nyarko and Prof. Walter Ambrosini. Their insight and kind assistance enabled me to complete this work on schedule.

I acknowledge the assistance received from Prof. Mrs. A. B. Andam, Nana Prof. Ayensu Gyeabour I, Dr. Kwaku Aboagye Danso, Prof. J. J. Fletcher, Prof. Y. Serfo-Armah, Prof. S. Dampare and Mr. I. Ennison during the course of my research work.

I commend Mr. William Ampomah, Ms. Rebecca Antwiwaa, Ms. Victoria Darkwa, Uncle Richard Addai Boateng, Uncle Benjamin Badu Boateng, Uncle William Addai Parku and Uncle Adusa for their excellent support to my academic pursuits.

I appreciate the staff of Ghana Atomic Energy Commission for the immeasurable assistance received during my studies. Special mention is made of Mr. Seth Kofi Debrah and Mr. Kwame Gyamfi who assisted me in diverse ways during the course of my research work.

I acknowledge the support received from Mrs. Bernice Amankwaa, Mrs. Juliana Aggrey, Miss Afua Boatemaa-Oti, Mr. William Ampomah (my brother), Very Rev. Joseph Atuahene, Rev. Klaus Langerneck, Mr and Mrs. Mbeng, Dr. Giuliano Manara, Silvia Manara, Irene Grassi and the entire congregation of Chiesa Valdese, Pisa.

I acknowledge the financial support received from the IAEA for the Sandwich programme under the Technical Cooperation Project GHA/0/11. I also appreciate the role played by the International Centre for Theoretical Physics (ICTP) in facilitating the Sandwich programme at the University of Pisa, Italy.

The IAEA is again acknowledged for including the research performed at the University of Pisa in the Co-ordinated Research Project in 'Heat transfer behaviour and thermo-hydraulics code testing for super-critical water cooled reactors (SCWRs)', through the Research Agreement No. 14272.

Cd-Adapco, the developers of STAR-CCM+, is acknowledged for making this work possible.

TABLE OF CONTENTS

LIST OF TABLES

LIST OF FIGURES

NOMENCLATURE

Roman Letters

A,B	arbitrary constants
b,c,d	arbitrary constants
C	precursor concentration (W/m^3)
C_d	density reactivity coefficient (m^3/kg)
C_T	Doppler reactivity coefficient (K^{-1})
C_{max}	maximum value of the Courant number
C_p	specific heat at constant pressure [J/(kgK)]
D_h	hydraulic diameter [m]
f	friction factor
g	gravity [m/s^2]
h	fluid specific enthalpy [J/kg]
K_{in}, K_{out}	Inlet and outlet singular pressure drop coefficient
k	thermal conductivity (W/mK)
L	channel length [m]
N_{SPC}	sub-pseudocritical number
N_{TPC}	apparent and true trans-pseudocritical numbers
P	power (W/m^3)

$\dot{Q}$	power [W]
r	reactivity (-)
T	temperature [K] or period [s]
t	time [s]
v	specific volume [m^3/kg]
W	inlet mass flow rate (kg/s)
w	velocity [m/s]
y	general variable
Z_R, Z_I	exponents of transient behaviour

Greek Letters

β	isobaric thermal expansion coefficient [K^{-1}] or delayed neutron fraction
Δ	change in
Λ	prompt neutron lifetime (s)
λ	delayed neutron decay constant (s^{-1})
Θ	order of integration scheme
ρ	density [kg/m^3] or spectral radius
τ	period of oscillations (s)

Subscripts

avg,coolant	*coolant average value*
avg,fuel	*fuel average value*
i	*i-th node*
inlet	inlet channel conditions
n,n+1,n-1	*time levels*
p	constant pressure
pc	pseudocritical
0	reference value

Abbreviations

BOP	Balance of Plant
BWR	Boiling Water Reactor
BWROG	United States BWR Owners' Group
CAD	Computer-aided Design
CAE	Computer-aided Engineering
CFD	Computational Fluid Dynamics
CHF	Critical Heat Flux
CHT	Conjugate Heat Transfer

DOM	Discrete Ordninates Method
DNA	Direct Nyquist Array
DR	Decay Ratio
DUT	Delft University of Technology
FPP	Fossil Power Plant
RPV	Reactor Pressure Vessel
RST	Reynolds Stress Transport
SC	Supercritical
Super FR	Super Fast Reactor
SWFR	Supercritical pressure Water-cooled Fast Reactor
GE	General Electric
GFR	Gas-cooled Fast Reactor
GIF	Generation IV International Forum
HP	High Pressure
HPLWR	High Performance Light Water Reactor
HTC	gap thermal conductance
ICTP	International Centre for Theoretical Physics
IP	Intermediate Pressure
LFR	Lead-cooled Fast Reactor

LP	Low Pressure
LWR	Light Water Reactor
MIMO	Multiple-Input Multiple-Output
MSL	Main Steam Lines
MSR	Molten Salt Reactor
PID	Proportional Integral Derivative
PWR	Pressurized Water Reactor
RPV	Reactor Pressure Vessel
SCC	Stress Corrosion Cracking
SCFR	Supercritical Fast Reactor
SCFPP	Supercritical Fossil Power Plant
SCLWR-H	High temperature Supercritical Light Water Reactor
SCWR	Supercritical Water Reactor
SFR	Sodium-cooled Fast Reactor
SISO	Single-Input Single-Output
VHTR	Very High-Temperature Reactor

ABSTRACT

The study addresses the stability and control of nuclear systems with emphasis on the Supercritical Water Reactor (SCWR) as proposed in the Generation IV International Forum. The literature on the stability and control of the SCWR is presented. A Computational Fluid Dynamics code, STAR-CCM+, is used to study the flow stability problems in circular channels, fuel bundle slices with and without heating structures. Some of the effects of numerical discretisation, turbulence model effects, flow direction with respect to gravity and fluid properties are studied by comparing the stability thresholds identified by transient calculations with maps set up by 1D codes developed and used in previous work and results that were obtained by the 1D RELAP5 code.

Flow stability in fuel bundle slices with upward, horizontal and downward flow orientations are addressed. Square and triangular lattice slices are both studied based on the work performed on the circular channel. A uniform heat flux is applied to the slice walls without addressing the internal structure of the rod. The results obtained from STAR-CCM+ by a 3D model are compared with those that were obtained by the use of RELAP5 code. The steady state characteristics of the two models are considered and the thresholds of instability identified by transient calculations are compared with maps from the 1D codes developed using a dimensionless formalism as was performed for the circular channel. Both static and dynamic instabilities are observed, in the circular channel and the fuel bundle slices, clearly showing the contiguity of these two kinds of phenomena as a function of inlet fluid subcooling.

A coupled neutronic-thermal hydraulic instabilities in a subchannel slice with square lattice assembly is studied. A more realistic system is considered dealing with a slice of a fuel assembly subchannel containing the regions of pellet, gap and cladding and also including the effect of inlet and outlet throttling. A point kinetics neutronic model including six delayed neutron groups with a global Doppler and fluid density feedbacks was adopted. The response of the model to perturbations applied starting from a steady-state condition at the rated power is compared with that of a similar

model developed for a 1D system code. Upward, horizontal and downward flow orientations are addressed making use of uniform and bottom peaked power profiles and changing relevant parameters as the gap equivalent conductance and the density reactivity coefficient. Though the adopted model can still be considered simple in comparison with actual details of fuel assemblies, the obtained results demonstrate the potential of the adopted methodology for more accurate analyses to be made with larger computational resources.

CHAPTER 1

INTRODUCTION

1.1 GENERAL BACKGROUND

The control and stability of nuclear systems is of paramount interest to the nuclear industry. From the first nuclear fission experiment led by Enrico Fermi seventy years ago at Argonne National Laboratory, safety has characterised the progress made in the industry. In the development of the Generation IV reactors, the need to maintain this culture has led to varied studies that have enabled six nuclear systems to be considered for possible construction to assist in meeting the energy needs of the world. The Supercritical Water Reactor (SCWR) [1-3] is one of the six reactors under consideration in the Generation IV International Forum (GIF). This reactor inherits many of the advantages of the Pressurized Water Reactors (PWRs) and Boiling Water Reactors (BWR) and has good prospects to meet the electricity needs of the expanding economies across the globe. A common feature shared with the BWR is that a dense fluid enters the reactor core, being subjected to considerable expansion and acceleration along the fuel channels; this phenomenon is the basis for a possible unstable behaviour that may occur especially in conditions of high power-to-flow ratios.

The General Design Criterion 12 of United States 10 CFR 50 recommends that the reactor core and associated coolant, control, and protection systems shall be designed to assure that power oscillations which can result in conditions exceeding specified acceptable fuel design limits are not possible or can be reliably and readily detected and suppressed. This criterion is relevant for Generation IV proposed designs also. The development of methodologies for analysing stability of nuclear reactors is relevant to reactor design, in addition to the good practices needed to be applied to assess the level of stability of a reactor once it is built.

There is a poor availability of experimental data for stability analysis of SCWRs. Xiong et al. [4] has recently presented some results which could be adopted for such studies. The current study has

not made use of this data. In the absence of experimental data, the need to use computational tools becomes very relevant for safety analysis of nuclear reactors. The development of a methodology to use computational fluid dynamics (CFD) for stability analysis of SCWR is continued in this study.

The work reviews the stability and control methodologies adopted for the SCWR design and further conducts a step-by-step analysis of the stability of a supercritical heated channel starting with a circular channel through assembly subchannel slices to a more realistic assembly subchannel slice which includes a fuel rod, throttling and point kinetics.

The objectives of the study are discussed in the next section.

1.2 OBJECTIVES

This study extends a previous feasibility analysis about the application of CFD for stability analysis of SCWR by Sharabi [5] in order to develop a methodology for the analysis of flow stability in heated channels with supercritical fluids by CFD.

The specific objectives have been to conduct analyses about the effects on stability predictions of the following:

- different numerical schemes;
- turbulence treatment;
- inert and active walls;
- flow direction;
- power distribution;
- similarity in fluid-to-fluid behavior;
- wall surface roughness;
- presence of fuel rods in rod bundle slices with their typical structures; and

- neutron kinetics.

In achieving these goals, three categories of models have been adopted for the analyses conducted in this work. A circular supercritical heated channel is analysed in the first phase of the work. The effects of numerical schemes have been studied along with the effect of the turbulence model, wall surface roughness and wall thickness. Stability thresholds are identified and compared with 1D maps for vertical upward, horizontal (no gravity) and vertical downward flows. The stability thresholds for four supercritical fluids; water, ammonia, Freon and carbon dioxide, are compared for the circular channel.

In the second phase, assembly subchannel slices are analysed, starting from previous results [5] to provide the threshold of instability for the square and triangular lattice assemblies.

The third and final phase saw the introduction of fuel rod with clad and gas-filled gap to the slice discussed in the second phase. Throttles are introduced and point kinetics with six delayed neutron groups was applied. The uniform and bottom peaked power distributions are applied to the model and the results are discussed.

The next section presents the outline of the current study.

1.3 DISSERTATION OUTLINE

Chapter 2 discusses a review of the literature on stability and control of the SCWR concept, elaborating on the Generation IV objectives and the application of CFD for stability analysis of SCWR.

Chapter 3 presents the computational tools adopted for the current study. The chapter discusses the dimensionless formulations used in the analysis of stability and the method for evaluating the decay

ratios and periods of oscillation used to characterise the damping or amplification of the perturbations observed in the study.

Chapter 4 discusses the stability analysis of a circular supercritical heated channel. The effects of numerical schemes, time step, turbulence treatment, internal Courant number (the product of fluid velocity by the ratio of time step to the mesh size), mesh discretization on the stability prediction are addressed. Fluid-to-fluid analysis is also presented.

Chapter 5 discusses the analysis of stability for slices of the square and triangular lattice assemblies. Effect of flow direction on stability is also discussed.

Chapter 6 presents the results obtained from the stability analysis of the square lattice slice assembly subchannel with fuel rod and throttling. The effect of power distribution on the stability is addressed.

Chapter 7 provides the general conclusion of the work and outlines possible areas of further studies envisaged from the work performed and discussed.

CHAPTER 2

LITERATURE REVIEW

2.1 INTRODUCTION

Nuclear systems comprise nuclear power plants, research reactors, material testing reactors, submarines and space rockets. The nuclear system studied in this work is the Supercritical Water Reactor (SCWR). It is one of the six innovative nuclear reactor concepts under consideration in the Generation IV International Forum (GIF).

The SCWRs [1-3] are believed to be possibly prone to thermal-hydraulic unstable behaviour in similarity with boiling water reactors [6-9]. The known instability mechanisms occurring when a light fluid enters a heated channel and expands because of heating are presumably active even in the case of supercritical fluids.

Models do predict limited degrees of stability for heated channels with supercritical fluids [10-14] and, given the similarity of the dynamics of boiling and supercritical fluids close to the pseudo-critical threshold, there is little doubt that similar phenomena can really be observed. Recently, experimental evidence of unstable behaviour in experimental apparatuses reinforced this conviction, providing further material and motivation for model development [4].

Models based on one-dimensional cross section averaged balance equations are a straightforward choice for predicting unstable behaviour by numerical or analytical means. These models have been at the basis of many time-domain or frequency domain models and codes developed in the past mainly for boiling water reactor stability [7, 8]. More sophisticated techniques, like CFD, seem difficult to be applied to two-phase flows in transient conditions as those addressed for stability issues. On the contrary, it was shown by previous work [5, 15-17] that this is not the case for supercritical fluids that, being single-phase fluids, though with very peculiar features, are in principle amenable to be treated by the mature CFD techniques developed for single-phase flow.

2.2. GENERATION IV NUCLEAR REACTORS

The Generation IV Forum has selected six nuclear reactor designs for careful consideration to be used for electricity production, hydrogen production, among others. The six reactors are described below:

2.2.1. Sodium-Cooled Fast Reactor (SFR): The SFR system features a fast-spectrum, sodium-cooled reactor and a more fully closed fuel cycle for efficient management of actinides and conversion of fertile uranium [18]. The fuel cycle employs full actinide recycle. Plant size options under consideration range from smaller sized (150 to 500 MWe) modular reactors to larger plants (up to 1500 MWe). Fuel cycle options are either a metal alloy fuel that contains uranium and transuranic elements, supported by pyrometallurgical processing of spent fuel in facilities integrated with several collocated reactors, or a mixed uranium-transuranic oxide fuel supported by advanced aqueous processing of spent fuel at a central location serving a number of reactors. The outlet temperature is approximately 550 °C for all options.

2.2.2. Lead-Cooled Fast Reactor (LFR): The LFR system features a fast-spectrum reactor using pure lead or lead/bismuth eutectic liquid as coolant and a more fully closed fuel cycle for efficient conversion of fertile uranium and management of actinides [18]. Options include a range of plant ratings: a battery of 50 – 150 MWe that features a very long interval between refuelling to reduce the number of shipments of nuclear fuel, a modular system rated at 300-400 MWe, and a large plant option at 1200 MWe. The fuel is metal or nitride, containing fertile uranium and transuranics. The LFR battery concept is cooled by natural circulation with current development on a reactor outlet coolant temperature of 550 °C, possibly ranging up to 800 °C with advanced structural materials. The higher temperature enables process heat applications including the production of hydrogen by high-temperature electrolysis processes.

2.2.3. Gas-Cooled Fast Reactor (GFR): The GFR system features a fast-spectrum, helium-cooled reactor and a more fully closed fuel cycle [18]. Like thermal-spectrum helium-cooled reactors, the high outlet temperature of the helium coolant makes it possible to deliver electricity, hydrogen, or process heat with high efficiency. The reference reactor is a helium-cooled system, ranging from 288 MWe to 1200 MWe, operating with an outlet temperature of 850 °C. Several innovative fuel forms are candidates that hold potential to operate at very high temperatures and to ensure an excellent retention of fission products: composite ceramic fuel, advanced fuel particles, or ceramic clad elements of actinide compounds. Core configurations may be based on prismatic blocks, pin- or plate-based fuel assemblies. The GFR reference has an integrated, on-site used fuel treatment and refabrication plant. The reference GFR uses a direct Brayton cycle helium turbine for high-thermal efficiency in electricity generation or can optionally use its process heat for production of hydrogen.

2.2.4. Molten Salt Reactor (MSR): The MSR is a liquid-fueled reactor that can be used for production of electricity, actinide burning, production of hydrogen, and production of fissile fuels [19, 20]. Fissile, fertile, and fission isotopes are dissolved in a high-temperature molten fluoride salt with a very high boiling point, 1400 °C, that is both the reactor fuel and the coolant. The near-atmospheric-pressure molten fuel salt flows through the reactor core. The traditional MSR designs have a graphite core that results in a thermal to epithermal neutron spectrum. Alternative designs are being explored with no reactor internals and a fast neutron spectrum. In the core, fission occurs within the flowing fuel salt that is heated to ~700 °C, which then flows into a primary heat exchanger where the heat is transferred to a secondary molten salt coolant. The fuel salt then flows back to the core of the reactor. The clean salt in the secondary heat transport system transfers the heat from the primary heat exchanger to a high-temperature Brayton cycle that converts the heat to electricity. The Brayton cycle (with or without a steam bottoming cycle) may use either nitrogen or helium as a working gas.

2.2.5. Very High-Temperature Reactor (VHTR): The VHTR is a helium-cooled, graphite-moderated, graphite-reflected, metallic-vessel reactor plant with the capability for the generation of electricity with possible co-generation of process steam using a Brayton gas-turbine cycle, and high-temperature process heat for chemical process and hydrogen co-production [21]. The major VHTR design options are: Prism versus pebble fuel, Direct versus indirect power conversion cycles, Water versus air-cooled Reactor Cavity Cooling System, Filtered confinement versus low leakage containment and Below-grade embedment versus above-ground nuclear islands. The United States of America, Russia, France. Japan and South Korea are pursuing similar goals for the VHTR with varied specifications.

2.2.6. Supercritical Water Reactor (SCWR): The Supercritical Water-Cooled Reactor (SCWR) is a high-temperature, high-pressure water-cooled reactor that operates above the thermodynamic critical point of water (374°C, 22.1 MPa), which enables combination of a once-through reactor and a direct cycle system [22]. The SCWR has potential advantage of low capital cost owing to its high thermal efficiency and plant system simplifications. The reference system is 1500 MWe with an operating pressure of 25 MPa, and a reactor outlet temperature of 500°C or more, possibly ranging up to 625°C. The fuel is uranium dioxide, MOX or possibly thorium dioxide. Passive safety features shall be incorporated similar to those of simplified boiling water reactors. The SCWR design has no steam generators or steam separators and recirculation pumps as pertains to BWR and PWRs [23]. The design does not include a pressurizer as in BWRs but has a small reactor pressure vessel, control rods are inserted from top to bottom as in PWRs. It has only two steam lines as compared to four for PWRs and BWRs and has a very small containment. Due to higher operating temperatures, SCWRs can facilitate an economical co-generation of hydrogen through thermochemical cycles [24].

The development of the SCWR concept was started by the University of Tokyo in 1989, which acquired worldwide interest and was selected as one of the six Generation IV nuclear energy

systems by the Generation IV International Forum (GIF) in 2002 [25]. The GIF roadmap for SCWR [25] describes specific goals which all future nuclear reactor concepts shall fulfill:

Sustainability–1 Generation IV nuclear energy systems will provide sustainable energy generation that meets clean air objectives and promotes long-term availability of systems and effective fuel utilization for worldwide energy production.

Sustainability–2 Generation IV nuclear energy systems will minimize and manage their nuclear waste and notably reduce the long-term stewardship burden, thereby improving protection for the public health and the environment.

Economics–1 Generation IV nuclear energy systems will have a clear life-cycle cost advantage over other energy sources.

Economics–2 Generation IV nuclear energy systems will have a level of financial risk comparable to other energy projects.

Safety and Reliability–1 Generation IV nuclear energy systems operations will excel in safety and reliability.

Safety and Reliability–2 Generation IV nuclear energy systems will have a very low likelihood and degree of reactor core damage.

Safety and Reliability–3 Generation IV nuclear energy systems will eliminate the need for offsite emergency response.

Proliferation Resistance and Physical Protection–1 Generation IV nuclear energy systems will increase the assurance that they are a very unattractive and the least desirable route for diversion or theft of weapons-usable materials, and provide increased physical protection against acts of terrorism.

As the system uses existing light water reactor technology, there is already extensive worldwide experience in constructing and operating this sort of reactor [19]. A SCWR design could be developed with a fast neutron spectrum. Using fast neutrons with higher kinetic energies would enable the system to produce at least as much fissile material as it consumes. By so doing, it will fulfill the sustainability goal as set out in the Generation IV roadmap. This concept's tendency to have a positive void reactivity coefficient together with the potential for design basis loss-of-coolant accidents are likely to make this difficult to develop. The other major challenges for the SCWR are to develop a viable core design, accurately estimate the heat transfer coefficient and develop materials for the fuel and core structure that will be sufficiently corrosion-resistant to withstand SCWR conditions.

2.3 SUPERCRITICAL WATER REACTOR DESIGN CONCEPTS

In the field of system integration and assessment, the main activities were the development of pre-conceptual SCWR designs, including core design with thermal or fast neutron spectrum, pressure tube and pressure vessel design, as well as first plant layout. The European concept [26], High Performance Light Water Reactor (HPLWR) is presented in Figure 2.1 below.

The HPLWR features a pressure vessel type reactor with a thermal core which is heating up the coolant with inlet flowrate of 1160 kg/s at 280 °C in three steps to 500°C average core outlet temperature, and includes mixing chambers above and underneath the core to minimize peak cladding temperatures. The gross plant electric output is 1000 MWe and it operates with a system pressure of 25 MPa. An active core height of 4.2 m has been specified by Squarer et al. [27]. Coupled neutronic and thermal-hydraulic analyses of the core demonstrate that the envisaged power profile is feasible, which differs significantly from the core design of conventional light water reactors by different power density levels in different core regions. Burn-up analyses have been performed to estimate redistribution of the power profile during a burn up cycle and to determine

refueling intervals. A first layout of the containment and its safety systems is based on the design of latest boiling water reactors. It includes a pressure suppression pool, four (4) core flooding pools, depressurization systems, and a passive high pressure residual heat removal system, which need to be analyzed next for a number of postulated accident scenarios.

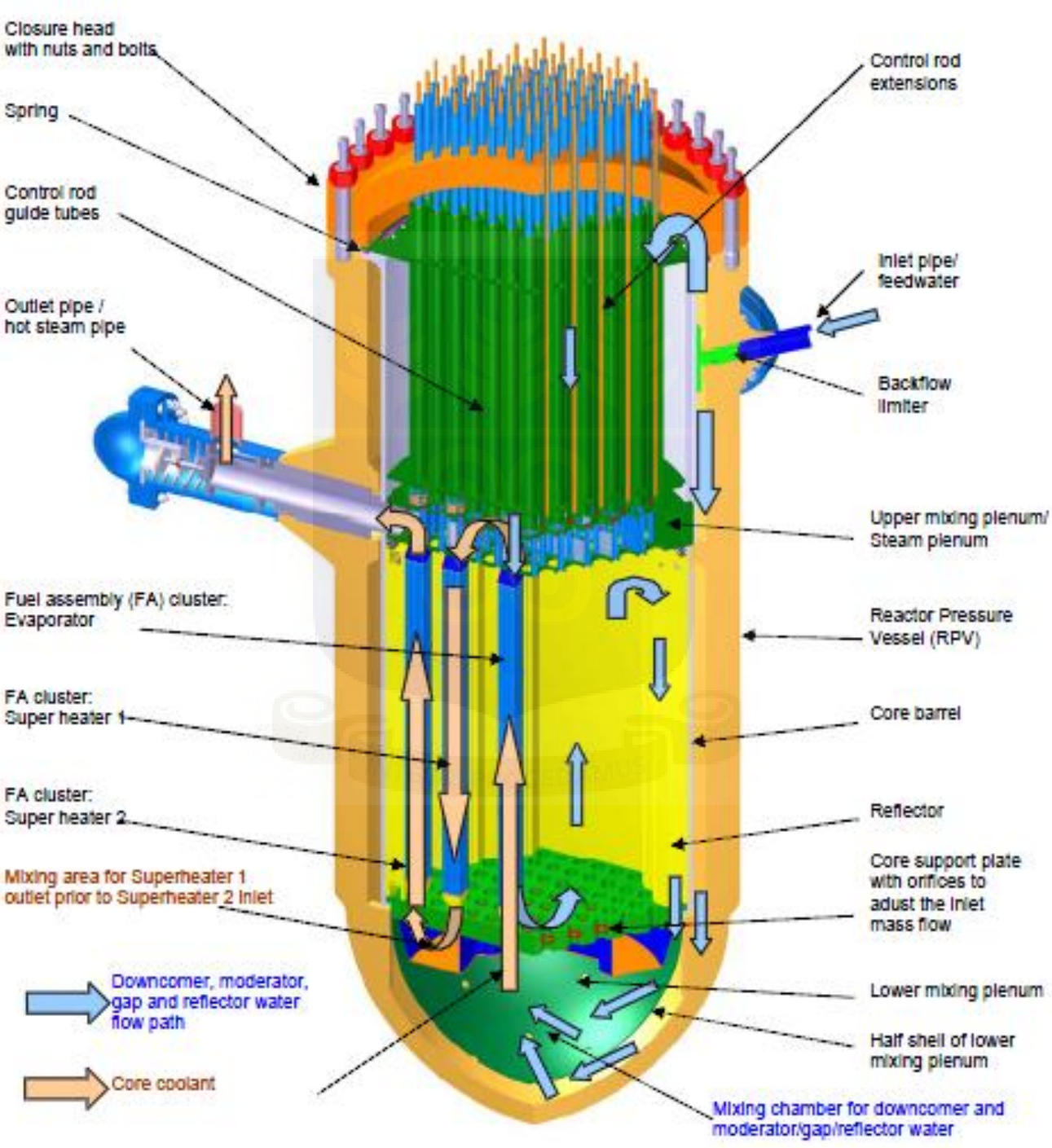

Figure 2.1: Reactor Pressure Vessel (RPV) design with internals [26]

A once-through supercritical steam cycle for the HPLWR with high pressure (HP), intermediate pressure (IP) and low pressure (LP) turbines has been optimized by Brandauer et al. [28] for full load operation conditions. Figure 2.2 below shows the steam cycle of the HPLWR.

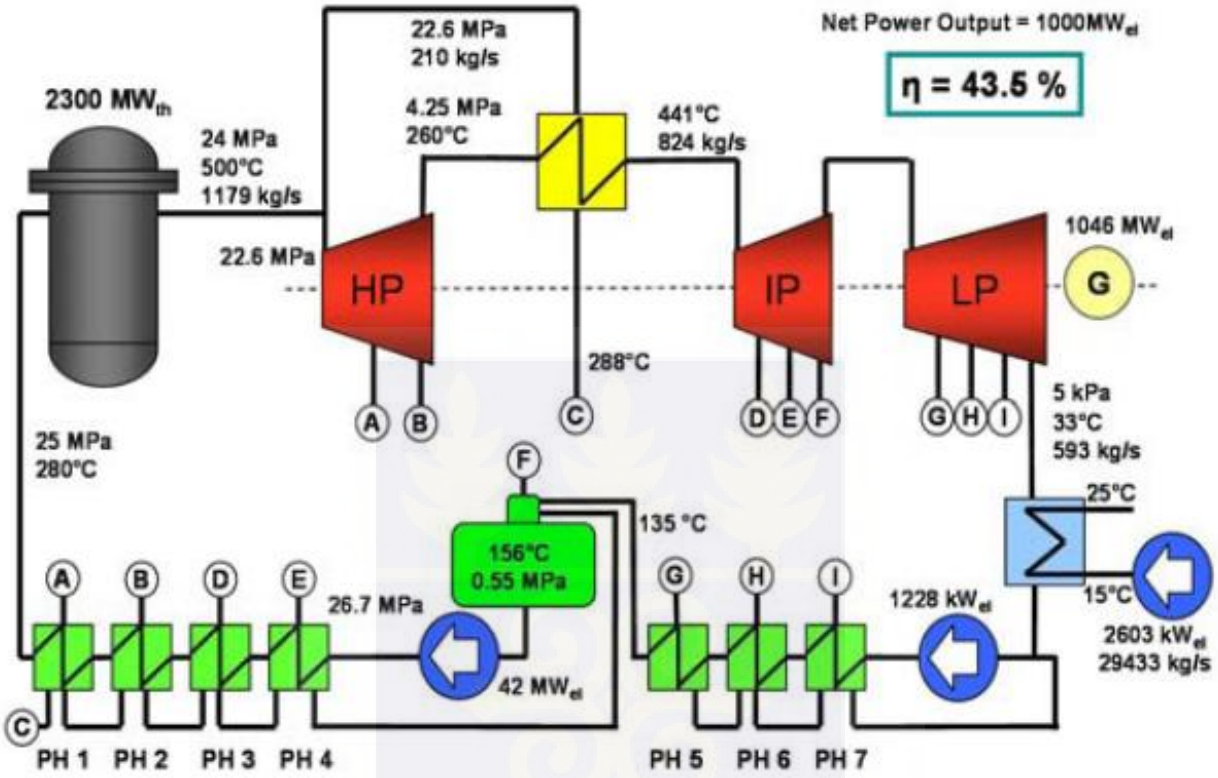

Figure 2.2: Heat flow diagram of the HPLWR steam cycle by Brandauer et al. [28].

The CANDU [29] also offers a SCWR system concept which has advantages in the areas of sustainability, economics, safety and reliability and proliferation resistance. Firstly, since the moderator is located in the calandria vessel and is separated from the coolant, the coolant has relatively less effect on the neutronics. Secondly, since the channel flows can be bi-directionally interlaced (opposite flow direction in adjacent channels), the density gradients are balanced and a more axially uniform flux profile is achievable. The other advantage is that the pressure boundary (pressure tube) can be easier to be fabricated which can accommodate much higher pressure.

Canada has been focusing on the general layout and thermodynamic cycle options for pressure tube reactors. Main objectives for developing and utilizing SCWRs are an increase of gross thermal efficiency of current nuclear power plants from 33-35% to approximately 45–50%, decrease of the capital and operational costs and in doing so, decrease of electrical energy costs, and co-generation of hydrogen through thermo-chemical cycles, as outlined by Naidin et al. [30]. To decrease significantly the development costs of a SCWR, to increase its reliability, and to achieve similar high thermal efficiencies as the advanced fossil steam cycles, it should be determined whether the SCWR power plant can be designed with a steam-cycle arrangement which closely matches that of latest supercritical fossil power plants. A two loop system with supercritical water in the primary loop and a steam generator for a secondary loop has been assessed for comparison. First coupled neutronics / thermal-hydraulics analyses of a fuel channel for a pressure tube SCWR with 625°C outlet temperature have been presented, indicating the need for further core optimization to meet material limits.

A Japanese consortium consisting of the Institute of Applied Energy, the University of Tokyo, Kyushu University, Kyoto University, Japan Atomic Energy Agency, Hitachi-GE Nuclear Energy Ltd., Hitachi Ltd., and Toshiba Corporation has been working together to establish the concept and to implement key technology developments [22].

The basic philosophy of the JSCWR development is to utilize proven light water reactor and supercritical fossil-fired power plant technologies as much as possible to minimize the research and development cost, time and risks. So the JSCWR is designed as a thermal neutron spectrum reactor using light water as moderator and reactor coolant. The JSCWR plant consists of a pressure-vessel type, once-through reactor and a direct Rankine cycle system. Reactor coolant fed through inlet nozzles is heated up in the core and flows through outlet nozzles with no recirculation in the vessel. The core outlet coolant, which is customarily called ‘steam’ although there is no distinction between steam and water above the supercritical pressure, is directly delivered to the turbine

system, and the feedwater comes back directly from the feedwater pumps. The balance of plant (BOP) consists of three-stage turbines, condensers, and condensate and feedwater system, and electricity is generated by a generator driven by the turbines, which is a well-matured technology and needs essentially no additional research and development.

The electrical output is assumed to range from 600 MWe to 1700 MWe class to fulfill user's requirements as much as possible. The reference value is selected as 1725 MWe, which corresponds to a reactor thermal output of 4039 MWth. The operating pressure and temperature ranges are shown in Figure 2.3 below.

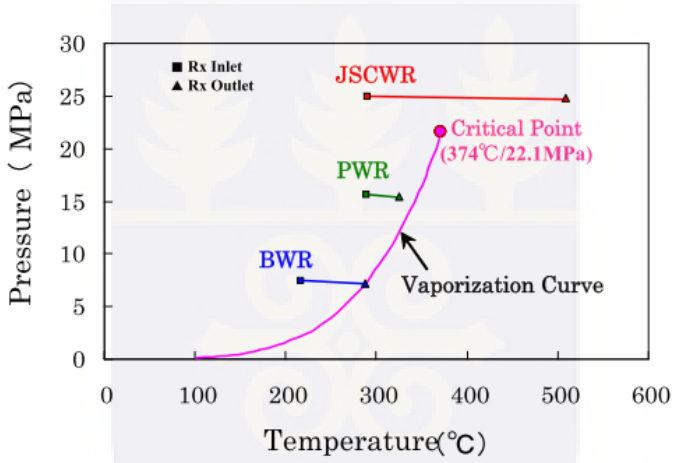

Figure 2.3: Operating pressure and temperature ranges of SCWR, PWR and BWR [22].

The primary circuit of the JSCWR constitutes a direct Rankine cycle consisting mainly of a reactor pressure vessel (RPV), main steam lines (MSLs), a turbine system, low-pressure and high-pressure condensate water pumps, feedwater heaters, feedwater pumps.

Control rods are used for primary reactivity control. The control rod drives are mounted on the bottom of the RPV. Cruciform control rods are vertically inserted into and withdrawn from the core by the control rod drives. To ensure adequate shut down margin and to minimize the local peaking during the entire operation cycle, gadolinia (burnable poison) is incorporated in the fuel.

The cross sectional view and the loading pattern of the JSCWR is shown in Figure 2.4 and that of the fuel assembly is presented in Figure 2.5.

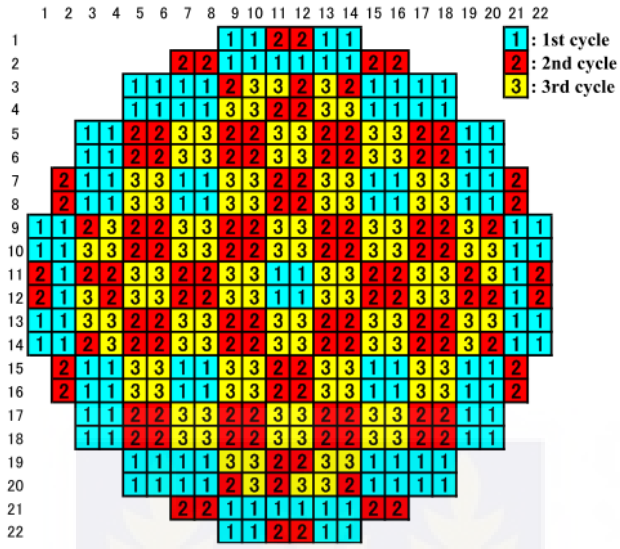

Figure 2.4: Cross sectional view of the JSCWR core and its loading pattern [22].

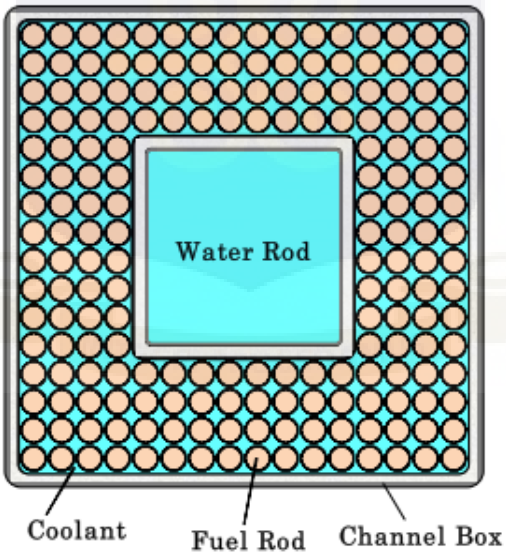

Figure2.5: Cross sectional view of the JSCWR fuel assembly [22].

The flow in the RPV is depicted in Figure 2.6. The coolant is provided through cold legs (inlet nozzles) and flows out through hot legs (outlet nozzles). Most of the coolant flows downward through the annulus region between the RPV wall and the shroud (downcomer), and flows

into the lower plenum. A part of coolant is directed to the upper dome to remove heat from the shroud head and flows into the bypass line. The coolant from the downcomer mixes with the coolant from the bypass line in the lower plenum and flows upward through the core.

The inner surface of RPV wall is cooled by the inlet coolant as in PWRs to keep the temperature low enough to use the same materials used for PWRs.

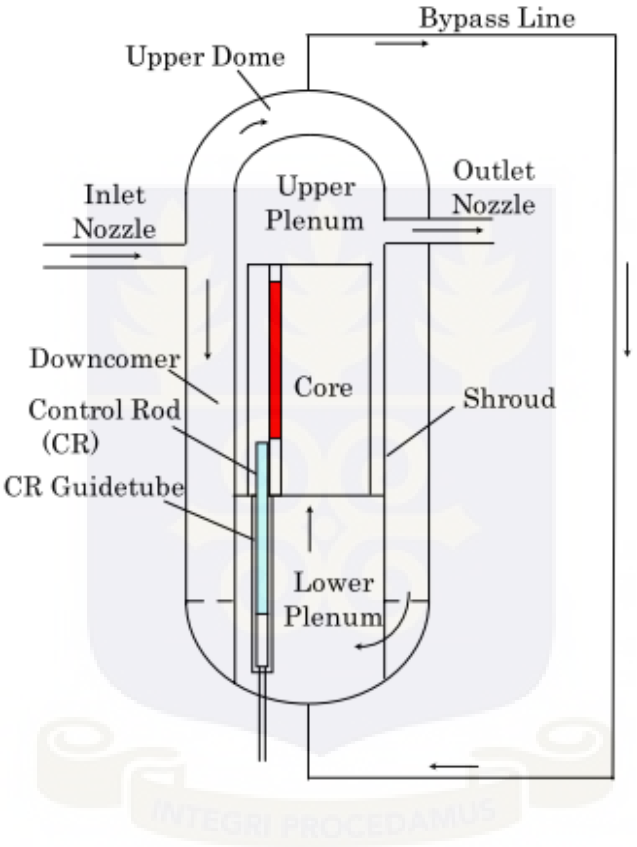

Figure 2.6: Configuration of Reactor Pressure Vessel and Coolant Flow [22].

The balance of plant system of the JSCWR is shown in Figure 2.7 below.

The SCLWR-H is a variant of the JSCWR with electric power of 1000 MW and an efficiency of 43.5 %, Doppler coefficient of -1.2×10^{-5} dk/k/°C, coolant flowrate of 1190 kg/s, fuel rod diameter of 10.2 mm, lattice pitch of 11.2 mm, core height of 4.2 m, core diameter of 3.6 m and density

coefficient of reactivity of 0.2 dk/k/(g/cm^3) [31]. The parameters of this design informed the Square lattice assembly choice of this study.

Japan is pursuing two pressure vessel designs (thermal and fast spectrum), as summarized by Ishiwatari et al. [32]. The fast reactor (Super Fast Reactor) is expected to be designed with a similar plant system as the thermal reactor. The fast reactor will produce a higher power density than the thermal reactor because less moderator is needed, and thus more thermal power can be produced using the same reactor pressure vessel size, which will further reduce the unit capital costs. The University of Tokyo, Kyushu University, JAEA and TEPCO are contributing to it.

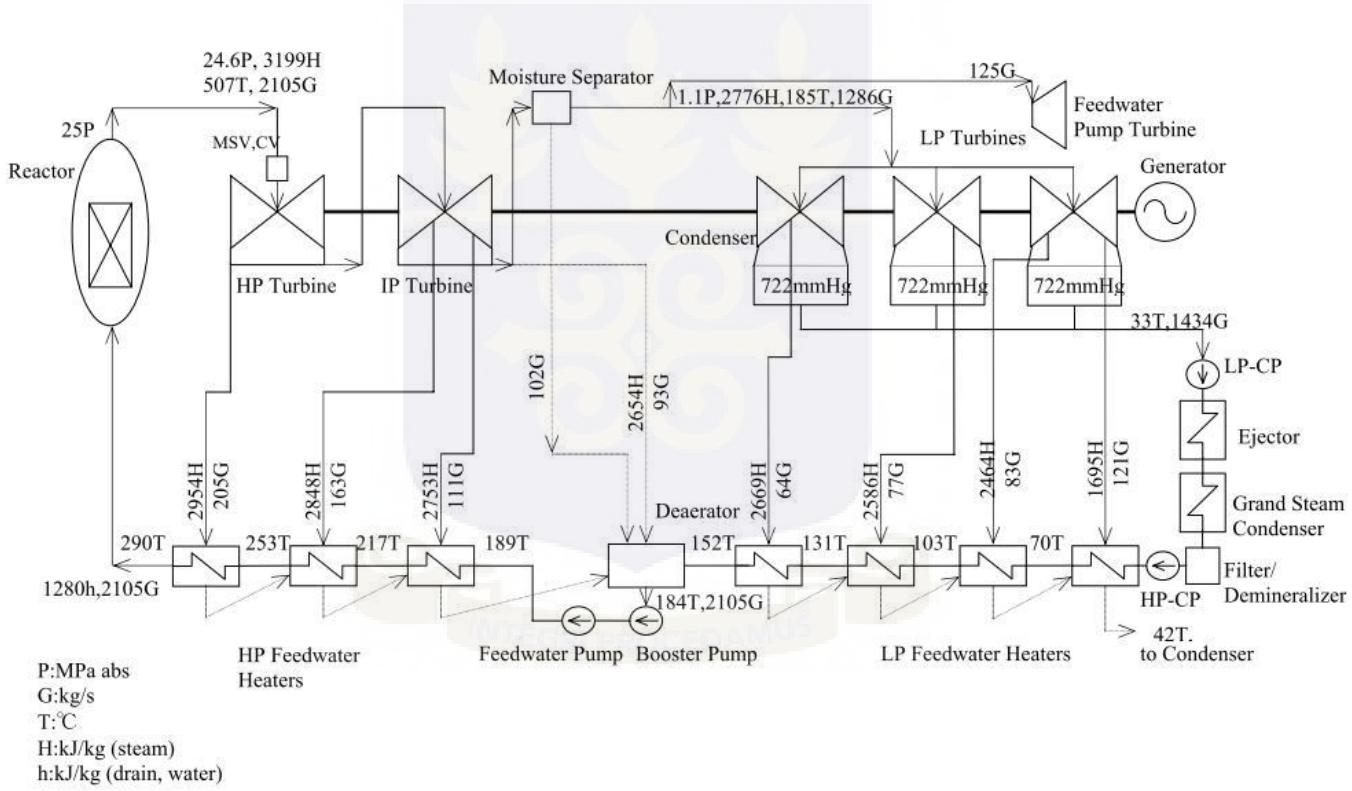

Figure 2.7: Balance of Plant system of JSCWR [22].

The purpose of the concept development is to pursue the advantage of high power density of fast reactors over thermal reactors to achieve economic competitiveness of fast reactors for its deployment without waiting for exhausting uranium resources. The design goal is not breeding but

maximizing the power density and utilizing plutonium from the LWR spent fuel. The reference fuel rod and core have been designed. Solid moderator (ZrH) in the blanket assembly enables the Super Fast Reactor to have negative void reactivity without adopting a flat core shape. A 3D neutronic/thermal-hydraulic coupled calculations have been used for the core design. Sub-channel analyses have been performed for all the fuel assemblies to calculate the maximum cladding surface temperature.

The Republic of Korea continued further assessment of a conceptual SCWR design [33]. It features a 1400 MWe reactor core with a solid moderator, ZrH_2, showing reasonable results although a further refinement is definitely needed. The idea of a solid moderator has been introduced since it was intended to simplify the coolant passage in a reactor upper dome. The shape of the solid moderator is basically a cross type but alternative versions are being studied in parallel. As shown in Figure 2.8, the fuel assembly has a 21×21 fuel rods array with a pitch of 1.15 cm, and the fuel assembly pitch is 25.15 cm, including a 1 cm gap between the fuel assemblies. The fuel assembly is composed of 300 fuel rods in 193 fuel assemblies [34], 25 cruciform-type solid moderator pins, and 16 single solid moderator pins. The pellet diameter and the outer diameter of the cladding are 0.82 cm and 0.95 cm, respectively. The clad material is a nickel-based alloy, which is highly resistant to a stress corrosion cracking (SCC) at a supercritical water condition. The design limit for the maximum linear heat generation rate is assumed to be 390 W/cm, which is the same as that of a light water reactor, while the average linear heat generation of the conceptual SCWR core is 144.2 W/cm. Therefore, the power peaking factor limit associated with the maximum linear heat generation rate is determined to be 2.7.

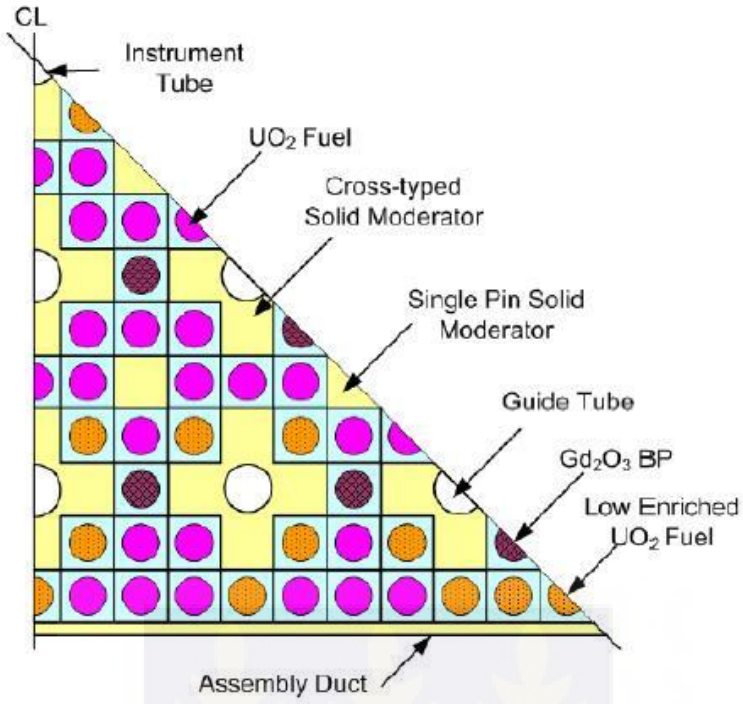

Figure 2.8: Fuel assembly design of a 1400 MWe core [33].

In China, some preliminary reactor core concepts have been worked out, among them a novel concept with mixed neutron spectrum [35]. The core concept, sketched in Figure 2.9, combines the merits of both thermal and fast spectrum as far as possible. The basic idea is to divide the reactor core into two zones with different neutron spectrum. In the outer zone, the neutron energy spectrum is similar to that of a thermal reactor. In this zone, the fuel assembly has a square arrangement but with downward, co-current flow of coolant and moderator water.

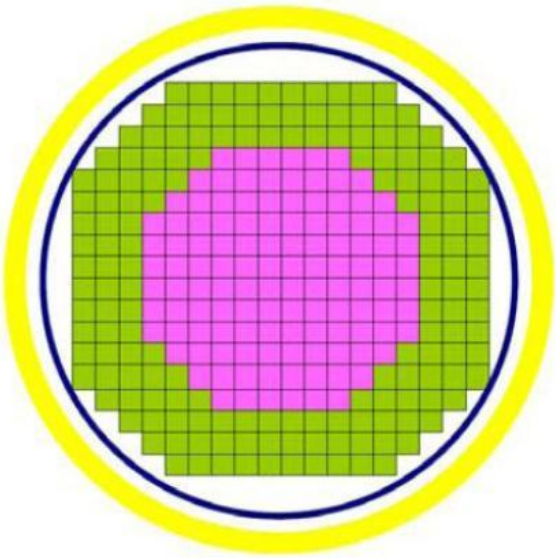

Figure 2.9: Scheme of the mixed SCWR core [35].

From the above discussion, it can be observed that the variant versions of the SCWR have significant advantages and the coordination in the design among the various countries involved is going to enable the final SCWRs that will be constructed to be very versatile in safety and utilization.

The next section discusses the stability concerns of SCWRs.

2.4 STABILITY CONCERNS OF SUPERCRITICAL WATER REACTORS

The SCWR technology challenges include reactivity effects of the supercritical core to be studied to prove the stability of power control in normal and transient conditions [36]. The concept provides a technological challenge in the fields of design, neutronics, thermal-hydraulics and heat transfer, materials and safety [37].

At supercritical pressures, water density changes greatly near the pseudo critical temperature. Due to low coolant flowrate and large density change in the core, undesirable flow instabilities may occur in the fuel channels of SCLWR-H [31]. In the supercritical region, thermophysical properties

vary dramatically with a small change in temperature over certain temperature range [23]. Convection heat transfer of fluids at supercritical pressures exhibits many special features due to the sharp variations of the thermophysical properties and buoyancy forces resulting from the non-uniform density distribution across the cross-section of the tube during both heating and cooling process. Although water does not undergo a phase change at supercritical pressures, the thermophysical properties and transport properties change greatly near the pseudocritical temperature, which is about 385 °C at 25 MPa. Since the core inlet temperature of the SCWR, which is 280 °C, is lower than the pseudocritical temperature and the core outlet temperature of 500 °C is above the pseudocritical temperature, the coolant density changes greatly in the core as it flows upwards through the fuel channels [38]. Although the coolant flow in SCWR is a single phase flow, the axial coolant density change is about five times that of Boiling Water Reactors (BWRs), because of larger enthalpy difference between the core inlet and core outlet. The coolant flowrate of SCWR is only approximately one-tenth of the current light water reactors.

It is envisaged that the instability phenomenon in SCWRs will follow similar principles as in the case of BWRs due to their characteristic density variations in the cores. Thus criteria for BWR stability are usually adopted for SCWRs [38].The instability phenomena associated with BWRs is thus reviewed below.

The core power oscillation phenomenon inherently exists in BWR cores [8], as generally called by the BWR stability or instability. The BWR instability is possible even at the normal plant operation conditions and significant core power oscillations may threaten core fuel integrity due to the fuel cladding dryout occurrence and/or due to the strong pellet-cladding mechanical interaction (PCMI)[39]. Therefore, an accurate prediction of the onset of BWR instability is indispensable for the safety of BWR core design and operation. Hence, numerous efforts have been paid to understand the complicated BWR instability mechanism and to develop the advanced analysis models.

The stability problem has become an important concern on safety of BWR operations, in particular, after the instability incident at LaSalle-2. The applied analysis code predicted a stable core condition while instability actually occurred [39]. Therefore, General Electric (GE) and US BWR Owners' Group (BWROG) have improved the stability analysis models which can be adequately applicable to the actual core design and operation, and have developed the long-term stability solution methodologies with several modifications in the plant installation. Ikeda et al [39] reviewed the BWR stability issues in Japan.

A flow is stable if, when disturbed, its new operating conditions tend asymptotically towards the original ones [9]. Mathematically it is to say that the original operating point is a solution to a system with the property that slight perturbations damp out to produce the original state. If the flow and the temperature show some oscillations, but the amplitude of the oscillations and the sign of the velocity stay constant in time, the system can be called "neutral". If finally the system shows oscillations which grow in time and lead to flow reversal, the system can be called "unstable". It may be noted that the amplitude of oscillations cannot go on increasing indefinitely even for unstable flow. Instead, for almost all cases of instability the amplitude is limited by nonlinearities of the system and limit cycle oscillations (which may be chaotic or periodic) are eventually established [40]. The time series of the limit cycle oscillations may exhibit characteristics similar to the neutrally stable condition. Further, even in the steady state case, especially for two-phase systems with slug flow, small amplitude oscillations are visible. Thus, for identification purposes especially during experiments, often it becomes necessary to quantify the amplitude of oscillations as a certain percentage of the steady state value. Amplitudes more than $\pm$ 10% of the mean value is often considered as an indication of instability. However, some authors even use $\pm$ 30% of the mean as the cut-off value [41].

Instability is undesirable as sustained flow oscillations may cause forced mechanical vibration of components. Further, premature critical heat flux (CHF) occurrence can be induced by flow

oscillations as well as other undesirable secondary effects like power oscillations in BWRs. Instability can also disturb control systems and cause operational problems in nuclear reactors [42]. Over the years, several kinds of instabilities have been observed to be excited by different mechanisms. Differences also exist in the transport mechanism, oscillatory mode, the nature of the instability threshold and its prediction methods. Under the circumstances, it looks relevant to classify instabilities into various categories which will help in improving our understanding and hence control of these instabilities.

Two categories of classifications shall be employed in this study to represent the different models adopted. The first category (Category I) shall encapsulate static and dynamic thermal-hydraulic instabilities while the second category (Category II) shall involve nuclear-coupled instabilities. The two categories are discussed below.

2.4.1. Category I - Thermal-Hydraulic Instabilities

Thermal-hydraulic instabilities can be classified using a variety of methods [8]. Two broad classes of thermal-hydraulic instabilities are generally acknowledged; static instabilities and dynamic instabilities. Static instabilities are explainable in terms of steady state laws, whereas dynamic instabilities require the use of time dependent conservation equations. Table 2.1 provides a classification and brief description of thermal-hydraulic instabilities in terms of these two broad classes.

Table 2.1.Classification of thermal hydraulic instabilities [8]

Class	Type	Mechanism	Characteristic
Static Instabilities			
Fundamental (or pure) static instabilities	Flow excursion or Ledinegg instabilities	$\left.\frac{\partial \Delta p}{\partial G}\right\|_{\text{int}} \leq \left.\frac{\partial \Delta p}{\partial G}\right\|_{ext}$	Flow undergoes sudden, large amplitude excursion to a new, stable operating condition.
	Boiling crisis	Ineffective removal of heat from heated surface	Wall temperature excursion and flow oscillation
Fundamental relaxation instability	Flow pattern transition instability	Bubbly flow has less void but higher ΔP than that of annular flow	Cyclic flow pattern transitions and flow rate variations
Compound relaxation instability	Bumping, geysering, or chugging	Periodic adjustment of metastable condition, usually due to lack of nucleation sites	Period process of super-heat and violent evaporation with possible expulsion and refilling

Dynamic Instabilities			
Fundamental (or pure) dynamic instabilities	Acoustic oscillations	Resonance of pressure waves	High frequencies (10-100Hz) related to the time required for pressure wave propagation in system
	Density wave oscillations	Delay and feedback effects in relationship between flow rate, density, and pressure drop	Low frequencies (1Hz) related to transit time of a continuity wave
Compound dynamic instabilities	Thermal oscillations	Interaction of variable heat transfer coefficient with flow dynamics	Occurs in film boiling
	BWR instability	Interaction of void reactivity coupling with flow dynamics and heat transfer	Strong only for small fuel time constant and under low pressures
	Parallel channel instability	Interaction among small number of parallel channels	Various modes of flow redistribution
Compound dynamic	Pressure drop	Flow excursion	Very low frequency

instability as secondary phenomena	oscillations	initiates dynamic interaction between channel and compressible volume	periodic process (0.1Hz)

The flow excursion or Ledinegg instabilities is the static instability predicted for SCWR design by Ambrosini and Sharabi [14]. Many others [1-3, 5,13-16] have predicted that the dynamic instability to be catered for in SCWR is the density wave oscillations. The study on a supercritical circular channel reported in Chapter 4 and that for supercritical assembly slices reported in Chapter 5 shall employ computational fluid dynamic tools and a system code to predict the occurrence of these two instabilities.

The next section discusses the nuclear-coupled instabilities which were observed in the model that included fuel rod and kinetics.

2.4.2. Category II - Nuclear-Coupled Instabilities

The nuclear-coupled instability can be categorized into the three phenomena [39]:

(1) channel instability (density wave oscillation);

(2) core instability (global core power oscillation); and

(3) regional instability (powers in two halves of a core oscillate with an out-of-phase mode).

The categories are discussed below.

2.4.2.1. Channel instability

The channel instability is equivalent to the coolant density wave oscillation in a boiling channel, where the channel pressure drop is kept constant by any constraint [43, 44].

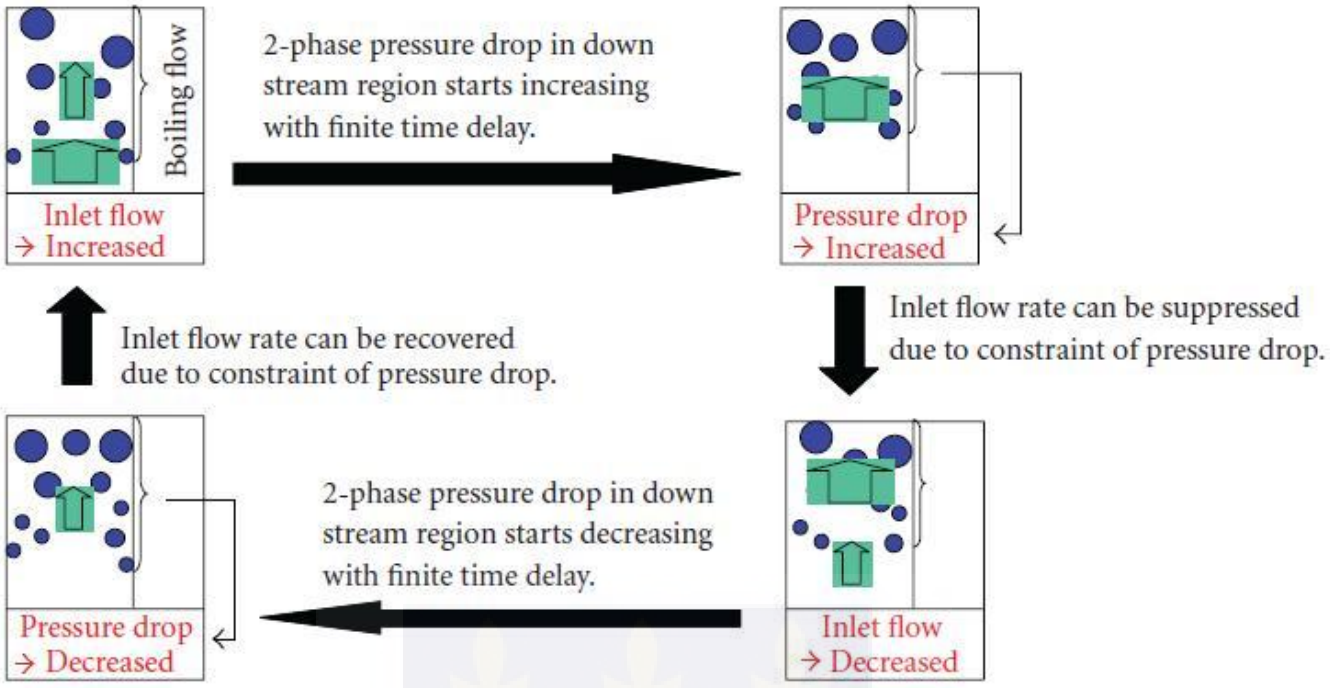

Figure 2.10: Schematic description for channel instability mechanism [39]

As shown in Figure 2.10, the coolant void sweeps in the boiling region, which significantly affects the two-phase pressure drop, consequently leads to the coolant mass flow oscillation at the channel inlet. Hence, the channel instability can be invoked in a channel, where the two-phase pressure drop is relatively larger than the single-phase pressure drop, for such conditions as

(1) higher channel power and lower flow rate,

(2) lower inlet coolant subcooling,

(3) down-skewed axial power shape,

(4) numbers of fuel rods and of fuel spacers which tend to generate the larger pressure drop in the 2-phase boiling region.

In general, however, excitation of the channel instability can be suppressed by many other stable channels through the neutronic coupling effect among fuel bundles in an actual core.

2.4.2.2. Core Instability

The coupled neutronic and thermal-hydraulic power oscillation can be categorized into the global instability and into the regional instability [39]. In the first mode, the global core power oscillates in-phase, while in the regional oscillating mode, the power in a half core oscillates in an out-of-phase mode with respect to the other half. The core power oscillation is mainly driven by the negative coolant void feedback with the finite time delay due to the fuel heat conduction [43]. This power oscillation can actually be excited by synchronizing with the mentioned density wave oscillation, as schematically described in Figure 2.11 a range from 0.3 to 0.6Hz [45, 46], which are correlated with the wave propagation velocity through the core fuel channel.

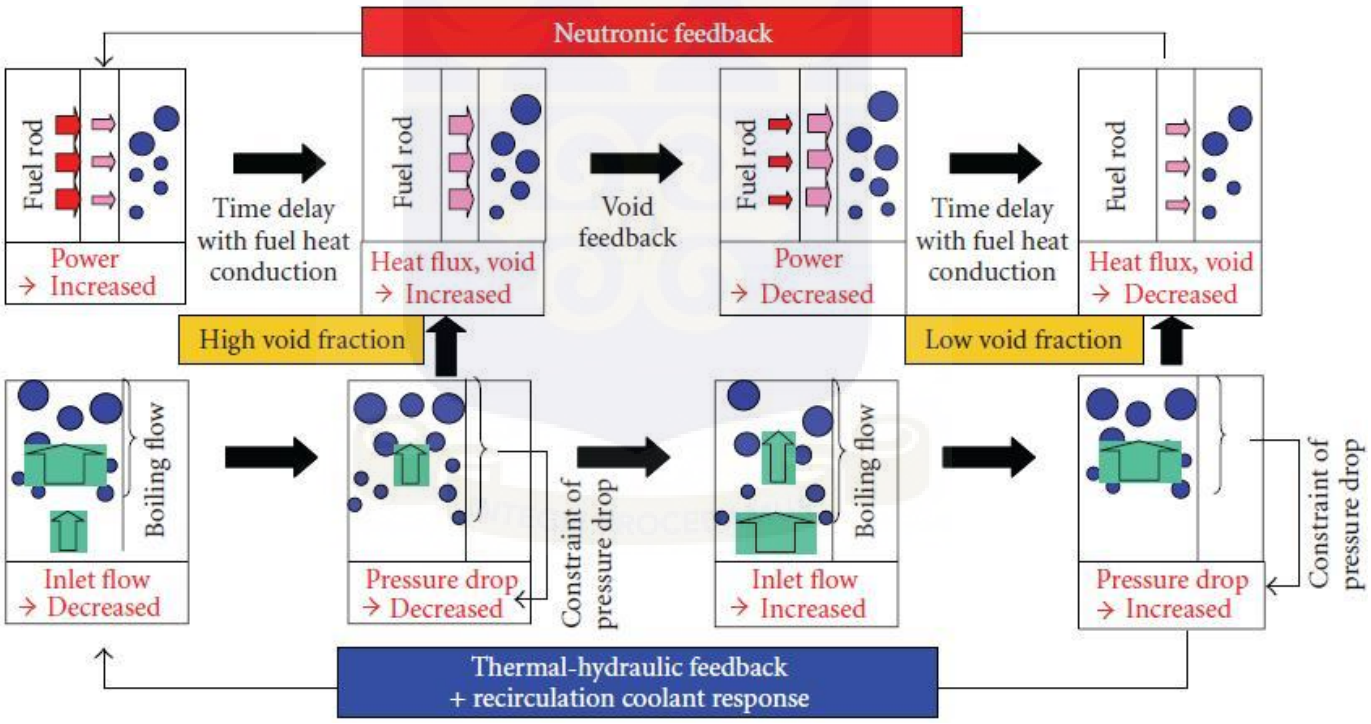

Figure 2.11: Schematic description for core instability mechanism [39].

The core power oscillation becomes unstable under the lower flow and higher power core operation condition, corresponding to the density wave oscillation behavior. Large negative void feedback and faster fuel heat conduction make the core state unstable. In addition, the past investigation using

frequency-domain stability analysis codes revealed interesting sensitivity with respect to the core power distribution, as shown in Figure 2.12 [39].

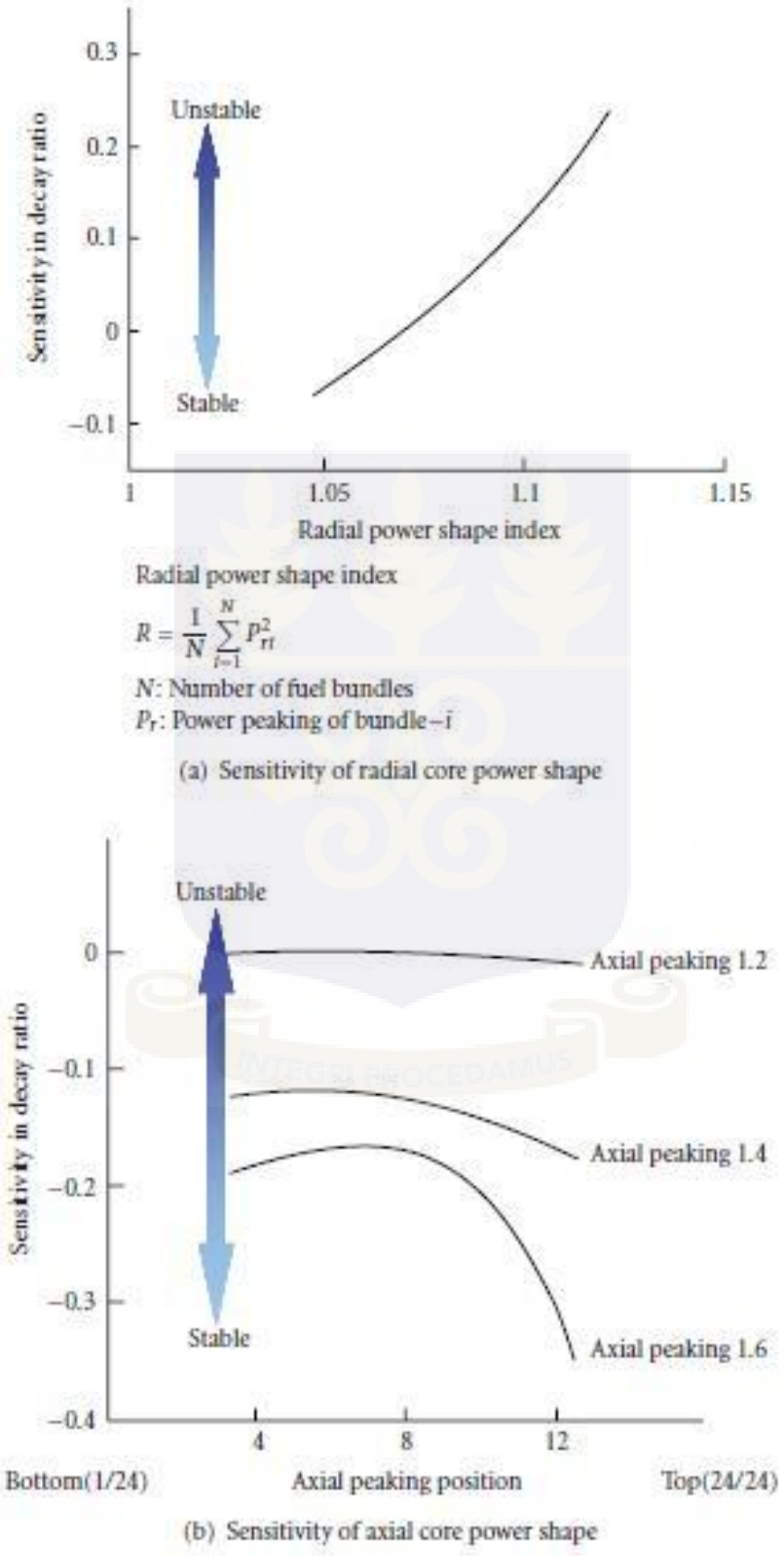

Figure 2.12: Sensitivity of core power shape to core stability decay ratio [39].

As for the radial power shape, fuel bundles with high power peaking factors tend to reduce the channel stability in the entire core, resulting in the core instability. The sensitivity regarding the axial power shape has more complicated nature as described below. The down skewed shape leads to the longer boiling length, which makes the frequency of the density wave oscillation greater than the time constant in the fuel heat conduction. This mismatch tends to result in the stable core power oscillation. On the other hand, the flat and/or the middle-skewed shapes make the greater influence of neutronics in the high void region of the core, inducing the core instability due to increase in the negative void feedback.

2.4.2.3. Regional Instability

The basic phenomenon dominating the regional instability is similar to that for the core instability, and the coupled neutronic and thermal-hydraulic oscillation can be individually excited in two halves of a core with an out-of-phase mode. Previous researchers proposed that the regional instability is equivalent to the oscillation of the higher harmonics (1st azimuthal mode) of the neutron flux distribution, while the core instability is to the oscillation of the fundamental mode [47]. Hashimoto [48] derived the so-called 'modal point neutron kinetics equations in order to analytically represent the phenomenon, instead of the ordinary point kinetics equations:

$$\frac{dN_m(t)}{dt} = \frac{\rho_m^s - \beta}{\Lambda_m} N_m(t) + \frac{\rho_{m0}(t)}{\Lambda_m} N_0 + \sum_{n=0}^{\infty} \frac{\rho_{mn}(t)}{\Lambda_m} N_n(t) + \lambda c_m(t) \tag{2.1}$$

$$\frac{dc_m(t)}{dt} = \frac{\beta}{\Lambda_m} N_m(t) - \lambda c_m(t) \tag{2.2}$$

where

$$\rho_m^s = 1 - \frac{1}{k_m} \tag{2.3}$$

$$\rho_{mn} = \left\langle \phi_m^*, (\delta M - \delta L)\phi_n \right\rangle \Big/ \left\langle \phi_m^*, M_0 \phi_m \right\rangle \tag{2.4}$$

m is the order of the higher harmonic mode (m = 1, 2, . . .); N, c, and β are the core-averaged neutron flux, delayed neutron precursor, and delayed neutron fraction, respectively.

Physically, ρ_m^s represents the subcriticality of the mth harmonic mode, which is mathematically corresponding to the eigenvalue separation, and is a negative value in the above definition. Hashimoto [48] and Takeuchi et al. [49] pointed out that a smaller absolute value of the subcriticality makes the feedback gain of the regional oscillation larger, which is correlated to the first term of the right-hand side of Equation (2.1), inducing the regional instability.

As mentioned above, powers in two halves of a core oscillate with an out-of-phase mode; therefore, significant oscillations cannot be observed in the core-averaged power and inlet coolant flow responses. This comes about because the hydraulic flow response through the recirculation loop is less sensitive to the regional stability.

The control strategies under consideration for SCWRs which inherit vast knowledge from existing Light Water Reactors (LWRs) and Supercritical Fossil Power Plants (SCFPPs) are discussed in the next section.

2.5 CONTROL STRATEGIES FOR SCWRs

There are two types of plant control strategies for steam cycle power stations [2]. One is the boiler (reactor)-following-turbine control as in PWRs, since the reactor power naturally follows the electric power or the turbine inlet flow rate through heat removal at steam generators. The other is the turbine-following-boiler (reactor) control as in BWRs, due to the reverse response of the reactor power to the electric power of the turbine inlet flow rate through void reactivity feedback in the core. Fossil Power Plants (FPPs) use boiler-turbine-coordinated control where both electric power and pressure are controlled by a combination of turbine control valves and boiler input.

The SCWR adopts a once-through coolant system as found in the BWR. The coolant transfers the heat generated through fission in the fuel rods and thereby produces steam through boiling for the BWR [50]. The steam is directly used to drive the turbine and condensed back into water in a condenser. The water is preheated and sent back to the reactor core to complete the cycle.

In a BWR, there are three main parameters to be controlled: pressure, reactor power, and water level. The reactor pressure is controlled by regulating the opening of the turbine control valve. The turbine control valve is adjusted to maintain relatively constant pressure in the BWR. The temperature of the saturated steam is a function of the pressure only therefore the steam temperature is kept constant by maintaining the constant reactor pressure. The reactor power is controlled by changes in the recirculation flow rate or by moving the control rods. When an increase in the recirculation flow happens, the volume of the steam in the reactor core will be temporarily reduced for a faster rate in removing the steam voids. This results in higher coolant density and further leads to an increase in the reactivity and reactor power level. Withdrawing a control rod reduces the neutron absorption and increases the reactivity, which leads to an increase in the reactor power. Control rod movement is the normal method of making large adjustments in the reactor power.

The water inventory in a BWR can be evaluated by the water level in the reactor core. The feedwater flowrate is controlled to maintain the water level within a predetermined range. The feedwater control system utilizes signals from reactor vessel water level, steam flow, and feedwater flow, referred to as the three-element control. The coolant in the BWR also serves as the moderator, and the disturbances in the coolant flow affects the neutronics and the change in the reactor power also influences the dynamics of the coolant. The feedwater flow can be adjusted to achieve the required water level. At the same time, the reactivity is also changed due to the reactivity feedback caused by the change in the feedwater flow. The recirculation flow is independent of the feedwater flow and has negligible effects on the water level directly. The reactivity caused by the change in the feedwater flow rate can be compensated by the recirculation flow rate.

Among the three control systems above, dynamics of the pressure are fastest and those of the water level are slowest. The control of the water level is the most complex aspect and the changes in the reactor power and pressure can affect the dynamics of the water level.

In a BWR, there is no steam generator as a cushion between the reactor and the turbine. The disturbances from the reactor directly affect the behavior of the turbine and viceversa. Thus, the reactor and the turbine are directly coupled but the level of the coupling between them is low due to the existence of the boiling process. The dynamic process of the reactor is slow compared to that of the turbine. When the load is increased, the opening of the turbine governor valve is increased and more steam is drawn from the reactor. The recirculation flow rate is increased to raise the power level to meet the desired load demand. The water level can be adjusted to the desired level by increasing the feedwater flow rate. The feedwater flow rate is regulated to be proportional to the load level at steady-state conditions.

In a Supercritical Fossil Power Plants (SCFPP), a once-through cycle coolant is also applied. The feedwater is pumped to the boiler. In the boiler, water is heated and superheated steam is generated. The steam is then sent to the steam turbine, which is coupled to a generator to produce electricity. The steam out of the turbine is cooled by the condenser and sent back to the boiler. There are mainly four parts in the boiler of an SCFPP: economizer, evaporator, superheaters and reheaters. In the economizer, the feedwater is preheated. In a subcritical once-through power plant, boiling takes place and the steam is produced in the evaporator. The heat flux in the evaporator is the highest with more than half of the temperature increase occurring in it. The large specific heat region of supercritical water is also located in the evaporator. The steam is superheated in the superheaters and reheated in the reheaters using the flue gas, before it is sent to the turbine. The load, the steam temperature and steam pressure of an SCFPP are all affected by the turbine control valve, fuel/air flow and feedwater flow rate. The SCFPP boiler can be modelled as a three-input and three-output system. The control strategy can be different depending on the operation mode selected.

In the turbine-following-boiler operation mode, the steam pressure is mainly regulated by the opening of the turbine control valve. The power is generated by a combustion process and determined by the fuel/air flow. The fuel/air flow is an index for the power output and used to follow the load demand. The water inventory of an SCFPP is evaluated by the intermediate temperature, which is measured at the outlet of the evaporator. The intermediate temperature is required to be slightly higher than the pseudo-critical temperature of the corresponding pressure to ensure the cooling capacity of the boiler. The main steam temperature is controlled by the fuel to feedwater flow ratio and superheater sprayer. The fuel to feedwater flow ratio is the main manipulated variable to regulate the main steam temperature. The superheater sprayer is a supplement and only used to reduce steam temperature at emergency conditions. The fuel to feedwater flow ratio is the most critical variable for the operation of an SCFPP. It is used not only to meet the steam requirement of the turbine but also to regulate the main steam temperature. Because of the presence of large time constants in the boiler due to the large metal mass and delays in the combustion system, the feed-forward control is introduced to maintain the fuel to feedwater flow ratio when it is required to operate the plant at large load gradients or to stress the plant as little as possible.

In the boiler-following-turbine mode, the turbine governor as a fast-acting load controller is used. Opening the governor valves releases the stored energy in the boiler and meets short-term increases in the electrical demand. These actions alter the main steam pressure, and the pressure controller adjusts the fuel-firing rate to maintain the main steam pressure.

The sliding pressure mode is an evolutionary extension from the constant pressure mode. When the load is varying, the steam pressure also varies. At a low load output, the reduced throttling-back action by the governor control valves leads to improved unit efficiency. Sliding pressure operation also provides fast unit loading, and enables stable operation of the turbine at lower temperature and pressure conditions.

The once-through cycle adopted in the SCFPP leads to a strong coupling between the boiler and the turbine. It is necessary to integrate the boiler and turbine as a whole and consider the balance of energy supply and demand. A coordinated control strategy is applied to coordinate the activities of various subsystems of an SCFPP so as to minimize the influence of both plant-wide interactions and disturbances and to avoid violating thermal constraints during large load changes and system disturbances. The coordinated control system, which unites the boiler and turbine controls, generates and regulates the setpoint of unit load. The demand signals are sent out to the Boiler Master and Turbine Master in parallel. The Boiler Master demand is used to regulate the feedwater flow and firing rate to improve the unit response to a load change. The Turbine Master demand controls the turbine control valves.

Several similarities between SCWR and BWR or PWR were identified to determine the control strategy [51]. The similarities for BWR are associated with the direct cycle with feedwater flow entering directly into the reactor vessel and steam flow going directly to the turbine. A balance between feedwater and steam is required to maintain the water inventory in the vessel.

The similarities for PWR are associated with the high operating pressure, the single-phase conditions at the core outlet and a core outlet temperature. Unique aspects of the SCWR that influence the control concept include the elimination of the recirculation pumps, the low water inventory in the reactor pressure vessel, the large change in the coolant density across the core, and the absence of a coolant level under supercritical conditions.

Considering the characteristics of SCWR, two recommendations were made for the SCWR control system based on the base load operation assumption:

a) Control of the main reactor parameters: The control rods are used to control the thermal power. The turbine control valve provides the control of the pressure, and the feedwater flow performs the control of the outlet temperature. The coolant inventory in the vessel is

controlled by assuring that the steam and the feedwater flow are balanced at the same time maintaining the correct core outlet temperature.

b) Integrated control system approach: The relatively small vessel water inventory, the neutronic/thermal-hydraulic coupling, the lack of level indication under supercritical conditions and the absence of recirculation flow make control more challenging. Thus, the use of an integrated control would allow the system to anticipate changes and react accordingly.

Nakatsuka et al [52] studied the control system design for a Supercritical Fast Reactor (SCFR) plant. A computer code was developed for transient behavior analysis of the SCFR. Lumped parameter and nodal methods were used for the thermal-hydraulic modeling. The reactor core was represented as a single channel. The dynamic behaviours of the SCFR were analyzed through introducing different perturbations of feedwater flow rate, control rods and turbine control valves. Based on the observations of the dynamic responses, the input-output pairings were determined: the pressure is controlled by the turbine control valves, the main steam temperature is controlled by the feedwater flow rate and the core power is controlled by the control rods. The control strategy of a BWR was applied to control system design of the SCFR. Sequential loop closing approach and trial and error method were carried out to tune the parameters of the control system. The chosen tuning criteria were damping ratio larger than 0.75 and overshoot less than 15%. Typical disturbances were introduced to investigate the reactor behavior with the designed control system. It was concluded that the designed control system could keep the SCFR plant stable against different disturbances, such as setpoint changes and feedwater temperature changes.

The work on the control system design for the SCFR was extended to the control system of High Temperature Supercritical Light Water Reactor (SCLWR-H) [53]. A similar design procedure was adopted in the control system design of SCLWR-H. Figure 2.13 presents the control system of SCLWR-H.

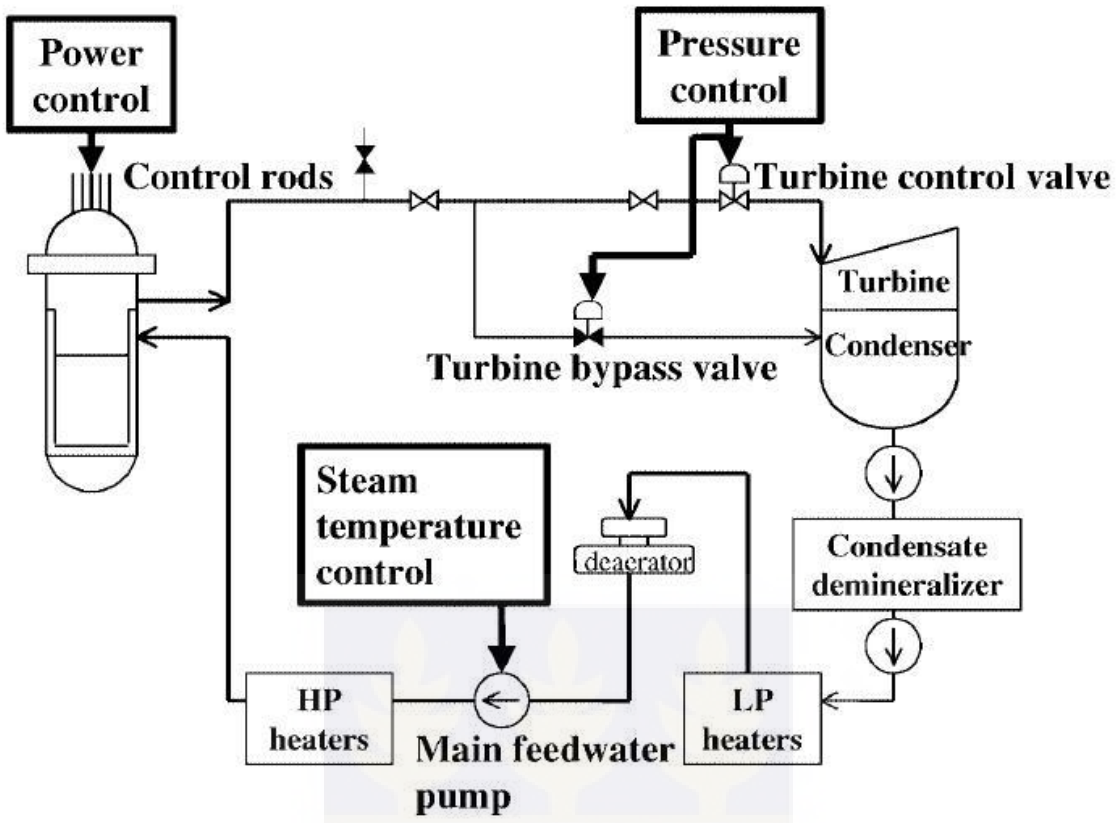

Figure 2.13: Control system of SCLWR-H [53]

It was discussed that the coolant density coefficient depended on the core design, while the Doppler coefficient is almost constant. From the viewpoint of plant control, it was argued that the coefficient of density should be neither too small nor too large. Variations of coefficient of density for the square assembly subchannel slice with rod are discussed in Chapter 6 of this work.

Ishiwatari et al [54] improved the feedwater controller for a Super Fast Reactor (Super FR) to suppress the variation of the main steam temperature. The plant system code SPART-F was used to model the Super FR. The original feedwater controller was designed only considering the deviation of the main steam temperature. The variation of the main steam temperature of the Super FR to different disturbances is large due to its high power-to-flow ratio. To reduce the variation, three parameters were considered in the modified feedwater controller design: the deviation of the power-to-flow ratio referred to as option A, the deviation of the power as option B, and the time derivative of the power as option C. The trial and error method was applied in the controller design. Five

typical perturbations were analyzed to confirm the performance of the new feedwater controllers. It was observed that the feedwater controller for option B gave a smaller or at least not large variation of the main steam temperature compared with the original one under all the perturbations, while the feedwater controllers for options A and C resulted in a larger variation in particular cases. It was concluded that the original feedwater was successfully improved by the feedwater controller for option B.

These systems are designed in a decentralized structure. Decentralized control techniques decompose the global system to a set of local sub-systems for which local controllers are designed. Decentralized control is only valid when the weakly-coupled requirement is satisfied. The SCWR is a Multiple-Input Multiple-Output (MIMO) system with strong interactions among inputs and outputs. Decentralized control can only achieve limited control performance and may even cause dynamic stability issues. Decoupling control is an efficient approach to deal with cross-coupling and has been applied in different industries [50].

The plant control system of the Super LWR was designed based on the PID control principle [2].The plant control strategies of BWRs, PWRs, FPPs, and the Super LWR are compared in Table 2.2[2].

Table 2.2: Comparison of plant control strategies [2]

Control strategy		**Control method**		
		Electric power	Steam pressure	Reactor or boiler power
Super LWR	Turbine following reactor	Reactor power	Turbine control valves	Control rods
BWR	Turbine following reactor	Reactor power	Turbine control valves	Control rods, recirculation

				pumps
PWR	Reactor following turbine	Turbine control valves	Reactor power	Control rods
FPP	Boiler turbine coordinated	Turbine control valves, boiler input		

Sun [50] considered three regions in the core of the Canadian SCWR depending on bulk and wall temperatures being higher or lower than the pseudo-critical temperature. The model was validated with both steady-state and transient simulations and was reported to predict the dynamic behavior of the reactor.

The control of the steam cycle of the HPLWR has been studied by Schlagenhaufer et al [55]. Different treatments were given to load range, when the turbine generator is connected with the grid, and a start-up range, when the system is pressurized, the thermal power of the reactor core is ramped up to a minimum power, and the components of the steam cycle are warmed up [3]. In order to keep the steam temperature at nominal temperature of 500 °C at the reactor outlet to gain plant load efficiency, Schlagenhaufer et al [55] has suggested that the core power be controlled by the control rods and the steam temperature by the speed of the feedwater pump as compared to the suggestion by Oka et al. [2] to control the core power by the feedwater pumps and the steam temperature by the control rods of the core. The control loop for the operation in the load range of the HPLWR is shown in Figure 2.14 below.

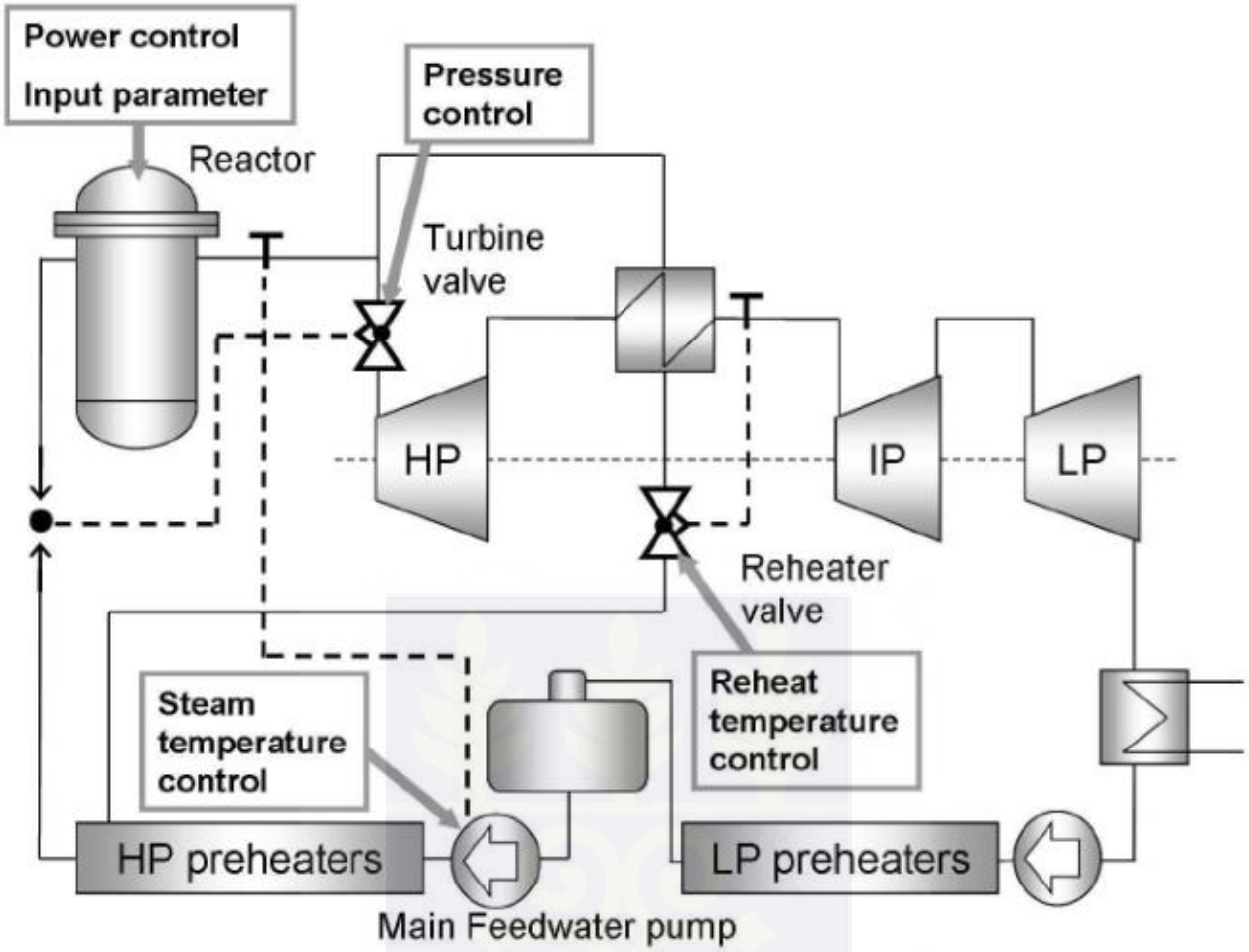

Figure 2.14: Control loops for operation in the load range of the HPLWR [55]

The control system has been modelled by Schlagenhaufer et al [55] with the system code APROS [56] to check its performance. A combined shut-down and start-up system, shown in Figure 2.15, has been proposed which allows to preheat the feedwater system and the turbines during start-up and to cool down all thick walled components slowly during shutdown [3].

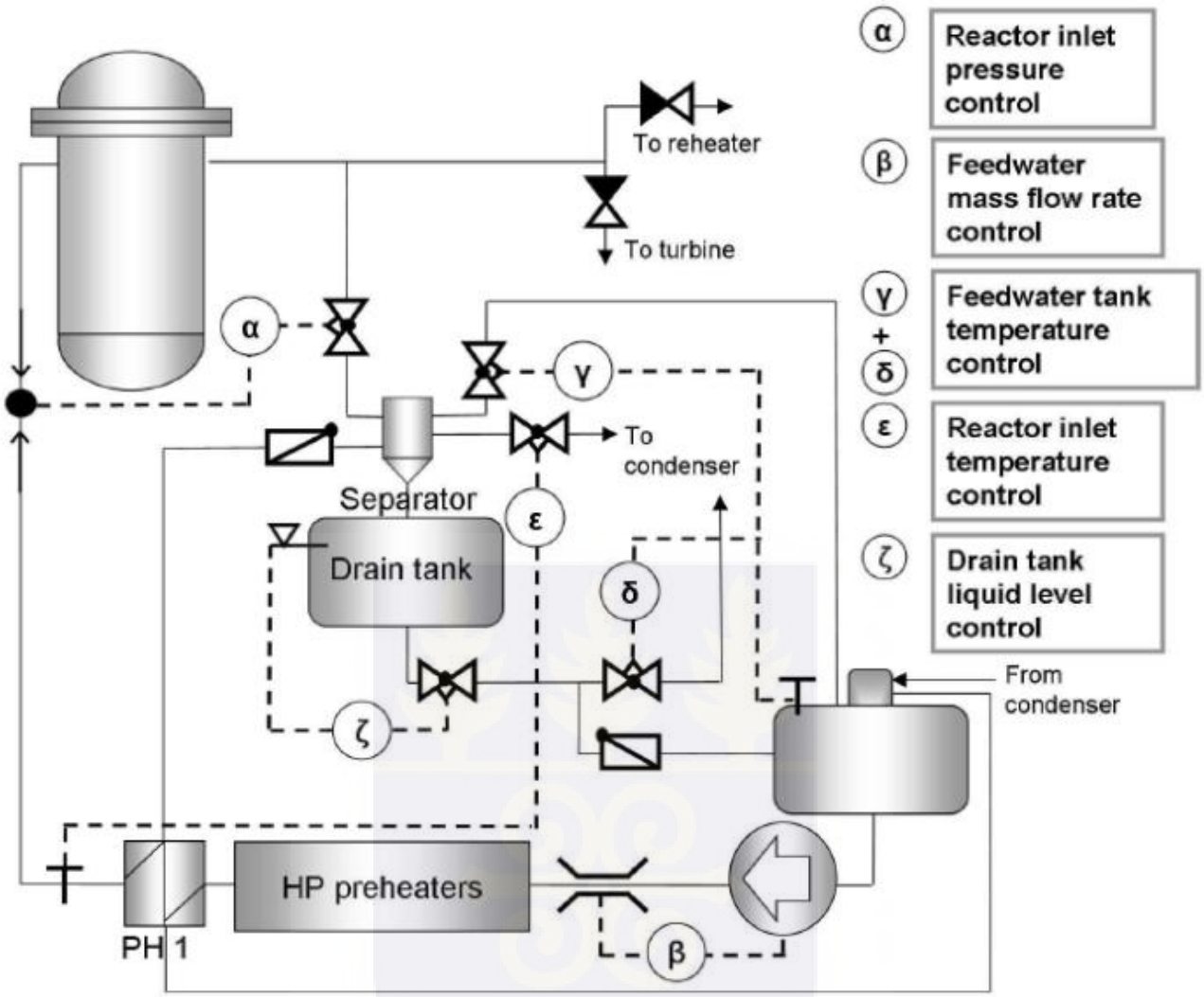

Figure 2.15: Control of the combined start-up and shutdown system for HPLWR [57].

From the above discussion, it can be seen that several efforts are underway to obtain viable control schemes for the SCWR concept. This study shall discuss the stability analysis of the SCWR in the ensuing chapters. The next section discusses the stability analysis of SCWRs with system codes and CFD tools.

2.6 APPLICATION OF SYSTEM CODES AND CFD TO STABILITY ANALYSIS

Stability analyses of the coolant flow through the three pass core of the HPLWR have been studied by Gòmez [58]. Like with BWR, Gomez showed that the most effective measure to avoid density wave oscillations in the core is the installation of orifices at the inlet of fuel assemblies. These orifices need to be customized for a hot fuel assembly.

The Delft University of Technology (DUT) has performed numerical as well as experimental work on a new facility, called DELIGHT and used codes based on COMSOL© and Matlab©[59].

Sanders [60] showed that the three-pass core configuration is more thermal-hydraulically stable than the single-pass configuration, which is mainly caused by the increased length the water needs to travel through the core. He also showed that, from the thermal-hydraulic stability point of view, the reactor becomes more stable if the inlet of the core would be at the outer peripheral of the core instead of the location of the current evaporator. Finally, increasing the pressure of the system by 1 MPa, if possible from the construction point of view, would significantly enhance the stability of the HPLWR due to the lowering of the density differences in the core section. Another numerical study showed that a natural-circulation driven supercritical water reactor shows an additional instability mode which might be related to a gravity-driven instability mechanism, similar to the one found in natural circulation driven BWR's.

Another stability issue, which was studied in the European Project, are xenon oscillations of the core power, like those known from conventional light water reactors (LWR). Reiss et al. [61, 62] studied these oscillations with single assembly clusters under HPLWR conditions. The diameter of the core of the HPLWR was about 3.5 meters, while the active height is 4.2 meters. These dimensions are in the range of LWRs where xenon oscillations were to be taken care of. On the other hand, due to the large density drop of water after crossing the pseudocritical point,

the migration length of the neutrons, which is an important parameter for the stability of the reactor against xenon oscillations, is larger than in current LWRs. The migration length in the HPLWR 3-pass core with a uniform fuel enrichment of 5% and a coarse, but representative temperature distribution was calculated to be 8.79 cm in the z direction (this is about twice as much as in a VVER-1000, where it is about 4.45 cm [63]). This finding and the strong temperature feedback may stabilize the reactor against xenon oscillations.

Thermal and stability considerations during power-raising phase of the SFR plant start-up were analysed [64, 65]. Ji et al. [66] carried out a linear stability analysis of an SCLWR-H with hexagonal fuel assembly.

Yi et al [38] summarized the analysis results of the thermal-hydraulic stability of the SCLWR-H using a linear stability analysis code in the frequency domain at constant supercritical pressure. The analytical method was based on linearization by perturbation of numerically-discretized one-dimensional single-channel single-phase conservation equations. The study reported that though the SCLWR-H has low coolant flow rate and large density change in the core, the thermal-hydraulic stability could be maintained both at normal operation and during power raising phase of constant pressure startup by applying an orifice pressure drop coefficient at the inlet of the fuel assemblies.

Yi et al.[31] employed the frequency domain linear analysis method to investigate the onset of instability of SCLWR-H. The analysis models contained six submodels - the neutronic kinetics models, the fuel rod heat transfer model, water rod heat transfer model, fuel channel thermal-hydraulic model, water rod thermal hydraulic model and the ex-core circulation system model. It was observed that unstable conditions may arise at low power operation and, in order to stabilize the reactor at startup, there is the need to decrease power to flow rate ratio at low power by increasing flow rate. It was reported that in order to satisfy the stability criterion, taken here as that of BWRs, the mass flow rate required for 40% core power was 50%, and the minimum mass flow rate required for 50% core power was about 59%.

Since the Supercritical pressure Water-cooled Fast Reactor (SWFR) is a fast reactor with supercritical pressure water coolant, only thermal hydraulic stability was considered in the work [64]. A frequency domain linear stability analysis code [31, 38, 67] was developed to investigate the thermal hydraulic stability of the SWFR. The stability analysis codes have been used to analyze the supercritical water-cooled thermal reactor successfully [31, 38, 67]. The governing equations were perturbed around steady state, linearized and Laplace-transformed from the time domain to frequency domain.

The resulting equations were used to construct the system transfer functions. The stability of the SWFR was investigated with respect to small perturbations in system parameters such as inlet flow velocity, inlet coolant pressure. The hottest channel was analyzed for thermal hydraulic stability analysis, because hotter channels are more unstable if all other factors are the same. The block diagram used for thermal hydraulic stability analysis is shown in Figure 2.16. Considering the fact that the volumes of the lower plenum, top dome, and upper plenum are greatly larger than the fuel channels, the velocity of the coolant in the lower plenum was significantly lower than that in the fuel channels; the coupled influence of downward channels and upwards channels on thermal hydraulic stability were neglected.

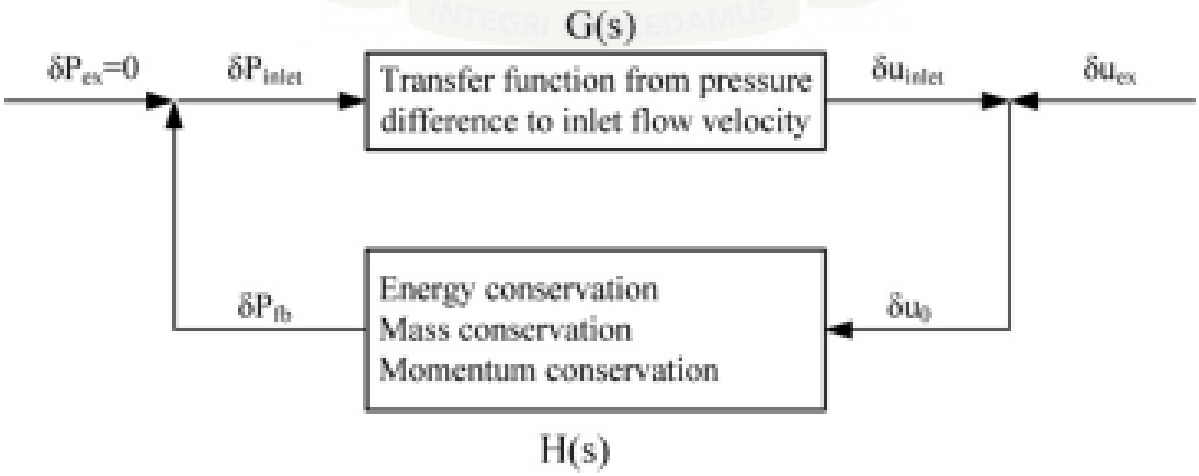

Figure 2.16: The block diagram for thermal-hydraulic stability of the SWFR [64].

Therefore, the thermal hydraulic stability analysis of upward channels and downward channels were carried out separately. The decay ratios for thermal hydraulic stability of the downward seed and blanket assemblies and upward seed assembly were also evaluated. According to core design [68], the orifice pressure drop coefficient was taken as 30.

Ambrosini and Sharabi [69] assessed the stability maps for heated channels with supercritical fluids as against the predictions of a system code. The physical system considered was a single channel with imposed external pressure drop. The results obtained in the study supported the correctness of the assumptions made in proposing dimensionless parameters for discussing the stability in heated channels with supercritical fluids. In particular, a good agreement was found between the dimensionless predictions of the simplified model and the data obtained in dimensional terms by RELAP5 for a realistic channel.

Ambrosini [70] presented results on the stability of a simple heated channel containing fluids at supercritical pressure with an external imposed pressure drop. Three different analysis tools, including a system code, RELAP5, and in-house linear and transient analysis programs, were adopted to evaluate stability thresholds at different channel throttling conditions and orientations. Four different supercritical fluids, carbon dioxide, water, ammonia and refrigerant R23, were considered. The diversity of the adopted tools and the good level of agreement observed in the comparison of their results provided adequate confidence on the general reliability of the results obtained.

Among the addressed phenomena, both Ledinegg and density-wave oscillations were considered, pointing out a fundamental continuity between the two phenomena that occurred in adjoining regions of the parameter space. Numerical effects were also highlighted, quantifying the impact of truncation error occurring in the use of system codes in the analysis of flow instabilities. The results obtained by different fluids provided further support to the conclusion that, when an appropriate

dimensionless formalism was used, the differences obtained in the stability behaviour at imposed heat flux were relatively small for a number of fluids of interest for experimental analyses.

Ambrosini and Sharabi [14] proposed dimensionless parameters for the analysis of stability in heated channels with supercritical fluids. The parameters were devised based on the classical phase change and sub-cooling numbers adopted in the case of boiling channels, proposing the novel formulation making use of fluid properties at the pseudo-critical temperature as a function of pressure. The adopted formulation for dimensionless density of a given fluid provided a unique dependence with respect to dimensionless enthalpy, in a reasonably wide range of system pressures, thus giving generality to the predictions of unstable conditions obtained as a function of dimensionless parameters. It was shown that the parameters allowed for setting up of quantitative stability maps for a single heated channel with imposed overall pressure drop, in analogy with the ones proposed in previous work concerning boiling channels. Similarities with the boiling channel stability phenomena were pointed out, also supporting the conclusions with system code predictions.

De Rosa et al [71] summarized the results obtained in the assessment of various CFD codes and models against experimental data related to heat transfer with fluids at supercritical pressure. The aim of the work was to summarise the lessons learned in this regard, drawing conclusions about model suitability. The results discussed addressed different codes, models, fluids and geometrical conditions. In particular, experiments with both water and carbon dioxide were considered, the FLUENT [72] and the STAR-CCM+ [73]commercial codes were used together with two different in-house codes adopting different k- ε , k- ω and k- τ models. Experimental data related to circular and non-circular ducts were addressed.

Ambrosini [74] explored the suitability of dimensionless numbers proposed in past work for the analysis of flow stability in heated channels containing fluids at supercritical pressure. The achievements obtained by their use in the application to heated channels with imposed heat flux

were summarised and the treatment was extended to imposed wall temperature conditions. Among the aspects considered to be relevant for analyses and experiments in support to the design of Supercritical Water Reactors, the following were given particular attention: basis for the selection of the dimensionless numbers; use of dimensionless numbers in defining stability boundaries; applications in fluid-to-fluid comparisons; dimensionless form to be adopted for temperature; identification of dimensionless numbers suitable for setting up heat transfer correlations with supercritical fluids. The lines of further research in the field were also discussed.

Ambrosini [75] assessed the capability of the commercial code STAR-CCM+ to predict heat transfer deterioration by the k-ε low-Re turbulent models, with main emphasis on the presence of heat deterioration in trans-pseudocritical conditions strongly affected by buoyancy; numerical aspects related to the implementation of fluid thermodynamic and thermophysical properties in the CFD code were also addressed. Parallel channel instability phenomena were considered, as predicted by the RELAP5 code, describing the instability patterns obtained in slightly asymmetric channels and the observed numerical stabilising effects occurring in perfectly symmetric channels. Relevant conclusions and future perspectives of the research were finally summarised. It was observed that the adopted low Reynolds number k-ε models available in the STAR-CCM+ code confirmed the results obtained in previous analyses, showing the capability to capture the conditions for the onset of deterioration in a reasonable way, though overestimating the consequent wall temperature increase. Some models conceived to deal with boundary layer phenomena by two-layer models were not necessarily able to simulate the buoyancy effects at the root of deterioration mechanisms. The analysis of parallel channel stability phenomena pointed out the possible numerical problems that may arise as a consequence of an unrealistic assumption of complete symmetry in the distribution of pressure drops in the parallel channels . Though the detailed reasons for the observed behaviour could be more clearly identified, the obtained results represented a clear warning about the possible occurrence of fictitious numerical stabilisation of unstable conditions. With the adopted boundary conditions, it was found that systems of two, three and four

parallel channels have stability thresholds for density-wave instabilities very close to the ones observed for a single channel with imposed pressure drop.

The researches on SCWR instabilities inherit a significant amount of knowledge and analysis tools from boiling water reactor studies. Many of the recent complex stability analyses developed for SCWR conceptual design derive methodologies and analytical tools from the wealth of methodologies and tools developed for BWR design. The similarities existing between boiling and supercritical pressure instability phenomena are, as expected, quite striking [13]. The techniques adopted for stability analysis of boiling water reactors are based on 1D thermal-hydraulic modelling and subchannel analysis, also because CFD techniques seem not to be mature enough to tackle efficiently so complex two-phase unsteady phenomena.

As a consequence, most of the recently adopted models for SCWR stability analyses are based on 1D cross section averaged mass, momentum and energy equations. Nevertheless, the absence of interfaces accompanying the remarkable property changes occurring at supercritical pressure allows for the application of CFD approaches based on the more mature techniques available for single-phase fluids. Though the flow of supercritical pressure fluids in heated channels is topologically simpler with respect to boiling flows, the presence of very dense and very light fluid regions has clear consequences in the resulting mixed convection conditions, which strongly affect the macroscopically observed heat transfer phenomena.

The use of CFD for the stability analysis of supercritical pressure flow stability problems is a recent approach. Sharabi et al. [76], making use of the FLUENT code, noted that in linearly increasing the power supplied to a vertical heated channel with time, it was possible to bring it to unstable behaviour, simulating self-sustained oscillations even in the lack of specific external perturbations. This behaviour, initially noted in a circular channel with 2D axial symmetric discretisation, was also obtained in 3D triangular and square pitch subchannel slices [15], showing approximately the same phenomenological features.

The first analyses for the circular channel and those for the subchannel slices were initially performed making use of the conventional near-wall treatment based on the use of wall functions. In such a case, the oscillations obtained were quite similar to those predicted by 1D models, except for the greater richness in spatial description of the phenomenon. However, in the case of the circular channel it was also tried to make use of a low Reynolds number k-ε model, obtaining less regular oscillation patterns, quite far from sinusoidal amplified or damped, involving also cycles of alternating heat transfer deterioration and restoration [76]. This behaviour is similar to that postulated during severe oscillations in boiling water reactor fuel, involving cycles of boiling transition and rewet. Nevertheless, since the evaluation of heat transfer deterioration by CFD models is still a challenge, with most of k-ε models predicting excessive overestimates of wall temperatures with respect to experimental data, this interesting prediction was considered a qualitative mimic of what could be possibly observed in real conditions.

Finally, it must be mentioned that a problem currently open in this field is the poor availability of experimental data to be used for comparison with code predictions. Only recently experiments that could be useful for such purpose have been made available [4]. As a consequence, the material presented in this study is limited to provide a preliminary basis for phenomenological assessment, addressing simple problems and comparing the results obtained for their stability as predicted by the CFD models with those available from 1D codes. This comparison, made in a more meaningful and comprehensive way than it was possible in previous analyses [76], provides a general picture of the capabilities of CFD models in predicting unstable behaviour in heated channels with supercritical fluids.

2.7 CONCLUDING REMARKS

The above review has highlighted many areas that still require further studies to facilitate the safety analysis of the SCWR. The current study extends the application of CFD in stability analysis of SCWR by analyzing the circular channel followed by the slices and then a square assembly slice with rod, kinetics, different flow directions, different power distributions, effect of throttling and many other details that shall be presented in the ensuing chapters.

Chapter 3 presents the tools and formulations that are adopted in the current study. The computational tools are described dwelling on input or model preparation, simulations and then post-processing options available in the computational tools. The dimensionless numbers mentioned in the review are also further discussed as they are implemented in the current study then the methodology used for computing decay ratios and period of oscillations are also presented in the next Chapter.

CHAPTER 3

TOOLS AND FORMULATIONS USED

3.1 INTRODUCTION

From the review presented in Chapter 2, it can be seen that the application of CFD for stability analysis of nuclear reactors is very limited. This Chapter discusses the computational tools used for this study and provides some review of the capabilities of the two main adopted codes which are STAR-CCM+ and RELAP5. The dimensionless numbers adopted in the study are also presented as well as the methodology for evaluating decay ratios and period of oscillations. The point kinetic models adopted are also discussed along with the properties of the fluids considered in this study.

3.2 COMPUTATIONAL FLUID DYNAMIC TOOL – STAR-CCM+

Computational Fluid Dynamics (CFD) codes are structured around the numerical algorithms that can tackle fluid flow problems accounting for turbulence effects [77]. The CFD codes contain three main elements: (i) a pre-processor, (ii) a solver and (iii) a post-processor. Pre-processing consists of the input of a flow problem to a CFD program by means of an operator-friendly interface and the subsequent transformation of this input into a form suitable for use by the solver. The three distinct streams of numerical solution techniques for CFD are finite difference, finite element and spectral methods. Finite volume method is used in the CFD adopted for the current study, STAR-CCM+ [73] which is equipped with versatile data visualization tools.

The STAR-CCM+ is an engineering program for solving problems involving flow of fluids or solids, heat transfer and stress in addition to its role as a CFD solver. The components of the suite include Three dimensional Computer-aided Design (3D-CAD) modeler, CAD embedding, Surface

preparation tools, automatic meshing technology, physics modeling, turbulence modeling, post-processing and Computer-aided Engineering (CAE) integration.

The object-oriented nature of the code can be seen in the user interface. An object tree is provided for each live simulation, containing object representations of all the data associated with the simulation.

3.2.1 Physics Models

The STAR-CCM+ physics modeling capabilities include:

(i) Solvers such as segregated, coupled and finite volume solid stress;

(ii) Time such as steady state, and implicit or explicit unsteady;

(iii) Turbulence such as RANS, RSM , LES/DDES and laminar-turbulent transition;

(iv) Compressibility such as ideal gas and real gas;

(v) Heat transfer such as conjugate heat transfer (CHT), multiband and grey thermal surface to surface radiation, solar radiation and discrete ordinates radiation (DOM) including participating media;

(vi) Multiphase such as Lagrangian particle tracking, Volume of Fluid (incompressible and compressible) among others;

(vii) Moving mesh such as dynamic fluid body interaction, rigid body motion, meshing morphing and multiple reference frames;

(viii) Combustion and chemical reaction such as reaction kinetics, eddy break up, presumed probability density function, complex chemistry, ignition and NOx modeling; and

(ix) Distributed resistance such as anisotropic, orthotropic, user defined and porous baffles as was used in implementing throttles discussed in Chapter 6.

3.2.2 Description of Turbulence models used in the analysis

In addition to its provision for inviscid and laminar flow, STAR-CCM+ has a comprehensive range of turbulence models:

(i) k-ε (standard, V2F, realizable and two-layer, etc.),

(ii) k-ω (standard, SST and Baseline (BSL)), Reynolds stress (RSM – linear and quadratic),

(iii) Spalart-Allmaras turbulence models,

(iv) boundary layer transition and

(v) large eddy simulation (LES).

The turbulent flow equations for compressible flows are [77]:

Continuity

$$\frac{\partial \bar{\rho}}{\partial t} + \mathrm{div}\left(\bar{\rho}\tilde{\mathrm{U}}\right) = 0 \tag{3.1}$$

Momentum equations

$$\frac{\partial\left(\bar{\rho}\tilde{U}\right)}{\partial t} + \mathrm{div}\left(\bar{\rho}\tilde{U}\tilde{\mathrm{U}}\right) = \frac{\partial \bar{P}}{\partial x} + \mathrm{div}\left(\mu \mathrm{grad}\tilde{U}\right) + \left[-\frac{\partial\left(\overline{\bar{\rho}u'^2}\right)}{\partial x} - \frac{\partial\left(\overline{\bar{\rho}u'v'}\right)}{\partial y} - \frac{\partial\left(\overline{\bar{\rho}u'w'}\right)}{\partial z}\right] + S_{Mx} \tag{3.2}$$

$$\frac{\partial\left(\bar{\rho}\tilde{V}\right)}{\partial t} + \mathrm{div}\left(\bar{\rho}\tilde{V}\tilde{\mathrm{U}}\right) = \frac{\partial \bar{P}}{\partial y} + \mathrm{div}\left(\mu \mathrm{grad}\tilde{V}\right) + \left[-\frac{\partial\left(\overline{\bar{\rho}u'v'}\right)}{\partial x} - \frac{\partial\left(\overline{\bar{\rho}v'^2}\right)}{\partial y} - \frac{\partial\left(\overline{\bar{\rho}v'w'}\right)}{\partial z}\right] + S_{My} \tag{3.3}$$

$$\frac{\partial\left(\bar{\rho}\tilde{W}\right)}{\partial t} + \mathrm{div}\left(\bar{\rho}\tilde{W}\tilde{\mathrm{U}}\right) = \frac{\partial \bar{P}}{\partial z} + \mathrm{div}\left(\mu \mathrm{grad}\tilde{W}\right) + \left[-\frac{\partial\left(\overline{\bar{\rho}u'w'}\right)}{\partial x} - \frac{\partial\left(\overline{\bar{\rho}v'w'}\right)}{\partial y} - \frac{\partial\left(\overline{\bar{\rho}w'^2}\right)}{\partial z}\right] + S_{Mz} \tag{3.4}$$

Scalar transport equation

$$\frac{\partial\left(\bar{\rho}\tilde{\Phi}\right)}{\partial t}+\operatorname{div}\left(\bar{\rho}\tilde{\Phi}\tilde{U}\right)=\operatorname{div}\left(\Gamma_{\Phi}\operatorname{grad}\tilde{\Phi}\right)+\left[-\frac{\partial\left(\overline{\bar{\rho}u'\varphi'}\right)}{\partial x}-\frac{\partial\left(\overline{\bar{\rho}v'\varphi'}\right)}{\partial y}-\frac{\partial\left(\overline{\bar{\rho}w'\varphi'}\right)}{\partial z}\right]+S_{\Phi} \qquad (3.5)$$

where the overbar indicates a time-averaged variable and the tilde indicates a density-weighted or Favre-averaged variable, and S_{Mx}, S_{My}, S_{Mz}, S_{ϕ} are the mean strain tensors.

The three categories of methods used to capture the effects of turbulence are:

a) **Turbulence models for Reynolds-averaged Navier-Stokes (RANS) equations**: The mean flow and the effects of turbulence on mean flow properties are considered. The most common RANS turbulence models are classified on the basis of the number of additional transport equations that need to be solved along with the RANS flow equations. The Mixing length model solves only the RANS flow equations; the Spalart-Allmaras model solves one extra transport equation; the k-ε, k-ω and Algebraic models solve two additional transport equations while the Reynolds stress model solves seven additional transport equations.

   In this study, some of the k-ε, k-ω and Reynold stress models are considered for low y+, all y+ and high y+ treatments as present in STAR-CCM+.

b) **Large eddy simulation (LES)**: It involves space filtering of the unsteady Navier-Stokes equations prior to the computations, which passes the larger eddies and rejects the smaller eddies. This method requires much computational resources due to the effort to solve the unsteady flow equations.

c) **Direct numerical simulation (DNS)**: This method computes the mean flow and all turbulent velocity fluctuations. The unsteady Navier-Stokes equations are solved on spatial grids that are sufficiently fine. These calculations are highly costly in terms of computing resources.

The RANS models adopted in the current study are standard k-ε, standard (Lien) low-Reynolds number k-ε, realizable k-ε, standard k-ω, SST k-ω and Reynolds stress. STAR-CCM+ formulations for the models are discussed below.

3.2.2.1 Standard k-ε Model

The k-ε model focuses on the mechanisms that affect the turbulent kinetic energy. A k-ε turbulence model is a two-equation model in which transport equations are solved for the turbulent kinetic energy, *k*, and its dissipation rate, *ε* [73]. The standard k-ε model [78] has two model equations, one for *k* and one for *ε*. The transport equations are of the form suggested by Jones and Launder [79], with coefficients suggested by Launder and Sharma [80]. Some additional terms are added to the model in STAR-CCM+ to account for effects such as buoyancy and compressibility.

Basic Transport equations for the standard k-ε model are:

$$\frac{d}{dt}\int_V \rho k dV + \int_A \rho k\left(v - v_g\right).dA = \int_A \left(\mu + \frac{\mu_t}{\sigma_k}\right)\nabla k.dA + \int_V \left[G_k + G_b - \rho\left(\left(\varepsilon - \varepsilon_0\right) + \Upsilon_M\right) + S_k\right]dV \qquad (3.6)$$

$$\frac{d}{dt}\int_V \rho\varepsilon dV + \int_A \rho\varepsilon\left(v - v_g\right).dA =$$

$$\int_A \left(\mu + \frac{\mu_t}{\sigma_\varepsilon}\right)\nabla\varepsilon.dA + \int_V \frac{1}{T}\left[C_{\varepsilon 1} + \left(G_k + G_{nl} + C_{\varepsilon 3}G_b\right) - C_{\varepsilon 2}\rho\left(\varepsilon - \varepsilon_0\right) + \rho\Upsilon_y + S_\varepsilon\right]dV \qquad (3.7)$$

where S_k and S_ε are the user-specified source terms for which the default values were used in the study, ε_0 is the ambient turbulence value in the source terms that counteract turbulence decay [81], G_b is the production due to buoyancy [82], Υ_M is the dilatation dissipation, Υ_y is the Yap correction, μ_t is the turbulent viscosity, and *T* is the turbulent time scale.

Turbulent Production

The production G_k is evaluated as:

$$G_k = \mu_t S^2 - \frac{2}{3}\rho k \nabla \cdot \mathrm{v} - \frac{2}{3}\mu_t \left(\nabla \cdot \mathrm{v}\right)^2 \tag{3.8}$$

where $\nabla \cdot v$ is the velocity divergence and S is the modulus of the mean strain rate tensor:

$$S = |\mathrm{S}| = \sqrt{2\mathrm{S}:\mathrm{S}^T} = \sqrt{2\mathrm{S}:\mathrm{S}} \tag{3.9}$$

and

$$S = \frac{1}{2}\left(\nabla \mathrm{v} + \nabla \mathrm{v}^T\right) \tag{3.10}$$

3.2.2.2 Standard (Lien) Low-Reynolds Number k-ε Model

Equation (3.6) serves as the first of the two equations for the Lien model [83]. The second equation is:

$$\frac{d}{dt}\int_V \rho\varepsilon dV + \int_A \rho\varepsilon\left(v - v_g\right).dA =$$

$$\int_A \left(\mu + \frac{\mu_t}{\sigma_\varepsilon}\right)\nabla\varepsilon.dA + \int_V \frac{1}{T}\left[C_{\varepsilon 1}\left(G_k + G_{nl} + G' + C_{\varepsilon 3}G_b\right) - C_{\varepsilon 2}f_2\rho\left(\varepsilon - \varepsilon_0\right) + \rho\Upsilon_y + S_\varepsilon\right]dV \tag{3.11}$$

where μ_t is the turbulent viscosity, T is the turbulent time scale, G' is the additional production term given by:

$$G' = Df_2\left(G_k + 2\mu\frac{k}{y^2}\right)\exp\left(-ER\,\mathrm{e}_y^2\right) \tag{3.12}$$

f_2 is the damping function defined as:

$$f_2 = 1 - C\exp\left(\mathrm{Re}_T^2\right) \tag{3.13}$$

where

$$\mathrm{Re}_y = \frac{\sqrt{k}\,y}{\nu} \tag{3.14}$$

and

$$\mathrm{Re}_t = \frac{k^2}{\varepsilon\nu} \tag{3.15}$$

The coefficients *C* and *E* are assigned default values of 0.3 and 0.00375, respectively.

3.2.6.3 Realizable k-ε Model

Equation (3.6) serves as the first of the two equations for the Realizable k-ε model. The second equation is:

$$\frac{d}{dt}\int_V \rho\varepsilon dV + \int_A \rho\varepsilon\left(v - v_g\right).dA =$$

$$\int_A\left(\mu + \frac{\mu_t}{\sigma_\varepsilon}\right)\nabla\varepsilon.dA + \int_V\left[C_{\varepsilon 1}S\varepsilon + \frac{\varepsilon}{k}\left(C_{\varepsilon 1}C_{\varepsilon 3}G_b\right) - \frac{\varepsilon}{k+\sqrt{\nu\varepsilon}}C_{\varepsilon 2}\rho\left(\varepsilon - \varepsilon_0\right) + S_\varepsilon\right]dV \tag{3.16}$$

The turbulent viscosity is computed as:

$$\mu_t = \rho C_\mu \frac{k^2}{\varepsilon} \tag{3.17}$$

Where the coefficient C_μ is no longer constant as with the standard k-ε model, but is instead given by:

$$C_\mu = \frac{1}{A_0 + A_s U^{(*)} \frac{k}{\varepsilon}} \tag{3.18}$$

where

$$U^{(*)} = \sqrt{S:S - W:W} \tag{3.19}$$

The coefficients are given by:

$$\begin{aligned} A_s &= \sqrt{6}\cos\phi \\ \phi &= \frac{1}{3}\text{acos}\left(\sqrt{6}W\right) \\ W &= \frac{S_{ij}S_{jk}S_{ki}}{S^3} \\ A_0 &= 4.0 \end{aligned} \tag{3.20}$$

where S is the modulus of the mean strain rate tensor as defined in Equation (3.9).

3.2.2.4 Standard k-ω Model

The transport equations for the standard k-ω [84] model are:

$$\frac{d}{dt}\int_V \rho k dV + \int_A \rho k\left(v - v_g\right).dA = \int_A \left(\mu + \sigma_k \mu_t\right)\nabla k \cdot dA + \int_V \left(G_k - \rho\beta^* f_\beta\left(\omega k - \omega_0 k_0\right) + S_k\right)dV \tag{3.21}$$

$$\frac{d}{dt}\int_V \rho \omega dV + \int_A \rho \omega\left(v - v_g\right).dA = \int_A \left(\mu + \sigma_\omega \mu_t\right)\nabla \omega \cdot dA + \int_V \left(G_\omega - \rho\beta^* f_\beta\left(\omega^2 - \omega_0^2\right) + S_\omega\right)dV \tag{3.22}$$

where S_k and S_ω are user-specified source terms, k_0 and ω_0 are the ambient turbulence values in source terms that counteract turbulence decay [81], f_β is the vortex-stretching modification, and T is the turbulent time scale computed using Durbin's realizability constraint [85]

Turbulent Production

The production G_k is evaluated as in Equation (3.8) above.

The production of ω is evaluated as:

$$G_\omega = \rho\alpha\left[\left(\alpha^* S^2 - \frac{2}{3}\left(\nabla\cdot \mathrm{v}\right)^2\right) - \frac{2}{3}\omega\nabla\cdot \mathrm{v}\right] \tag{3.23}$$

where α and α* are constants, and S is the modulus of the mean strain rate tensor.

3.2.2.5 SST k-ω Model

The formulations used for the SST k-ω model are discussed in this section.

3.2.2.5.1 Basic Transport Equations

The transport equations for the SST k-ω model are:

$$\frac{d}{dt}\int_V \rho k dV + \int_A \rho k\left(v - v_g\right).dA = \int_A \left(\mu + \sigma_k \mu_t\right)\nabla k\cdot dA + \int_V \left(\gamma_{eff} G_k - \gamma'\rho\beta^* f_\beta\left(\omega k - \omega_0 k_0\right) + S_k\right)dV \tag{3.24}$$

$$\frac{d}{dt}\int_V \rho\omega dV + \int_A \rho\omega\left(v - v_g\right).dA = \int_A \left(\mu + \sigma_\omega \mu_t\right)\nabla\omega\cdot dA + \int_V \left(G_\omega - \rho\beta f_\beta\left(\omega^2 - \omega_0^2\right) + D_\omega + S_\omega\right)dV \tag{3.25}$$

where γ_{eff} is the effective intermittency provided by the Gamma ReTheta Transition model, D_{ω} is a cross-derivative term, T is the turbulent time scale computed using Durbin's realizability constraint [85]and $\gamma' = \min\left[\max\left(\gamma_{eff}, 0.1\right), 1\right]$.

3.2.2.5.2 Turbulent Production

The production of ω is evaluated as:

$$G_{\omega} = \rho\gamma\left[\left(S^2 - \frac{2}{3}\left(\nabla\cdot\mathrm{v}\right)^2\right) - \frac{2}{3}\omega\nabla\cdot\mathrm{v}\right] \tag{3.26}$$

where γ is a blended coefficient of the model and S is the modulus of the mean strain rate tensor.

3.2.2.6 Reynolds Stress Model (RSM)

The Reynolds Stress Turbulence node is the placeholder object to allow selection of Reynolds Stress turbulence sub-models. Reynolds stress transport (RST) models are the most complex turbulence models in STAR-CCM+. By solving the transport equations for all components of the specific Reynolds stress tensor, $R = -T_t/\rho \equiv \overline{\mathrm{v}'\mathrm{v}'}$, these models naturally account for effects such as anisotropy due to strong swirling motion, streamline curvature, rapid changes in strain rate and secondary flows in ducts.

The Linear Pressure Strain was adopted in the current study. The linear pressure-strain model of Gibson and Launder [86] uses a classic approach to modelling the pressure-strain term, splitting it up into a slow (return-to-isotropy) term, a rapid term, and a wall-reflection term.

3.2.2.6.1 Reynolds Stress Diffusion

A simple isotropic form of the turbulent diffusion is adopted such that:

$$\mathrm{D} = \left(\mu + \frac{\mu_t}{\sigma_k} \right) \nabla \mathrm{R} \tag{3.27}$$

where the turbulent Schmidt number is $\sigma_k = 0.82$ and the turbulent viscosity is computed as:

$$\mu_t = \rho C_\mu \frac{k^2}{\varepsilon} \tag{3.28}$$

With the turbulent kinetic energy *k* being defined as:

$$k = \frac{1}{2} \mathrm{tr}\left(\mathrm{R}\right) \tag{3.29}$$

3.2.6.6.2 Turbulent Dissipation Rate

The isotropic turbulent dissipation rate is obtained from a transport equation analogous to the k-ε model and with identical boundary conditions:

$$\frac{d}{dt}\int_V \rho\varepsilon dV + \int_A \rho\varepsilon\left(v - v_g\right).dA = \int_A \left(\mu + \frac{\mu_t}{\sigma_\varepsilon} \right) \nabla\varepsilon.dA + \int_V \left\{ \frac{\varepsilon}{k} \left[C_{\varepsilon 1} \left(tr\left(P\right) + C_{\varepsilon 3} tr\left(G\right) \right) - C_{\varepsilon 2}\rho\varepsilon \right] \right\} dV \tag{3.30}$$

where the coefficient $C_{\varepsilon 1} = 1.44$ and $C_{\varepsilon 2} = 1.92$ for the linear pressure-strain used in this work.

The effect of the turbulence models on the stability analysis is discussed in Chapter 4.

3.2.7 Post-Processing

STAR-CCM+ has a comprehensive suite of post-processing tools designed to obtain maximum value and understanding for the CFD simulations. This includes scalar and vector scenes, streamlines, scene animation, numerical reporting, data plotting, import and export of table data, and spectral analysis of acoustical data.

3.3 SYSTEM CODE – RELAP5

The RELAP5 code is a system code that provides best-estimate transient simulation of light water reactor coolant systems during postulated accidents [87]. RELAP is an acronym for Reactor Excursion and Leak Analysis Program. The code models the coupled behaviour of the reactor coolant system and the core for loss-of-coolant accidents and operational transients such as anticipated transient without scram, loss of offsite power, loss of feedwater and loss of flow. A generic modeling approach is used that permits simulating a variety of thermal hydraulic systems. Control system and secondary system components are included to permit modeling of plant controls, turbines, condensers, and secondary feedwater systems.

The RELAP5/MOD3.3 code used in this work is based on a nonhomogeneous and nonequilibrium model for the two-phase system that is solved by a fast, partially implicit numerical scheme to allow for economical calculation of system transients. The code includes many generic component models from which general systems can be simulated. The component models include pumps, valves, pipes, heat releasing or absorbing structures, reactor point kinetics, electric heaters, jet pumps, turbines, separators, accumulators, and control system components. In addition, special process models are included for effects such as form loss, flow at an abrupt area change, branching and choked flow.

The system mathematical models are coupled into an efficient code structure. The code includes extensive input checking capability to help the user discover input errors and inconsistencies. Also included are free-format input, restart, renodalization and variable output edit features.

3.3.1 Top Level Organization

RELAP5 is coded in a modular fashion using top-down structuring. The various models and procedures are isolated in separate subroutines. The top level structure is shown in Figure 3.1 below and consists of input (INPUT), transient/steady-state (TRNCTL) and stripping (STRIP) blocks.

The INPUT processes input, checks input data, and prepares required data blocks for all program options. The first phase reads all input data, checks for punctuation and typing errors, and stores the data keyed by card number such that the data are easily retrieved. A list of the input data is provided, and punctuation errors are noted. During the second phase, restart data from a previous simulation are read if the problem is a RESTART type, and all input data are processed. Some processed input is stored in fixed common blocks, but the majority of the data are stored in dynamic data blocks that are created only if needed by a problem and sized to the particular problem. In a NEW-type problem, as was used in this work, dynamic blocks must be created. Extensive input checking is done, but at this level, checking is limited to new data from the cards being processed.

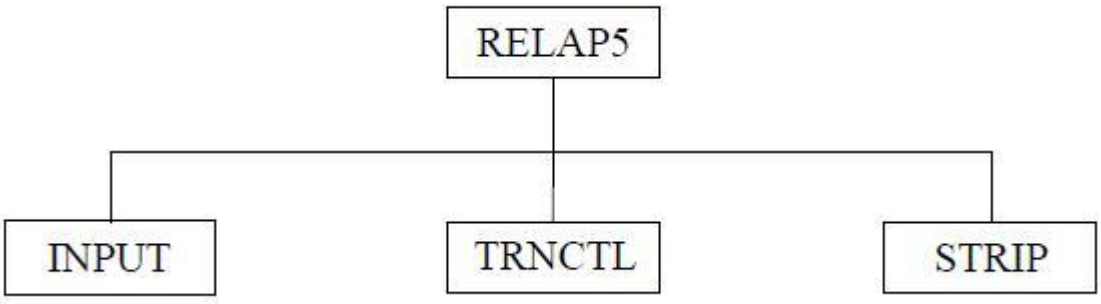

Figure 3.1. RELAP5 top level structure [87].

The third phase of processing begins after all input data have been processed. Since all data have been placed in common or dynamic data blocks during the second phase, complete checking of interrelationships can proceed. The initialization required to prepare the model for the start of the transient advancement is done at this level.

The TRNCTL handles both transient and the steady-state options. The steady-state option determines the steady-state conditions if a properly posed steady-state problem is presented. Steady state is obtained by running an accelerated transient until the time derivatives approach zero. Thus, the steady-state option is very similar to the transient option but contains convergence testing algorithms to determine satisfactory steady state, divergence from steady state, or cyclic operation. If the transient technique alone were used, approach to steady state from an initial condition would be identical to a plant transient from that initial condition. Pressures, densities, and flow distributions would adjust quickly, but thermal effects would occur more slowly. To reduce the transient time required to reach steady-state, the steady-state option artificially accelerates heat conduction by reducing the thermal capacity of the conductors. The STRIP extracts simulation data from a restart plot file for convenient passing of RELAP5 simulation results to other computer programs.

3.3.2 Hydrodynamic Model

The RELAP5 hydrodynamic model is a one-dimensional, transient, two-fluid model for flow of a two-phase steam-water mixture that can contain noncondensable components in the steam phase and/or a soluble component in the water phase. The options of simpler hydrodynamic models include homogeneous flow, thermal equilibrium, and frictionless flow models. The two-fluid equations of motion that are used as the basis for the model are formulated in terms of volume and time-averaged parameters of the flow. Phenomena that depend upon transverse gradients, such as

friction and heat transfer, are formulated in terms of the bulk properties using empirical transfer coefficient formulations. The system model is solved numerically using a semi-implicit finite difference technique.

The basic two-fluid differential equations possess complex characteristic roots that give the system a partially elliptic character and thus constitute an ill-posed initial boundary value problem [97]. In RELAP5, the numerical problem is rendered well-posed by the introduction of artificial viscosity terms in the difference equation formulation that damp the high frequency spatial components of the solution.

The RELAP5 thermal-hydraulic model solves eight field equations for eight primary dependent variables. The primary dependent variables are pressure, phasic specific internal energies, vapour volume fraction or void fraction, phasic velocities, noncondensable quality, and boron density. The independent variables are time and distance. The secondary dependent variables used in the equations are phasic densities, phasic temperatures, saturation temperature, and noncondensable mass fraction in incondensable gas phase.

The constitutive relations include models for defining flow regimes and flow-regime-related models for interphase drag and shear, the coefficient of virtual mass, wall friction, wall heat transfer, and interphase heat and mass transfer. RELAP5/MOD3 computes junction interfacial friction coefficient using junction properties so that the interfacial friction coefficient can be consistent with the state of the fluid being transported through the junction. The code uses the drift flux and the drag coefficient methods for the phasic interfacial friction force computation.

3.3.3 Heat Structure Models

Heat structures provided in RELAP5 permit calculation of the heat transferred across solid boundaries of hydrodynamic volumes. Modeling capabilities of heat structures are general and

include fuel pins or plates with nuclear or electric heating, heat transfer across steam generator tubes, and heat transfer from pipe and vessel walls. Heat structures are assumed to be represented by one-dimensional heat conduction in rectangular, cylindrical or spherical geometry. Surface multipliers are used to convert the unit surface of the one-dimensional calculation to the actual surface of the heat structure. Temperature-dependent thermal conductivities and volumetric heat capacities are provided in tabular or functional form either from built-in or user-supplied data.

Finite differences are used to advance the heat conduction solutions. Each mesh interval may contain a different mesh spacing, a different material, or both. The spatial dependence of the internal heat source may vary over each mesh interval. The time-dependence of the heat source can be obtained from reactor kinetics, one of several tables of power versus time, or a control system variable. Boundary conditions include symmetry or insulated conditions, a correlation package, tables of surface temperature versus time, heat transfer rate versus time, and heat transfer coefficient versus time or surface temperature.

The RELAP5 dynamic gap conductance model defines an effective gap conductivity based on a simplified deformation model generated from FRAP-T6 [88]. The model employs three assumptions as follows: (a) the fuel-to-cladding radiation heat transfer, which only contributes significantly to the gap conductivity under the conditions of cladding ballooning, is neglected unless the cladding deformation model is activated; (b) the minimum gap size is limited such that the maximum effective gap conductivity is about the same order as that of metals; (c) the direct contact of the fuel pellet and the cladding is not explicitly considered.

3.3.4 Trip System

The trip system consists of the evaluation of logical statements. Each trip statement is a simple logical statement that has a true or false result and an associated variable, TIMEOF. The TIMEOF

variable is -1.0 whenever the trip is false, and contains the time the trip was last set true whenever the trip is true. This variable allows for time delays and unit step functions based on events during the transient. Within the structure of RELAP5, the trip system is considered to be only the evaluation of the logical statements. The decision of what action is needed, based on trip status, resides within other models.

3.3.5 Control System

The control system provides the capability to evaluate simultaneous algebraic and ordinary differential equations. The capability is primarily intended to simulate control systems typically used in hydrodynamic systems, but it can also model other phenomena described by algebraic or ordinary differential equations. Another use is to define auxiliary output quantities so they can be printed in major and minor edits and be plotted.

The control system consists of several types of control components. Each component defines a control variable as a specific function of time-advanced quantities. The time-advanced quantities include hydrodynamic volume, junction, pump, valve, heat structure, reactor kinetics, trip quantities, and the control variables themselves.

3.3.6 Point Reactor Kinetics Model

The point reactor kinetics model can be used to compute power behavior in a nuclear reactor. The power is computed using space-independent or point kinetics approximation which assumes that power can be separated into space and time functions. This approximation is adequate for cases in which the space distribution remains nearly constant. The model computes both the immediate

fission power and the power from decay of fission products. The model was adopted in the computations on the Square assembly subchannel with rod discussed in Chapter 6.

3.4 ONE-DIMENSIONAL MODEL FOR GENERATING STABILITY MAPS

The following balance equations are adopted respectively for the one-dimensional mass, momentum and energy equations along the models employed in this study in terms of cross-section averaged variables [5]:

$$\frac{\partial \rho}{\partial t}+\frac{\partial (\rho W)}{\partial z}=0 \tag{3.31}$$

$$\frac{\partial (\rho W)}{\partial t}+\frac{\partial \left(\rho W^{2}\right)}{\partial z}+\frac{\partial p}{\partial z}=-\rho g-\left[\frac{f}{D_h}+2K_{in}\delta_d(z)+2K_{out}\delta_d(z-L)\right]\frac{\rho W^{2}}{2} \tag{3.32}$$

$$\frac{\partial (\rho H)}{\partial t}+\frac{\partial (\rho H W)}{\partial z}=q'\frac{\prod_h}{A}f_q(z) \tag{3.33}$$

where W is the fluid velocity and K_{in} and K_{out} denote the singular pressure loss coefficients at inlet and outlet, respectively. The two functions δ_d appearing in the above equations represent dimensional Dirac delta functions [m^{-1}] centred at channel inlet and outlet respectively, translating the effect of localized pressure drops into mathematical formalism. In the energy equation, the terms related to flow-work and friction dissipation have been omitted, accepting a well-known approximation which is fully acceptable for the present purposes. A heat flux distribution function, $f_q(z)$ is introduced to allow the effect of different axial power distributions to be studied. This feature is adopted for the analyses involving bottom-peaked power profile in the current study.

3.5 ADOPTED DIMENSIONLESS PARAMETERS

The CFD calculations provide a considerable amount of data. Among the most interesting ones for our present use there are the inlet and outlet flow rates, which clearly show the tendency of the system to dampen or amplify perturbations.

In particular, the inlet flow rate, being generally characterised by larger excursions during unstable behaviour than the outlet one, is used to define a dimensionless power-to-flow ratio named "trans-pseudocritical number" and introduced in previous work together with other dimensionless parameters characterising the stability of a supercritical fluid flow system [14]. Among the most important dimensionless variables and parameters introduced, the following ones must be mentioned:

- a dimensionless fluid density:

$$\rho^* = \frac{\rho}{\rho_{pc}} \tag{3.34}$$

- a dimensionless bulk fluid enthalpy:

$$h^* = \frac{1}{v_{pc}}\left(\frac{\partial v}{\partial h}\right)_{p,pc}\left(h - h_{pc}\right) = \frac{\beta_{pc}}{C_{p,pc}}\left(h - h_{pc}\right) \tag{3.35}$$

- a pseudo-subcooling number:

$$N_{SPC} = \frac{\beta_{pc}}{C_{p,pc}}\left(h_{pc} - h_{in}\right) = -h_{in}^* \tag{3.36}$$

- a trans-pseudocritical number:

$$N_{TPC} = \frac{\dot{Q}}{W_{in}}\frac{\beta_{pc}}{C_{p,pc}} \tag{3.37}$$

- a distributed friction parameter:

$$\Lambda = \frac{f\ L}{2\ D_h} \tag{3.38}$$

- a channel Froude number:

$$Fr = \frac{w_{in}^2}{g\,L} \tag{3.39}$$

- a dimensionless fluid velocity:

$$w^* = \frac{w}{w_{in}} \tag{3.40}$$

- a dimensionless time:

$$t^* = \frac{t w_{in}}{L} \tag{3.41}$$

- a dimensionless z spatial coordinate:

$$z^* = \frac{z}{L} \tag{3.42}$$

- a dimensionless pressure:

$$p^* = \frac{p}{\rho_{pc} w_{in}^2} \tag{3.43}$$

- a dimensionless mass flux:

$$G^* = \rho^* w^* \tag{3.44}$$

As these definitions, in addition to a few others, make dimensionless the 1D balance equations governing the channel behaviour, it is therefore expected that they fully characterise the flow evolution in such an approximation. In this respect, it is quite interesting to compare this approach with CFD results obtained using STAR-CCM+ and RELAP5/MOD3.3 codes.

The distributed friction factors adopted in the study are presented in Table 3.1 below.

Table 3.1. Distributed friction factors adopted in the study

Model	SC-Channel	Square Slice	Triangular Slice
STAR-CCM+	4.5	6.0	8.0
RELAP5	4.5	6.0	8.0

3.6 EVALUATION OF PERIOD OF OSCILLATIONS AND OF THE DECAY RATIO

The time trends of the trans-pseudocritical number or of flow rate obtained after each stepwise change in power were processed in order to extract the relevant information on the period of oscillations and on the decay ratio. By definition, the latter is the ratio between the amplitudes of oscillations separated in time by a period and it could be measured graphically at each couple of oscillations. For a second order system, the equation governing the dynamics is

$$\ddot{y} + b\dot{y} + cy + d = 0 \tag{3.45}$$

and having the form

$$y(t) = e^{z_R t}\left[A\sin(z_I t) + B\cos(z_I t)\right] \tag{3.46}$$

a least square fit of the coefficients appearing in Equation (3.45) allows for calculating the exponents in the second order response and then the period (τ) and the decay ratio (DR):

$$\tau = \frac{2\pi}{z_I} \qquad DR = e^{z_R \tau} \tag{3.47}$$

Whenever an oscillatory behaviour is obtained, the coefficients appearing in the equation define the degree of damping and or amplification of the perturbations and the frequency of oscillations. As said, the algorithm adopted here for evaluating decay ratio and period of the oscillations is based on a least square determination of these coefficients, on the basis of the time series of the variable y

(N_{TPC} or inlet flowrate in the present case), assumed to satisfy the second order differential equation. In particular, the values of the variable *y* and finite difference approximations of the first and second time derivatives are adopted in order to obtain the least square fit of the constants.

This algorithm has demonstrated its usefulness in repeated applications, though it cannot be considered flawless, especially if applied to time windows in which the decay ratio varies strongly with time or if the oscillations contain evidently more than a single mode. These cases must be therefore discussed separately.

3.7 POINT NEUTRON KINETICS EQUATIONS

The seven point kinetics equations are solved assuming an equilibrium initial concentration of delayed neutron precursors; it is therefore

$$\begin{cases} \dfrac{dP}{dt} = \dfrac{r-\beta}{\Lambda} P + \displaystyle\sum_{i=1}^{6} \lambda_i C_i \\ \dfrac{dC_i}{dt} = \dfrac{\beta_i}{\Lambda} P - \lambda_i C_i \qquad (i = 1, \ldots, 6) \end{cases} \tag{3.48}$$

with initial conditions for the precursor concentrations obtained by:

$$C_i(0) = \frac{\beta_i}{\lambda_i \Lambda} P(0) \qquad (i = 1, \ldots, 6) \tag{3.49}$$

The simple time-integrated version of the point kinetics equations adopted in this work is the following:

$$\begin{cases} \dfrac{\Delta P}{\Delta t} = \dfrac{r^n-\beta}{\Lambda}\left(P^n + \theta \Delta P\right) + \displaystyle\sum_{i=1}^{6} \lambda_i \left(C_i^n + \theta \Delta C_i\right) \\ \dfrac{\Delta C_i}{\Delta t} = \dfrac{\beta_i}{\Lambda}\left(P^n + \theta \Delta P\right) - \lambda_i \left(C_i^n + \theta \Delta C_i\right), \qquad (i = 1, \ldots, 6) \end{cases} \tag{3.50}$$

where the seven unknowns are the time increments of power and concentrations, $\Delta P = P^{n+1} - P^n$ and $\Delta C_i = C_i^{n+1} - C_i^n, (i = 1,\ldots,6)$, and it is $0 \le \theta \le 1$, in order to obtain explicit, Crank-Nicholson or implicit integration schemes. Whatever the chosen value of θ, the values of the ΔC_i's can be eliminated in the first equation, making use of each precursor concentration equation, and an explicit formulation for power advancement can be reached. Once ΔP is known, the values of concentrations at the new time-step are then easily retrieved. A similar technique was used for the case of the single group of delayed neutrons considered in previous analyses [16].

The equation of the precursors' concentration can be rewritten as follows:

$$\Delta C_i = \frac{1}{1+\lambda_i \theta \Delta t}\left[\frac{\beta_i}{\Lambda} P^n - \lambda_i C_i^n\right]\Delta t + \frac{\frac{\beta_i}{\Lambda}\theta \Delta t}{1+\lambda_i \theta \Delta t}\Delta P \tag{3.51}$$

which can be written in the form:

$$\Delta C_i = \Theta_i + \Gamma_i \Delta P \qquad (i = 1,\ldots,6) \tag{3.52}$$

where

$$\Theta_i = \frac{1}{1+\lambda_i \theta \Delta t}\left[\frac{\beta_i}{\Lambda} P^n - \lambda_i C_i^n\right]\Delta t$$
$$\Gamma_i = \frac{\frac{\beta_i}{\Lambda}\theta \Delta t}{1+\lambda_i \theta \Delta t} \tag{3.53}$$

Substituting this expression into the equation of power, we get the power increment of the form:

$$\Delta P = \frac{\frac{\rho^n - \beta}{\Lambda} P^n \Delta t + \sum_{i=1}^{6} \lambda_i \left[C_i^n + \theta \Theta_i\right]\Delta t}{1 - \frac{\rho^n - \beta}{\Lambda}\theta \Delta t - \left(\sum_{i=1}^{6} \lambda_i \Gamma_i\right)\theta \Delta t} \tag{3.54}$$

In order to assess the validity of the adopted integration approach and the differences obtained by using different sets of constants for neutron kinetics parameters, a dedicated FORTRAN program developed to perform sensitivity analyses and the input deck are presented in Appendix. In all the considered cases, the prompt neutron lifetime was assumed to be assigned as $\Lambda=5\times10^{-5}$ s, while two different sets of delayed neutron fractions and of the related decay constants were considered, namely the ones reported in two well-known textbooks [89, 90] for U^{235} fuelled reactors moderated by H_2O.

Figure 3.2 to Figure 3.4 present the results of the sensitivity analyses.

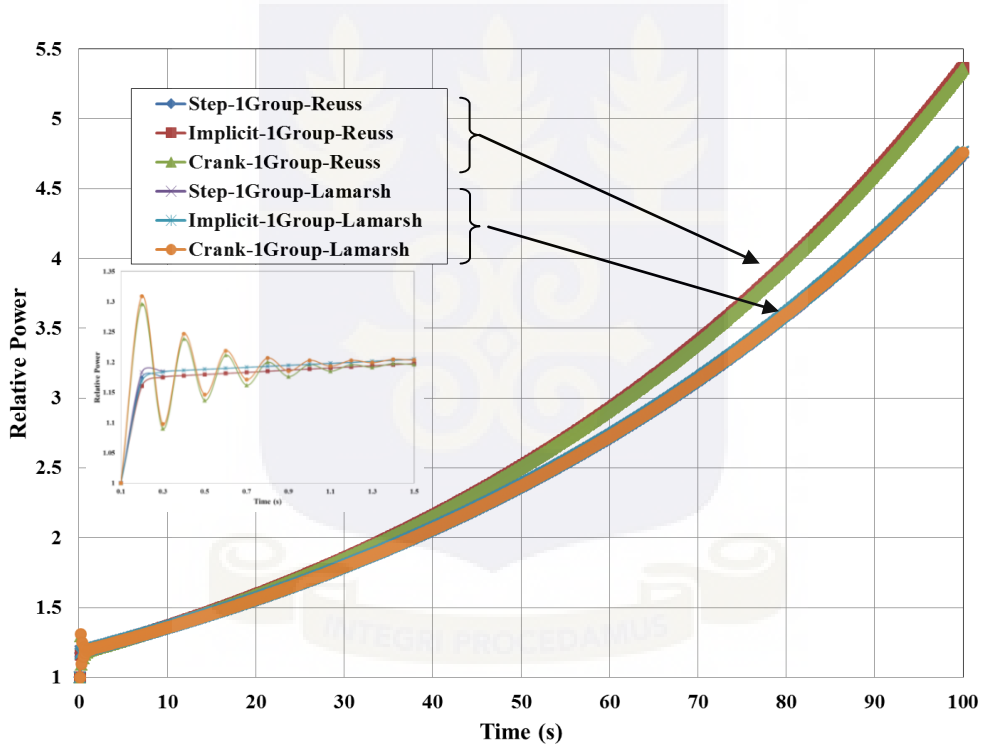

Figure 3.2. Sensitivity analyses on point kinetics: relative power vs. time for a 100 pcm step reactivity insertion with one delayed-neutron group compared with the exact solution (Step) for different options

In particular, Figure 3.2 compares the trends obtained in the calculation of a 0.001 step (100 pcm) in reactivity with both sets of constants for kinetics, the Crank-Nicholson or the implicit schemes and by analytical integration for the single delayed neutron group model. The adopted single group

parameters were obtained by an appropriate weighting. As can be noted, the constants suggested by Reuss [90] provide steeper increases in normalized power than the Lamarsh [89] ones. The comparison of the Crank-Nicholson and the implicit integration scheme results with the analytical solutions ("Step" in the legend) are both very satisfactory in the long term, though, as partly expected, the second order Crank-Nicholson integration scheme is prone to numerical oscillations, as highlighted in the zoomed snapshot reported on the left side of the figure.

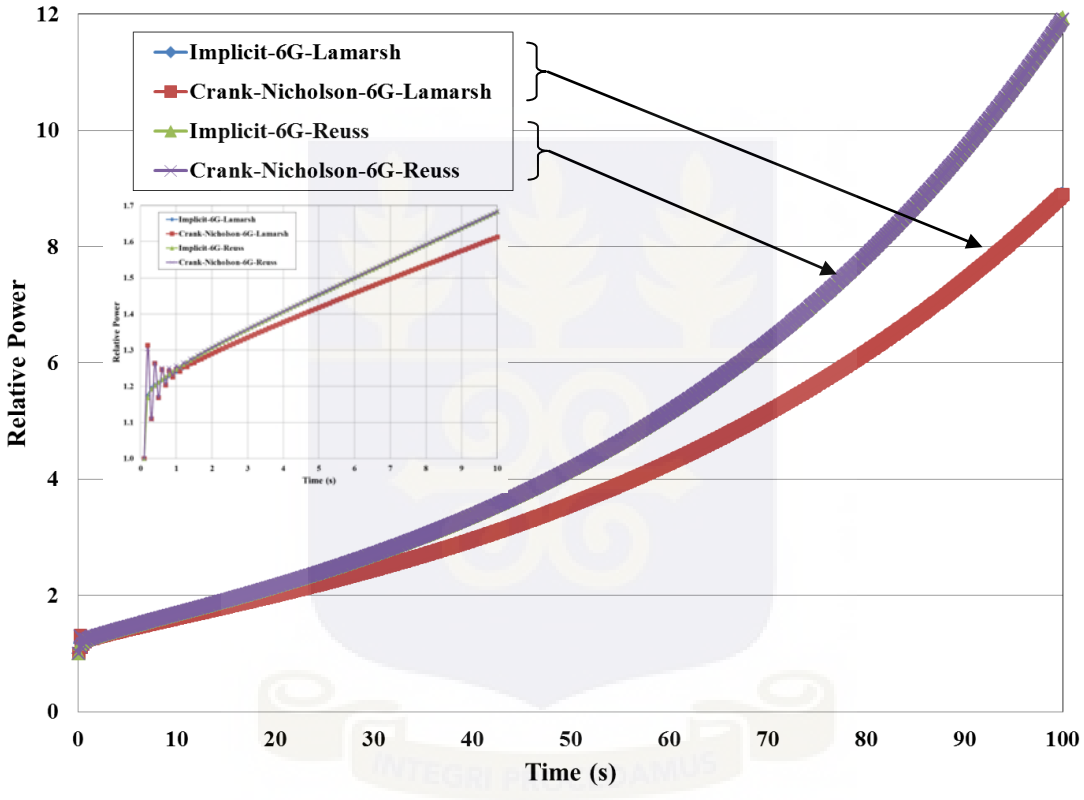

Figure 3.3.Sensitivity analyses on point kinetics: relative power vs. time for a 100 pcm step reactivity insertion with six delayed-neutron groups for different options

Figure 3.3 presents similar data for the six delayed neutron group model. In this case the analytical solution was not computed for comparison; however, the results obtained by the calculations for the Lamarsh [89] set of parameters compare very well with the data reported in Fig. 12-2 of the textbook. Finally, Figure 3.4 reports an overall comparison of all the considered cases; as a

consequence of this comparison and also because of the a posteriori consideration that the parameters proposed by Reuss [90] are similar to the default ones adopted in RELAP5, the six delayed neutron group model with Reuss [90] parameters was finally adopted in the java routine coupled with the CFD code in analyses that will be described later on.

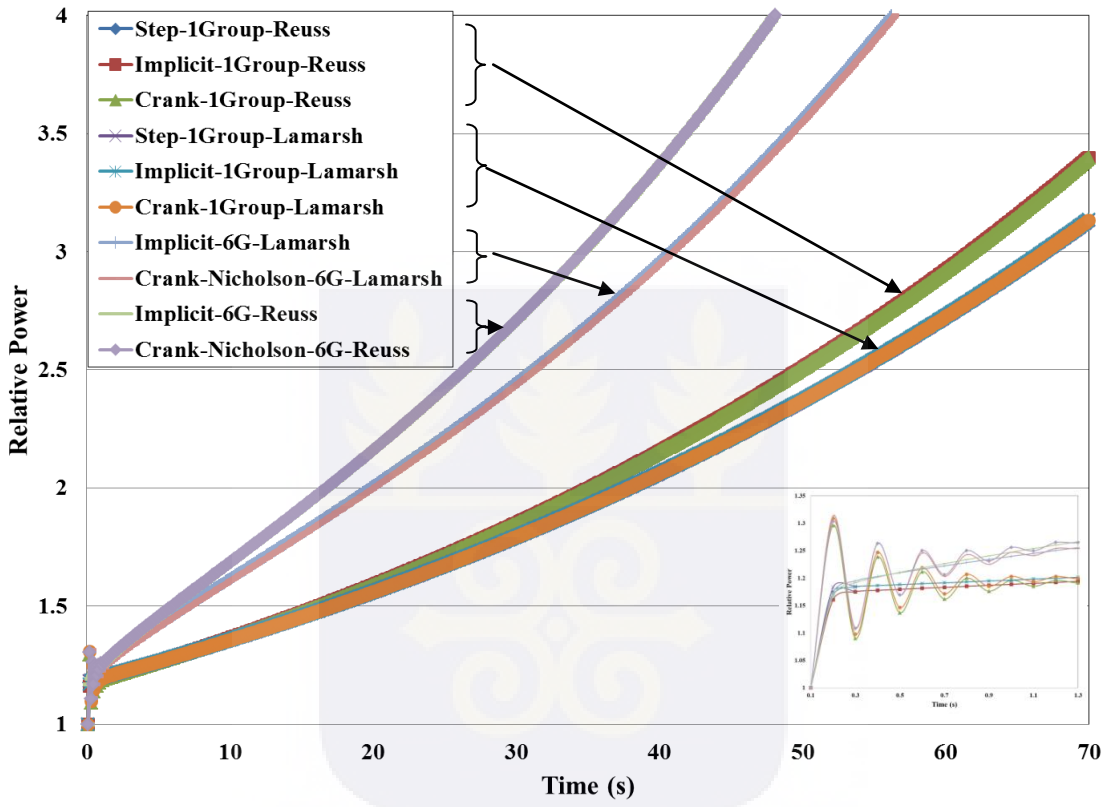

Figure 3.4.Sensitivity analyses on point kinetics: overall comparisons of the considered options

3.8 FLUID PROPERTIES

In previous work [70, 75], the results of one-dimensional codes were compared with the stability maps obtained for a circular pipe system considered in this work or for a variant obtained from it by different inlet and outlet throttling conditions. In these applications, water and other three fluids at supercritical pressures were considered, in order to assess the degree of generality of the dimensionless numbers proposed for representing results concerning stability. The fluids considered

in the fluid-to-fluid comparison for the circular channel are water, carbon dioxide, Freon-23 (R23) and ammonia. The operating conditions of these considered fluids are listed in Table 3.2, together with some of their relevant properties at the pseudocritical threshold for each selected operating pressure.

Table 3.2. Operating pressures and related pseudo-critical characteristics of the considered fluids

Fluid	P [MPa]	T_{pc} [K]	ρ_{pc} [kg/m^3]	h_{pc} [J/kg]	β_{pc} [1/K]	$C_{p,pc}$ [J/(kg K)]
Water	25.0	658.04	317.03	2152539	0.129	76445
CO_2	8.0	307.82	459.49	341448	0.299	35267
R23	5.7	306.37	537.01	288279	0.127	9941
NH_3	15.0	422.55	239.29	1314996	0.055	24292

Table 3.3 presents the fluid temperatures corresponding to different values of N_{SPC} for the four fluids at operating conditions of Table 3.2. Concerning the reasons for their choice, water at 25 MPa was obviously chosen as it represents a quite common reference condition for reactor applications, while carbon dioxide and R23 are substitute fluids used in different experimental facilities operated for studying heat transfer and stability. On the other hand, the choice of ammonia can be considered relatively exotic; nevertheless, its selection for these computational analyses is justified by the greater similarity that this fluid has with water with respect to the two other ones.

Table 3.3. Values of fluid temperatures corresponding to different values of N_{SPC} for the four different fluids at the operating conditions of Table 3.2

N_{SPC}	Water	CO_2	R23	NH_3
0.50	648.55 K	302.85 K	299.25 K	409.05 K
1.00	613.15 K	284.60 K	280.95 K	378.40 K
1.50	559.15 K	258.45 K	255.95 K	337.00 K
2.00	495.75 K	228.90 K	227.25 K	290.50 K
2.50	427.30 K	-	196.25 K	241.40 K

Figure 3.5 compares the dimensionless densities of the four considered fluids with each other as a function of dimensionless enthalpy. The great similarity of the obtained trends, except for slight deviations in the liquid-like region, justifies the adoption of a single dimensionless state equation for different fluids at very different supercritical pressures. The dimensionless state equation was used in setting up stability maps based on 1D balance equations [14]. However, when heat transfer phenomena are considered, it is less straightforward to make fluids compare successfully to each other, as demonstrated by recent attempts carried out with this aim [91], since properties as thermal conductivity and viscosity are more difficult to scale in a meaningful way. This consideration supports the choice made in Chapters 4 and 5 to use wall functions in place of low-Reynolds number models, in order to avoid mixing phenomena depending on the detailed behaviour at the wall with the overall bulk flow behaviour. A reliable analysis of near wall behaviour requires appropriate models for predicting heat transfer deterioration, which are not yet available at the moment.

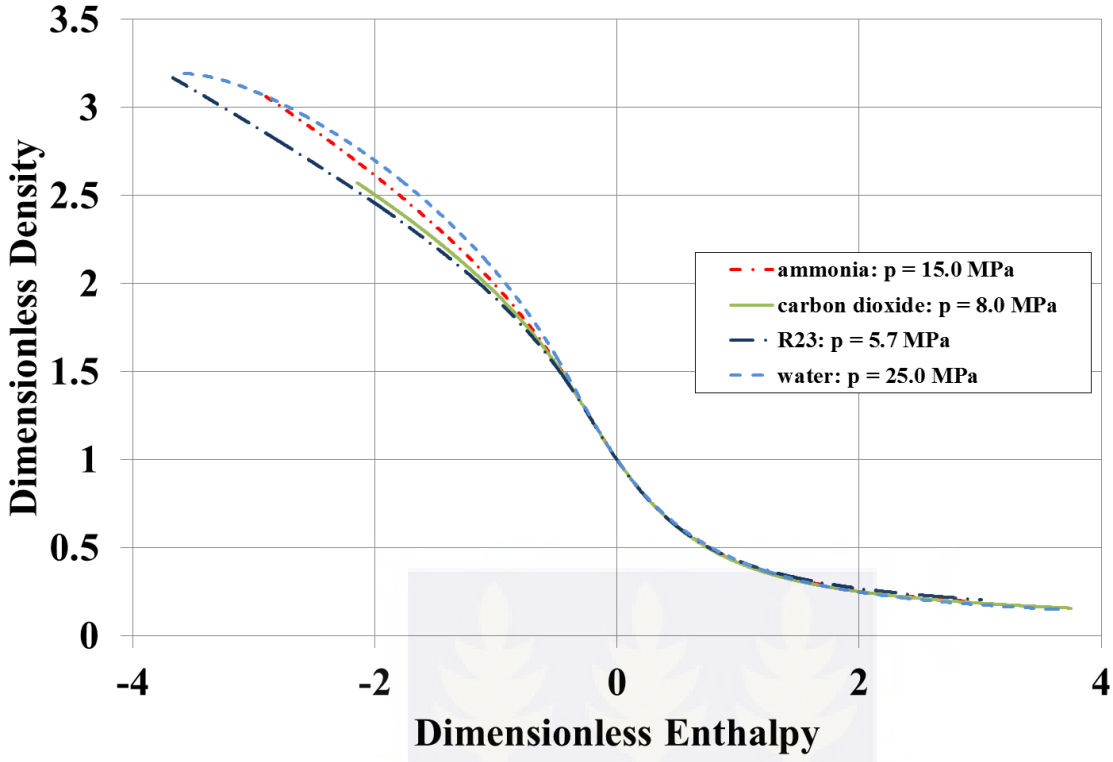

Figure 3.5. Dimensionless density as a function of dimensionless enthalpy for the considered fluids

While adopting the above simplification, it could not be taken for granted that stability thresholds obtained by CFD codes could be directly compared with those obtained in dimensionless form using as unique state relationship the mentioned universal trend of dimensionless density as a function of dimensionless enthalpy. Figure 3.6 present detailed characteristics of water adopted in the work.

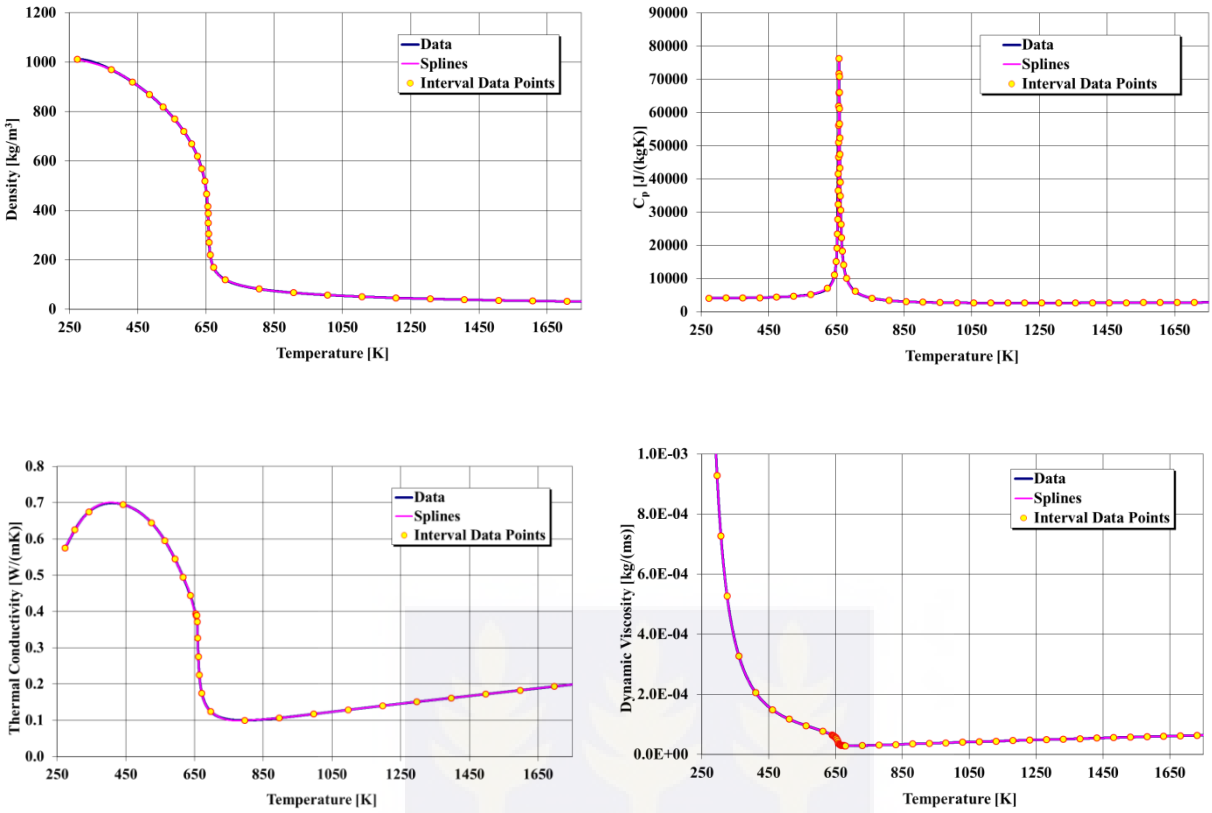

Figure 3.6. Properties of water at 25 MPa and their cubic splines approximations

The properties of the fluids at supercritical pressure (density, specific heat, dynamic viscosity and thermal conductivity) were assigned in the form of cubic splines, according to a procedure set up in previous applications of the STAR-CCM+ code to supercritical fluids. The data necessary to determine the coefficients of the polynomials were obtained from the NIST package [92]. As known, the properties of a supercritical fluid are characterised by sharp changes across the pseudo-critical temperature, where, by definition, the specific heat has a large peak. Figure 3.6 shows the detailed properties of water at the selected operating pressure as a function of temperature, together with the adopted cubic spline approximations.

CHAPTER 4

ANALYSIS OF SUPERCRITICAL HEATED CIRCULAR CHANNEL

4.1 INTRODUCTION

This Chapter presents the first results of a systematic methodology aimed at assessing the feasibility of analyses by CFD codes of flow instabilities in heated channels containing supercritical fluids. The work performed in this frame makes use of features presently available in CFD models, in the aim to move step-by-step from simple channel cases towards the analysis of more realistic fuel bundle subchannels.

In the present step, basing on previous experience, the STAR-CCM+ code [73] is adopted to solve flow stability problems in circular channels and fuel bundle slices without heating structures, in the aim to characterise the response of CFD models in the analysis of purely thermal-hydraulic instability phenomena. Some of the effects related to numerical discretisation, turbulence, wall thickness, flow direction with respect to gravity and fluid properties are studied, comparing the stability thresholds identified by transient calculations with maps set up by in-house 1D codes developed and adopted in previous work. Both static and dynamic instabilities are observed, clearly showing the contiguity of these two kinds of phenomena as a function of inlet fluid subcooling. The RELAP5/MOD3.3 code [93] was also used for comparison, providing additional insight into the corresponding similarities in the prediction of stability by the two computational tools.

First conclusions are finally drawn about the promising features of CFD codes for such applications, sketching the lines of the work in order to address more realistic reactor scale conditions.

4.2 CONSIDERED SYSTEM AND METHODOLOGY OF ANALYSIS

4.2.1 Geometry, discretization and modelling choices

The system studied in this Chapter is a circular pipe of length 4.2672 m (14 ft) and an internal diameter 8.36 mm. A similar simplified system was studied by Sharabi et al [82]. Figure 4.1 presents models of the circular pipe adopted for the STAR-CCM+ and RELAP5 codes.

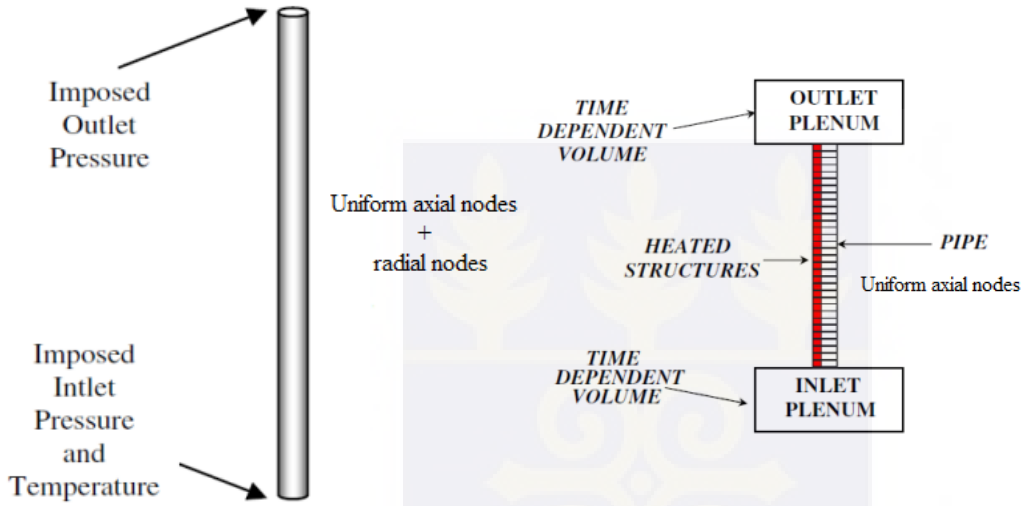

a) CFD model b) 1 D model

Figure 4.1. Circular pipe adopted in the study [14]

Figure 4.2 depicts the radial meshes adopted in the CFD models.On the basis of previous experience [76] and of several preliminary calculations made in the frame of this work with different choices of nodes for the radial and the axial numbers of nodes, a reasonable axi-symmetric 2D discretisation of the circular pipe was selected, having 40 uniform 0.1 mm nodes along with a single node of size 0.18 mm close to the wall, as can be seen in Figure 4.2b below, in order to allow for the applicability of wall functions.

a) Model with refined meshes close to wall b) Model with large mesh close to wall

Figure 4.2. Radial meshes adopted in the study [94]

The other model with refined meshes close to the wall was used in the turbulence analysis of the SC-Channel for low Reynolds treatments. On the other hand, the axial discretisation was fixed in 200 uniform nodes.

A Coupled Implicit or Implicit Unsteady advancement scheme was used for time discretisation, considering both the first and the second order time advancement schemes with different time steps and internal Courant numbers. Some calculations were also run with a Segregated Flow and Energy approach, in which flow and energy equations, as presented in Section 3.2.6, are solved separately. The coupled implicit approach with a very large internal Courant number (mostly equal to 20,000) was chosen, providing a rather robust time advancement and a good degree of convergence in the 20 iterations allowed for the advancement at each time step. This strategy of running the calculations represents one of the possible ways to use the STAR-CCM+ code for such problems and it was finally selected because it was found suitable in all the addressed cases.

As will be shown later on, on the basis of numerical diffusion considerations, a time step of 0.1 s with the use of a second order time advancement scheme were found a suitable choice,

compromising between accuracy and computational efficiency. In all the equations, advection terms were discretised at second order, being the default choice in STAR-CCM+.

Concerning the turbulence model, a standard k-ε model with "high y^+" treatment (i.e., with wall functions) was selected for the circular channel as discussed in detail below. The initial studies tried to avoid detailed wall treatments that could lead to strong overestimates in wall temperatures, as observed in analyses related to the prediction of heat transfer deterioration [71]. Similarly, inlet and outlet throttling, e.g., simulated by porous interfaces, or conjugated heat transfer modelling of the solid wall, were not introduced. All these aspects have been considered in the research, but they were ruled out in these first phases in order to avoid masking the pure thermal-hydraulic effects being the target of this Chapter. A uniform heat flux was imposed at the inner wall surface disregarding heat conduction effects. From the hydraulic point of view, the surface was assumed to be smooth, but sensitivity analyses on roughness are also presented.

It must be clarified that a limitation of the work presented in this Chapter is in the choice to use only wall functions (i.e., "high y^+" approaches) for near wall treatment. This is a consequence of the observed over prediction of wall temperature obtained by presently available low-Reynolds number models in case of heat transfer deterioration [71]. On the other hand, the use of wall functions in CFD models leads to complete disregard of heat transfer deterioration, making predictions more similar to those of present 1D models. While waiting for the development of CFD models suitable for an accurate prediction of heat transfer deterioration, it seemed prudent to avoid mixing different sources of inaccuracy, ruling out the high temperatures predicted by many low-Re turbulence models when dealing with mixed convection conditions to supercritical fluids.

Fluid properties were assigned as polynomial functions of temperature (for density and specific heat) or as field functions (for thermal conductivity and dynamic viscosity), making use in all the cases of a cubic spline piecewise interpolation of values provided by the NIST package [92]. A

home-made FORTRAN program was used to semi-automatically adjust the values of the required temperature intervals to a reasonable number, assuring relatively high accuracy.

4.2.2 Methodology of analysis

The methodology of analysis was slightly changed with respect to past work for CFD and RELAP5 analyses. In particular, the following steps were performed for each calculation with STAR-CCM+:

- a mass flow (or velocity) inlet boundary condition is firstly selected at the channel entrance, also assigning a specified inlet temperature, and a "pressure outlet" (i.e., an imposed value of outlet pressure) is adopted at the channel exit; with these boundary conditions and constant heat flux, the transient calculation is allowed to stabilise at the assigned power and flow levels, while monitoring the residuals and the inlet and outlet flow rates for assessing the obtained degree of convergence;
- after attaining steady-state, the boundary condition at channel inlet is changed to a "stagnation inlet", allowing for a value of pressure upstream of the inlet section to be assigned at the one calculated at channel entrance in the previous phase; this boundary condition preserves the value of flow rate reached in steady-state, leaving the channel free to oscillate. In STAR-CCM+, as in other codes, the "stagnation inlet" implies a reduction in inlet channel pressure with respect to the stagnation value (i.e., the value upstream of the inlet section), due to the fluid acceleration experienced in entering the channel, evaluated by applying the Bernoulli equation;
- then, instead of using a linear increase of power with time up to the point in which unstable behaviour is observed, as done in previous work, multiple stepwise increases of power was adopted, thus allowing the flow to oscillate after each step in a converging or diverging way as can be observed in Figure 4.3; a disadvantage of this procedure is the discontinuity with which the power interval is spanned but, as a compensation, there are relevant advantages:

- after a step change is assigned to the heating power, the system evolves towards stability or instability without the inertial effects that are brought about by the continuous linear increase with a finite rate; in previous analyses with different codes, care had to be taken to minimise, as far as possible the power increasing rate in order to avoid inaccuracies; this was not always possible with CFD codes because of the resulting long elaboration times;
- in case of oscillatory instabilities, this procedure provides data used to evaluate the decay ratio and the period of oscillations at each power level, making use of an appropriate algorithm, described in Section 3.6, thus drawing plots of both variables as a function of selected values of heating power or of a dimensionless power-to-flow ratio;
- in case of excursive instabilities, it is thus possible to provide a lower and an upper bound of the exact value of power at which the excursion starts; actually, in previous analyses it was not possible to achieve this result with a linear increase in power, since in such a case it was practically impossible to detect the exact start of the exponential excursion.

In the case of oscillatory behaviour each stepwise increase of power results in a finite perturbation that is damped or amplified according to the stable or unstable character of the addressed operating conditions.

The model adopted for RELAP5/MOD3.3 [93] is similar to the one used in previous applications [13, 91], but it was customised for the specific analysis reported here. It consists of two “time dependent volumes”, simulating the large inlet and outlet plena with assigned fluid thermodynamic conditions, connected by “single-junctions” to a “pipe” component, discretised with 48 nodes for the circular channel as shown in Figure 4.1b.Very thin heat structures with large conductivity and low heat capacity, one per each hydrodynamic node, are in thermal contact on the outer surface with the fluid. The full flow cross section of the channel is considered in the model, corresponding to a full perimeter of the rod.

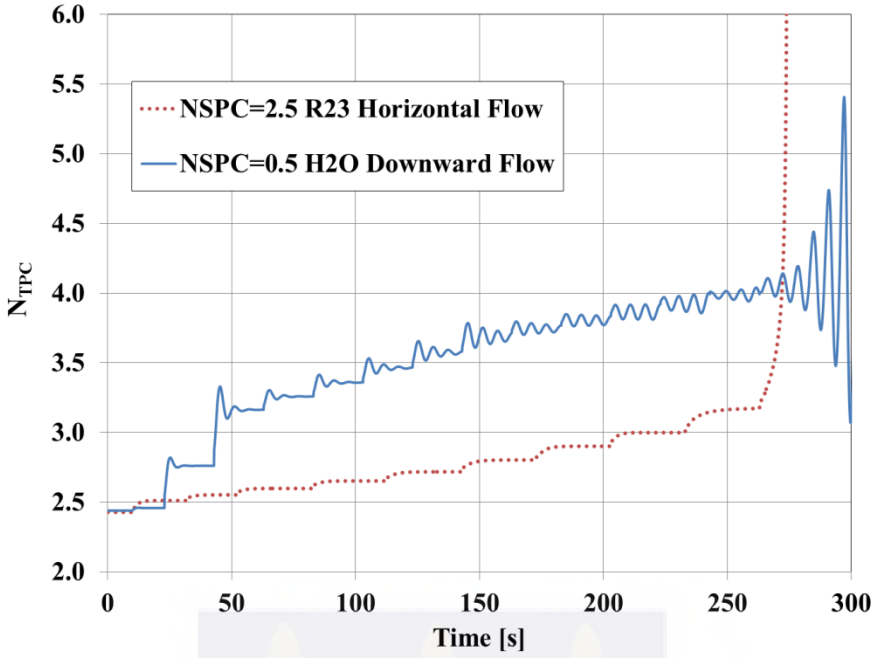

Figure 4.3. Time trends of N_{TPC} obtained by STAR-CCM+ for the bare tube in oscillatory and excursive cases

The hydraulic diameter of the channel is equivalent to the diameter of 8.36 mm. A similar step increment in power was adopted for the RELAP5 computations as well.

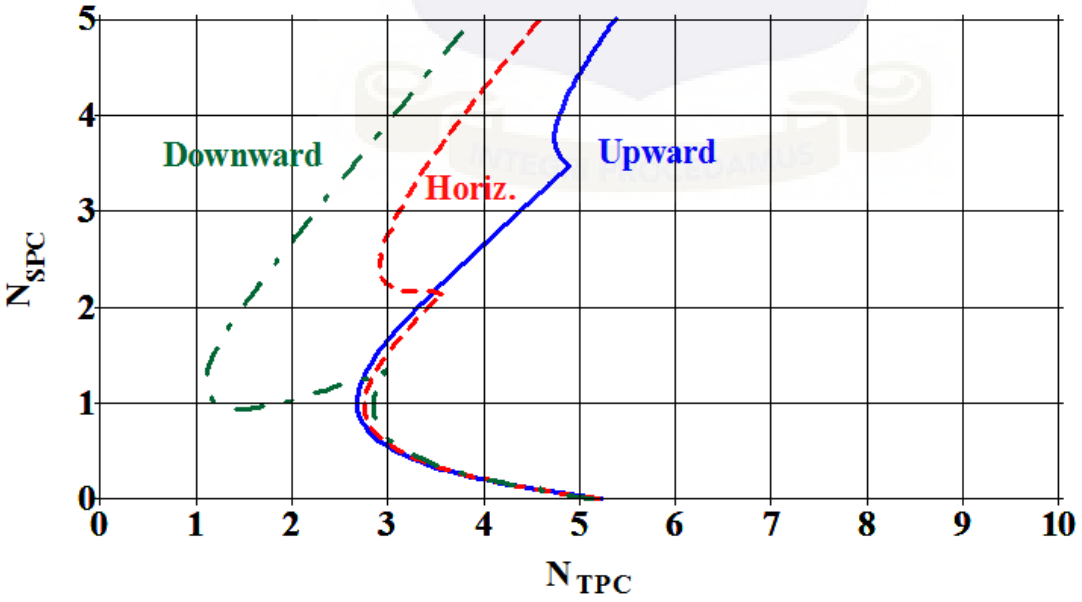

Figure 4.4. Comparison of the stability boundaries calculated for upward (Fr=0.03), horizontal (Fr=10^5) and downward (Fr=-0.03) flow (Λ=4.5, 48 nodes, C_{max} = 0.9) by the 1D model

Figure 4.4 reports the stability boundaries evaluated by the 1D linearised code, discussed in Section 3.4, in dimensionless form for operating conditions involving upward, horizontal and downward flow. In upward and downward flow the magnitude of the Froude number was kept nearly the same, corresponding to a same inlet velocity (around 1.12 m/s) adopted for initialising the CFD calculations. The horizontal flow case is instead characterised by a very large Froude number, as a consequence of the assumption of a vanishing component of gravity along the channel axis. As the figure clearly shows, the main difference between the three stability boundaries lies in the location of the upper lobe, representing the region of the Ledinegg excursive instability, while the lower lobe, related to the density wave instability mechanism, is nearly the same for the three cases.

4.3 RESULTS FOR BARE CHANNEL

4.3.1 Effect of the Numerical Scheme and of Time Step

A base case considered in the calculations is an upward vertical supercritical water channel operating at 25 MPa with inlet and outlet channel temperatures of 280 °C and 500 °C, respectively. This case, corresponding to a value of N_{SPC} around 1.55, represents conditions similar to those envisaged for fuel channels in some of the proposed reactor designs.

The first addressed issue was the one related to numerical diffusion. The axial discretisation of the channel, including 200 nodes, was considered fine enough on the basis of previous experience and of a few sensitivity analyses performed in the frame of this work. On the other hand, the radial discretisation, including 40 uniform 0.1 mm nodes with a single larger size node at the wall, was considered comparable with choices made in previous analyses [76].

With this discretisation, it was observed from the first runs that the use of a first order time advancement scheme, even with a second order treatment of advection terms in the equations, provides rather diffusive results. In particular, while from the stability map developed by a

linearised 1D code [14] and from previous results by FLUENT [72] a threshold of instability around $N_{TPC}\approx 3$ (see Figure 4.5) was expected, the onset of oscillations was considerably delayed to larger values of the dimensionless power-to-flow ratio. This situation is depicted in Figure 4.6a, where it can be noted that for the first order scheme the oscillations obtained in N_{TPC} at each stepwise increase of power show a large degree of damping in the mentioned region of N_{TPC}.

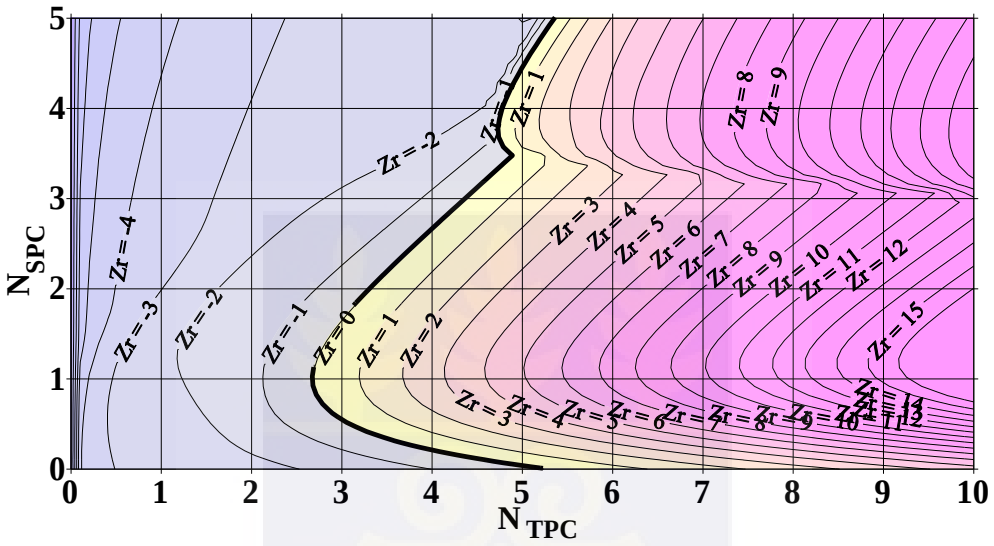

Figure 4.5. Stability map obtained for the circular pipe in the vertical upward case

(Fr=0.03, Λ=4.5, 48 nodes, C_{max} = 0.9)

After this observation, the second order implicit unsteady time advancement algorithm available in STAR-CCM+ was then considered. This scheme is based on the following finite difference approximation for the time derivative

$$\frac{dT}{dt} \rightarrow \frac{3T_i^{n+1} - 4T_i^n + T_i^{n-1}}{2\Delta t} \tag{4.1}$$

resulting in second order accuracy. The result of this choice is shown in Figure 4.6b, where it is clear that, keeping the other choices the same, the threshold of instabilities is now calculated by the second order scheme slightly above $N_{TPC}\approx 3.1$, as expected from 1D predictions.

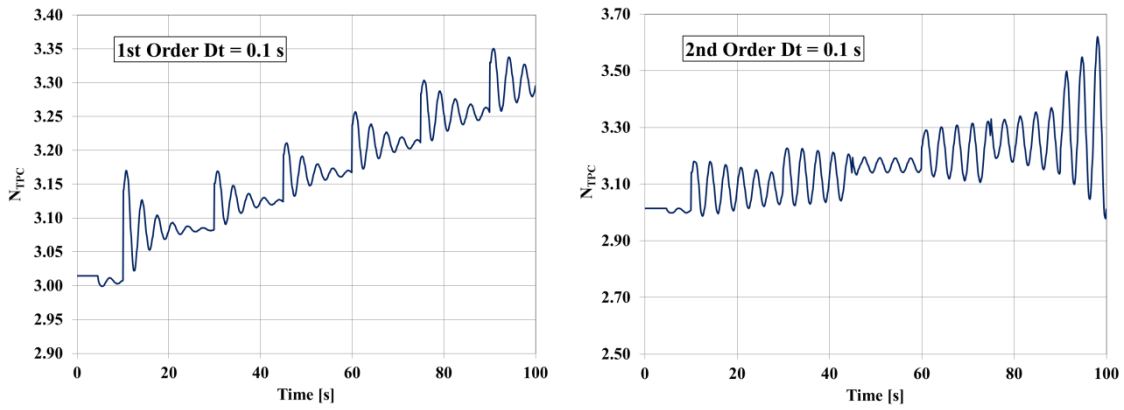

a) first order time advancement b) second order time advancement

Figure 4.6. Time trends of N_{TPC} obtained by STAR-CCM+ for the base case of the circular tube [16]

Figure 4.6 is also helpful to better understand the methodology of analysis discussed in the previous section. As it can be noted, after changing the boundary conditions of the channel to "stagnation inlet" and "pressure outlet", the system has initially small oscillations, due to the imperfect match between the previously imposed inlet flow boundary conditions and the new ones; then, at prescribed time intervals, power is increased in steps giving rise to oscillations whose period and decay ratio can be identified by the algorithm described in Section 3.6. While the data reported in Figure 4.6 are related to oscillatory behaviour (i.e., density wave oscillations), Figure 4.3 presents two sample time trends of N_{TPC} for both oscillatory and excursive behaviour (Ledinegg instabilities). As it can be noted, the presently adopted methodology, based on stepwise increases in power, allows to efficiently deal with excursive behaviour, since the steps in power (hence in N_{TPC}) provide a clear bounding of the conditions for the start of instabilities with respect to the linear increase of power adopted in previous work.

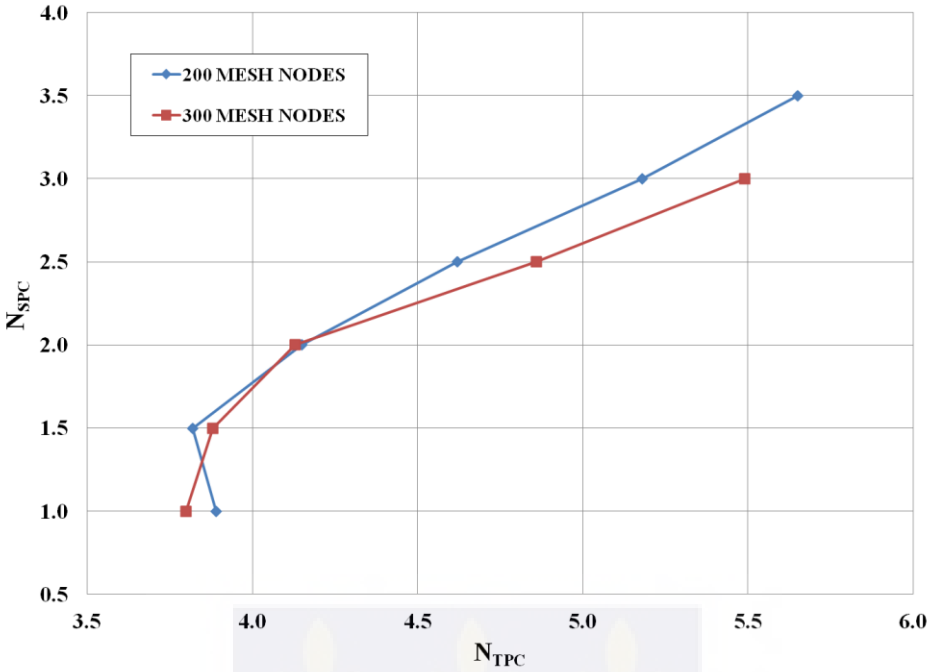

Figure 4.7. Axial mesh size effect for the bare cylindrical tube with water and upward flow

Once the main numerical dissipative effect was resolved by the use of the second order implicit advancement scheme, it was possible to perform a limited analysis on space and time discretisation. Concerning axial discretisation, the differences obtained between 200 and 300 nodes were found to be relatively small at least in the regions close to the operating points for a nuclear reactor (Figure 4.7) and the former discretisation was accepted as a reasonable compromise between accuracy and efficiency in these analyses. Concerning radial discretisation, after different trials that showed changes in the wall temperature distribution, involving the appearance of deteriorated heat transfer behaviour when the meshes at the wall were too small, the mentioned 40 plus one node discretisation was retained.

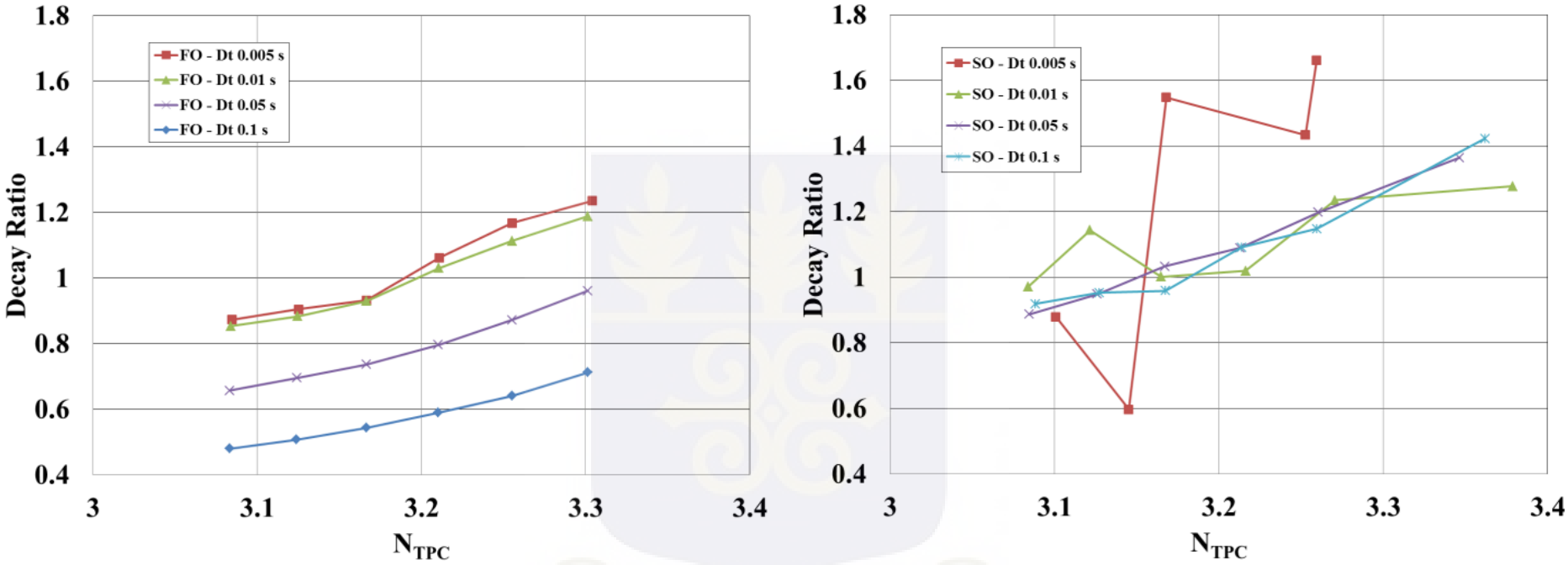

a) first order

b) second order

Figure 4.8. Effect of the adopted time step on decay ratio for the first and second order schemes

In order to ascertain the effects of truncation error on the computed decay ratio and on the period of oscillations computed at the onset of unstable behaviour, different values of the time step were adopted with both numerical schemes. Figure 4.8 reports in two separate plots these effects in terms of decay ratio as a function of N_{TPC}; it can be noted that:

- the first order advancement scheme with a time step in the order of 0.1 s results in a considerable damping, showing a decay ratio that increases when the time step is decreased to 0.01 or 0.005 s; this behaviour is fully understandable for an implicit first order scheme, which tends to be much more diffusive when the "actual" Courant number (the product of fluid velocity by the ratio of time step to the mesh size) is increased;
- From Figure 4.8b, it can be observed that the second order scheme with 0.1 s provides decay ratios that are in the range obtained by the first order scheme at low time steps; the same behaviour is observed for the time step of 0.05 s, but degenerates for lower values of the time step, mainly because of the appearance of higher frequency modes superposed to the main oscillation that are misinterpreted by the algorithm adopted for processing the results obtained.

Concerning these higher frequency modes, it is quite difficult to assess whether they are a fundamental feature of the 2D solution of flow equations or they are the results of dominant dispersive effects appearing in the truncation error when using the second order scheme. For the time being their nature was considered not relevant for discussing the general flow stability, which is mainly decided by the damping or the amplification of the fundamental oscillating mode. For this reason, the value of 0.1 s for the time step was considered reasonable for the second order scheme, since the decay ratio obtained by its use is in the range of the one obtained by the first order scheme with much lower time step. These aspects will require a specific inquiry in future analyses.

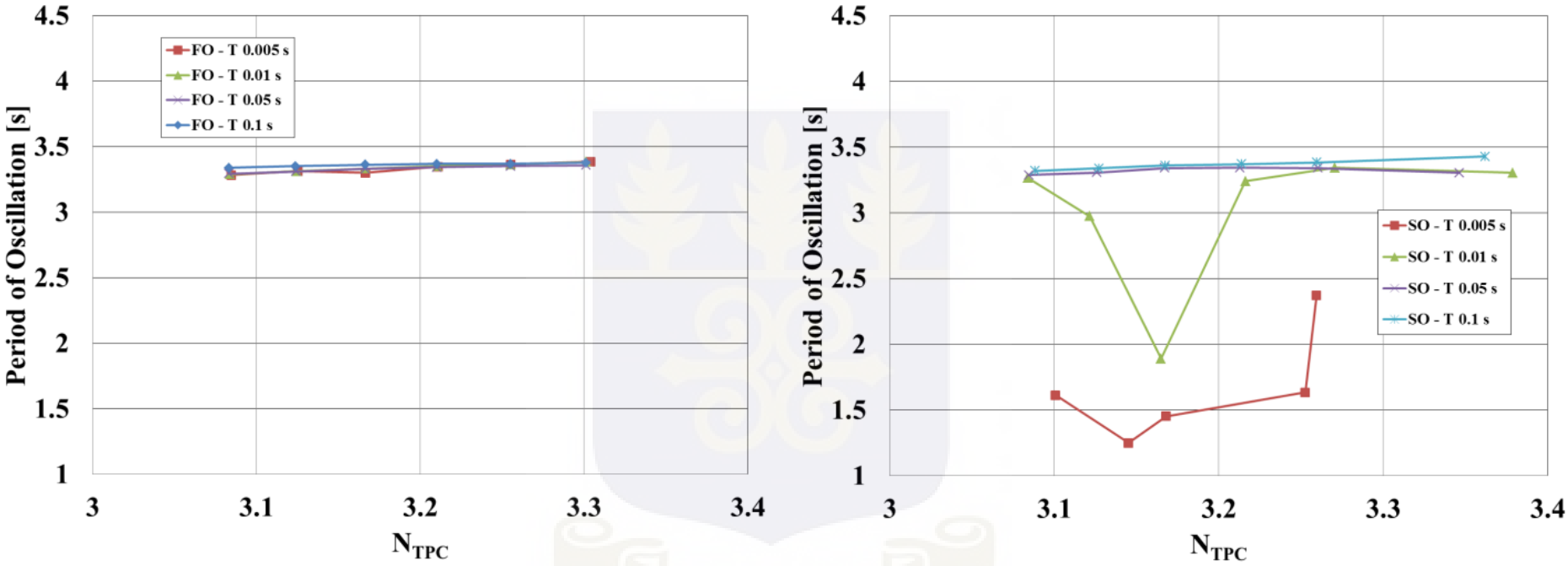

a) first order

b) second order

Figure 4.9. Effect of the adopted time step on the period of oscillation for the first and the second order schemes

The effect of the adopted time step on the oscillation period is very small for the first order scheme as shown in Figure 4.9a; so, the dramatic effects observed on the predicted decay ratio have no real counterpart in terms of this variable. In the case of the second order scheme (Figure 4.9b), the period of oscillations predicted is comparable to the one obtained by the first order scheme for time steps of 0.05 and 0.1 s; for lower values of the advancement step, the mentioned higher frequency oscillations come into play, leading the algorithm to predict an average smaller period in their presence. It must be explicitly noted that the values of the period of oscillations are also coherent with those obtained by 1D models.

It can be concluded that, in the present case, characterised by velocities in the order of 1 m/s at the inlet and of about 10 m/s at the outlet (depending case by case on the heating power), the use of 0.1 s as time step for the advancement of the calculation with the second order scheme seems acceptable, since the obtained values of the decay ratio and of the period are the same obtained asymptotically by the more diffusive first order scheme when used with much lower time steps.

A common choice in the calculations was to use an “internal” Courant number (the one used in internal pseudo-transient iterations) in the order to 20,000. This choice was dictated by the reasonably high speed of convergence it allows in the limited number of iterations adopted per each advancement step (chosen to be 20). An analysis of the effect of this choice on the calculated decay ratio and period of oscillations was made for the case of a time advancement step of 0.05 s (Figure 4.10), showing that the use of larger values of this Courant number (CN in the figures) brings no real advantage in the computations; this is the reason why this choice was kept in all the calculations performed later on.

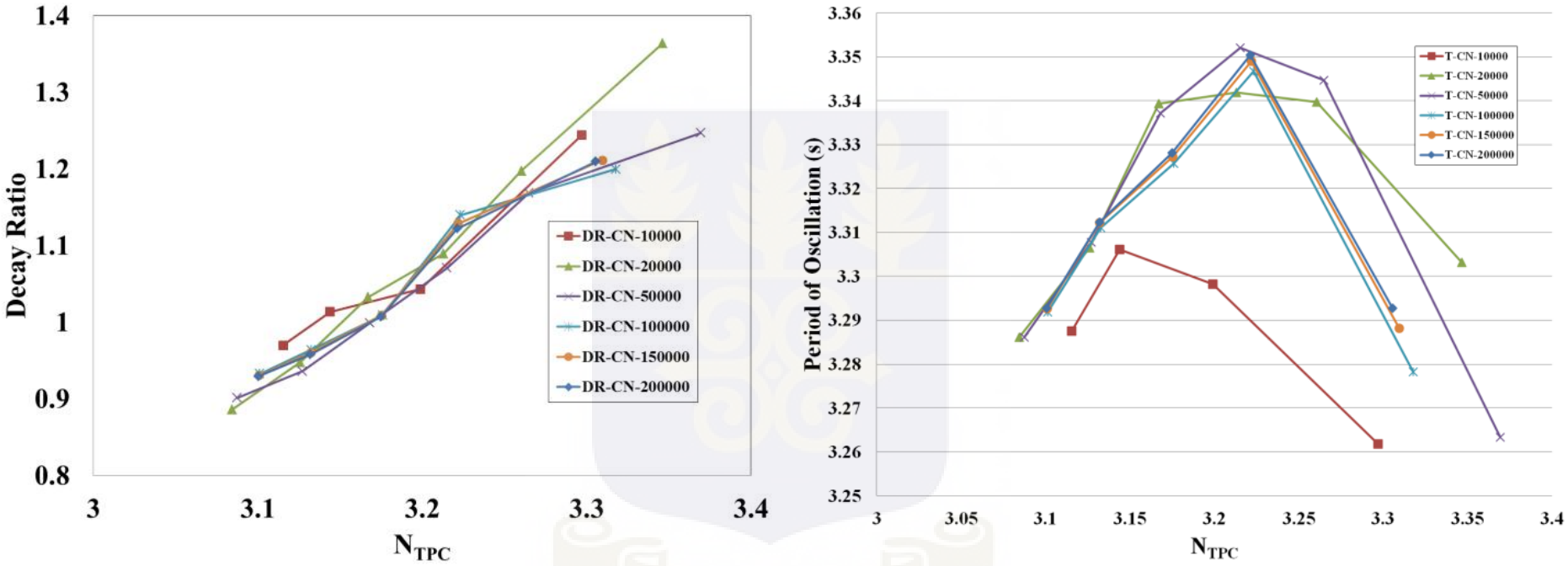

Figure 4.10. Effect of the internal Courant number on the decay ratio and the period of oscillations for the circular vertical channel in the base case with the second order scheme and a time step of 0.05 s.

4.3.2 EFFECT OF TURBULENCE MODELS ON STABILITY PREDICTION

The stability map obtained for the high y+ turbulence models on the SC-channel with vertical flow is presented in Figure 4.11 below [94]. It can be observed that Reynold Stress Model, Standard k-ε and Realizable k-ε provided comparable thresholds of instability for the pseudocritical temperatures studied. The Standard k-ω model predicted a much unstable channel at N_{SPC} = 1.0 along with the SST k-ω model.

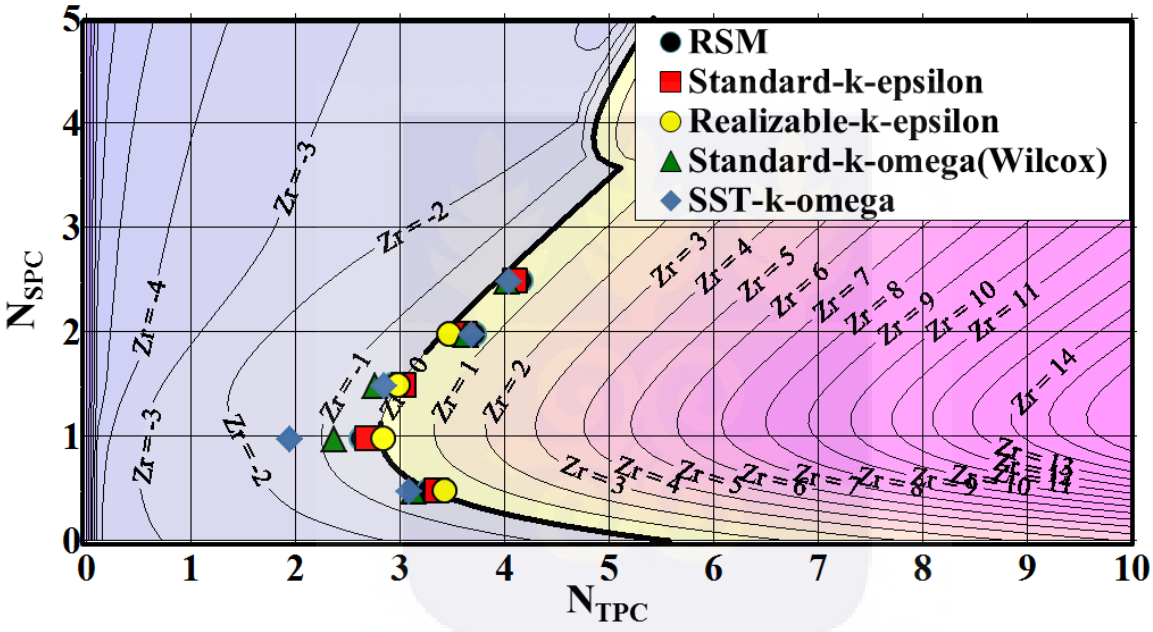

Figure 4.11:Comparison of the stability thresholds obtained for the circular channel against the dimensionless stability map in the case of vertical flow with high y+ turbulence models generated for Fr= 0.030, Λ = 4.5, 48 nodes, C_{max} = 0.9

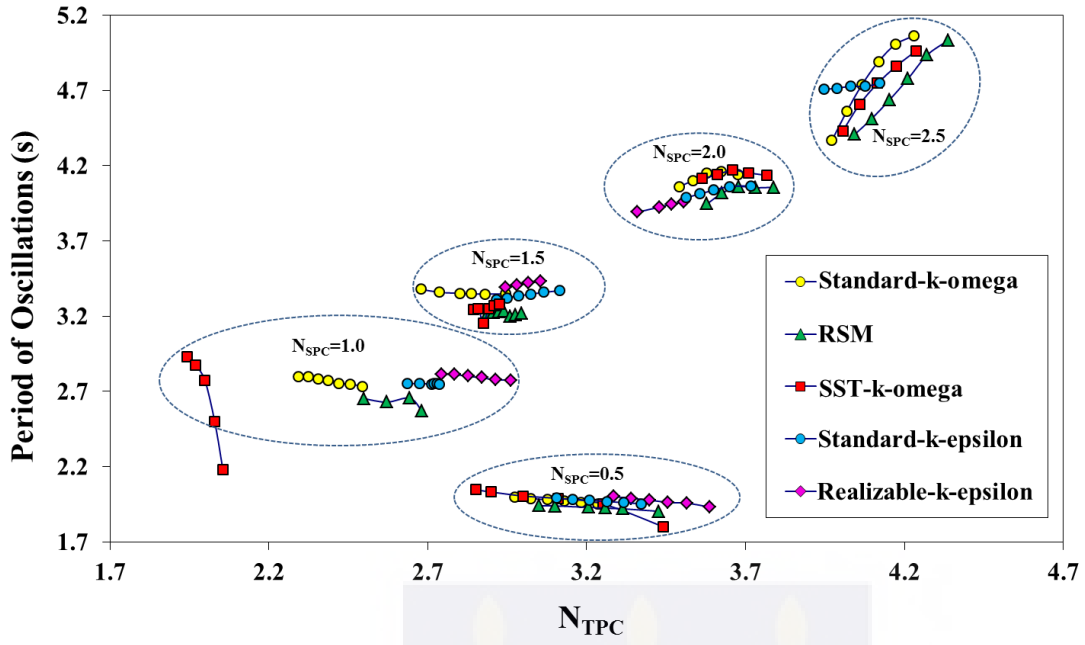

Figure 4.12: Periods of oscillations for the high y+ with vertical flow for the circular channel at different values of pseudo-subcooling calculated around the onset of oscillations.

It can be observed from Figure 4.12 that the periods of oscillations of the models compared well with eachother, except in the case of the SST k-ω for N_{SPC} = 1.0 as was observed in Figure 4.12 above.

Figure 4.13 presents a comparison of the results obtained for the All-y+ models. The standard k-ε model for all-y+ treatment was studied for the two radial meshes presented in Figure 4.2 above; with Figure 4.2a mesh results represented as k-epsilon-refined-wall-mesh-All-y-plus and that for Figure 4.2b represented as k-epsilon-All-y-plus. It can be observed from the map that both meshes provided similar thresholds of instability for the N_{SPC}s considered. The Standard k-ω, represented in the legend as Wilcox-All-y-plus, and the SST k-ω, represented as SST-All-y-plus, predicted lower margins of stability at N_{SPC} = 1.0.

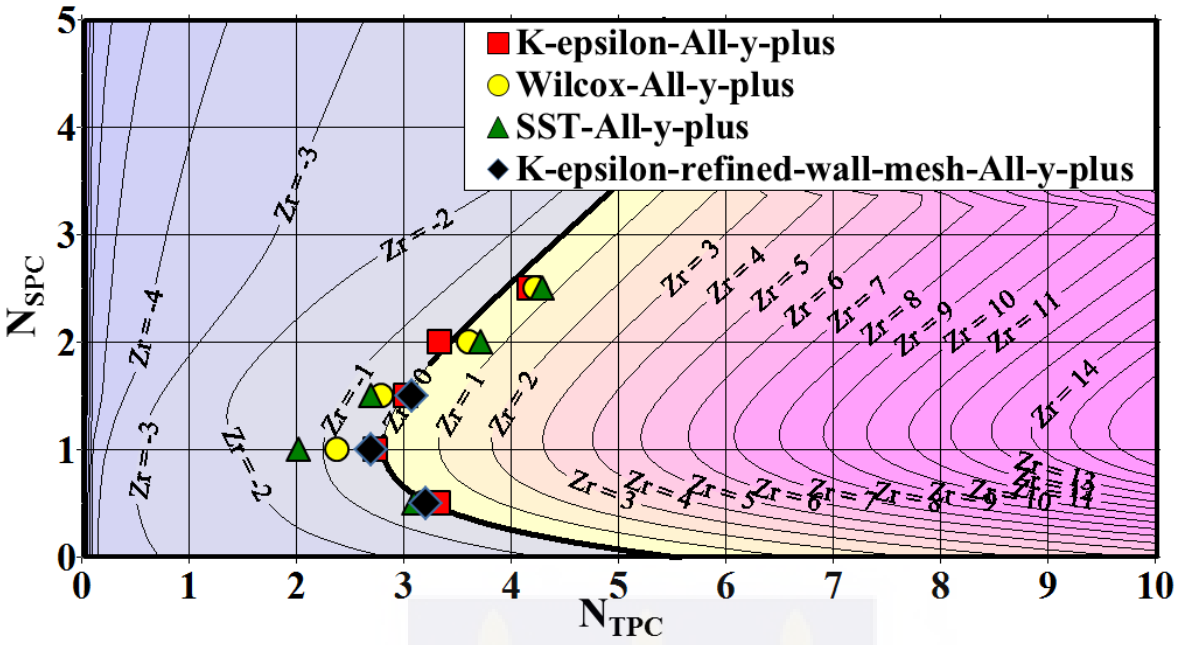

Figure 4.13:Comparison of the stability thresholds obtained for the circular channel against the dimensionless stability map in the case of vertical flow with all-y+ turbulence models generated for Fr= 0.030, Λ = 4.5, 48 nodes, C_{max} = 0.9

Figure 4.14 shows that the trend of periods of oscillations predicted in Figure 4.12 for the high-y+ models pertains for the all-y+ models as well with the period increasing with increasing N_{SPC}.

Figure 4.15 presents the comparison of the thresholds of instability for the low y+ models considered in the study. It can be observed that the standard low-Reynolds model (Lien) provided thresholds of instability that are comparable with the 1D map for N_{SPC} less than 2.0. It over-predicted far above that for the N_{SPC}=2.0. The standard k-ω model (Wilcox-Low-y-plus) predicted thresholds comparable to the map at N_{SPC}s=0.5 and 2.0 while the SST k-ω model (SST-Low-y-plus) had three results comparable to the map at N_{SPC}=0.5, 2.0 and 2.5.

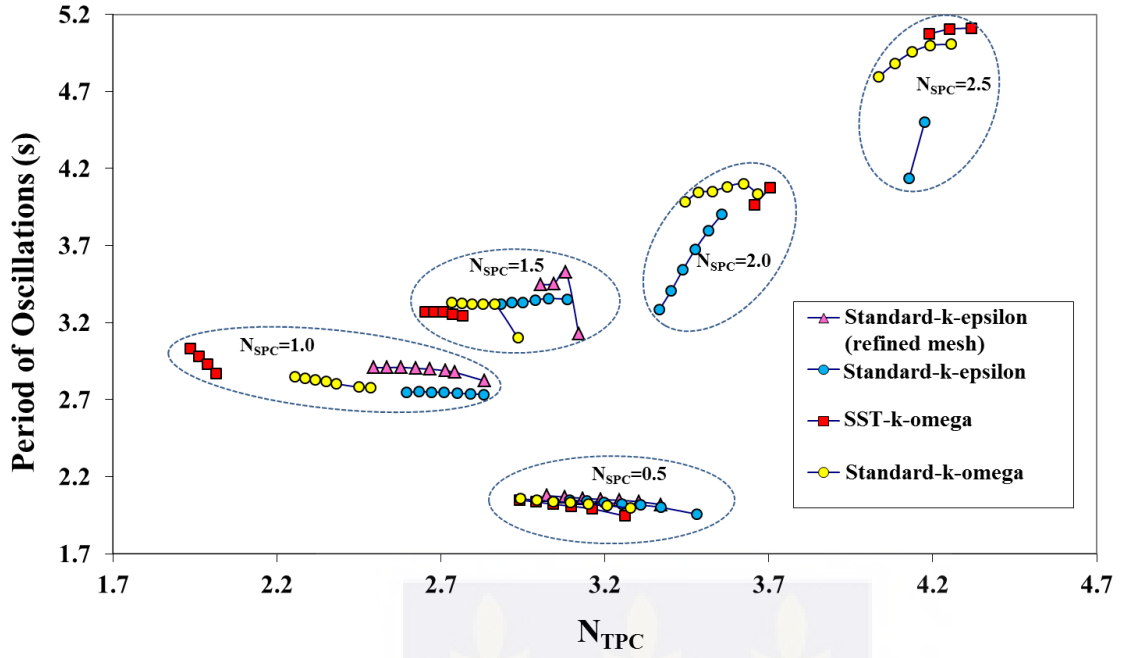

Figure 4.14: Periods of oscillations for the all y+ models with vertical flow for the circular channel at different values of pseudo-subcooling calculated around the onset of oscillations.

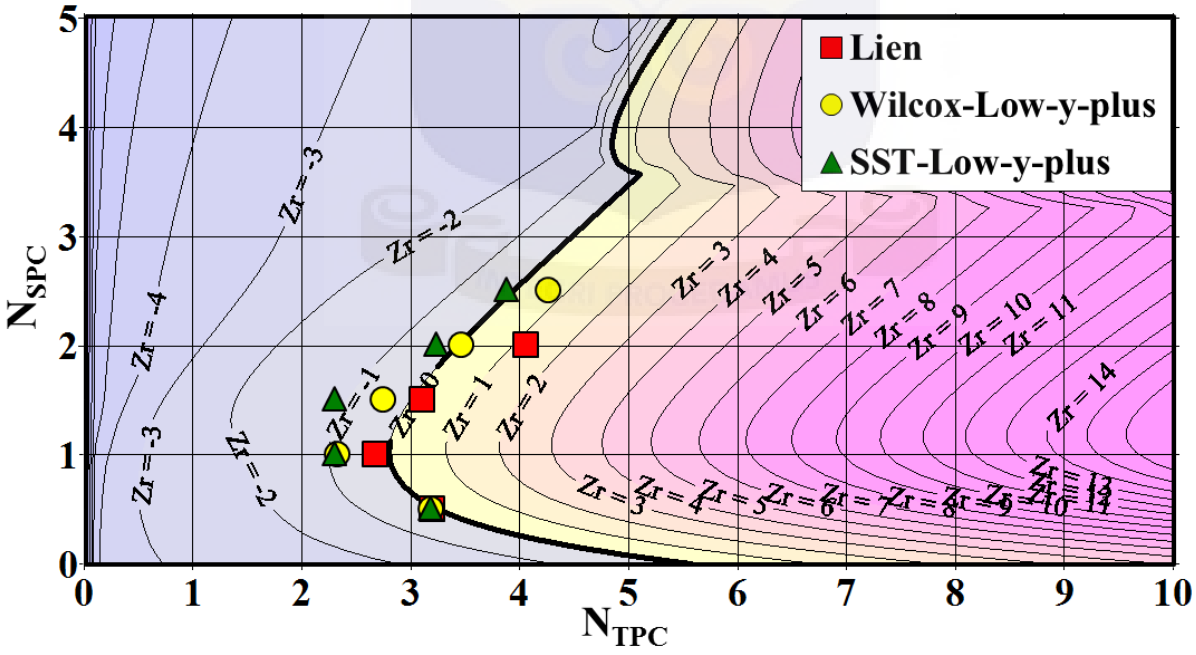

Figure 4.15:Comparison of the stability thresholds obtained for the circular channel against the dimensionless stability map in the case of vertical flow with low y+ turbulence models generated for Fr= 0.030, Λ = 4.5, 48 nodes, C_{max} = 0.9

Figure 4.16 presents the period of oscillation plots for the low y+ models. It can be observed that the trends observed in the high and all y+ models is also present here as well with the period of oscillations increasing with increasing N_{SPC}s. It can be observed that at high N_{SPC}s the models were predicting similar period of oscillations.

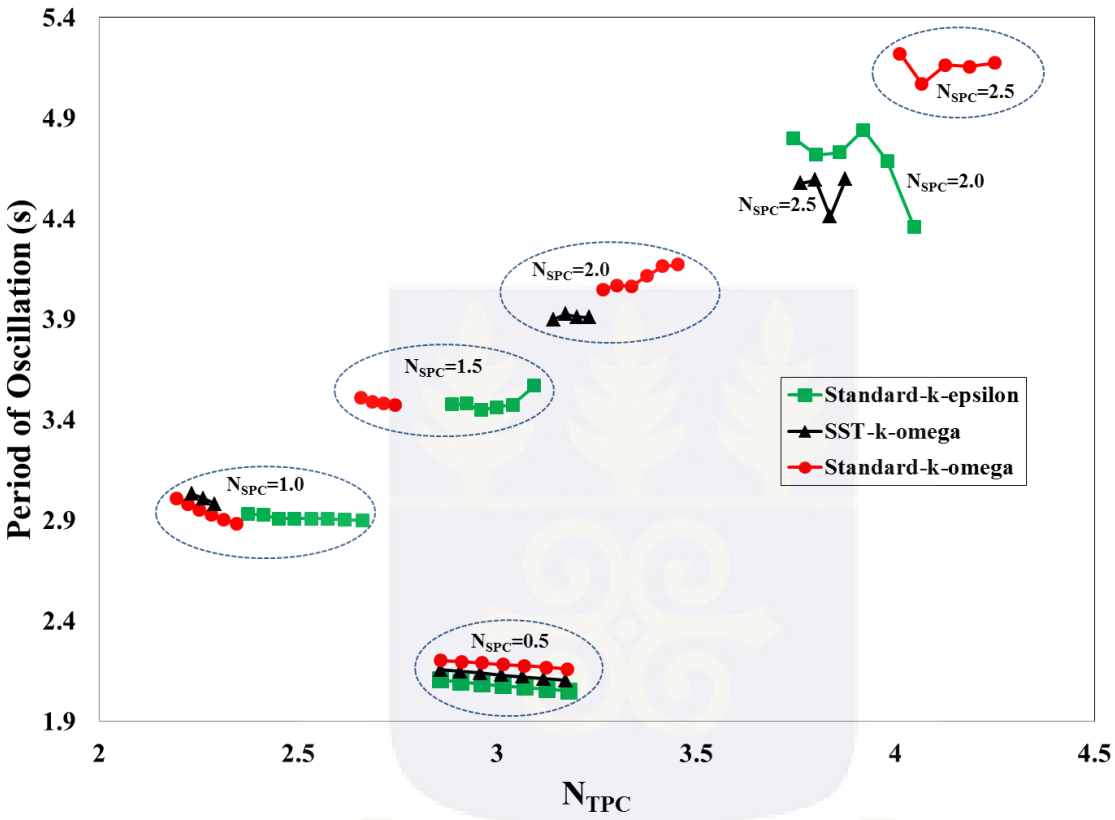

Figure 4.16: Periods of oscillations for the low y+ models with vertical flow for the circular channel at different values of pseudo-subcooling calculated around the onset of oscillations.

In order to ascertain the effect of flow direction on the prediction of the threshold of unstable behavior by the low and high y+ models, the standard k-ε's low and high y+ models were studied for horizontal (no gravity) and downward flow as presented in Figures 4.17 to 4.19.

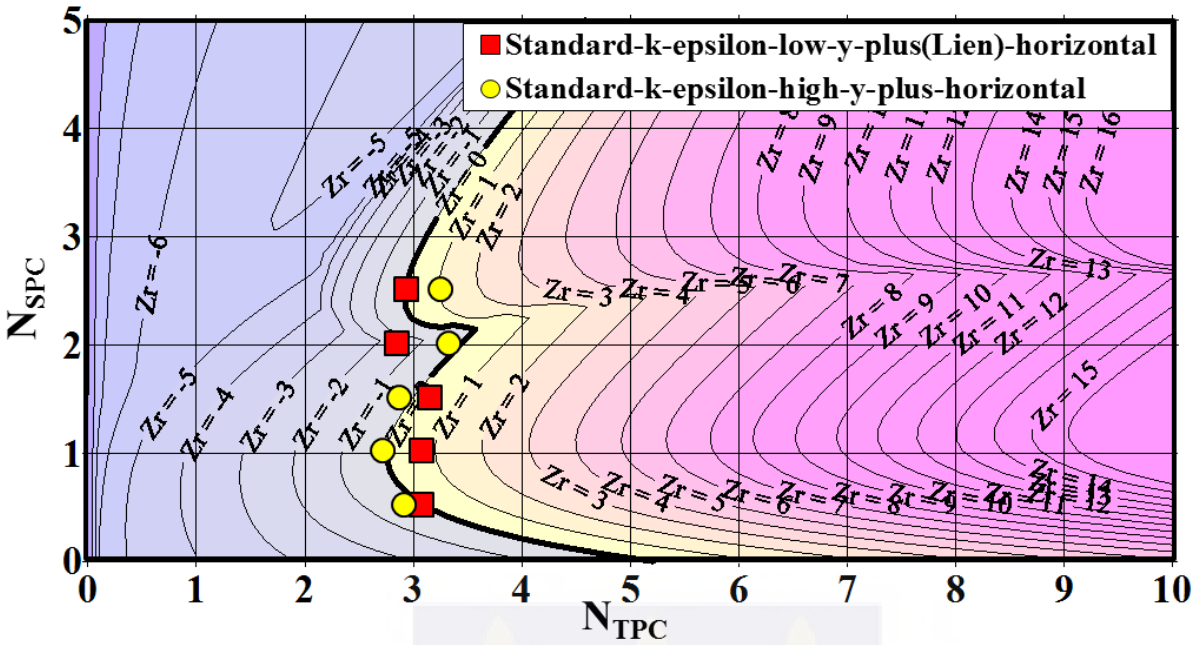

Figure 4.17: Comparison of the stability thresholds obtained for the circular channel against the dimensionless stability map in the case of horizontal flow with low and high y+ turbulence models generated for Fr= 10^5, Λ = 4.5, 48 nodes, C_{max} = 0.9

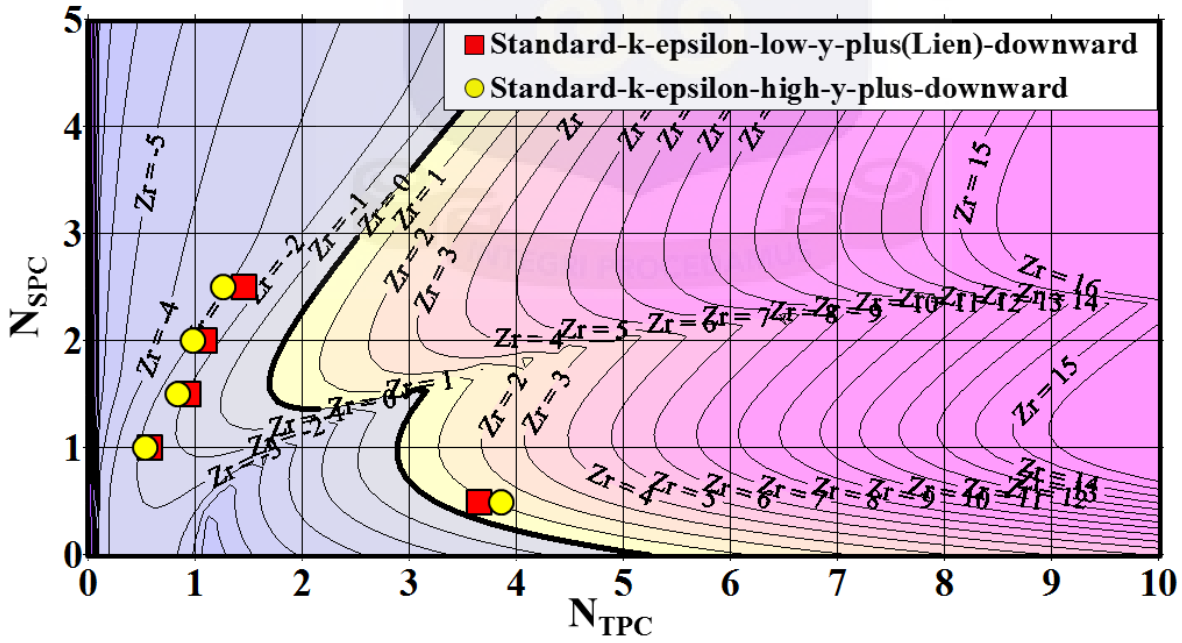

Figure 4.18: Comparison of the stability thresholds obtained for the circular channel against the dimensionless stability map in the case of downward flow with low y+ turbulence models generated for Fr= -0.030, Λ = 7.0, 48 nodes, C_{max} = 0.9

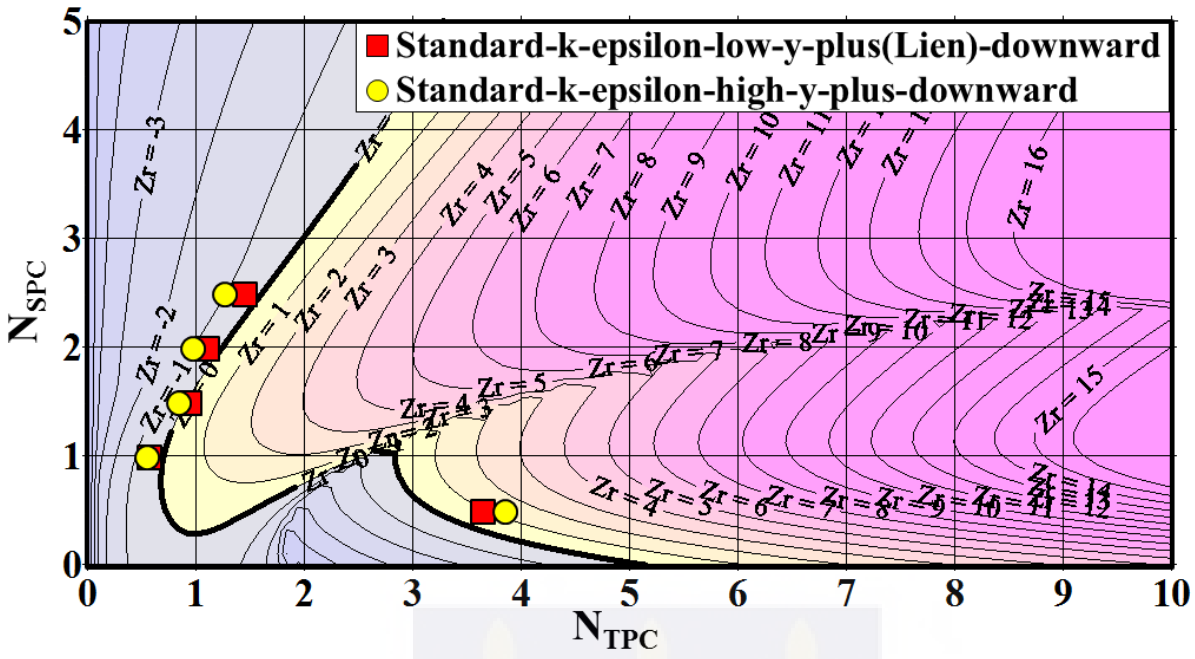

Figure 4.19: Comparison of the stability thresholds obtained for the circular channel against the dimensionless stability map in the case of downward flow with low y+ turbulence models generated for Fr= -0.030, Λ = 3.0, 48 nodes, C_{max} = 0.9

From Figure 4.17, it can be observed that the high y+ model predicted thresholds that were closer to the 1D map than the low y+ model. Figure 4.18 shows that the two models predicted similar thresholds of instability for vertical downward flow. The difference observed between Figure 4.18 and Figure 4.19 related to the Λ adopted in the two cases. A detailed discussion on the effect of the friction factor, Λ, on the maps shall be discussed under the fluid-to-fluid comparisons below.

Based on the observations made in this section and on previous studies with turbulence models [71], the standard k-ε model was adopted in the analysis on the SC-channel with high y+ treatment.

4.3.3 EFFECT OF WALL THICKNESS ON SC-CHANNEL ANALYSIS

This section discusses the results of the study conducted on the effect of wall thickness on the SC-channel analysis using STAR-CCM+ and RELAP5.

From Figure 4.20a with STAR-CCM+, it can be observed that the increase in wall thickness from 0.1 to 0.8 mm improved the stability margin of the SC-channel with a decrease in decay ratio. Figure 4.20b for RELAP5 predicts a systematic reduction in decay ratio with continuous increment in the wall thickness from 0.02 mm to 0.8 mm. The similarities observed in the predictions of the two computational tools indicate a consistent outlook of the effect of wall thickness on the stability of the supercritical channel.

Figure 4.21 presents the comparison of the periods of oscillations obtained for the two computational codes.

Figure 4.21a indicates that the periods of oscillation for the SC-channel with wall thicknesses less than 0.8 remained in the 3.1 to 3.5 s range while that for the wall thickness of 0.8 mm was higher probably due to the lower decay ratios recorded for the case. From Figure 4.21b, it can be observed that the periods of oscillation for wall thicknesses lower than 0.8 mm was approximately equal to 3 as was observed for STAR-CCM+. Higher periods of oscillations were recorded for wall thickness of 0.8 mm as was found with STAR-CCM+ but with a lower magnitude in RELAP5 predictions.

These observations indicate that wall thickness may be able to increase the stability margin of the SC system. This effect is anyway under investigation at the present time and needs further clarifications to draw general conclusions.

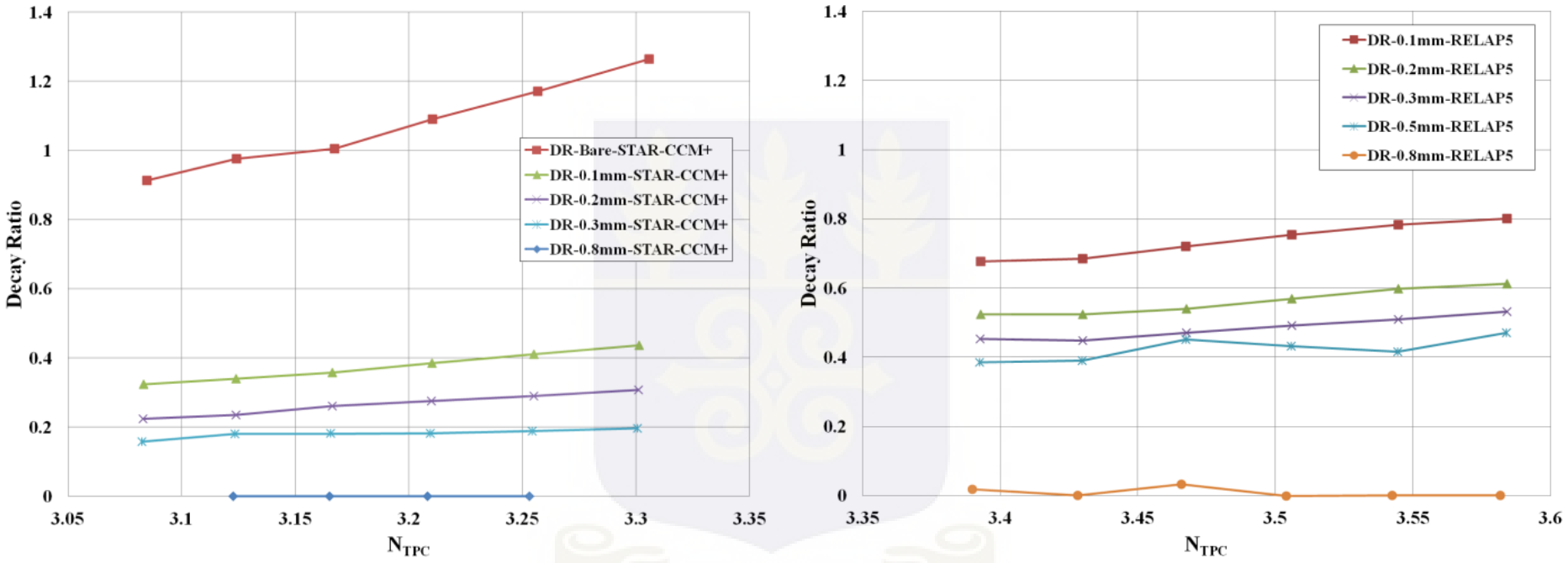

a) STAR-CCM+

b) RELAP5

Figure 4.20: Decay ratio plot for wall thickness effect on stability of SC-Channel using STAR-CCM+ and RELAP5

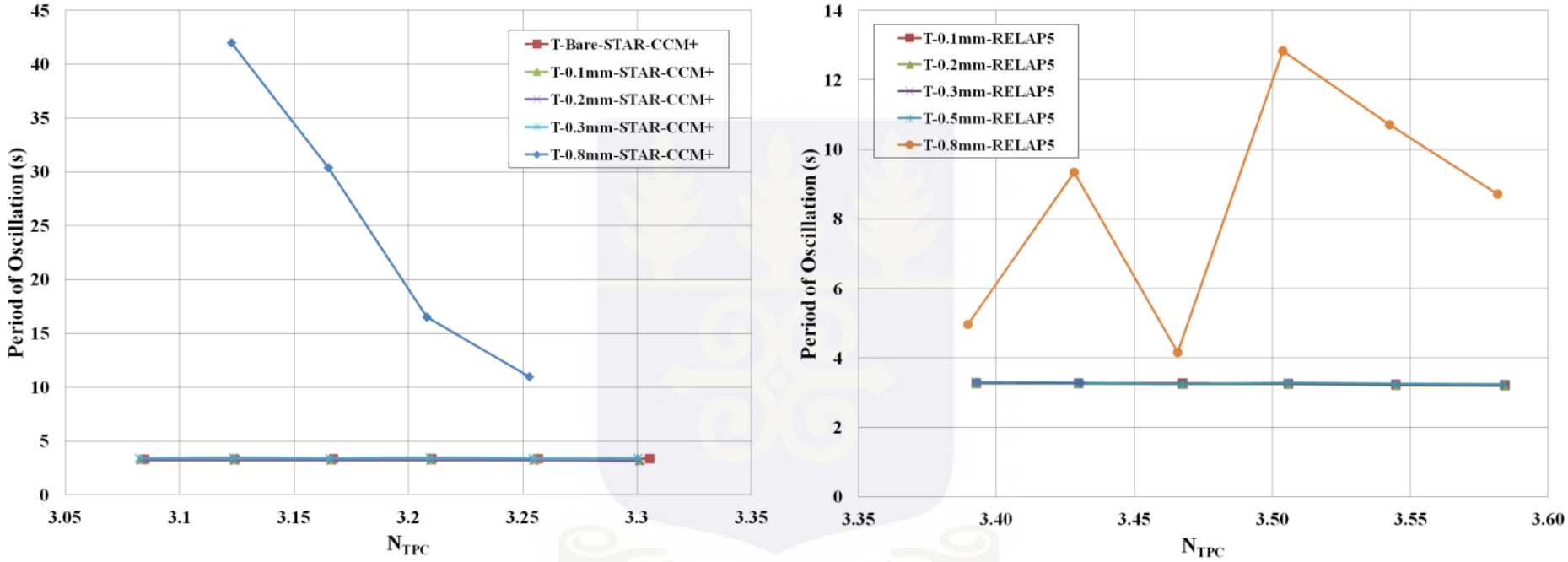

a) STAR-CCM+ b) RELAP5

Figure 4.21: Period of oscillation plot for wall thickness effect on stability of SC-Channel using STAR-CCM+ and RELAP5

4.3.4 EFFECT OF WALL ROUGHNESS ON SC-CHANNEL ANALYSIS

The study on the effect of wall surface roughness on stability analysis of SC-channel was conducted using STAR-CCM+ at power levels close to the unstable threshold. It was generally observed that as the roughness increased above 4×10^{-6} m, the channel became unstable from the beginning of the analysis. Figure 4.22 presents the decay ratio plots for the study in the operation region of the SCWR, N_{SPC}=1.55.

It can be observed from Figure 4.22 that the roughness effect on stability of the SC-channel is marginal for thicknesses below 3×10^{-6} m. The effect really became clearer with the highest roughness of 4×10^{-6} m employed in this study. Figure 4.23 presents the period of oscillation plots for the study. It can be seen that the period reduces only slightly with increasing wall surface roughness.

This study suggests that roughness has a marginal effect on the stability analysis of the SC-channel. This may be the situation in the SCWR and requires further analysis to ascertain the influence on stability analysis.

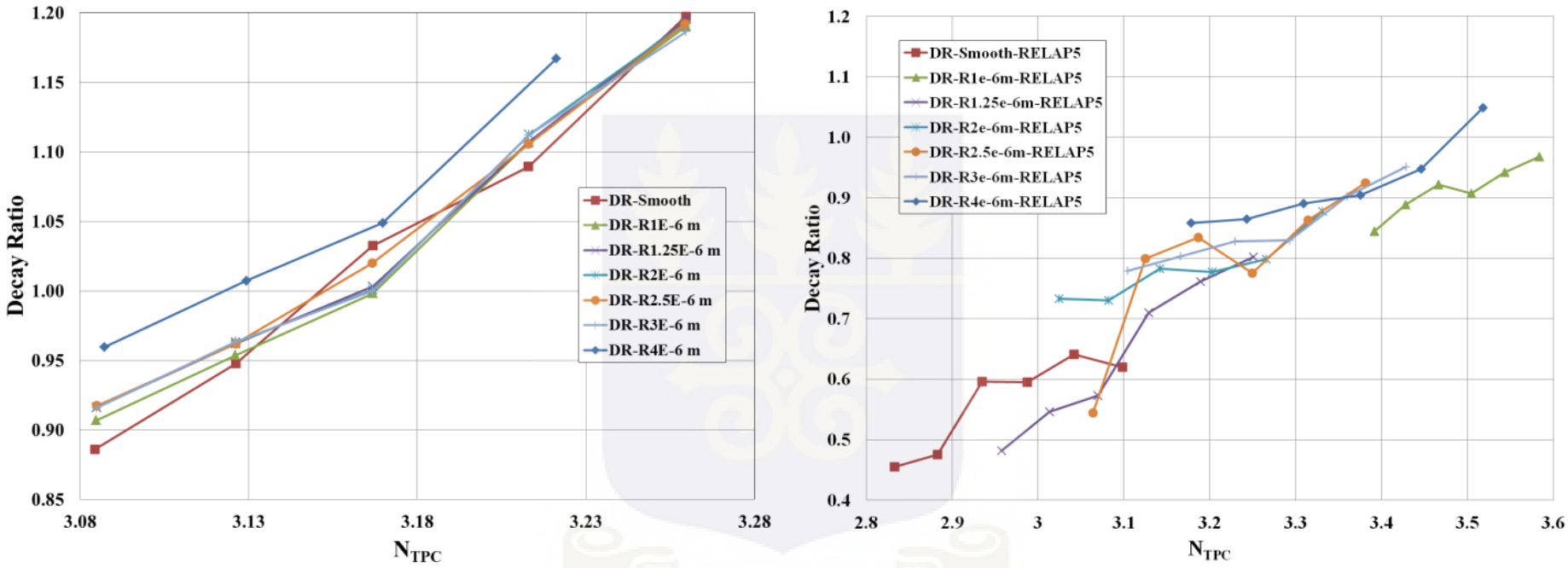

Figure 4.22. Decay ratio plot for effect of wall surface roughness on SC-Channel analysis using STAR-CCM+ and RELAP5.

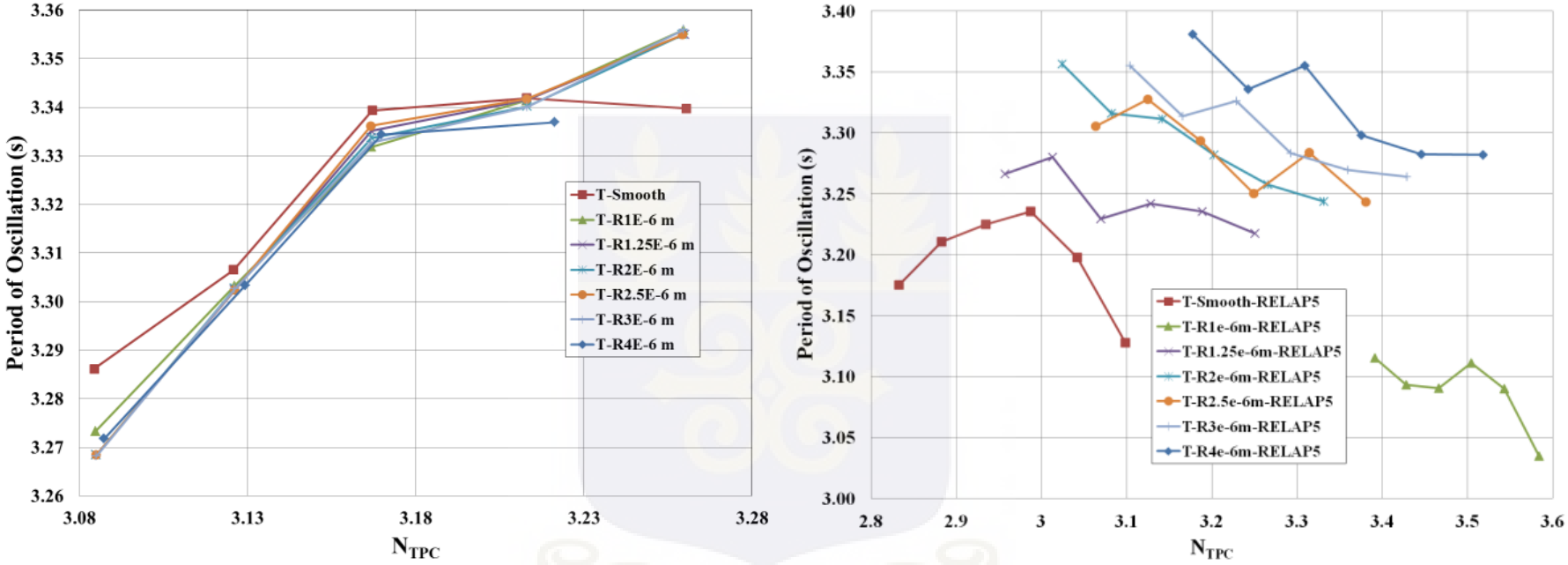

Figure 4.23. Period of oscillation plot for effect of wall surface roughness on SC-Channel analysis using STAR-CCM+ and RELAP5.

4.3.5 COMPARISON OF STABILITY THRESHOLDS FOR STAR-CCM+ AND RELAP5

The models for STAR-CCM+ and RELAP5 for the circular channel were used to simulate the thresholds of instability for the channel using water since it is the common fluid for the two computational tools. The resulting thresholds were compared to the 1D maps discussed in Section 3.5. Figure 4.24 compares the results for the vertical flow showing that the RELAP5 predicts a much more stable channel as compared to the STAR-CCM+. Figure 4.25 compares the period of oscillations for the two computational tools. The trend observed for both codes provides an assurance of the methodology employed.

Figures 4.26 and 4.27 present the horizontal (no gravity) case. RELAP5 again predicts a much stable channel than STAR-CCM+. It can be observed that while STAR-CCM+ predicts a Ledinegg form of instability at both values of N_{SPC} = 2.0 and 2.5, RELAP5 predicts a density wave oscillation at N_{SPC} = 2.0 and a Ledinegg form of instability at N_{SPC} = 2.5.

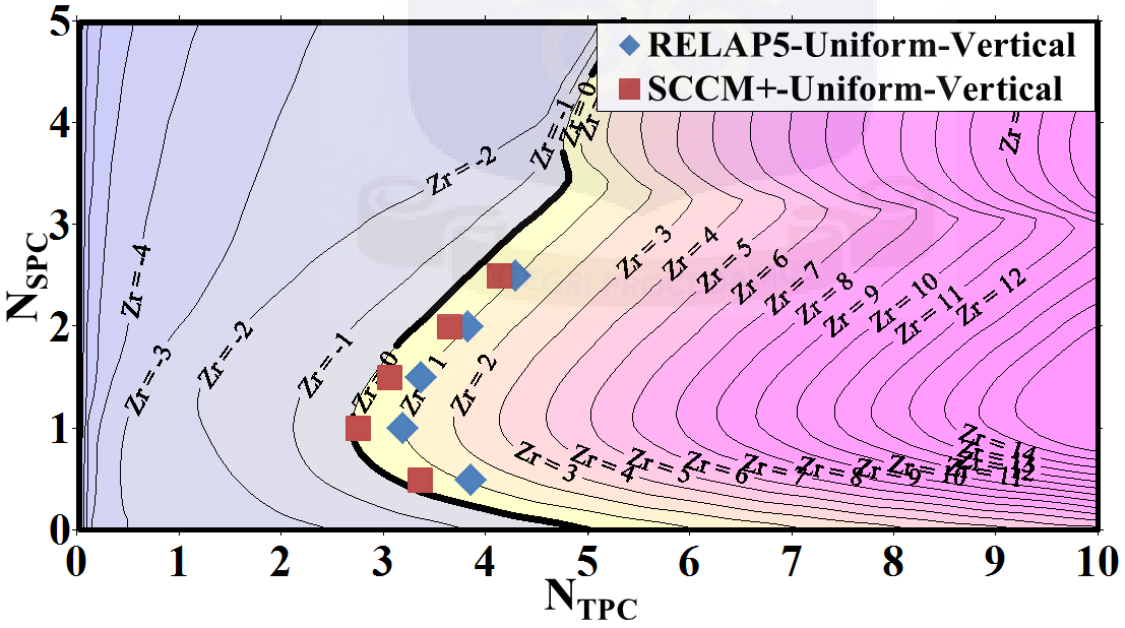

Figure 4.24: Comparison of the stability thresholds obtained for the circular channel against the dimensionless stability map in the case of vertical flow generated for Fr = 0.030, Λ = 4.5, 48 nodes, C_{max} = 0.9

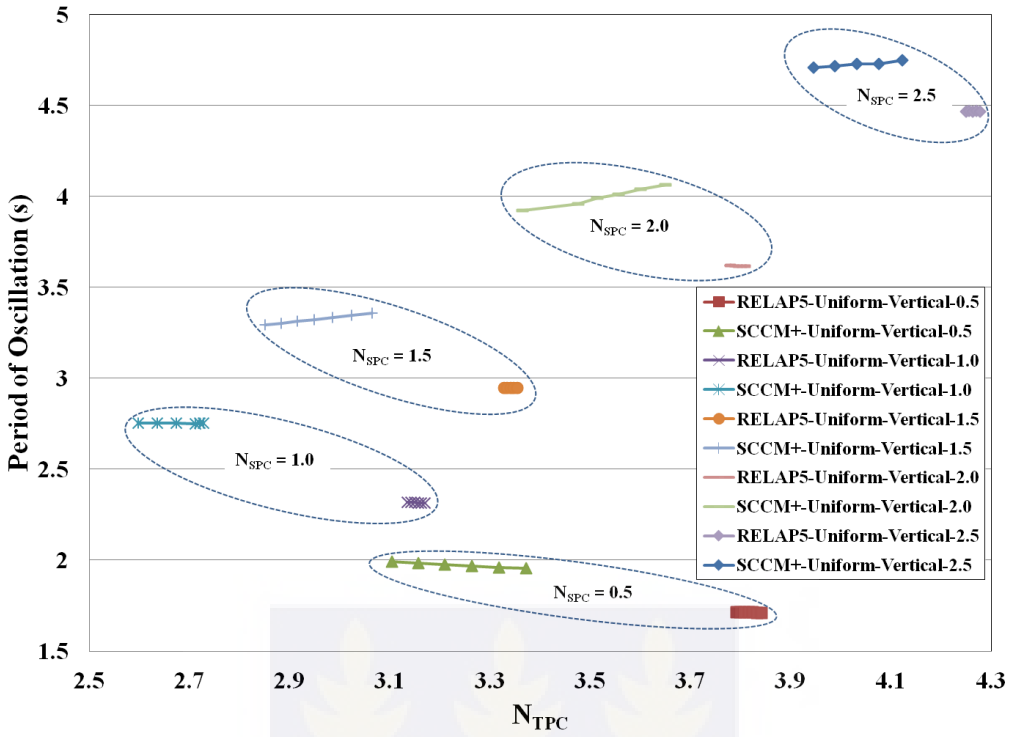

Figure 4.25. Period of oscillations for STAR-CCM+ and RELAP5 in vertical upward flow case at different values of pseudo-subcooling calculated around the onset of oscillations

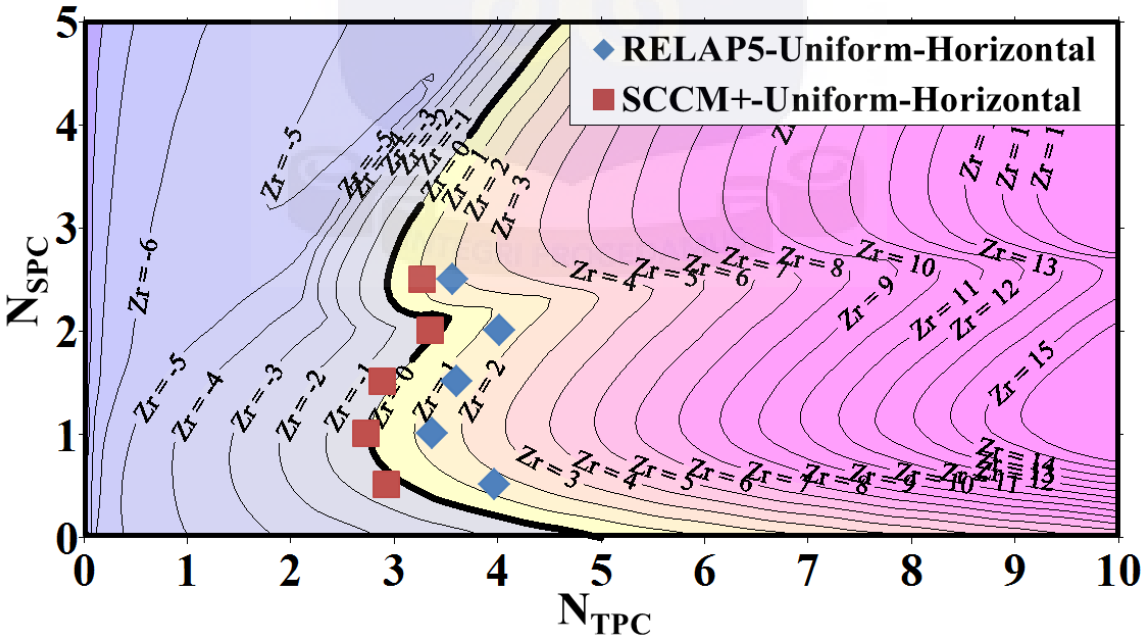

Figure 4.26: Comparison of the stability thresholds obtained for the circular channel against the dimensionless stability map in the case of horizontal flow generated for Fr= 10^5, Λ = 4.5, 48 nodes, C_{max} = 0.9

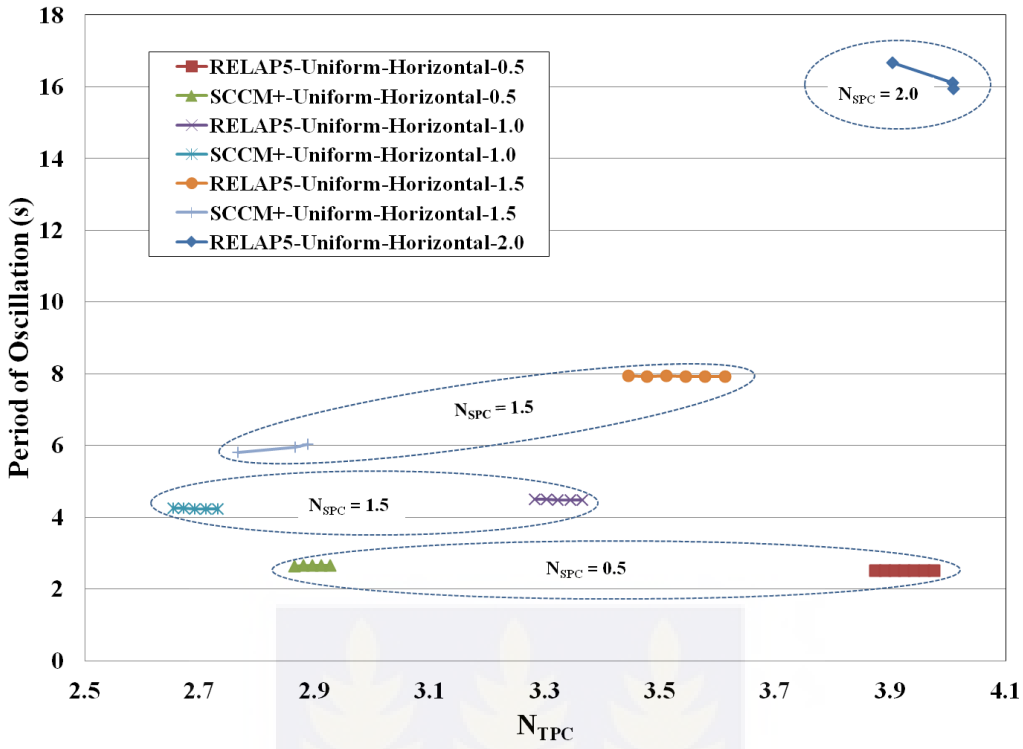

Figure 4.27. Period of oscillations for STAR-CCM+ and RELAP5 in horizontal (no gravity) flow case at different values of pseudo-subcooling calculated around the onset of oscillations

From Figures 4.28 and 4.29, it can be seen that the predictions of both codes are very similar for the downward flow. The significance of the friction factor shall be discussed in the next Section on fluid-to-fluid comparisons.

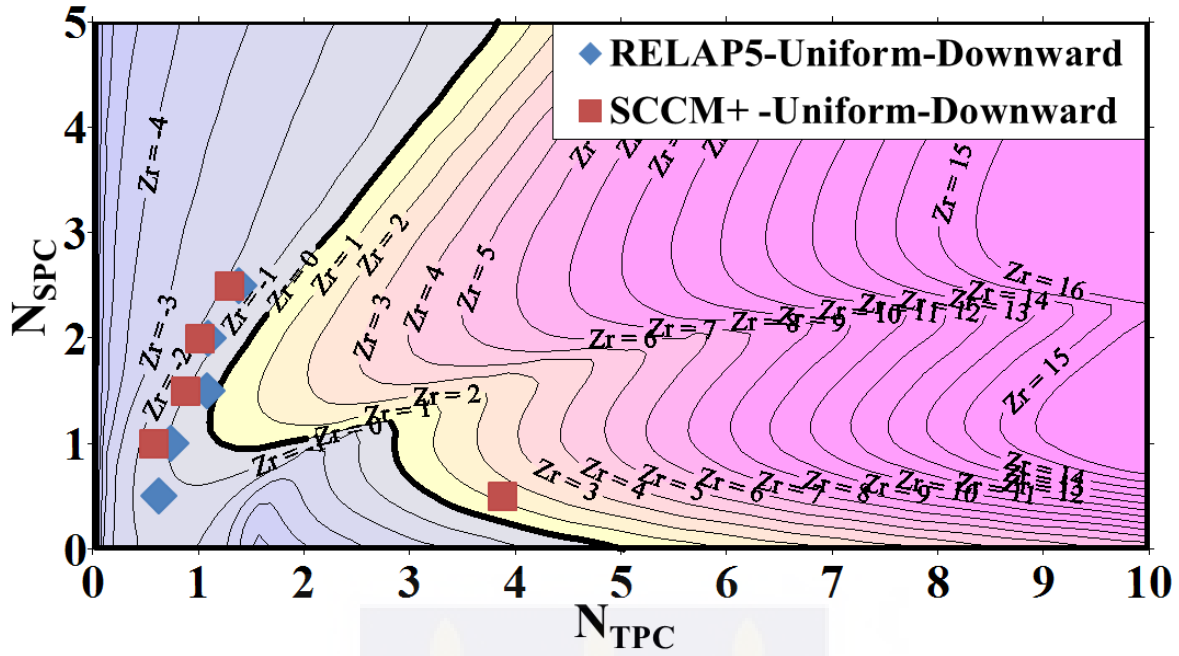

Figure 4.28: Comparison of the stability thresholds obtained for the circular channel against the dimensionless stability map in the case of downward flow generated for Fr= -0.030, Λ = 4.5, 48 nodes, C_{max} = 0.9

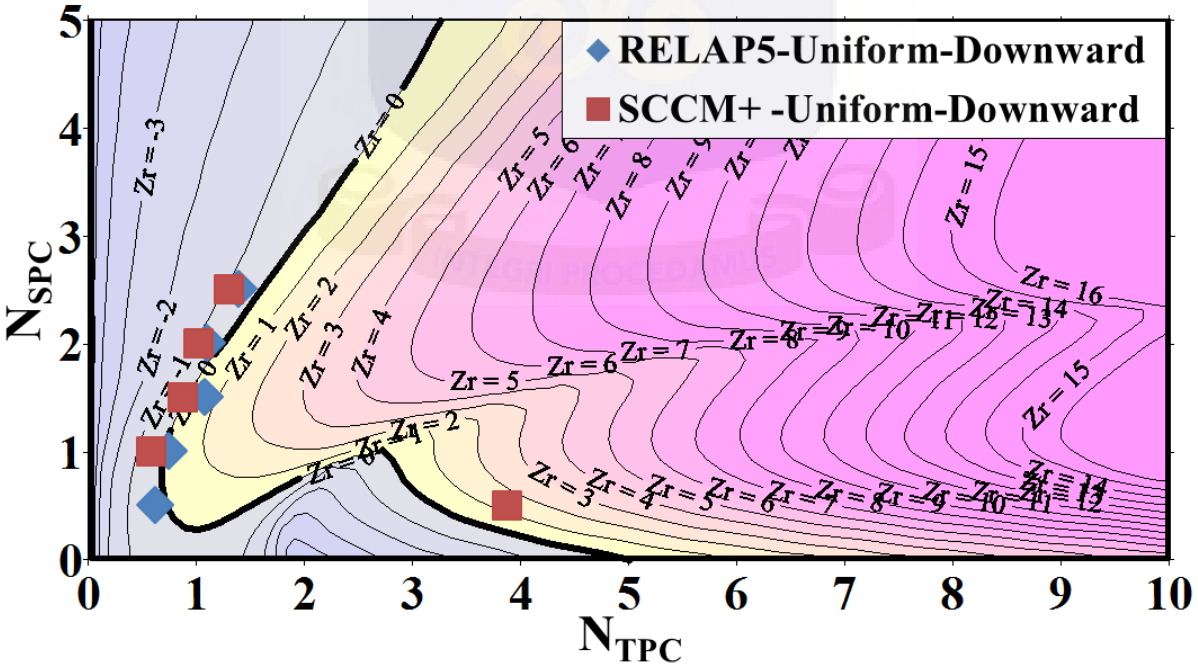

Figure 4.29: Comparison of the stability thresholds obtained for the circular channel against the dimensionless stability map in the case of downward flow generated for Fr= -0.030, Λ = 3.0, 48 nodes, C_{max} = 0.9

The bottom peaked power distribution was applied to the circular channel and the map in Figure 4.30 was obtained for vertical flow. It can be seen that here too RELAP5 predicted a larger margin of stability than STAR-CCM+. From Figures 4.24 and 4.28, it can be deduced that the uniform power distribution provides a larger margin of stability than the bottom peaked power distribution. This result will be further discussed in Chapter 6 when the bottom peaked distribution is applied to the Square assembly slice with kinetics and other realistic characteristics of the SCWR.

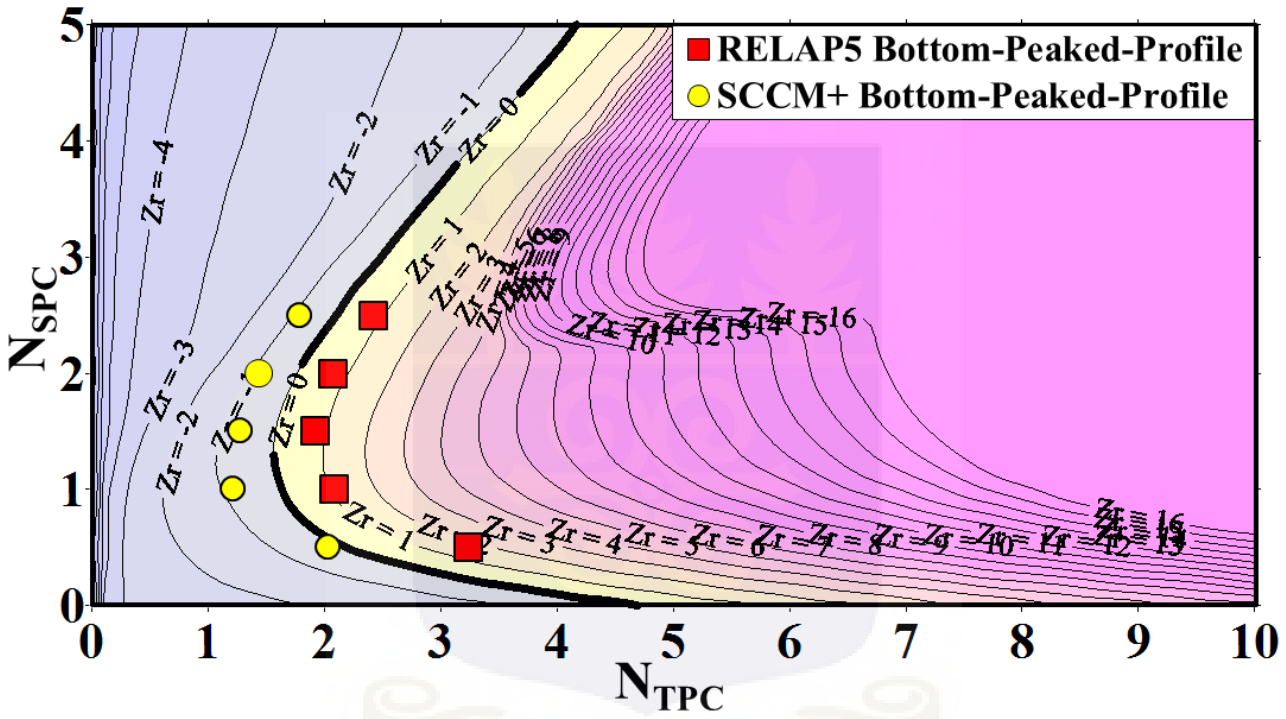

Figure 4.30: Comparison of the stability thresholds obtained for the circular channel against the dimensionless stability map in the case of bottom peaked profile and vertical flow generated for

Fr= 0.030, Λ= 4.5, 48 nodes, C_{max} = 0.9

4.3.6 FLUID TO FLUID ANALYSIS WITH STAR-CCM+

In previous work [17, 70, 75], the results of one-dimensional codes were compared with the stability maps obtained for the same circular pipe system considered here or for a variant obtained from it by different inlet and outlet throttling conditions. In these applications, water and other three fluids at supercritical pressures were considered, in order to assess the degree of generality of the dimensionless numbers proposed for representing results concerning stability. A similar study is reported here on the basis of the results of CFD calculations. Figure 4.31 to Figure 4.34 present the results of the calculations performed by the CFD code in terms of couples of N_{TPC} and N_{SPC} values representing the thresholds of instability identified by the methodology described in the previous sections.

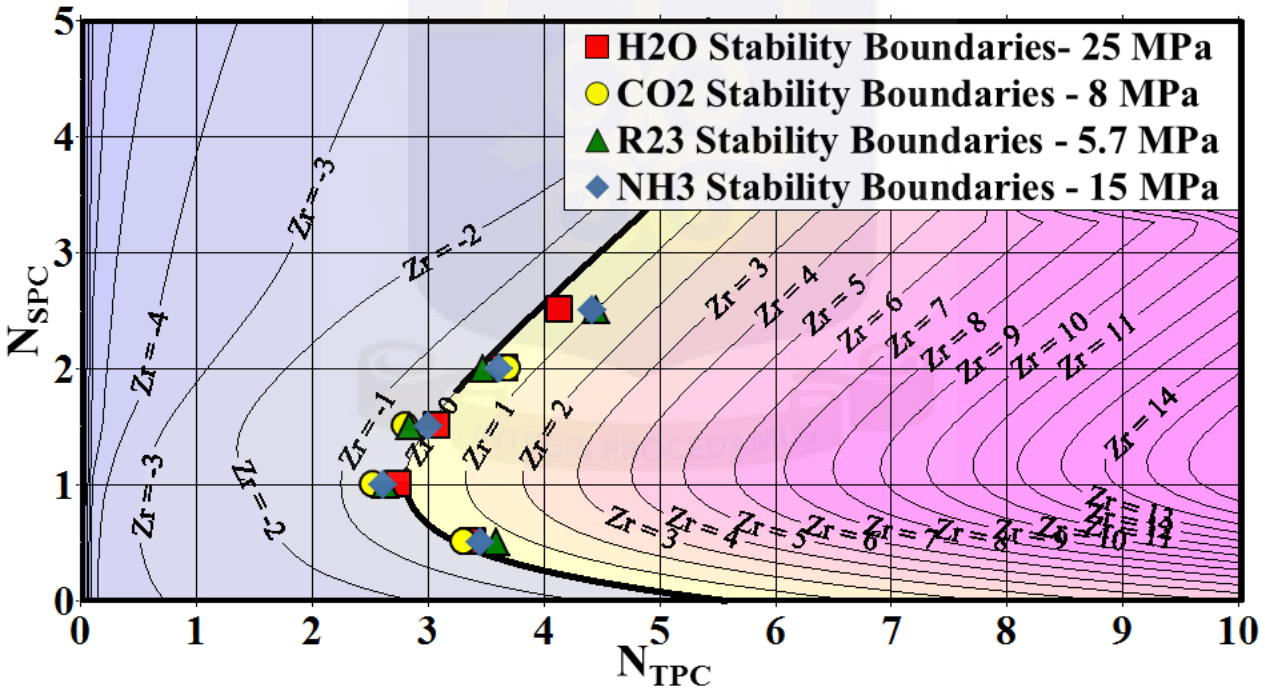

Figure 4.31. Comparison of the stability thresholds obtained for the four fluids against the dimensionless stability map in the case of vertical upward flow generated for Fr=0.03, Λ=4.5, 48 nodes, C_{max} = 0.9

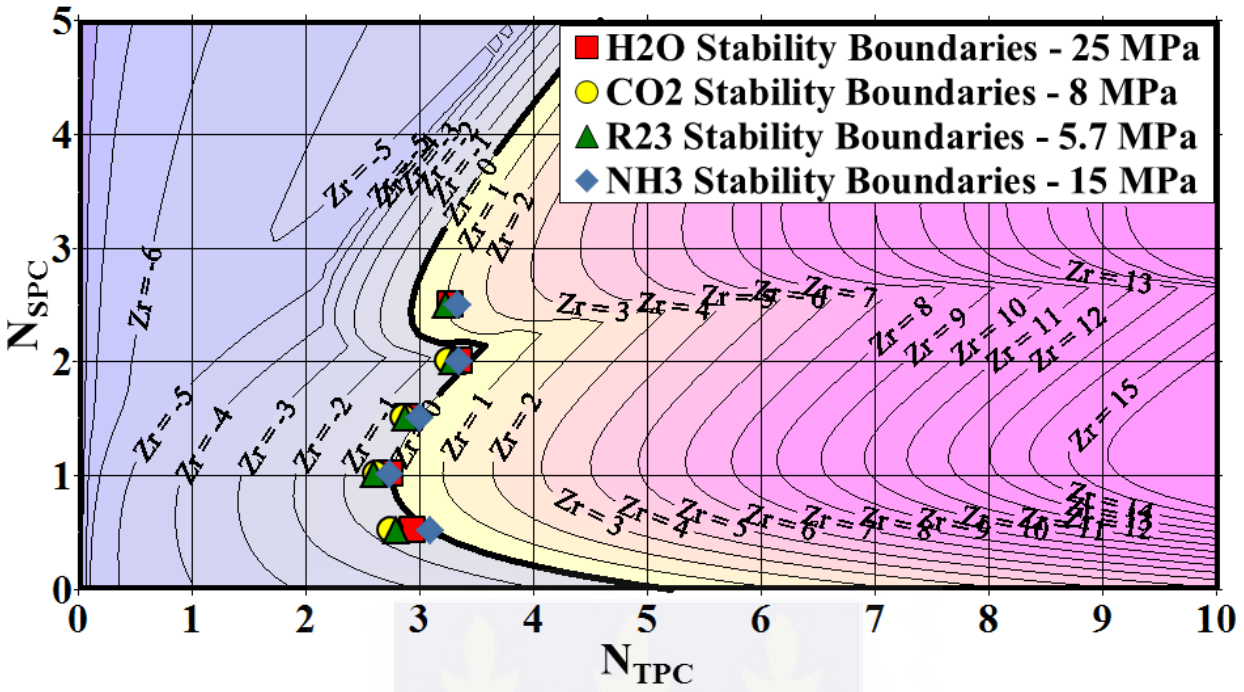

Figure 4.32. Comparison of the stability thresholds obtained for the four fluids against the dimensionless stability map in the case of horizontal flow generated for $Fr=10^5$, $\Lambda=4.5$, 48 nodes, $C_{max} = 0.9$

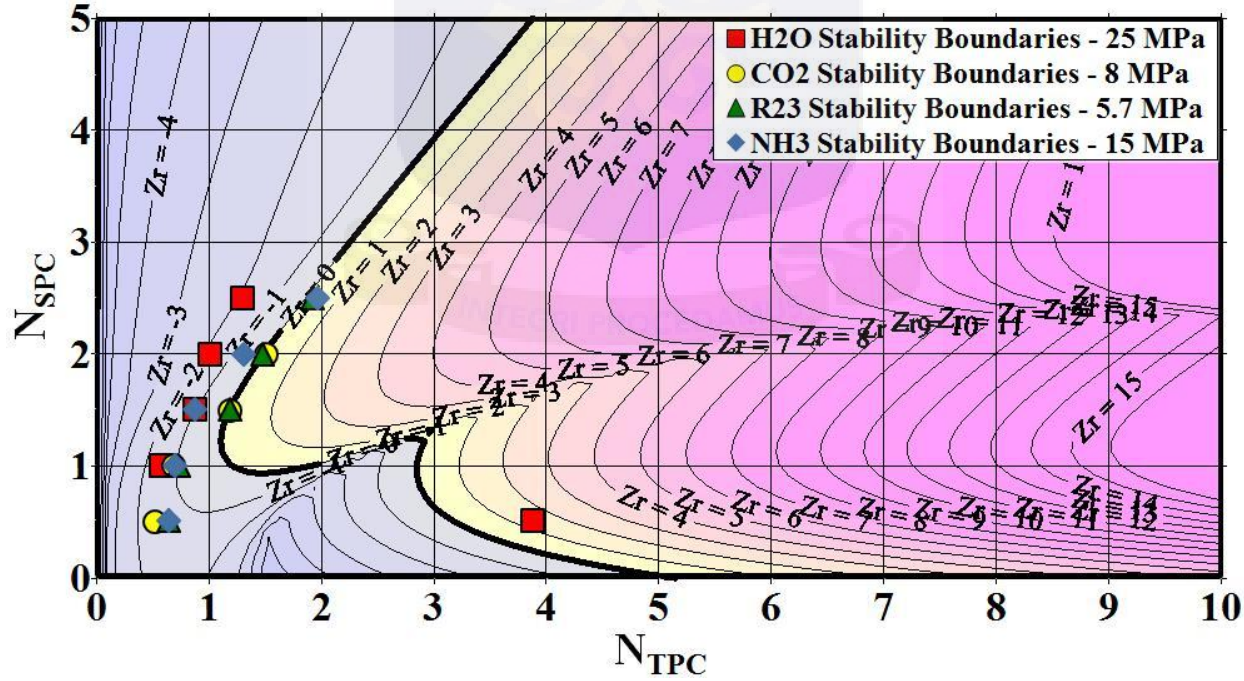

Figure 4.33. Comparison of the stability thresholds obtained for the four fluids against the dimensionless stability map in the case of vertical downward flow generated for $Fr= - 0.03$, $\Lambda=4.5$, 48 nodes, $C_{max} = 0.9$

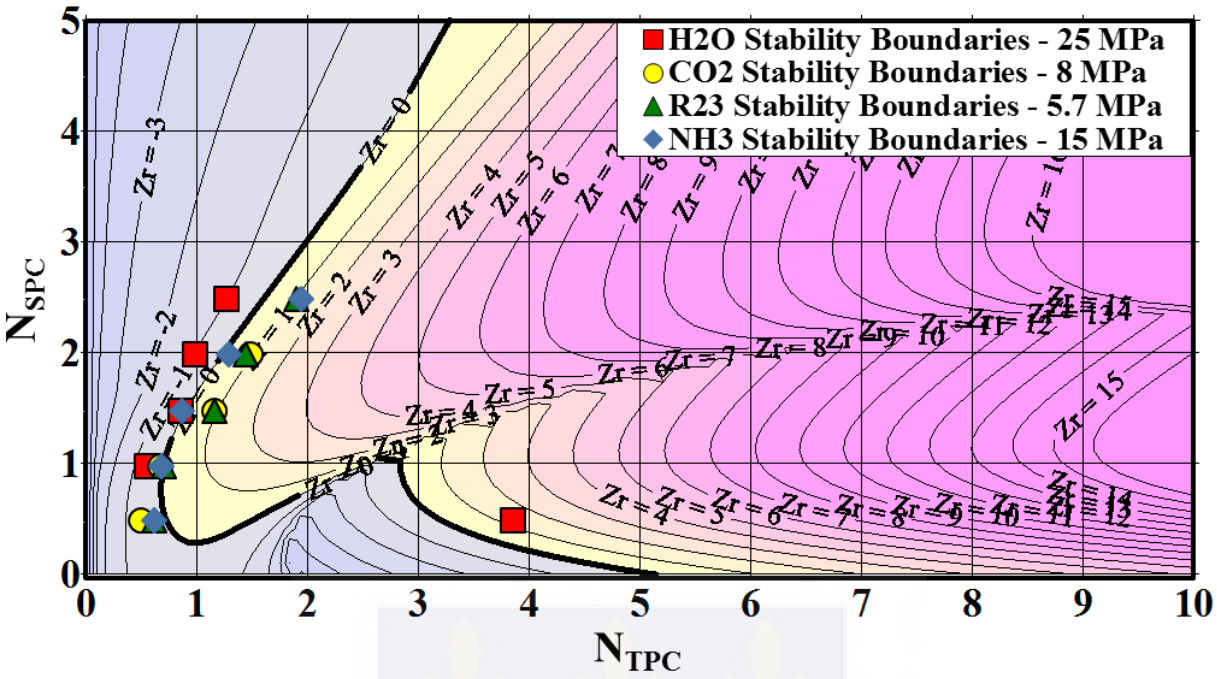

Figure 4.34. Comparison of the stability thresholds obtained for the four fluids against the dimensionless stability map in the case of vertical downward flow generated for Fr= - 0.03, Λ=3.0, 48 nodes, C_{max} = 0.9

As it can be noted, and as it was in the case of 1D models [74], the CFD code provides comparable stability thresholds for the four different fluids, with close resemblance to the trend of the solid lines of the stability maps for the upward and the horizontal flow cases. The downward flow case, which is plagued by a wide region of Ledinegg instability, is affected by possible effects due to the choice of the value of the friction parameter, Λ (compare Figure 4.33 with Figure 4.34) and shows larger discrepancies at low pseudo-subcooling.

In this respect, it must be noted that the assumption of a constant friction factor is really suitable only for rough pipes at large enough Reynolds number. In the case of a smooth pipe, as it is assumed here, the friction factor may vary strongly throughout the map and also from the inlet to the outlet of the channel. The assumptions of Λ = 4.5 and Λ = 3 imply friction factors close to 0.018 or 0.011, respectively, while for water at 25 MPa with N_{SPC} = 1.55 (280 °C inlet temperature, i.e., postulated reactor conditions) the McAdams relationship provides values of $f \approx$ 0.018 at the inlet of

the channel and $f \approx 0.012$ at the outlet in nominal conditions. It is therefore understandable that with decreasing N_{SPC} (e.g., in the region of the large upper lobe of the downward flow map), where the fluid is mostly gas-like, the most appropriate value of the average friction factor along the smooth pipe should be lower and lower. The precise values of the friction factor could be evaluated locally for each fluid and each working condition, which is beyond the approximation adopted in setting up the stability maps.

On this basis, it can be concluded that the results obtained by the CFD code compare reasonably well with the maps and that the dimensionless parameters allow to effectively collapse the obtained stability thresholds for the four fluids in relatively narrow regions close to the stability boundaries evaluated by the 1D model in dimensionless form. It must be reiterated that the presently adopted similarity theory is based on 1D flow balance equations, involving further simplifications, as the assumption of a constant value of the friction factor; therefore, its comparison with results of CFD models is clearly expected to be only approximately accurate, notwithstanding the already discussed role of the use of wall functions.

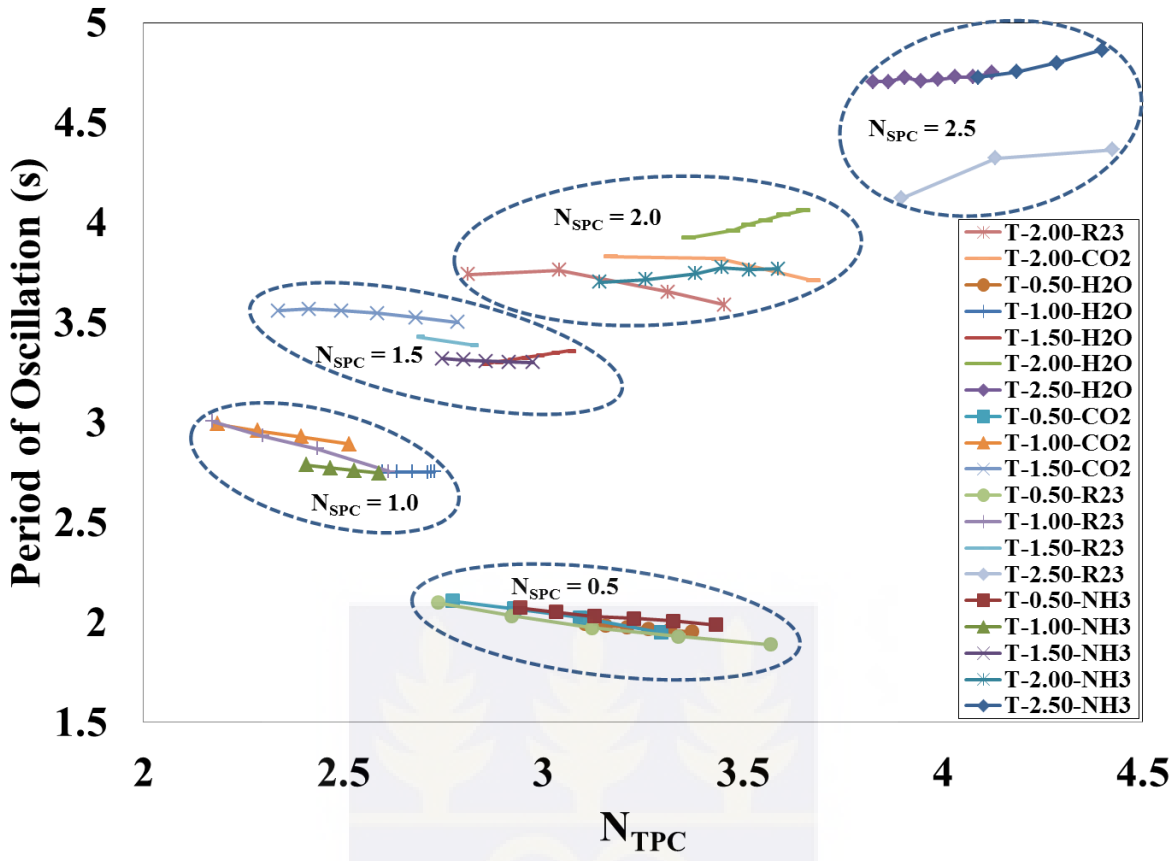

Figure 4.35. Period of oscillations for the four fluids in the case of vertical upward flow at different values of pseudo-subcooling calculated around the onset of oscillations

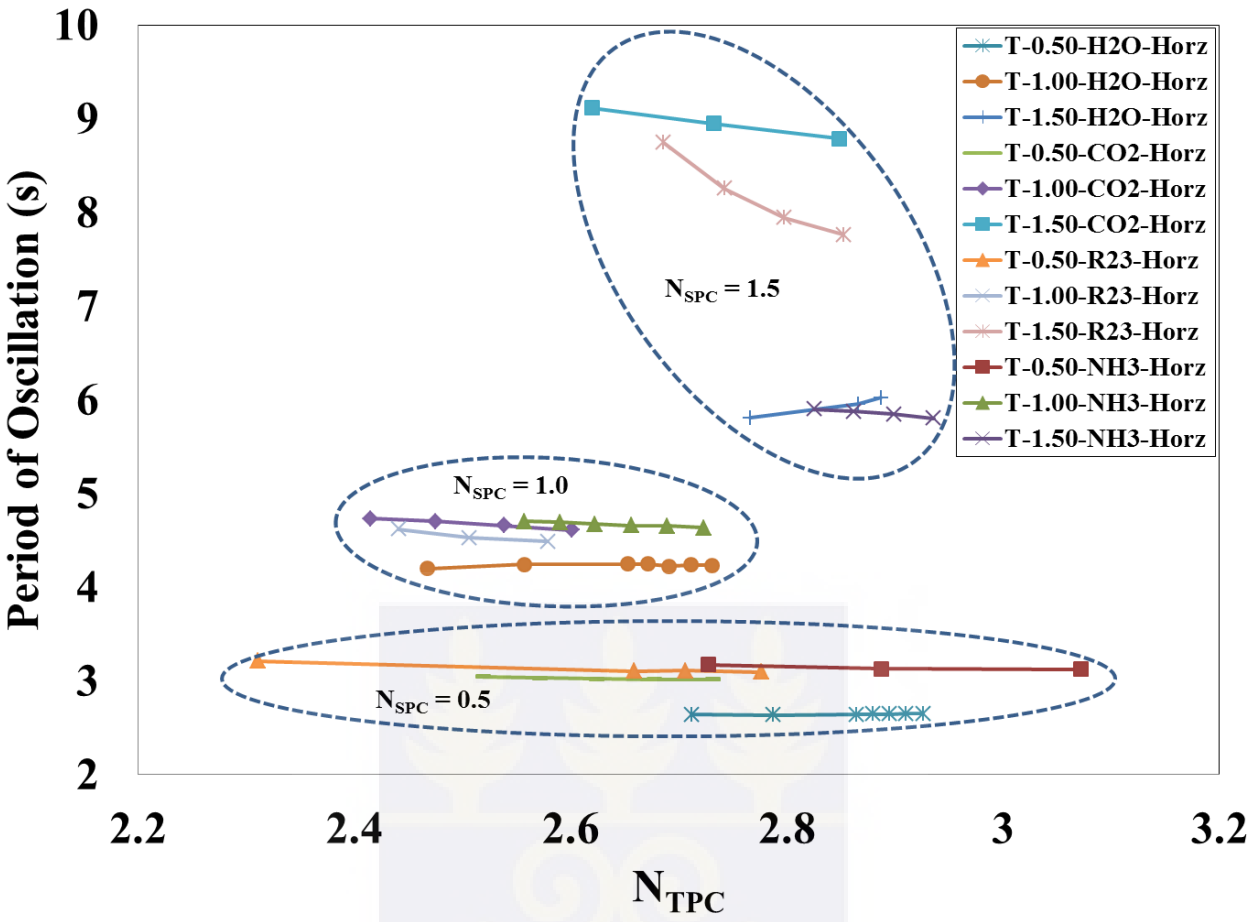

Figure 4.36. Periods of oscillations for the four fluids in the case of horizontal flow at different values of pseudo-subcooling calculated around the onset of oscillations

The conclusion about the similarity in the behaviour of the four different fluids can be further confirmed considering the period of oscillations. Since in the adopted set of dimensionless parameters time is scaled by the time constant obtained by the channel length divided by the inlet velocity, it is expected that in conditions assuring similarity (i.e., equal Λ, Fr, N_{TPC} and N_{SPC}) both the dimensionless and the real periods of oscillations are the same. Figure 4.35 and Figure 4.36 confirm at different extents this expected consequence of the similarity between the different fluids. In particular, it can be noted that:

- for vertical flow, the periods of oscillations for the different fluids are approximately the same and increase with increasing inlet pseudo-subcooling; the latter effect can be explained by the fact that the closer the operating conditions are to the Ledinegg instability region, where the period of oscillation becomes eventually infinite, the smaller becomes the frequency of density wave oscillations; this continuity between the density-wave and the Ledinegg instability conditions was already noted in previous work [13];
- for horizontal flow, the match between the period of oscillation for different fluids is poorer at N_{SPC}= 1.5, i.e., when the period becomes relatively long; this can be explained by the vicinity of these operating conditions to the Ledinegg instability region, that must be understood to be located at slightly different operating conditions for the four fluids, due to the approximate nature of the similarity principles here discussed.

It must be noted that it was not possible to construct a reasonable plot related to the period of oscillations for downward flow, because most of the operating conditions are affected by the Ledinegg instability, being characterised by a virtually infinite period owing to its excursive nature.

In relation to the occurrence of the Ledinegg instability at sufficiently large pseudo-subcooling, Figure 4.37 adds a final detail, showing the shape of the pressure drop vs. flow rate characteristics in the case of horizontal flow for water at 25 MPa with a constant heating power. As it can be noted, for increasing pseudo-subcooling number the curves show an increasingly deep depression, with the characteristic non-monotonic trend expected for such conditions.

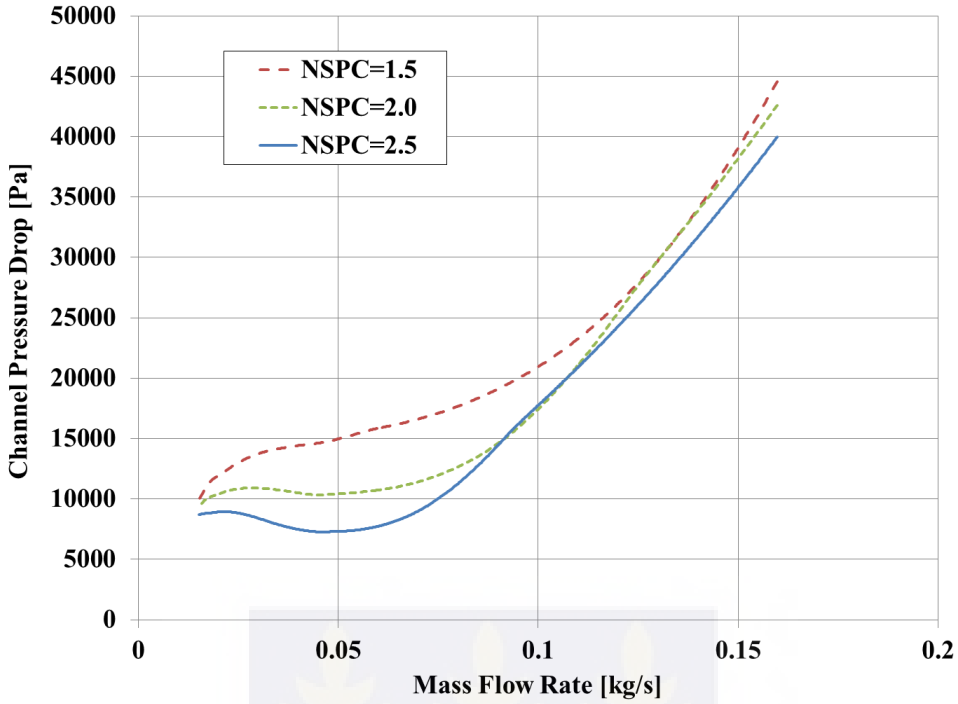

Figure 4.37. Channel pressure drop vs. flow characteristics for different values of pseudo-subcooling in horizontal flow for water at 25 MPa

4.4 CONCLUDING REMARKS

The analyses whose results were presented in this Chapter were aimed at providing a basis for making use of CFD codes in evaluating the stability of supercritical water reactor channels. A strong motivation for continuing in such an endeavour is, in addition to scientific curiosity, the consideration that the first analyses performed just few years ago in first attempts could now be repeated, extended and made more meaningful with greater ease, thanks to the improved computational hardware and software. This suggests that preparing a CFD methodology for addressing problems pertaining up to now to the domain of application of 1D system codes and of subchannel models can turn out more and more convenient in the near future, possibly providing greater detail, accuracy and reliability.

Chapter 5 extends the scope of this study to cover slices of a typical SCWR fuel assembly. The square and triangular slices are studied and their stability thresholds are predicted.

CHAPTER 5

ANALYSIS OF SUPERCRITICAL REACTOR SUBCHANNEL SLICES

5.1 INTRODUCTION

The chapter presents the results of the analysis of flow stability performed with CFD models about the flow stability in fuel bundle slices with upward, horizontal and downward flow orientations. Square and triangular lattice slices are both studied, based on previous work discussed in Chapter 4 that demonstrated the feasibility of such analyses. A uniform heat flux is applied to the slice walls without addressing the internal structure of the rod. The STAR-CCM+ code [73] is adopted, comparing the results obtained by a 3D model with those that were obtained by the 1D RELAP5 code. The analysis is limited to consider water at supercritical pressure, relevant for nuclear reactor application. The steady-state characteristics of the two models are considered and the thresholds of instability identified by transient calculations are compared with maps set up by an in-house 1D code using a dimensionless formalism discussed in Chapter 3. Both static and dynamic instabilities are observed, in similarity with previous analyses presented in Chapter 4 for circular channels. The work represents a further step in the research aimed at establishing a methodology for the analysis of flow stability in nuclear reactor cores by CFD codes.

5.2 ADDRESSED GEOMETRY AND ADOPTED MODEL CHARACTERISTICS

The two slices considered in this section; they are a square and a triangular pitch rod bundle slices having the following characteristics [15]:

- for the square pitch subchannel: rod diameter = 10.2 mm; pitch = 11.2 mm; active height = 4.2 m;

- for the triangular pitch subchannel: rod diameter = 7.6 mm; pitch = 8.664 mm; active height = 3 m.

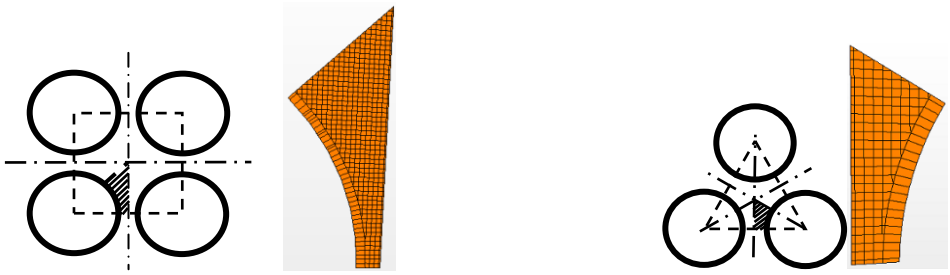

a) 1/8 square pitch assembly slice b) 1/6 triangular pitch assembly slice

Figure 5.1. Fuel bundle slices considered in the present work with their radial discretisation [17]

The geometries of the two bundle slices, shown in Figure 5.1, are coherent with previous proposals about different core configurations of thermal and fast supercritical water reactors [68, 95]. The 1/8th square and 1/6th triangular pitch assembly slices were selected taking advantage of the symmetry existing for both situations in the design. No throttling was considered at the inlet and at the outlet of the subchannel and the wall surface was assumed to be smooth.

Among the various possibilities offered by STAR-CCM+, a "trimmed" mesh made of regular hexahedral nodes was adopted to discretise the two configurations, making use of a mesh base size of 0.1 mm. The node close to the wall was chosen to be larger, making use of a "prism layer" with a single radial node, in order to adopt a "high y+" approach (i.e., allowing for the use of wall functions); the selected depth of the node at the wall was 0.19 mm. As in the case of the circular pipes considered in the previous Chapter [17], this choice was made in order to avoid the complications brought about by a detailed treatment of the near wall phenomena. It is necessary to consider that CFD codes, even when used with low-Reynolds number RANS approaches, do not yet have enough capabilities to simulate the effects of heat transfer deterioration due to buoyancy and, especially k-ε models, tend to strongly overestimate the wall temperatures [74]. This represents an

additional effect that was considered worth to be minimised in the present analyses, with the aim to focus on more general behaviour. The turbulence model adopted in the present analyses was selected to be the standard k-ε one available in the STAR-CCM+ code.

The axial discretisation included 200 nodes for the square lattice subchannel and 100 for the triangular lattice subchannel. The procedure to obtain this result starting from the "trimmed" mesh, made of cubic 0.1 mm nodes, was to resize a small piece of subchannel up to the desired length after meshing it, thus obtaining long parallelpipedal nodes with square base.

The choice of the solver and time discretisation were the subject of an attentive analysis in the previous phase of the work related to circular channels [17] and reported in Chapter 4; the present calculations were therefore performed in accordance, taking benefit from the experience gained. In particular, since the flow is strongly affected by buoyancy, the "coupled flow" and "coupled energy" options were preferred to the "segregated" flow and energy ones. Moreover, since considerable numerical diffusion effects were noted in the case of circular channels by the use of the first order implicit time advancement, the second order implicit one available in STAR-CCM+ was selected. The time step, also in agreement with previous experience, was chosen to be 0.1 s, as a reasonable compromise between accuracy and computational efficiency. Similarly, the maximum Courant number for inner iterations was selected as 20,000, in order to reach a reasonable convergence in 20 inner iterations. It must be noted that some calculation cases with the square sub-channel slice for horizontal and downward flow required lowering the value of this parameter to 10,000 to attain convergence. The properties of water used in this work have been presented in Section 3.8.

The model adopted for RELAP5/MOD3.3 [93] is similar to the one used in previous applications [13, 70], but it was customised for the specific analysis reported in this Chapter. It consists of two "time dependent volumes", simulating the large inlet and outlet plena with the fluid thermodynamic conditions assigned, connected by "single-junctions" to a "pipe" component, discretised with 48

nodes in both the square and triangular lattice slices. Very thin heat structures with large conductivity and low heat capacity, one per each hydrodynamic node, are in thermal contact with the outer surface with the fluid. The full flow cross section of the square lattice slice is considered in the model, corresponding to a full perimeter of the rod; in the triangular lattice case, instead, the double of the subchannel cross section was adopted, in order to correspond again to a full heated perimeter. This difference is an obvious consequence of the geometry of the two subchannels, shown in Figure 5.1, that involve a full rod in the square lattice case and half rod in the triangular one. It must be noted that these details play a minor role in a 1D model with imposed power, since only the total thermal power fed to the channel is relevant for the dynamics, no matter the length of the wetted perimeter.

A relevant detail for the 1D model is the hydraulic diameter to be assigned to the subchannel. Preparing for a comparison with a CFD model, in which the actual geometry of the subchannel is considered, the only available rule to be applied for defining the geometry in a 1D perspective is the definition of this parameter as four times the flow area divided by the wetted perimeter. The values used in the cases of the two lattices were computed to be 5.46 mm for the square and 3.29 mm for the triangular lattices, as in previous work [15]. It must be noted that the adopted engineering rule applicable in 1D calculation cannot exactly reproduce the actual 3D conditions, with the uneven distribution of flow in the different parts of the slice cross sections, which will contribute to the overall friction in different ways.

A further interesting aspect in order to make a meaningful comparison between the CFD code and the system code is related to the inlet and outlet pressure drops. RELAP5 was used in this as well as in previous stability studies with allowance for the consideration of inlet and outlet plena with very large volumes and stagnating conditions. This brings about a reversible restriction pressure loss at the inlet, corresponding to the value of the kinetic head, and a similar expansion pressure gain at the outlet; so the nodal pressure is seen to decrease because of this effect crossing the inlet section and

increase again across the outlet section. This effect is superimposed to distributed friction and gravity. On the other hand, the use of a "stagnation inlet" in the STAR-CCM+ code is accompanied by a similar reversible restriction pressure loss effect, as in the case of RELAP5, though the "pressure outlet" boundary condition is not accompanied by such consideration of outlet plena, imposing the assigned pressure exactly at the outlet pipe section.

This aspect may not only create a discrepancy in the comparison of pressure distributions along the channel, but it can also affect stability characteristics. Since in the calculations of stability the chosen boundary conditions are the values of the upstream and the downstream pressures, it must be expected that imposing a pressure in a plenum or exactly at an inlet or outlet section does change the dynamic response of flow rate to perturbations, since the internal pressure drop developed by the channel will be forced to be equal to the imposed one. In order to deal with this problem, it was chosen to keep the models for STAR-CCM+ and RELAP5 as coherent as possible, by imposing in the latter a pressure drop coefficient equal to 1 at channel outlet; this completely compensates the pressure recovery observed between the last node in the channel and the outlet plenum. In the following, therefore, it will be assumed that the actual situation simulated is in both cases the one of two plena with no irreversible pressure drop coefficient at the inlet and an irreversible pressure drop coefficient equal to unity at the outlet. This situation will be mentioned in the figures also for STAR-CCM+, meaning that stagnation inlet and pressure outlet conditions are used without imposing any irreversible pressure drop.

5.3. METHODOLOGY OF ANALYSIS

The procedure followed for obtaining the stability threshold at the different operating conditions was inherited from the previous work on the circular channel [17] as reported in Chapter 4 and was adapted to the present case.

In the case of STAR-CCM+, a "velocity" boundary condition is initially adopted to force flow through the subchannel at power conditions more or less close to those of the guessed stability boundary. This step is necessary because the subsequent stability analysis must be performed at constant imposed pressure drop across the duct, using increasing power levels to progressively destabilise the system; so, this pressure drop must be previously evaluated considering a value of inlet velocity selected as reference. For purpose of comparison with stability maps obtained in dimensionless form, this reference velocity was assigned to 1.12 m/s, corresponding to a value of the Froude number (*Fr*)

$$Fr = \frac{w_{in}^2}{g\,L} \tag{5.1}$$

around 0.03 in the case the square lattice duct and around 0.043 for the shorter triangular slice duct.

After guessing the needed pressure drop, the inlet boundary condition is then changed to "stagnation inlet", assigning the inlet pressure to it, evaluated by the previous steady-state analysis at imposed velocity. So, the combination of this boundary condition with the "pressure outlet" one assures the desired constant channel pressure drop, representing the situation of non-interacting "parallel channels". Once this condition is achieved, the power fed to the channel is increased in steps, leaving the system to freely evolve after each increase, before the next step increase is applied; this allows the lower and upper bounds of the value of power at which unstable behaviour is observed to be found.

The results of power and inlet flow rate are then processed to express the obtained results in the dimensionless formalism introduced by Ambrosini and Sharabi [14] and reported in Chapter 3.

In particular, the trans-pseudo-critical number, N_{TPC}, is the main monitored variable, aiming to ascertain the kind of behaviour (stable or unstable) exhibited by the system after each power step at any given value of the inlet enthalpy, i.e., of N_{SPC}, kept constant during the whole transient.

The procedure adopted with RELAP5 is nearly the same. In this case, owing to the shorter running time for each calculation case with respect to the CFD runs, the pressure drop to be assigned to the channel was guessed in repeated short transients with different pressures in the inlet plenum and the constant pressure of 25 MPa in the outlet one, up to the point in which velocity of 1.12 m/s is obtained at channel inlet. Then, the analysis with stepwise increasing power at constant pressure drop is performed, until unstable behaviour is observed.

Figure 5.2 to Figure 5.5 report sample time-trends of N_{TPC} obtained through this procedure by the two codes for corresponding cases. The following considerations apply:

- Figure 5.2 presents results for downward flow in the square lattice slice for a medium pseudo-subcooling; both codes predict an excursive (Ledinegg) instability occurring at N_{TPC} roughly equal to 1.5; as it will be shown later on, excursive instabilities characterise most of the downward flow cases;
- In Figure 5.3, also related to downward flow in the square lattice slice, but at lower pseudo-subcooling, it can be noted that the two codes predict different characters of the instability, also occurring at different levels of N_{TPC}; in particular, the unstable behaviour obtained by RELAP5 is of the oscillatory type, while Ledinegg excursions are obtained by STAR-CCM+; this discrepancy will be discussed later on;
- In Figure 5.4, related to horizontal flow in the triangular lattice slice at low/medium pseudo-subcooling, both codes predict oscillatory instabilities at a value of N_{TPC} slightly greater than 3;
- finally, in Figure 5.5, also related to horizontal flow in the triangular lattice slice at medium pseudo-subcooling, oscillatory behaviour is again predicted by the two codes at comparable values of N_{TPC}.

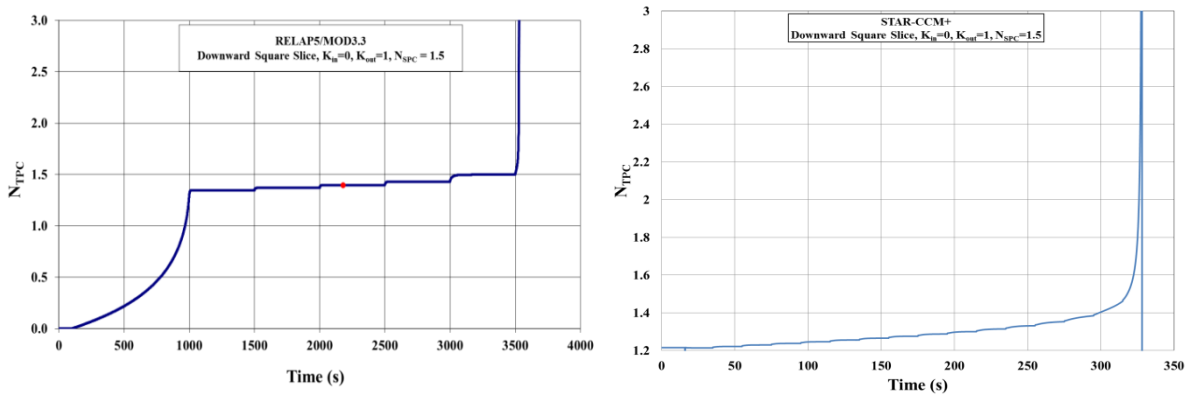

Figure 5.2. Sample trends of N_{TPC} for downward flow in the case of the square lattice slice at medium pseudo-subcooling

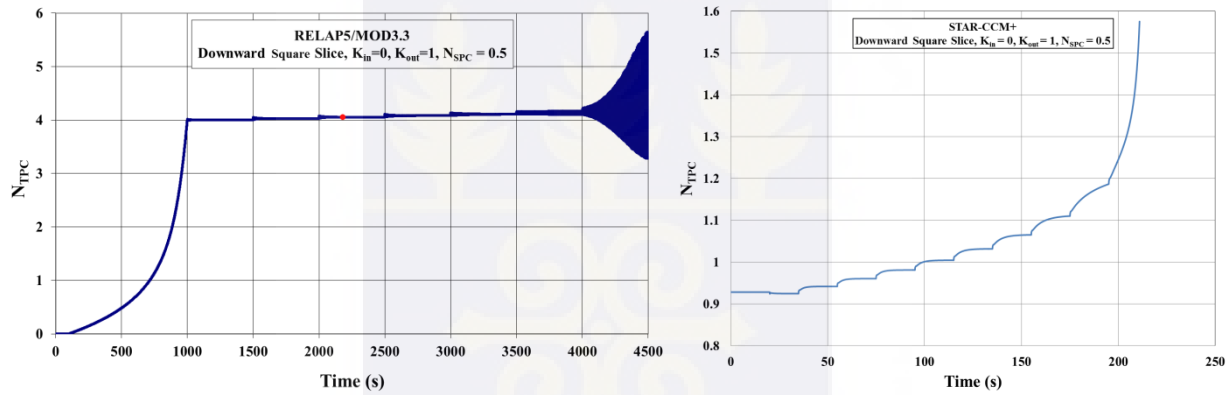

Figure 5.3. Sample trends of N_{TPC} for downward flow in the case of the square lattice slice at low pseudo-subcooling

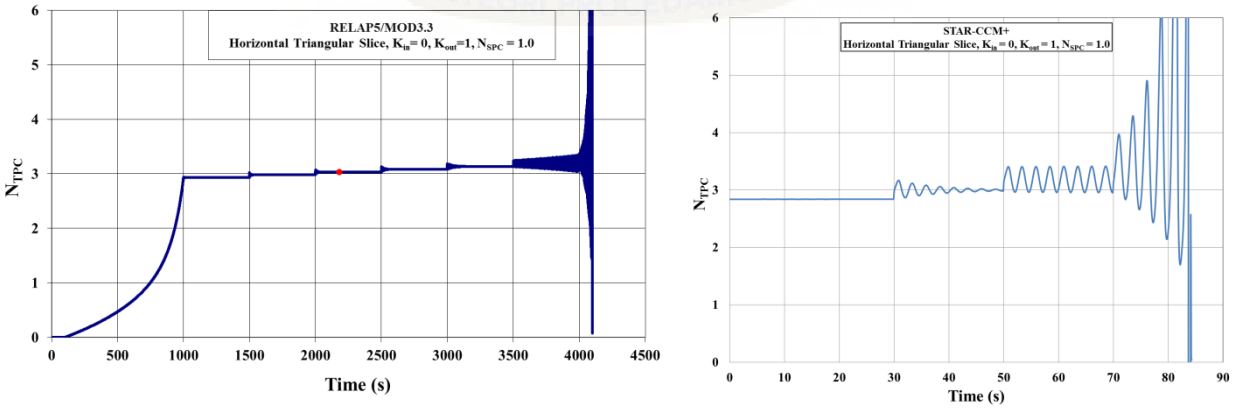

Figure 5.4. Sample trends of N_{TPC} for horizontal flow in the case of the triangular lattice slice at low/medium pseudo-subcooling

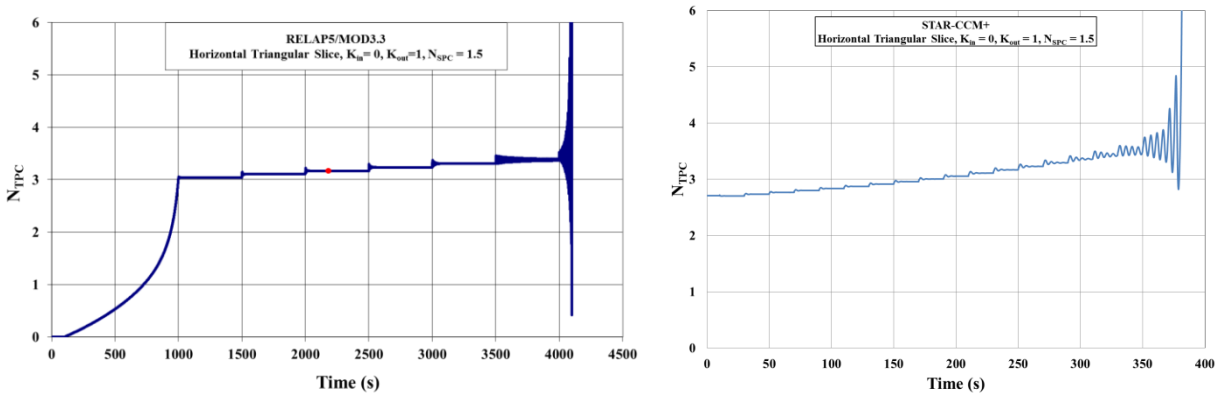

Figure 5.5. Sample trends of N_{TPC} for horizontal flow in the case of the triangular lattice slice at medium pseudo-subcooling

The time trends of N_{TPC} were processed by the formulation already adopted for the circular channel cases [17] and discussed in Section 3.6, in order to evaluate the decay ratio and the period of oscillations (if any) in each time window. The program interprets the oscillatory behaviour as an approximate second order model response, thus finding the angular frequency and the damping or amplification factors for the average value of N_{TPC} assigned in each interval.

It must be noted that the above described calculation procedure does not always assure a close match with the target values of the Froude number at the onset of instability. This occurs because the power at which the calculations are initialised with an inlet velocity of 1.12 m/s is lower than the one leading to unstable behaviour; the subsequent increases in power will lead to progressive decreases in the inlet flow rate, with corresponding decreases in inlet velocity. This means that the Froude number at the instability threshold will be generally lower than specified, especially when the initialisation power is far from the one at the onset of instabilities. In the case of RELAP5, it was possible to partly compensate for this problem running repeated calculations at different initial power levels to get close enough to the stability threshold in the initialisation phase; on the other hand, this was not feasible in the case of the CFD code, because of the lengthier processing time required for the transient analysis in the 3D geometry. As a consequence, it must be understood that

the comparison with stability maps obtained with a constant Froude number is more meaningful for RELAP5 results than for STAR-CCM+ ones, though in both cases it is not exact. This limitation is accepted considering that the value of the Froude number affects mainly the location of the Ledinegg instability threshold, as already shown in Chapter 4, while it generally has little influence on the density wave oscillation stability boundary.

5.4. OBTAINED RESULTS

Though the main focus of the present work is the comparison of the predictions of the two codes in transient conditions, a comparison of steady-state distributions obtained by both of them for relevant variables in reference conditions was performed. These reference conditions were chosen as an inlet velocity of 1.12 m/s, an inlet temperature of 280 °C and the value of power necessary in both cases to obtain 500 °C for the outlet fluid temperature. Figure 5.6 to Figure 5.10 present a selection of steady-state distributions of fluid velocity, pressure, temperature and density for the square and triangular lattice subchannel slices for the different flow directions considered in the study. It can be observed that the distributions for velocity, temperature and density are similar for the two codes in all flow directions in both the square and the triangular lattice cases. The pressure distribution varies depending on the flow direction, as can be seen in Figure 5.7. It can also be observed that the temperature distributions from STAR-CCM+, taken at different radial locations, compare well with the cross section averaged value obtained by RELAP5; the different spreads in fluid temperatures shown by the triangular and the square lattice cases is partly due to the different location of the nodes selected for the representation in the two cases and to the fact that the square slice has a greater degree of uneven distribution of flow in different parts of the subchannel, giving rise to larger maximum wall temperatures.

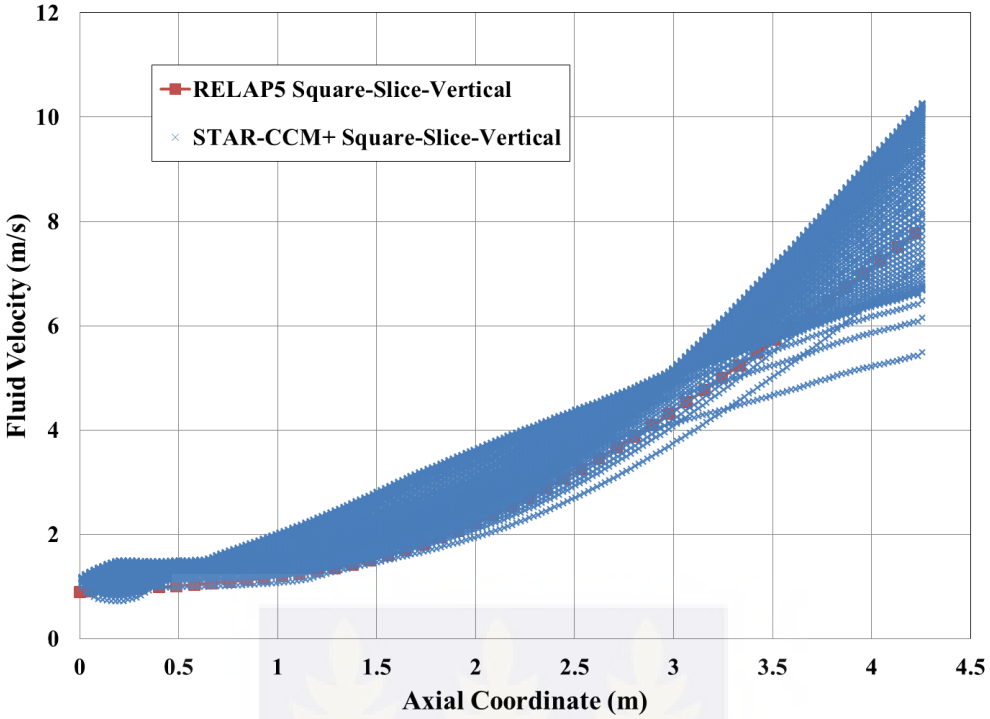

Figure 5.6. Steady-state fluid velocity distribution along the square lattice slice obtained by the two codes for vertical upward flow in corresponding conditions

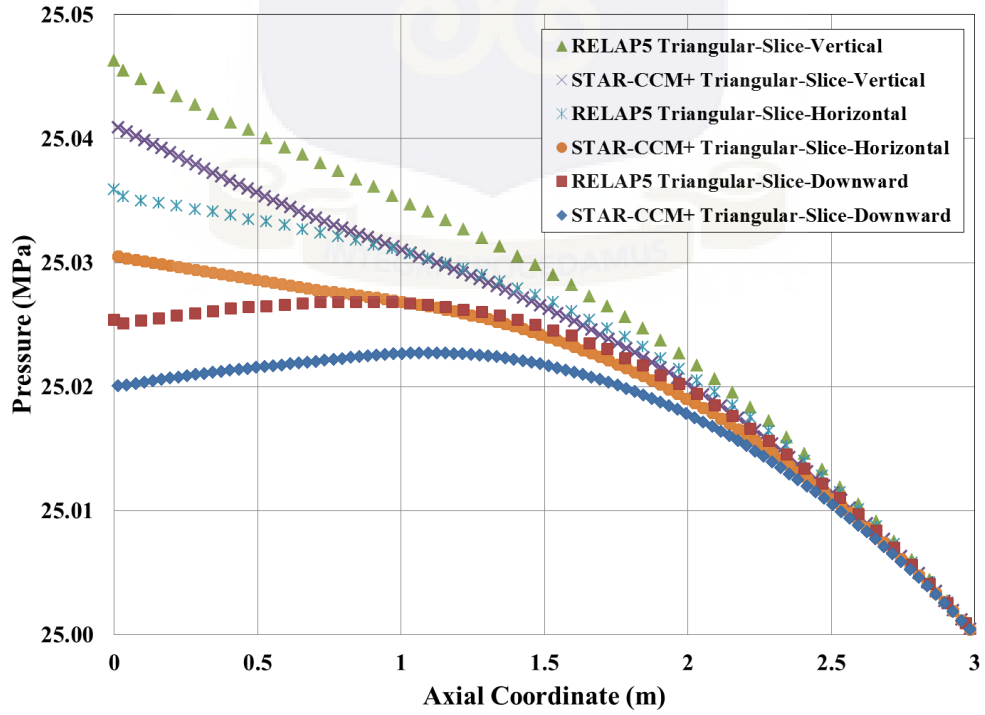

Figure 5.7. Steady-state pressure distribution along the triangular lattice slice obtained by the two codes in corresponding conditions

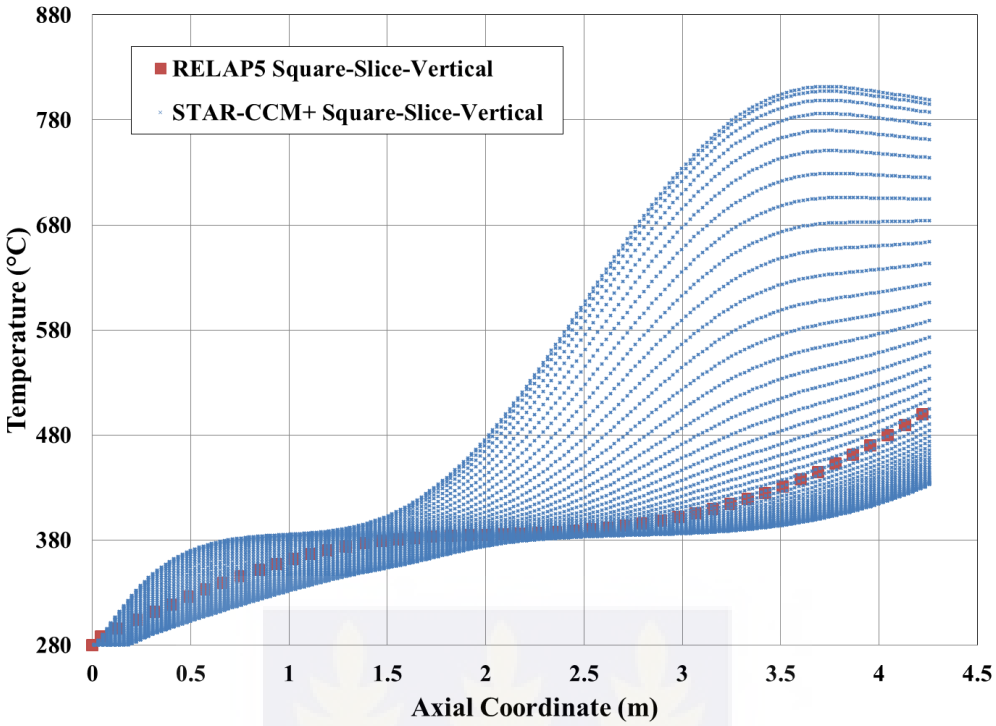

Figure 5.8. Steady-state temperature distribution along the square lattice slice obtained by the two codes in corresponding conditions

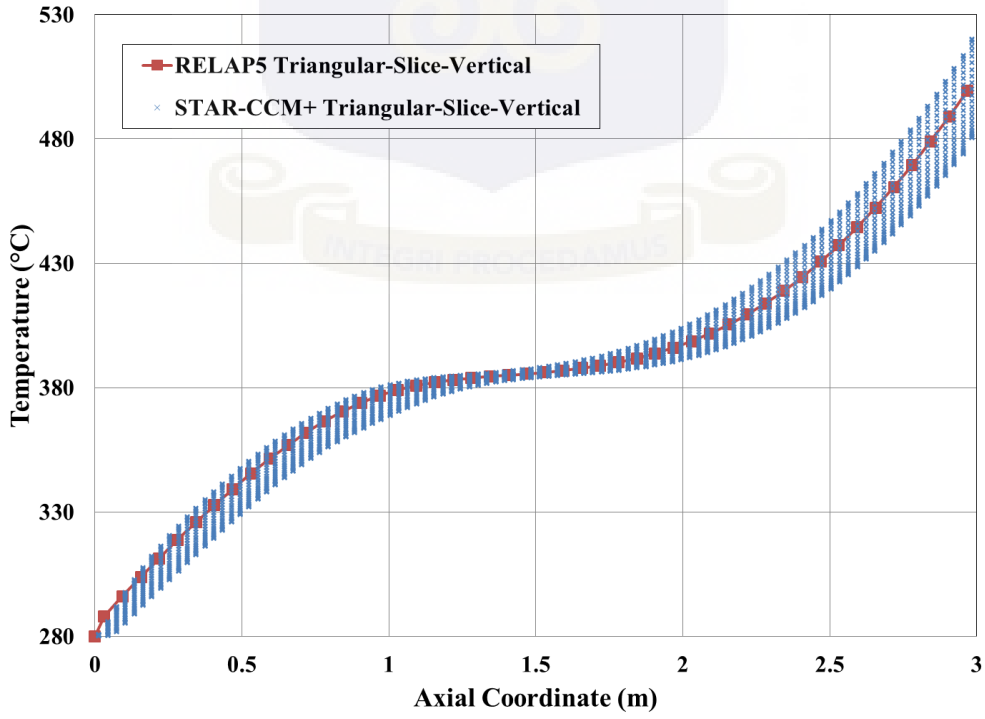

Figure 5.9. Steady-state temperature distribution along the triangular lattice slice obtained by the two codes in corresponding conditions

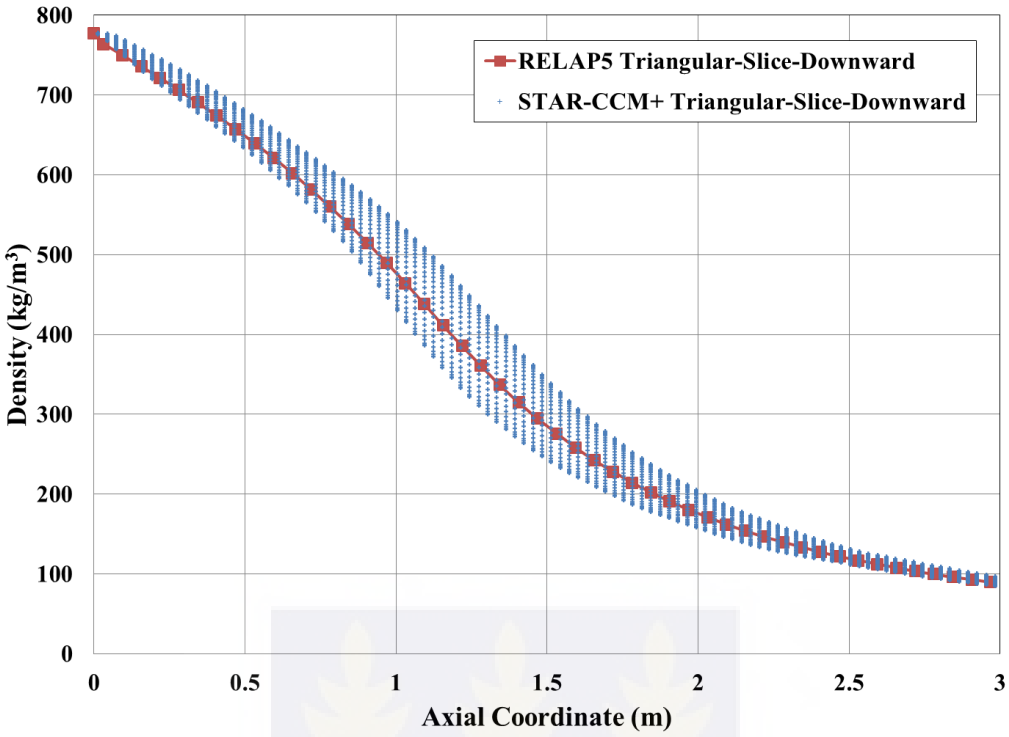

Figure 5.10. Steady-state density distribution along the triangular subchannel lattice slice obtained by the two codes in corresponding conditions

Figure 5.11 to Figure 5.18 present the stability maps obtained by the1D in-house program operating in dimensionless form [14] for the square and triangular lattice slices, compared with the stability thresholds obtained from the computations performed with RELAP5 and STAR-CCM+. The friction parameter appearing in the caption of the figures is defined as

$$\Lambda = \frac{f\ L}{2\ D_h} \tag{5.2}$$

and was selected based on the hydraulic diameter and on a reference value of the friction factor, considered roughly applicable in the addressed range. In dealing with a smooth surface with a range of considerable changes of viscosity, it is clear that the definition of a constant value of the friction factor, applicable for rough pipes with sufficiently turbulent flow, represents one of the limitations in this comparison. In all the maps, two main lobes can be recognised: the upper lobe is the locus of

Ledinegg instabilities, while the lower one is the locus of density wave unstable oscillations. As shown below, the results obtained by the two codes tend to conform to the structure of the map in relation to the character of the instabilities, with some exception due to local discrepancies.

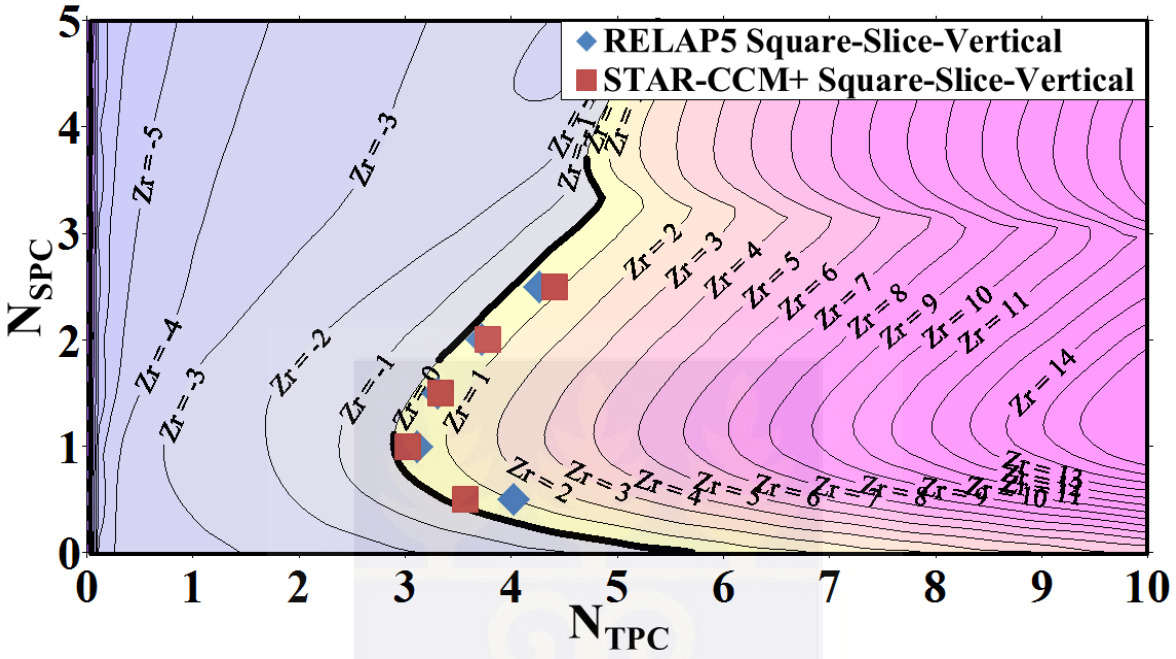

Figure 5.11. Comparison of the stability thresholds obtained for the square slice against the dimensionless stability map in the case of vertical upward flow generated for Fr=0.03, Λ= 6.0, 48 nodes, C_{max} = 0.9

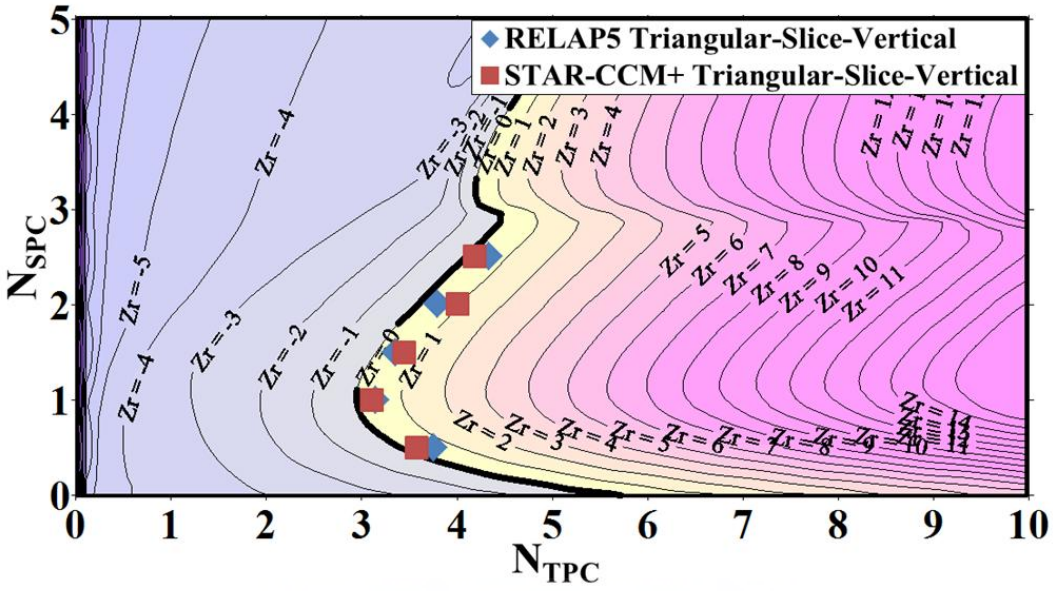

Figure 5.12. Comparison of the stability thresholds obtained for the triangular slice against the dimensionless stability map in the case of vertical upward flow generated for Fr=0.043, Λ=8.0, 48 nodes, C_{max} = 0.9

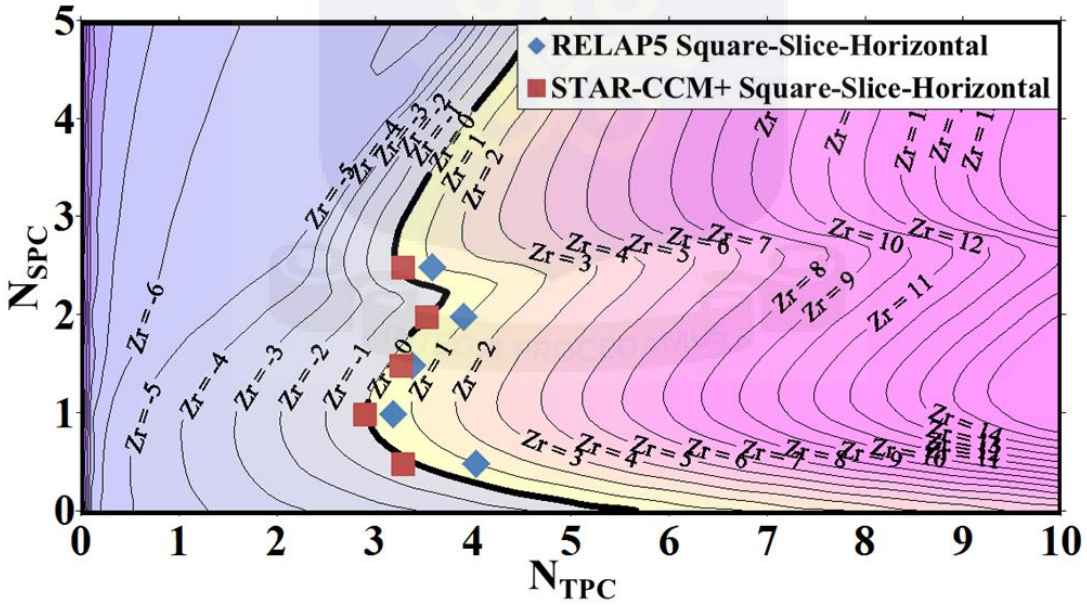

Figure 5.13. Comparison of the stability thresholds obtained for the square slice against the dimensionless stability map in the case of horizontal flow generated for Fr=10^5, Λ=6.0, 48 nodes, C_{max} = 0.9

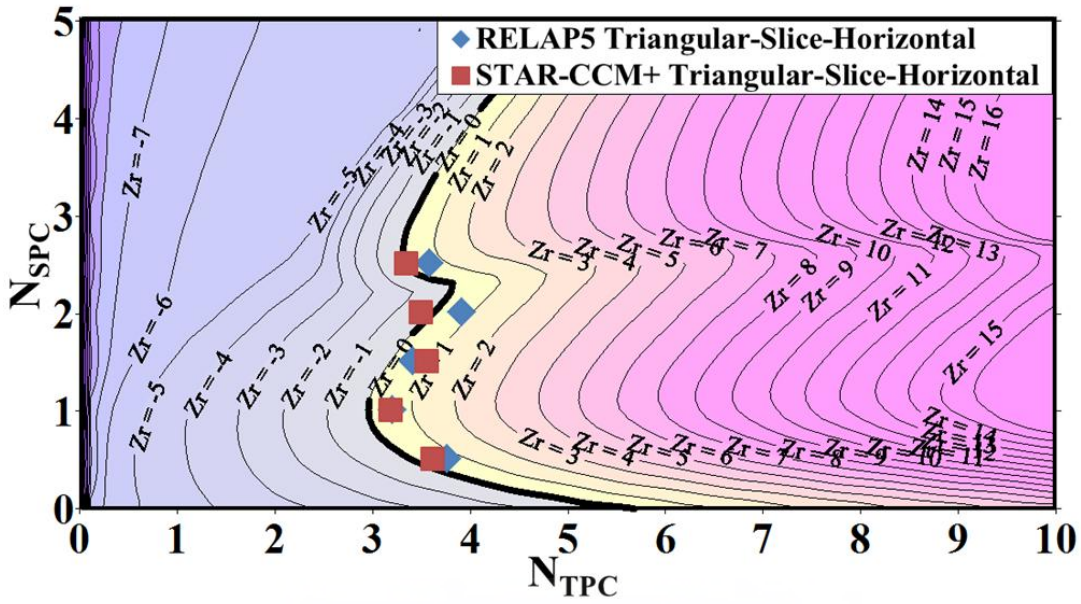

Figure 5.14. Comparison of the stability thresholds obtained for the triangular slice against the dimensionless stability map in the case of horizontal flow generated for $Fr=10^5$, $\Lambda=8.0$, 48 nodes, $C_{max} = 0.9$

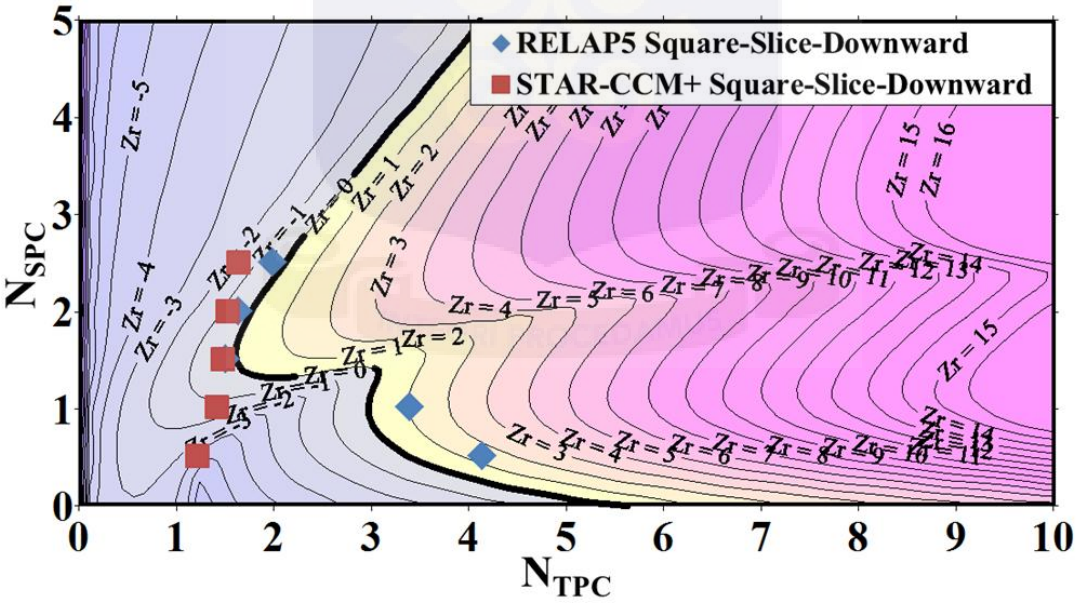

Figure 5.15. Comparison of the stability thresholds obtained for the square slice against the dimensionless stability map in the case of vertical downward flow generated for $Fr=-0.03$, $\Lambda= 6.0$, 48 nodes, $C_{max} = 0.9$

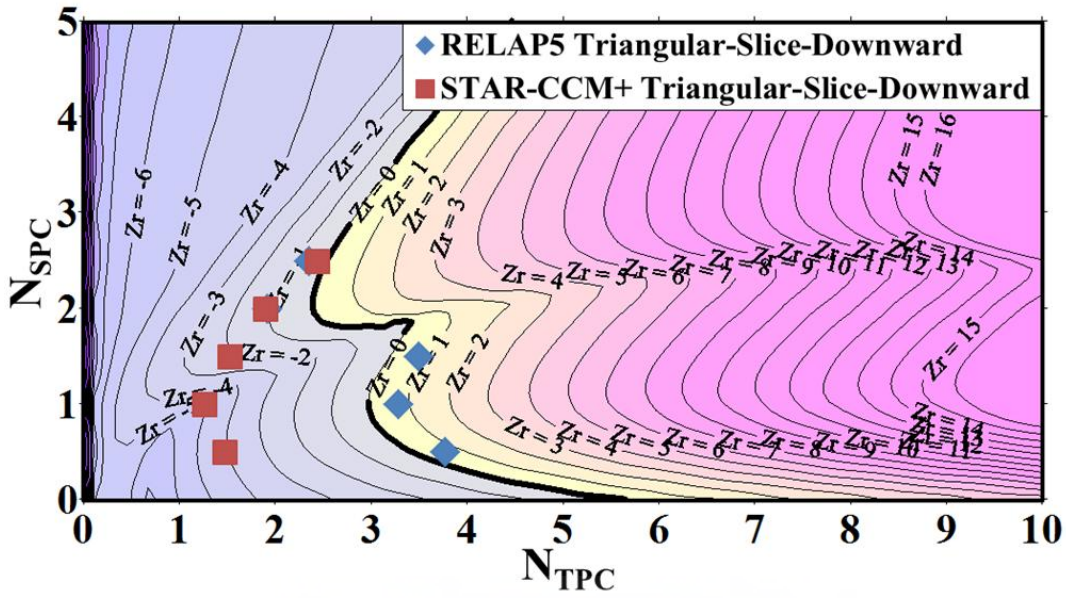

Figure 5.16. Comparison of the stability thresholds obtained for the triangular slice against the dimensionless stability map in the case of vertical downward flow generated for Fr=-0.043, Λ= 8.0, 48 nodes, C_{max} = 0.9

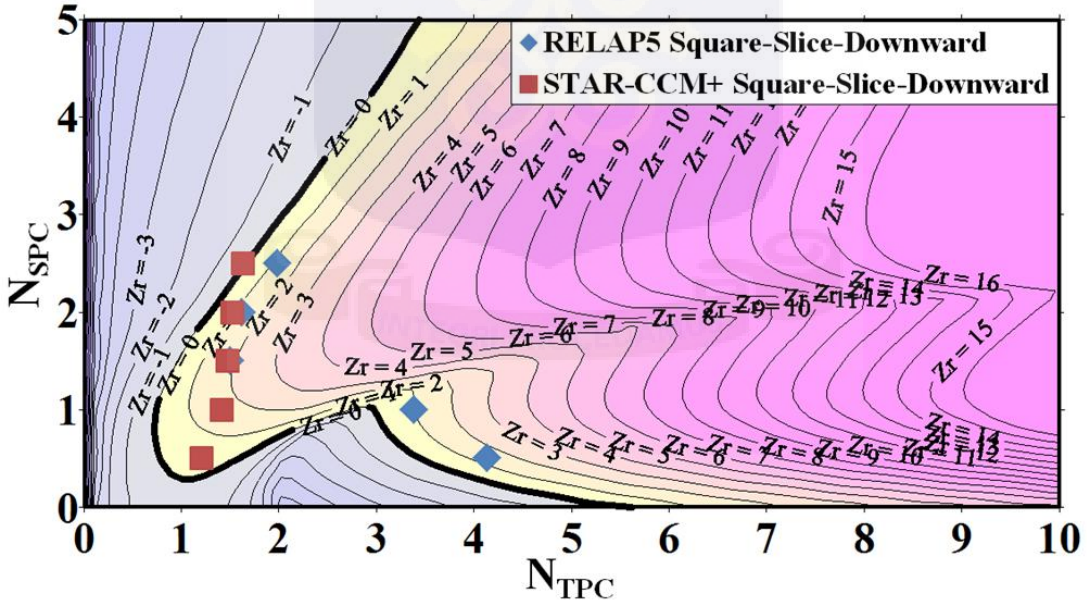

Figure 5.17. Comparison of the stability thresholds obtained for the square slice against the dimensionless stability map in the case of vertical downward flow generated for Fr=-0.015, Λ= 6.0, 48 nodes, C_{max} = 0.9

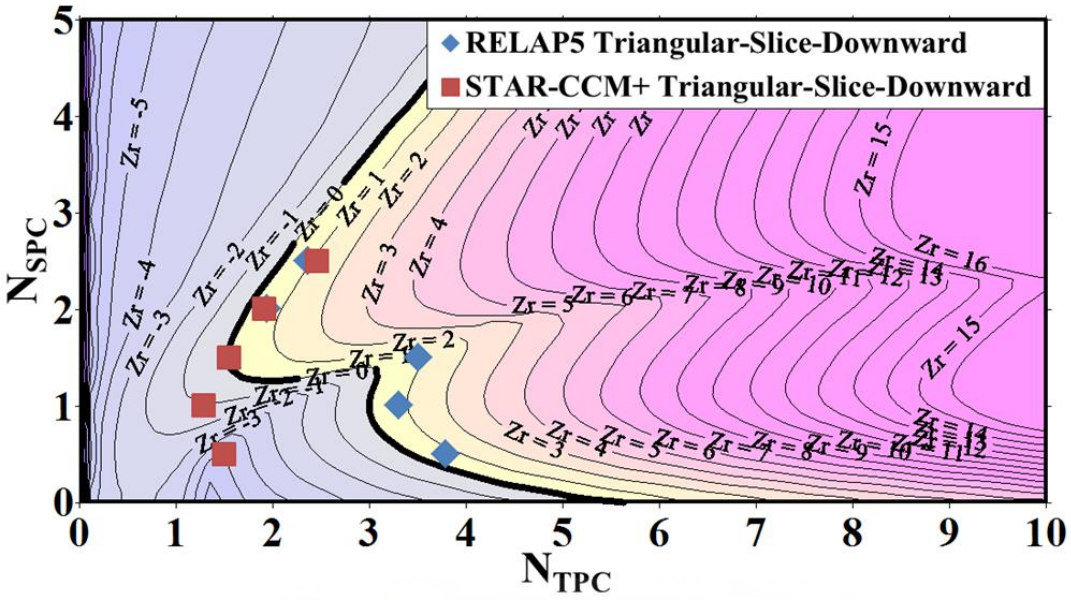

Figure 5.18. Comparison of the stability thresholds obtained for the triangular slice against the dimensionless stability map in the case of vertical downward flow generated for Fr=-0.0215, Λ= 8.0, 48 nodes, C_{max} = 0.9

It can be observed from Figures 5.11 and 5.12 that the Ledinegg region is lower in the triangular slice map than that for the square slice.

From the map in Figure 5.11, it can be seen that both computational tools provide comparable results for the stability thresholds in the case of the vertical square lattice slice, with RELAP5 predicting a slightly more stable system at N_{SPC} = 0.5. In particular, density wave oscillations are observed at the stability threshold in all the studied cases. In Figure 5.12, it can be observed that the vertical triangular lattice slice results are also similar for RELAP5 and STAR-CCM+, with the latter predicting a slightly more stable system at N_{SPC} = 2.0. Apart from the case with N_{SPC} = 2.5, which showed a Ledinegg instability for STAR-CCM+, perhaps due to the fact that the corresponding upper lobe of the map is not too far, all the remaining cases were predicted to be unstable with density wave oscillations.

Figure 5.13 indicates that RELAP5 predicts a slightly more stable behavior for the horizontal square lattice slice than STAR-CCM+. Both computational tools predict a Ledinegg form of instability at

N_{SPC} = 2.5; for N_{SPC} = 2.0, STAR-CCM+ predicts a Ledinegg instability, while RELAP5 shows density wave oscillations. From Figure 5.14, for the horizontal triangular lattice case, it can be observed that both computational tools provide comparable results in the density wave region; however, RELAP5 predicts density wave oscillations at N_{SPC}=2.0, while STAR-CCM+ predicts a Ledinegg form of instability at both N_{SPC}=2.0 and 2.5.

Figure 5.15 shows the comparison for the square lattice slice in downward flow. While RELAP5 predicts density wave oscillations at N_{SPC} equal to 0.5 and 1.0, STAR-CCM+ shows an excursive unstable behavior for all the addressed values of the pseudo-subcooling numbers. A similar behavior was observed in the case of the data in Figure 5.16: while the RELAP5 predicts a density wave form of instability for N_{SPC}=0.5, 1.0 and 1.5 and excursive instabilities in the remaining cases, STAR-CCM+ predicts a Ledinegg form of instability for all the inlet conditions considered in the study.

In summary, though there is a reasonable agreement between the predictions of the two codes and with the dimensionless stability maps, discrepancies do appear. Among the different contributors to these discrepancies, the following aspects can be considered:

- the 1D representation of an open subchannel, mainly based on the definition of the hydraulic diameter, is questionable in comparison with the consideration of the detailed features of a subchannel slice; in particular, local changes in fluid velocity and density may give rise to flow patterns and effective wall friction values than can be hardly represented by a 1D approach;
- since the main differences among the results of the two codes are related to the prediction of Ledinegg instabilities or density wave oscillations in horizontal or downward flow, the role of the actual Froude number reached at instability in the calculation procedure is necessarily in question; in fact, the value of this parameter is mainly responsible for the size and the location of the upper lobe in the stability maps; the fact that the Froude number could be better controlled in RELAP5 calculations than in STAR-CCM+ suggests a non-negligible role of this

aspect; Figure 5.17 and Figure 5.18, showing the comparison of the data with stability maps obtained with halved values of the Froude number, seem to fully support this conclusion.

Figure 5.19 to Figure 5.22 present plots of the period of oscillations against N_{TPC} for the various cases which resulted in density wave oscillations for vertical and horizontal flows.

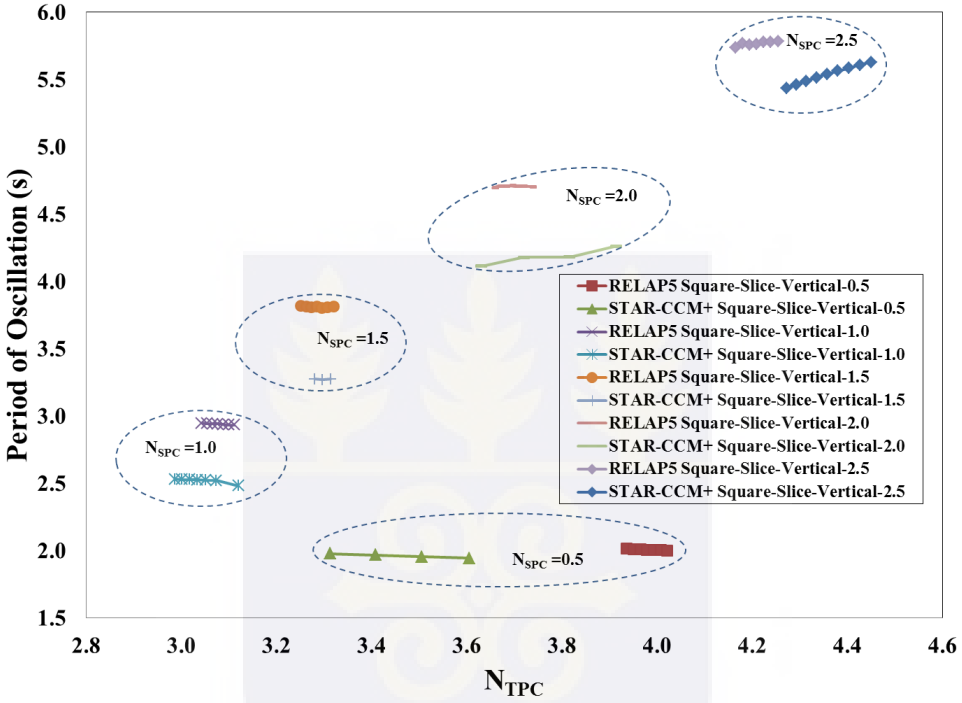

Figure 5.19. Period of oscillations for the fluid in the case of vertical upward flow at different values of pseudo-subcooling calculated around the onset of oscillations for the square lattice slice

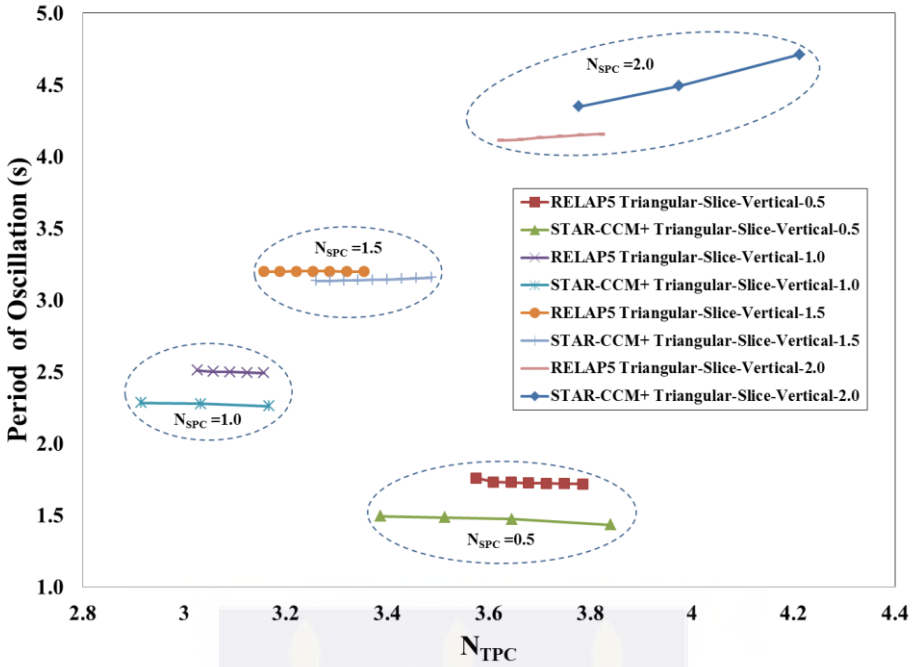

Figure 5.20. Period of oscillations for the fluid in the case of vertical upward flow case at different values of pseudo-subcooling calculated around the onset of oscillations for the triangular lattice slice

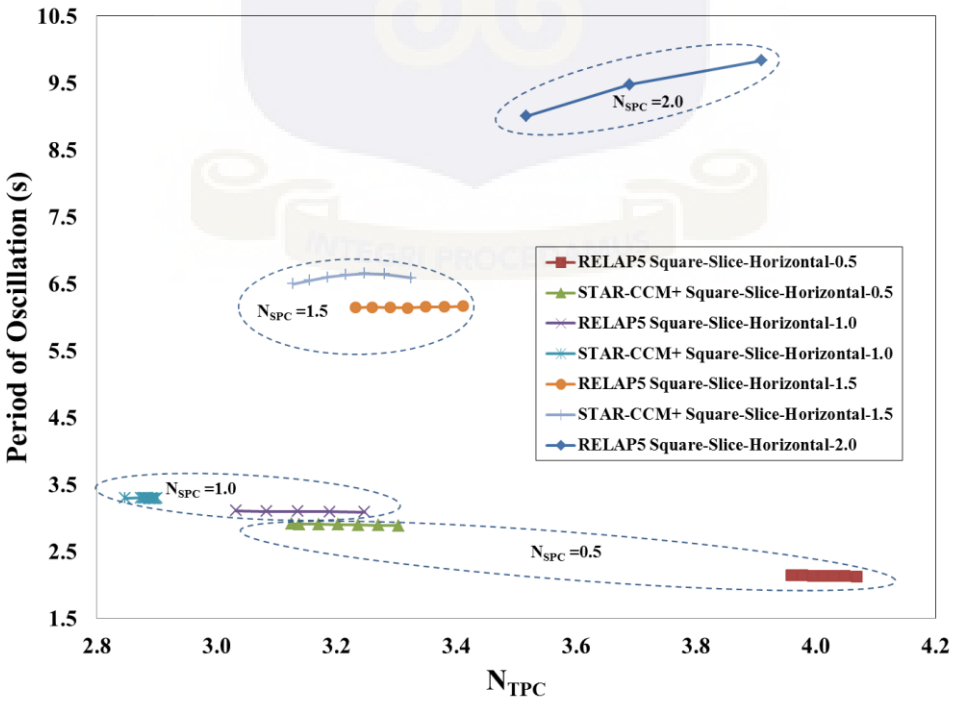

Figure 5.21. Periods of oscillations for the fluid in the case of horizontal flow at different values of pseudo-subcooling calculated around the onset of oscillations for the square lattice slice

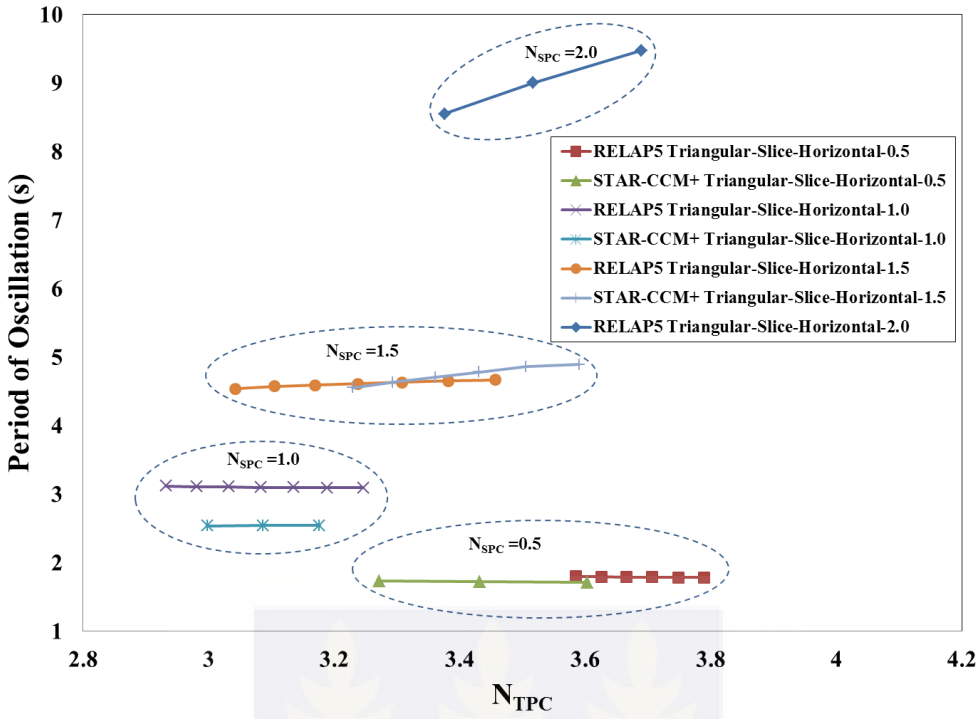

Figure 5.22. Periods of oscillations for the fluid in the case of horizontal flow at different values of pseudo-subcooling calculated around the onset of oscillations for the triangular lattice slice

In Figure 5.19, it can be seen that the period of oscillations for the square subchannel slice increases with increasing N_{SPC}; this result, obtained from both RELAP5 and STAR-CCM+, follows a trend similar to those reported in the previous Chapter on circular supercritical channel; similar considerations apply to the remaining Figures. As an overall observation, there is a reasonable agreement between the values of the period of oscillations obtained by the two codes when they both predict oscillatory behaviour; this is somehow reassuring, showing that the different models predict the global dynamics of the addressed systems in a similar way.

5.5. CONCLUDING REMARKS

The results presented in this Chapter confirm and extend the first conclusions obtained years ago about the capabilities of CFD codes in predicting the unstable flow behaviour of nuclear fuel subchannel slices cooled with supercritical water [15].

The systematic approach adopted in this work pointed out relatively coherent results of the adopted code models as well as discrepancies. The latter are mainly related to the prediction of oscillatory or excursive instabilities in similar operating conditions and can be attributed to the different representations of the physical features of the systems addressed, as well as to the adopted methodology of analysis that may introduce slight differences in the boundary conditions. In particular, the selection of constant friction factors and of a specific value of the Froude number in setting up the reference stability maps can be considered a weak point in the applicability of the related similarity theory to the considered conditions.

Indications that CFD codes are suitable for stability analyses with 3D channels were obtained by the results. In particular, the general coherence of the predictions about the stability thresholds and the periods of oscillations obtained by the different models support the conclusion that these instability phenomena are mainly characterised by 1D behaviour, though the application of CFD adds details that are difficult or impossible to be represented by simple cross section averaged balance equations.

A further step was made with respect to previous analyses, by shifting from the consideration of simple circular channels to 3D subchannel slices; however, it must be recognised that several aspects still require to be considered to reach the goal of a complete modelling of nuclear fuel elements. Some of these aspects, as inlet and outlet throttling, heat conduction in the fuel rod and nuclear reactor core kinetics are addressed in the next Chapter.

CHAPTER 6

ANALYSIS OF SQUARE SUBCHANNEL WITH FUEL ROD

6.1 INTRODUCTION

This Chapter presents the analysis of coupled neutronic-thermal hydraulic instabilities in a subchannel slice belonging to a square lattice assembly by use of a CFD code. The work represents a further phase in the assessment of the suitability of CFD codes for studies of flow stability of supercritical fluids. The research started in previous work with the analysis of bare 2D circular pipes and already addressed 3D subchannel slices with no allowance for heat conduction and neutronic effects. In the present phase, a more realistic system is considered, dealing with a slice of a fuel assembly subchannel containing the regions of the pellet, the gap and the cladding and also including the effect of inlet and outlet throttling. The adopted neutronic model is a point kinetics one, including six delayed neutron groups, as discussed in Chapter 3,with global Doppler and fluid density feedbacks.

The response of the model to perturbations applied starting from a steady-state condition at the rated power is compared with that of a similar model developed for a 1D system code. Upward, horizontal and downward flow orientations are addressed making use of a uniform and bottom peaked power profiles and changing relevant parameters as the gap equivalent conductance and the density reactivity coefficient. Though the adopted model can still be considered simple in comparison with actual details of fuel assemblies, the obtained results demonstrate the potential of the adopted methodology for more accurate analyses to be made with larger computational resources.

As in the previous phases, the STAR-CCM+ code [73] is adopted, taking benefit of the experience gained in the application of the code in previous phases. In particular, basic choices about different calculation options were tested in relation to the most appropriate scheme to be adopted for a

reasonable convergence during time advancement and the minimisation of numerical diffusion in operating conditions similar to those addressed in the present work.

The model adopted herein was already subjected to a limited qualitative testing in studies performed in parallel with the other phases of the work [16]. In this Chapter, the predictions by CFD are compared to those obtained by a 1D model developed for the RELAP5/MOD3.3 system code [93] making use of similar boundary conditions. The comparison is aimed at providing a reasonable confidence that the results of the CFD model are in line with those obtained by 1D models, though it is expected that differences exist as a consequence of the diversity in the adopted physical and numerical representation.

6.2 ADDRESSED GEOMETRY AND MODEL CHARACTERISTICS

6.2.1 Geometrical and physical characteristics

The main characteristics of the addressed subchannel model are similar to those considered in Ambrosini and Sharabi [14], inspired by published configurations of a proposed conceptual design [11, 38]. Table 6.1 summarises the values of the main parameters characterising the system and Figure 6.1 describes a cross section of the configuration addressed. With respect to the data adopted in Ambrosini and Sharabi [14], the hydraulic diameter, used only in the 1D model for RELAP5, considers the actual conditions of the single subchannel addressed, instead of representing an average value for the entire assembly; this is necessary for a better comparison of the 1D with the CFD model, though it is understood that characterising the friction characteristics of a subchannel only by an hydraulic diameter represents an engineering approximation that may lead to inaccuracies in the comparison with a detailed CFD model.

Table 6.1. Characteristics of the addressed fuel rod and subchannel

Rod outer diameter: 10.2 mm	System Pressure: 25 MPa
Lattice pitch: 11.2 mm	Inlet Temperature: 280 °C
Distance from the rod to the wall: 1 mm	Channel flow rate: 0.055 kg/s
Coolant flow area: 5.49×10^{-5} m^2	Reference linear power: 25 kW/m
Hydraulic diameter : 4.03 mm	Gap thickness = 0.12 mm
Channel length: 4.2672 m (14 ft)	Cladding thickness = 0.63 mm

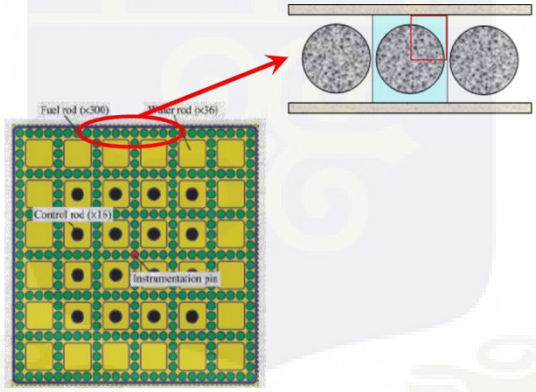

Figure 6.1. Reference configuration of the addressed fuel rod and subchannel [16]

Table 6.2 summarises the values of the parameters adopted to describe the conductive characteristics of the fuel rod, assumed to be constant to avoid differences in their local evaluation by the different models. The gap conductivity is assumed to be variable since the overall gap conductance is the subject of sensitivity analyses, owing to its known effect on stability. The cladding of the pellet, containing enriched uranium oxide, is assumed to be made of stainless steel.

The properties of fuel, gap and cladding are generally representative of those of the materials that could probably be selected in future SCWR design.

Table 6.2. Physical characteristics of the different regions of the rod model

Component	**ρ (kg/m^3)**	**C_p (J/(kg-K))**	**k (W/(m-K))**
Gap	3.58	5193	0.3-1.2
Clad (SS)	8000	502	16
Fuel (UO_2)	10900	320	2.8

Inlet and outlet throttling were imposed both in STAR-CCM+ and in RELAP5 calculations, trying to represent the condition of a narrow inlet orificing, corresponding to an irreversible pressure drop coefficient equal to 20, with a much milder outlet restriction, corresponding to a coefficient equal to 1. In this respect, the presence of plena in RELAP5 had to be taken into account, considering that reversible acceleration losses and gains are obtained at the inlet and outlet. In order to simulate orificing in STAR-CCM+, porous interfaces were included after splitting the fluid region into three parts; the two porous interfaces placed close to the inlet and the outlet sections were assigned the desired pressure drop law, taking into account the reversible loss that is implied in a "stagnation inlet" boundary condition.

6.2.2 Numerical discretisation

A view of the spatial discretisation adopted for the STAR-CCM+ code is shown in Figure 6.2a. As it can be noted, only one fourth of the subchannel is considered, taking advantage of the geometrical symmetry. Polyhedral meshes are adopted in a small inlet part of the fuel, cladding and fluid

regions, extruded in the axial direction to generate 200 prismatic meshes. For the gap, the thin mesher model was employed to generate two thin layers of nodes coherent with the ones in the fuel and the cladding regions.

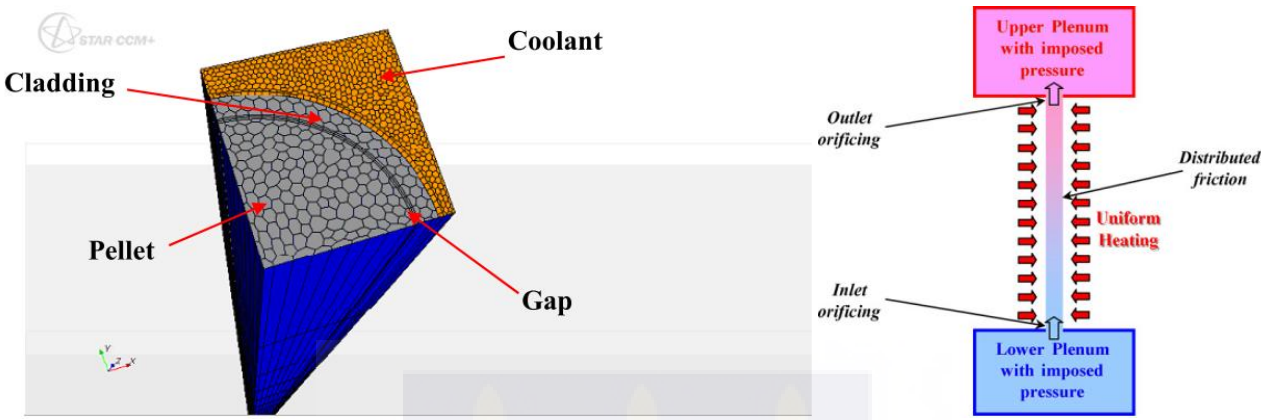

a) STAR-CCM+ b) RELAP5

Figure 6.2. Models developed for the CFD and the system code

The fluid region contains a "prism layer" close to the cladding wall, thick enough to assure a value of wall y+ greater than 30 all along the channel axis. This choice is coherent with the use of wall functions, in order to rule out a too detailed description of heat transfer conditions at the fuel rod surface that is presently unwanted, since it is still unreliable for supercritical fluids often leading to strong overestimates of the wall temperatures. However, a two-layer All y+ model was adopted, in order to assure that the model can accommodate local deviations from the high y+ (wall function) treatment, whenever during oscillations or change of operating conditions the related criterion is violated. The adopted turbulence model is the realisable k-ε available in the code. Water properties are supplied to the code algorithms in the form of piecewise cubic spline approximations, whose coefficients are derived on the basis of data obtained from the NIST property package [92].

The model adopted for RELAP5 is the usual one used for previous analyses, e.g. in Sharabi et al. [76] whose general configuration is reported in Figure 6.2b; in particular, two time-dependent volumes and two single junctions are used to impose boundary conditions to the 14 ft long pipe,

axially discretised by 48 nodes. With respect to previous applications, the fuel rod heating structure is added, with the three different material regions of the pellet, the gap and the cladding, discretised by 20 radial nodes. The fuel pellet region receives the volumetric power calculated by the built-in point kinetics model; at nominal conditions. This power corresponds to the 25 kW/m of rated linear power, assumed for the reference conditions.

Time discretisation is performed in different ways for the two codes, according to the suitability of their built-in numerical schemes for stability analyses. In particular:

- on the basis of previous experience [17], the Implicit Coupled, second order advancement scheme was adopted in STAR-CCM+, aiming to efficiently deal with the presence of large buoyancy forces and to minimise numerical diffusion; the constant time-step adopted for the calculation was 0.1 s that in previous work demonstrated to be a reasonable compromise between accuracy and computational efficiency; the Courant number adopted in the 20 inner iterations was kept in the order of 20,000, to achieve a good degree of convergence except for cases for horizontal and downward flow in which convergence was attained with internal Courant number of 5000.

RELAP5 was used with the “semi-implicit” numerical scheme, a classical choice for such applications, whose time-step is limited by the Courant-Friedrichs-Lewy numerical stability criterion; this was preferred to the “nearly-implicit” scheme, being tolerant to larger time steps, since it is less diffusive; the maximum time-step adopted in the calculations was 0.1 s, though during the time advancement the code adopted a smaller value to limit the maximum Courant number below the numerical stability threshold.

6.3 APPLICATION OF POINT NEUTRON KINETICS

In the aim to check the feasibility of the coupling of the CFD code with an external neutronic program, with the possibility to compare the results obtained with those of the 1D system code, a point neutron kinetics model implemented in a java routine was developed. In first tests [16], a model considering a single average group of delayed neutrons was adopted, making use of a numerical integration technique based on a Crank-Nicholson time discretisation. The model obtained was sufficiently simple to be implemented in the java macro and provided a first indication about the feasibility of similar but more complex approaches.

Basically, the java routine drives the calculation, calling the CFD solver and exchanging data with it. In particular, the values of the average pellet temperature and fluid density in the channel, weighted on the basis of an importance function, is supplied to the macro, that evaluates feedback reactivity and advances the point kinetics calculation with the same time step adopted for CFD. The instantaneous value of power is then written in the "field function" assigning volumetric power in the fuel pellet, thus completing a cycle by the ensuing advancement of the CFD model. This explicit coupling between kinetics and thermal-hydraulics was found reasonably effective. The feedback reactivity is evaluated by a linearized formulation having the form:

$$r = C_d \rho_{avg,coolant} + C_T T_{avg,\,fuel} - r_0 \tag{6.1}$$

where C_d is a fluid density reactivity coefficient having the order of 2×10^{-4} m^3/kg, C_T= -1.2×10^{-5} K^{-1} is the Doppler reactivity coefficient and r_0 is the bias reactivity at the start of the point kinetics calculation, introduced to assume zero reactivity in steady-state conditions. The values of the reactivity coefficients were drawn from a conceptual plant design analysis [31] and were used as reference values in the analyses. While the Doppler reactivity coefficient was kept the same in all the calculations, the density coefficients was also decreased with respect to the reference value to take into account the effect of the presence of non-expanding moderator located in the water boxes

of the fuel assembly; this allowed for information on the sensitivity of the observed dynamic evolutions of this parameter to be obtained.

With respect to the choices adopted in the first applications, in the frame of this work the point kinetics model was improved. In particular, six groups of delayed neutrons were implemented and the adequacy of the time discretization was better checked. Though this represents a minor detail in this context, since techniques for advancing point kinetics are well known, some detail is given hereafter on the results obtained by these improvements.

As mentioned above, in the exchange of information between the java routine and the CFD code the temperature of the fuel pellet and of the fluid must be weighted according to an importance function. In uniformly distributed power cases, this did not pose any problem; however, when a non-uniform power profile was adopted, the weighting was selected to be proportional to the squared power distribution. In particular, this was made for the bottom-peaked power profile shown in Figure 6.3, inspired to the work by Ammirabile [96]. “Field functions” and “reports” available in STAR-CCM+ were adopted to obtain the weighting; in RELAP5, the weighting coefficients available for both density and fuel temperature were activated instead, assigning a similar trend.

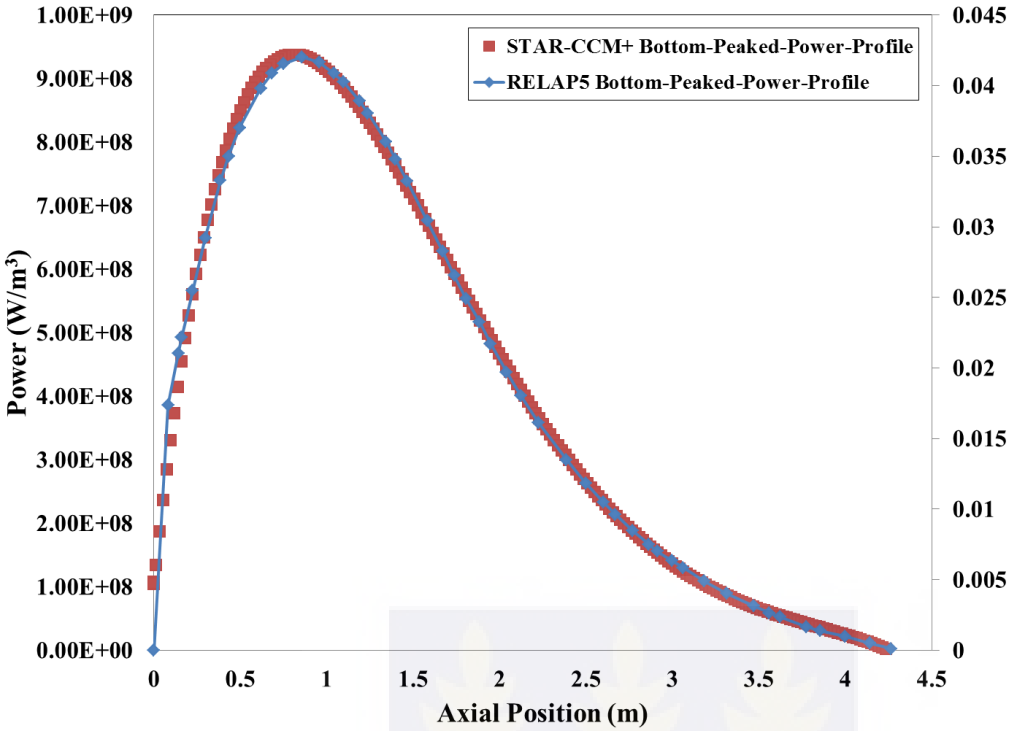

Figure 6.3. Bottom peaked axial profile of volumetric power adopted in the calculations

6.4. METHODOLOGY OF ANALYSIS

The evaluation of stability of each considered configuration was performed in both STAR-CCM+ and RELAP5 by firstly bringing the system to steady-state conditions with imposed channel pressure drop, at the rated values of power and of the other assigned parameters. A perturbation was then applied to the inlet pressure, thus observing the resulting oscillations in inlet flow rate.

The procedure for obtaining this result was different in the case of the CFD code, STAR-CCM+, and the system code, RELAP5. For the CFD code, a transient was initially started from a uniformly assigned initial condition; by imposing the inlet flow rate and temperature and the 25 kW/m of linear power and waiting for a reasonable convergence to a steady-state. Then, the inlet boundary condition was changed to a “stagnation inlet” one, imposing the value of pressure resulting at the inlet from the steady-state calculation. While doing this, it was necessary to take into account the

inlet pressure drop due to acceleration from the plenum assumed to be present in a stagnation inlet. After stabilization from the little perturbation imposed by the change in the boundary condition, the java routine calculating kinetics is then activated to drive the calculation with no perturbation in order to achieve steady-state conditions with kinetics. Then, the system is subjected to a perturbation in inlet pressure and the resulting flow rate trend is observed and quantitatively evaluated.

In the case of RELAP5, the calculation is started from the onset with the point kinetics model activated. However, a control strategy is implemented in order to reach the required power level by progressively adapting the "bias" reactivity that is brought about by the use of the feedback mechanisms. Trials were made with repeated calculations in order to obtain the pressure drop to be imposed to the channel providing the desired steady-state flow. After proper stabilisation, the inlet pressure is perturbed for a short time obtaining a free evolution of the system.

In both cases, of STAR-CCM+ and RELAP5, the trend of inlet mass flow rate versus time was finally processed by the formulation presented in Section 3.6 of this work. Figure 6.4 provides samples of the oscillations observed in various cases studied with STAR-CCM+ and RELAP5.

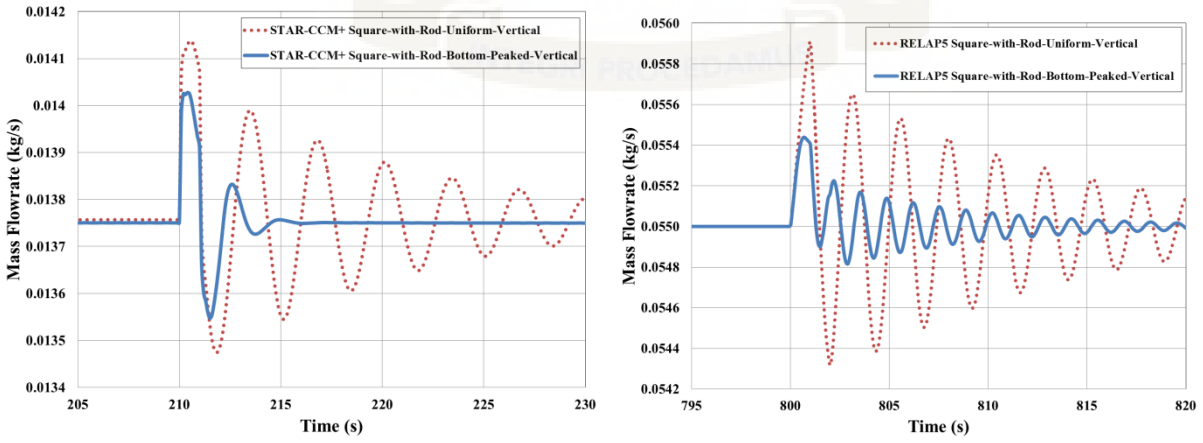

Figure 6.4. Sample oscillations obtained in the analyses by both codes.

6.5. RESULTS OBTAINED

Figure 6.5 to Figure 6.8 present the results obtained by both codes for the distributions of relevant computed variables during steady-state.

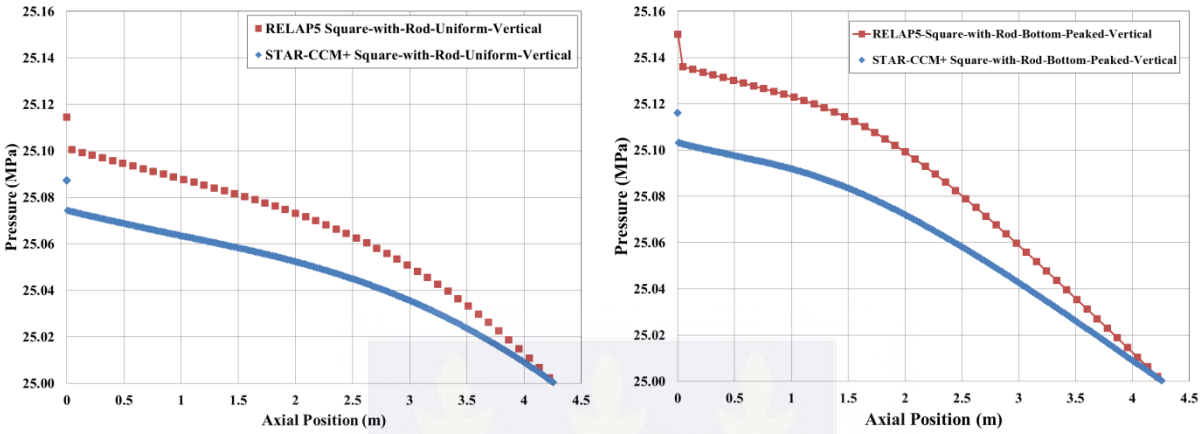

a) uniform power profile b) bottom peaked power profile

Figure 6.5. Steady-state pressure distributions along the subchannel assembly for vertical upward flow

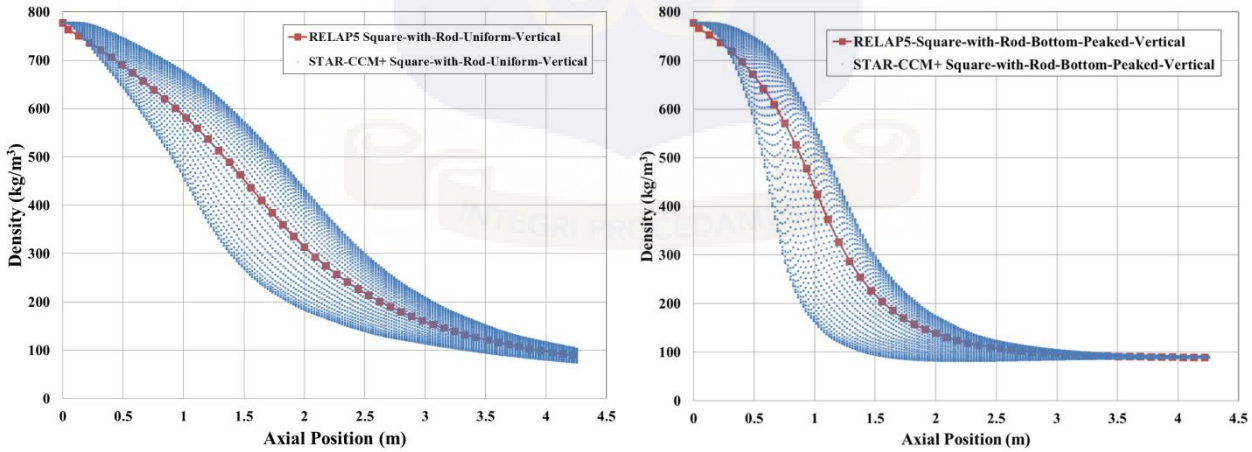

a) uniform power profile b) bottom peaked power profile

Figure 6.6. Steady-state density distributions along the subchannel assembly for vertical upward flow

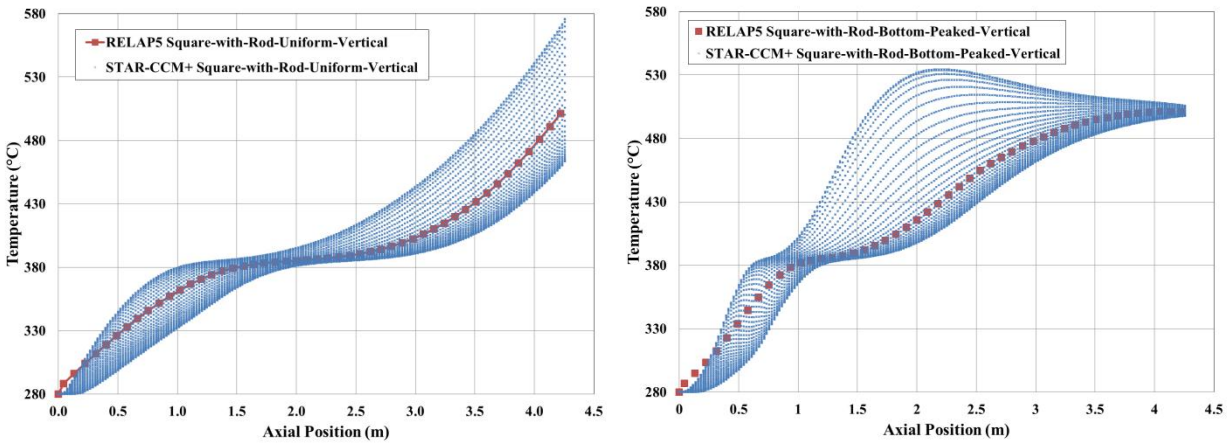

a) uniform power profile b) bottom peaked power profile

Figure 6.7. Steady-state fluid temperature distributions along the subchannel assembly for vertical upward flow

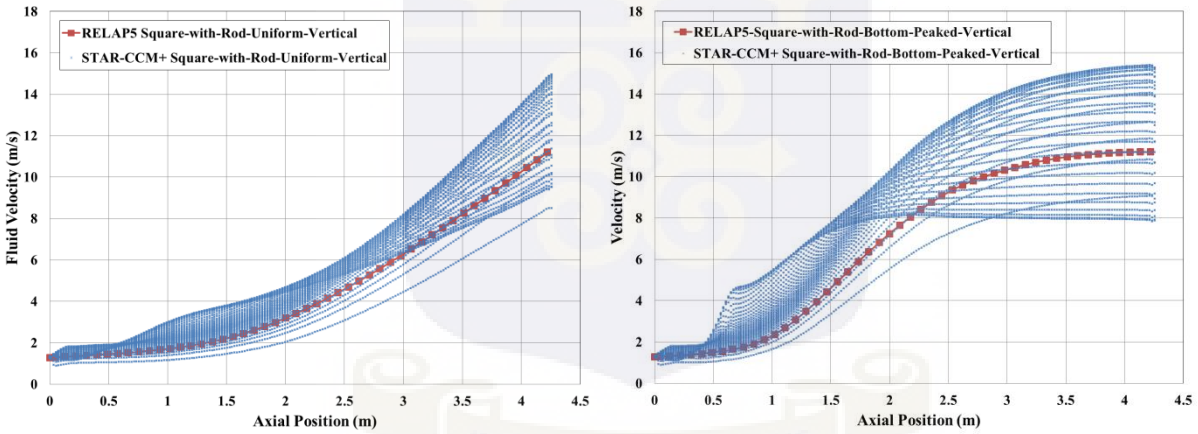

a) uniform power profile b) bottom peaked power profile

Figure 6.8. Steady-state velocity distributions along the subchannel assembly for vertical upward flow

In particular, Figure 6.5 shows the increase in pressure drop that is obtained shifting from the uniform power distribution to the bottom peaked one, predicted by both codes, owing to the larger light fluid region existing in the latter case along the channel; the latter detail is confirmed by Figure 6.6 related to density. As it was expected, quantitative differences appear in the evaluation of

the pressure drop by STAR-CCM+ and RELAP5. It is clear that the representation of the actual geometrical flow channel configuration by the CFD code is basically different from the simple adoption of the hydraulic diameter in a 1D model. Another possible contributing effect is the different way in which the two codes account for surface roughness, though in both codes a value of 2×10^{-5} m was used to characterise the rod surface. Figure 6.7 represents the fluid temperature distributions along the channel axis, clearly demonstrating the flattening of all the trends occurring when the pseudo-critical temperature is crossed. Finally, Figure 6.8 presents the results obtained for velocity for the two power distributions; though the cross section averaged values at the channel outlet predicted by RELAP5 are obviously equal in the two cases, the spread in the outlet values computed by the CFD code are actually different.

Stability analyses were performed by changing the values of the density reactivity coefficient and of the gap thermal conductance, indicated as HTC in the figures. The values of HTC were changed from 2500 to 10000 W/(m^2K), being characteristic values for PWRs [97]; the density reactivity coefficient was changed from the maximum value of 2×10^{-4} m^3/kg to lower ones, considering the role that should be played by water rods on the worth of the coolant density. The results of these analyses are shown in Figure 6.9 to Figure 6.20.

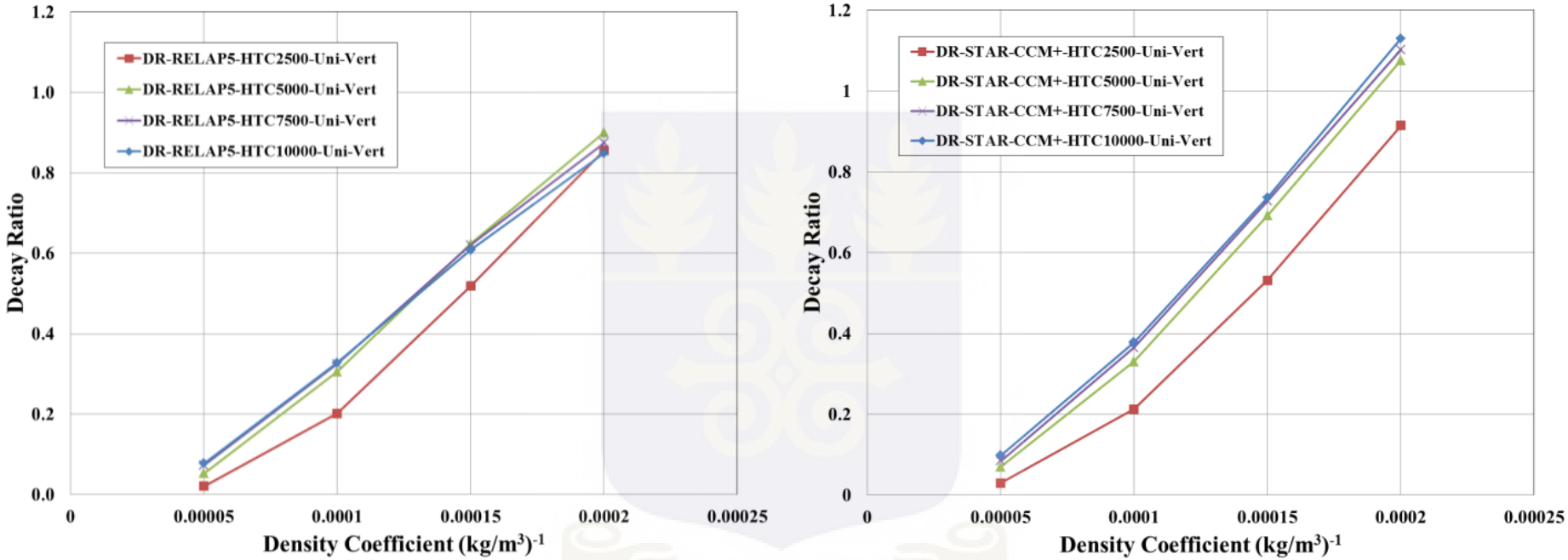

Figure 6.9. Decay ratio as a function of density reactivity coefficient at different values of the gap heat transfer conductance for uniform power and vertical upward flow

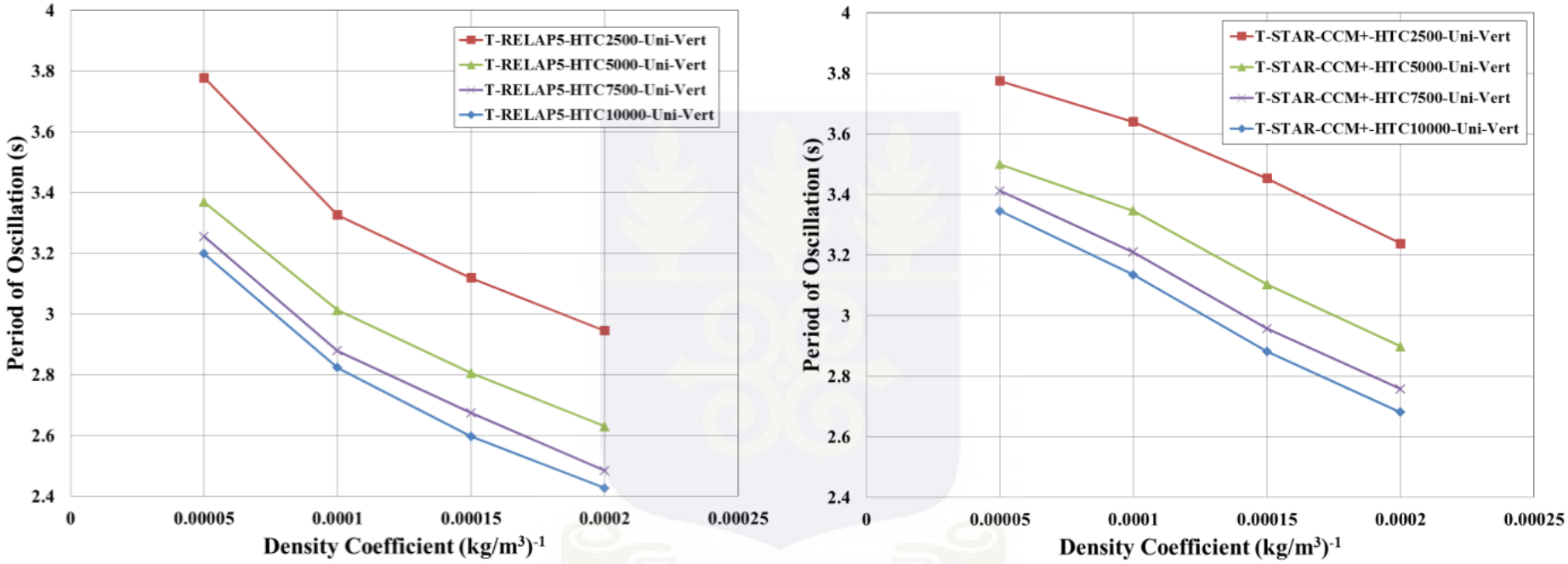

Figure 6.10. Period of oscillations as a function of density reactivity coefficient at different values of the gap heat transfer conductance for uniform power and vertical upward flow

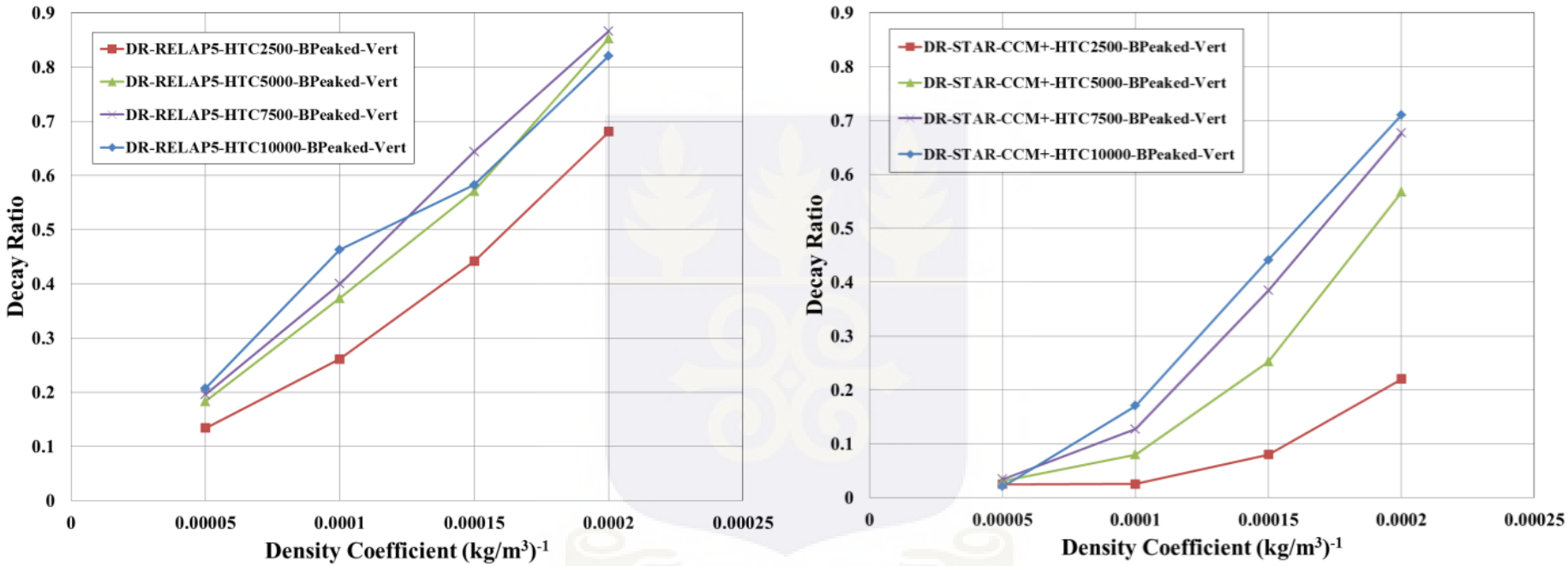

Figure 6.11. Decay ratio as a function of density reactivity coefficient at different values of the gap heat transfer conductance for bottom peaked power and vertical upward flow

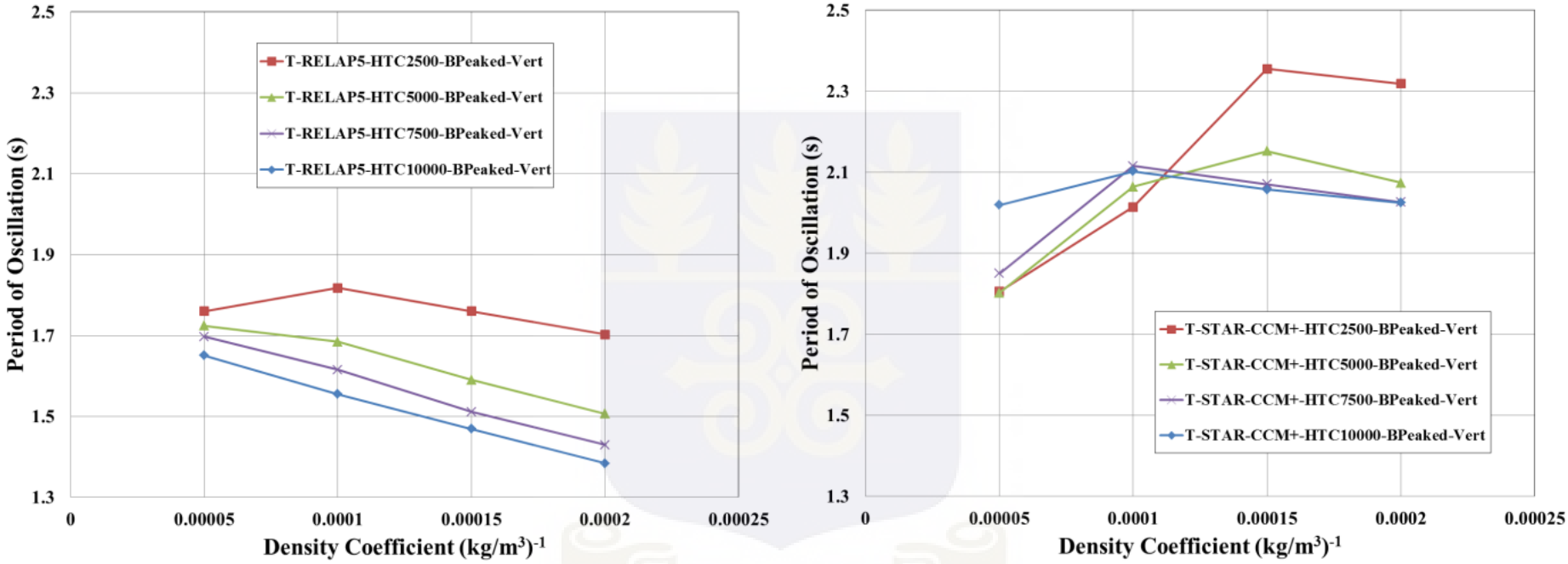

Figure 6.12. Period of oscillations as a function of density reactivity coefficient at different values of the gap heat transfer conductance for bottom peaked power and vertical upward flow

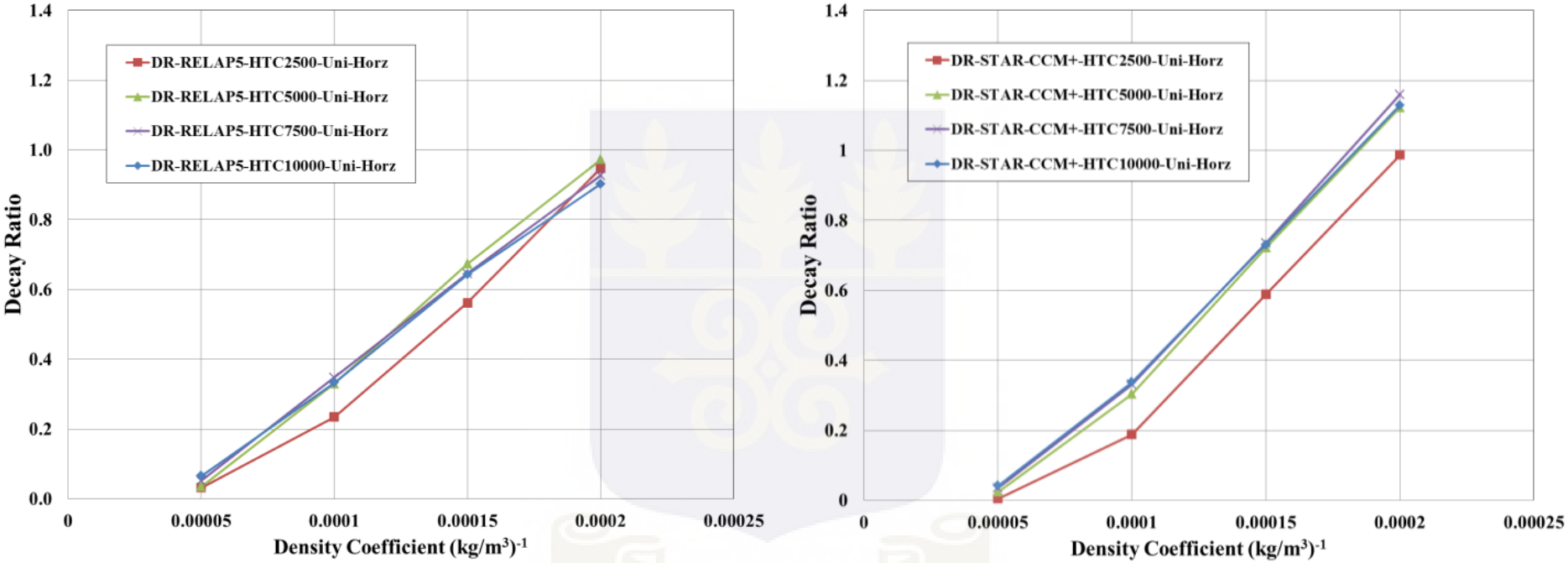

Figure 6.13. Decay ratio as a function of density reactivity coefficient at different values of the gap heat transfer conductance for uniform power and horizontal (no gravity) flow

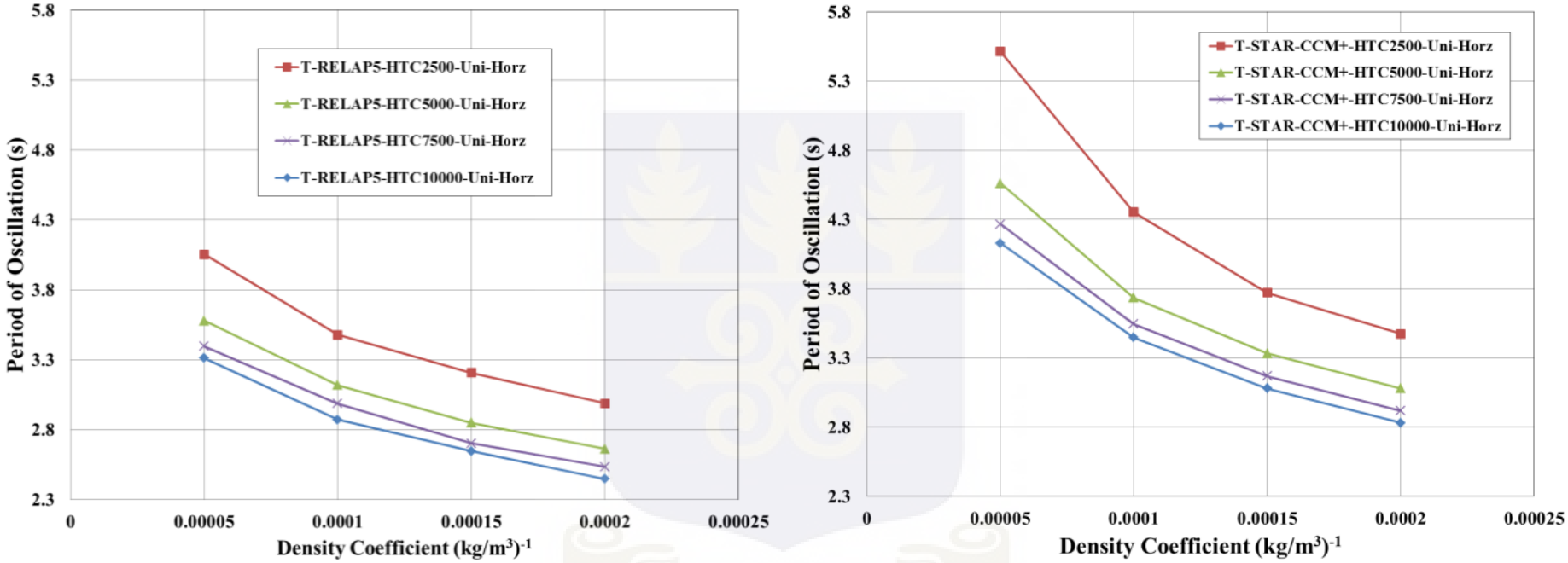

Figure 6.14. Period of oscillations as a function of density reactivity coefficient at different values of the gap heat transfer conductance for uniform power and horizontal (no gravity) flow

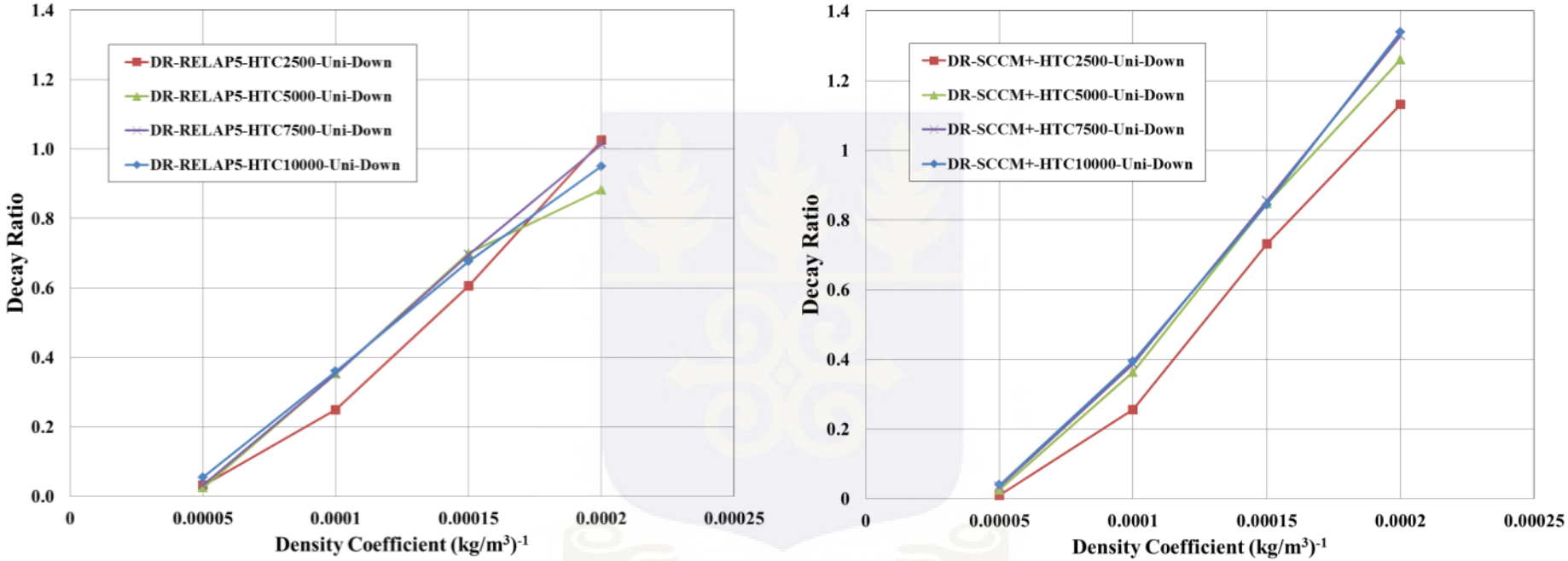

Figure 6.15. Decay ratio as a function of density reactivity coefficient at different values of the gap heat transfer conductance for uniform power and downward flow

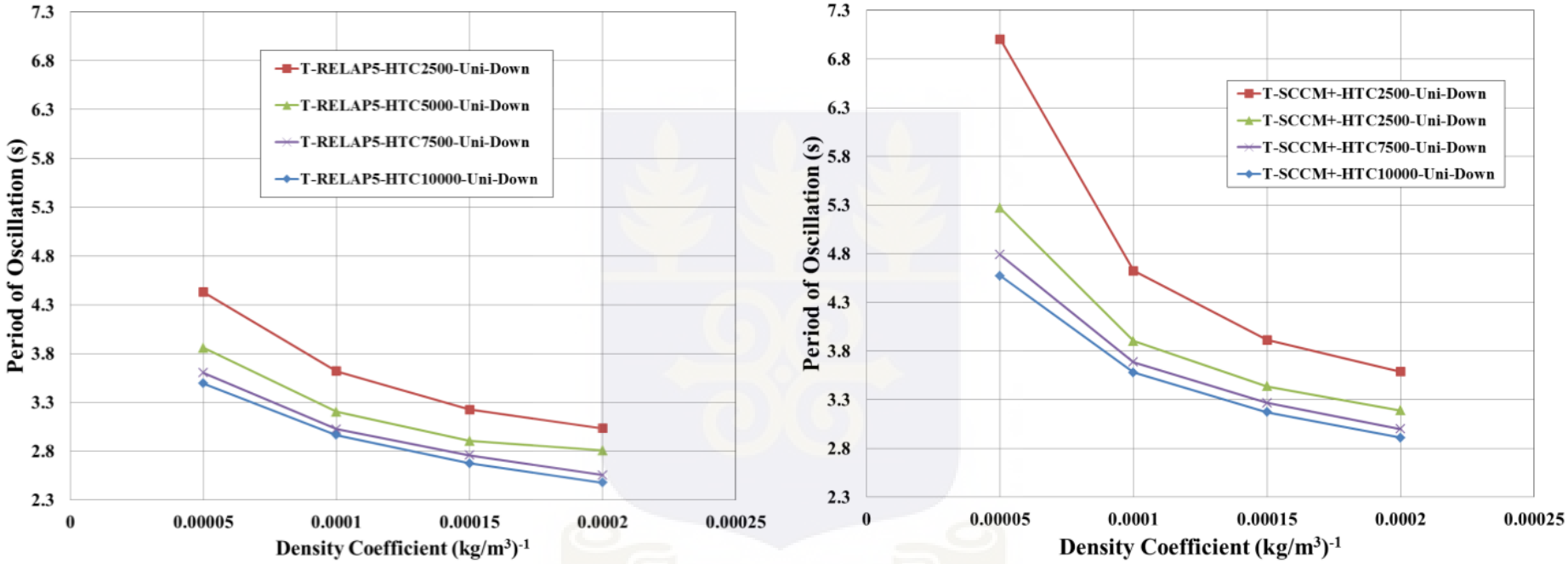

Figure 6.16. Period of oscillations as a function of density reactivity coefficient at different values of the gap heat transfer conductance for uniform power and downward flow

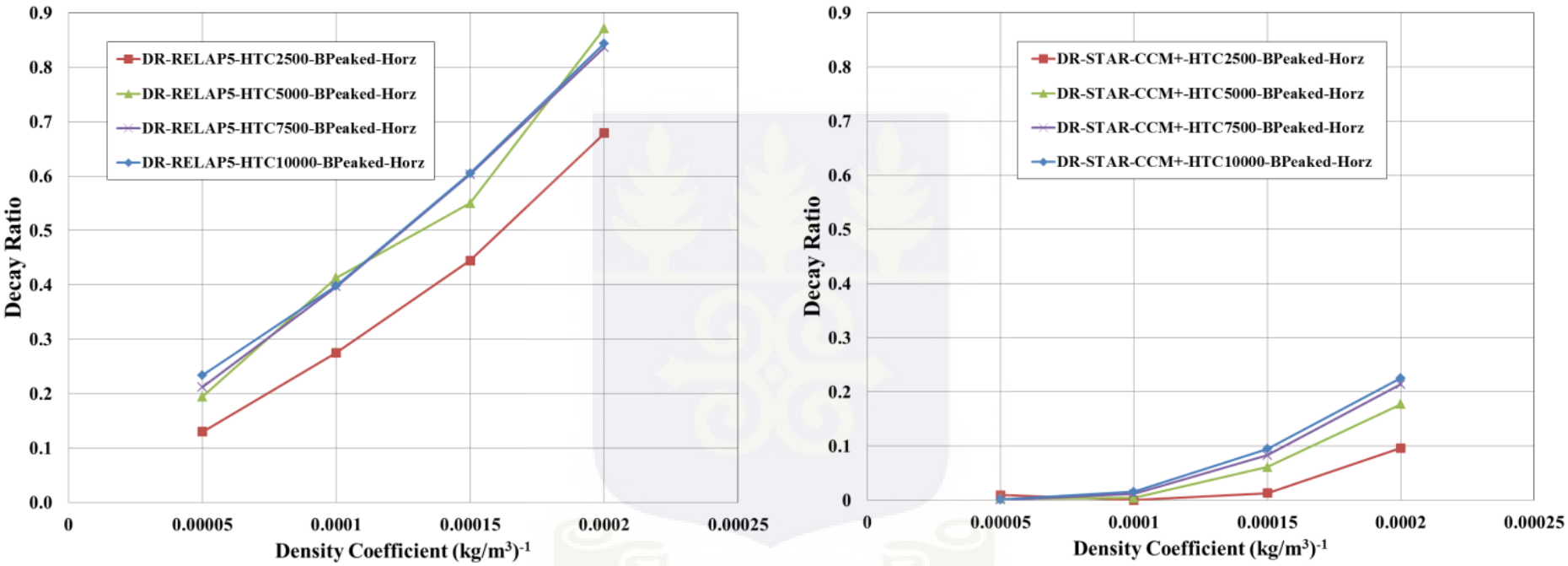

Figure 6.17. Decay ratio as a function of density reactivity coefficient at different values of the gap heat transfer conductance for bottom peaked power and horizontal (no gravity) flow

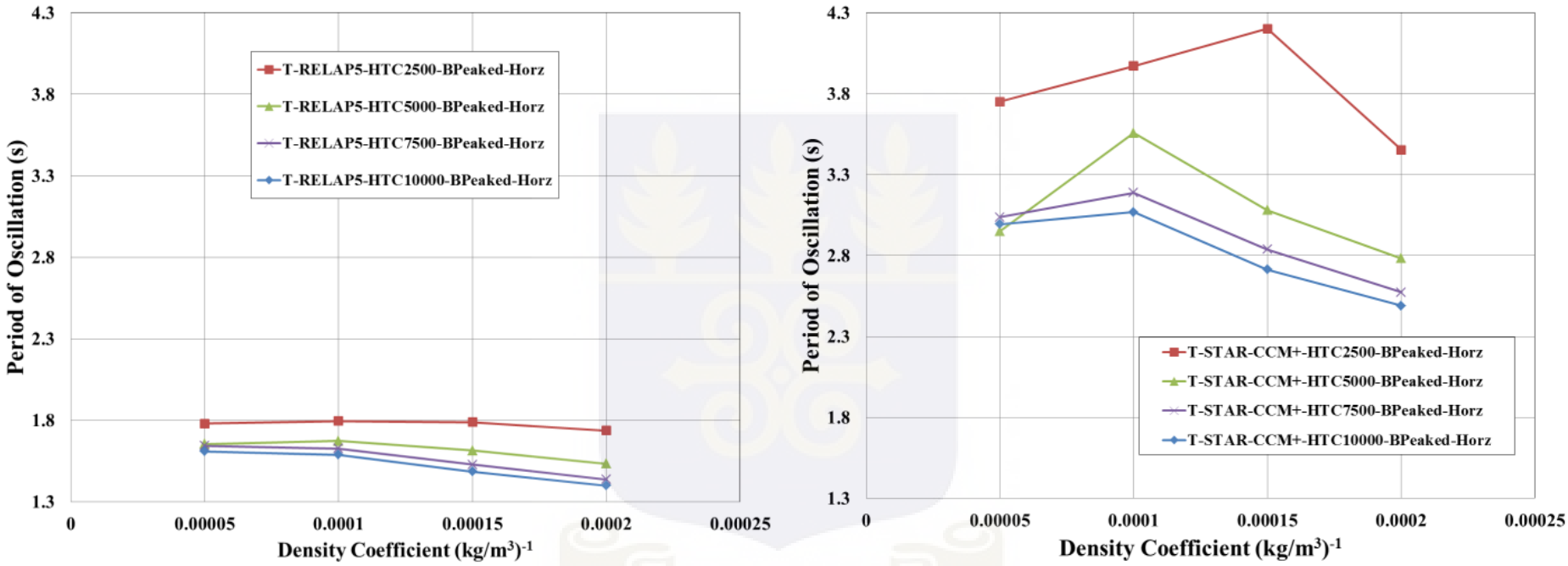

Figure 6.18: Period of oscillation as a function of density reactivity coefficient at different values of the gap heat transfer conductance for bottom peaked power and horizontal (no gravity) flow

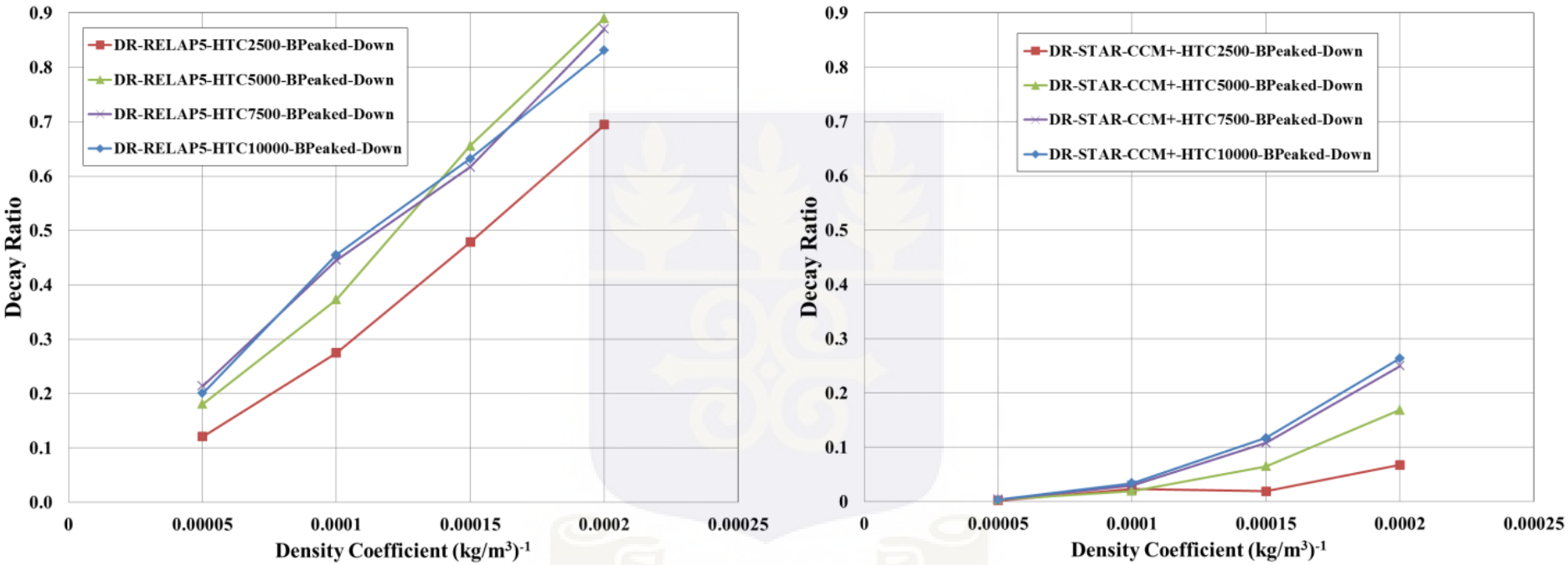

Figure 6.19: Decay ratio as a function of density reactivity coefficient at different values of the gap heat transfer conductance for bottom peaked power and downward flow.

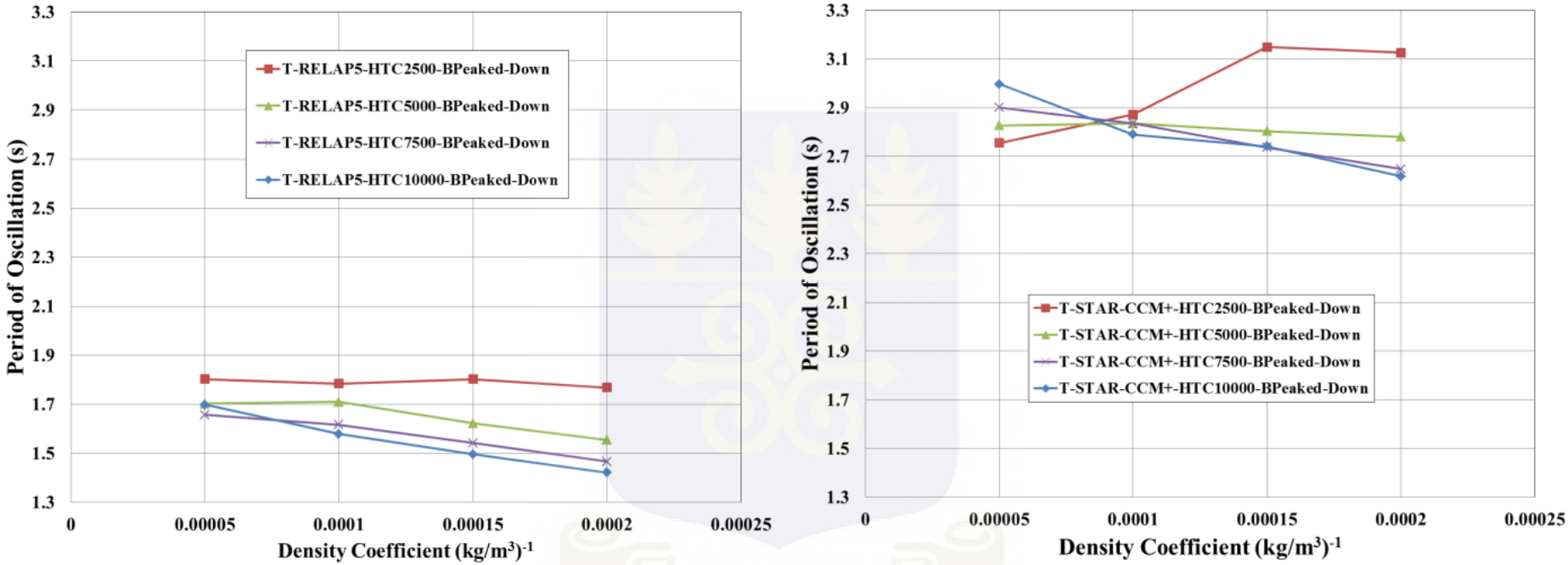

Figure 6.20: Period of oscillation as a function of density reactivity coefficient at different values of the gap heat transfer conductance for bottom peaked power and downward flow.

From these results the following considerations can be made:

- in the case of vertical upward flow with uniform power (Figure 6.9), the decay ratio increases, as expected, with the reactivity density coefficient; it also increases with the gap heat transfer conductance; it can also be noted that RELAP5 and STAR-CCM+ predict values of decay ratio in reasonable agreement; the mentioned effects of HTC and C_d are common to all the considered operating conditions addressed in the following figures;
- in Figure 6.10 it can be noted that the period of oscillations is decreasing with increasing density reactivity coefficient and HTC; this behaviour can be explained with the greater density feedback and with effects related to the change in fuel time constant depending on its overall conductivity;
- Figure 6.11 and Figure 6.12 show the different behaviour predicted by the two codes for the bottom peaked power distribution with vertical upward flow in terms of decay ratio and period of oscillations; in particular, it can be noted that, especially at large values of HTC, STAR-CCM+ predicts lower decay ratios and larger periods than RELAP5; this result must be considered in the light of similar effects known also for boiling water reactors, suggesting that longer light fluid regions may lead to shorter periods of oscillations (compare Figure 6.12 with Figure 6.10) that may result in more stable behaviour because of the interplay with the fuel time constant [39]; in fact, the density distribution presented in Figure 6.6 for the bottom peaked case, suggest a longer light phase region predicted by the CFD code than by the system code;
- a reasonable agreement between the results of the two codes is observed in the case of horizontal channel with uniform power profile (Figure 6.13 and Figure 6.14); it must be noted that the horizontal flow conditions were obtained in both codes by suppressing gravity along the channel axis; obviously, with the 3D CFD model it could be possible to consider different directions of gravity in a plane normal to the channel axis: this complexity was avoided in the present study;

- a similar agreement is shown in Figure 6.15 and Figure 6.16 for vertical downward flow with uniform power profile, which report larger decay ratios and oscillation periods for STAR-CCM+ than in the RELAP5 case.
- Figure 6.17 and Figure 6.18 present the results for the horizontal flow for the bottom peaked power distribution with similar trend as was observed in Figures 6.11 and 6.12 for the vertical upward flow discussed above. Figure 6.19 and Figure 6.20 show the trends for the downward flow for bottom peaked power distribution. Obtaining convergence for the two cases with Courant number of 20000 was not possible in these cases. A Courant number of 5000 enabled the required convergence to be obtained. This characteristic of the bottom peaked horizontal and downward flows will require further investigation to ascertain the effects of numerical schemes on the rod treatment.

6.6. CONCLUDING REMARKS

The results presented in this Chapter suggest that CFD models are able to predict stability conditions relevant for SCWR fuel rods, in similarity with classical system codes. A general good agreement between the predictions of STAR-CCM+ and RELAP5 was observed in most cases, though it was fully expected to find differences due to the diversity of the adopted modelling techniques.

It is known that the two codes make use of completely different mathematical models, numerical methods, equations of state and slight differences occur also in the adopted neutron kinetics features. In view of these differences, the similarity observed in qualitative and quantitative predictions can be considered a very good starting point for future analyses, providing better clarification of the advantages of adopting CFD in tackling stability analyses of nuclear reactor channels.

CHAPTER 7

GENERAL CONCLUSIONS AND RECOMMENDATIONS

7.1 CONCLUSIONS

The present work has dealt with thermal-hydraulic flow stability analyses in channels and fuel bundle slices containing supercritical fluids, making use of both 1D models and a CFD code.

Basing on previous experience, STAR-CCM+ and RELAP5 were adopted to solve flow stability problems in circular channels and fuel bundle slices without heating structures, in order to characterise the response of CFD models in the analysis of purely thermal-hydraulic instability phenomena. After gaining enough experience with these simpler cases, a more realistic system was then considered, consisting in a square lattice assembly subchannel including pellet, gap, cladding and coolant regions; the effects of inlet and outlet throttling and of a point kinetics neutronics model, including six delayed neutron groups with global Doppler and fluid density feedbacks, were also addressed in this case.

A review on the stability and control schemes for SCWR concept performed at the beginning of this work allowed setting up the general background necessary for planning a meaningful study. Then, the analysis of stability of a circular heated channel with supercritical fluids provided light on the capability of STAR-CCM+ to be used for the analysis of flow stability in supercritical systems. The step-by-step process adopted in the work led from the study of simple cases to a relatively more complex and realistic one. The experience obtained from the various computations for the circular channel and fuel bundle slices assisted in providing confidence in the methodology adopted for the more realistic model of the square lattice assembly subchannel slices.

A methodology of calculation was set up and partly qualified for the systems considered in the current study. The methodology of analysis was slightly changed with respect to past works on circular supercritical channels and fuel bundle slices that started this line of research. In particular,

in order to bring the systems towards unstable behaviour during analyses, instead of using a linear increase of power with time at constant imposed channel pressure drop, it was chosen to assign multiple stepwise increases, thereby allowing the flow to oscillate after each step in a converging or diverging way. This made it possible to evaluate decay ratio and period of oscillations at each power level for oscillatory instabilities; lower and upper bounds of the value of power at which excursion starts for excursive (Ledinegg) instabilities could be also obtained. In the case of the complete square lattice subchannel, a specific methodology of analysis was devised, including impressing a pressure perturbation at channel inlet to check the degree of stability of flow in any selected steady operating condition.

The study allowed assessing at different extents the effects of different numerical schemes, turbulence treatments, presence of walls, flow direction, power distribution, similarity in fluid-to-fluid behaviour, wall surface roughness, presence of fuel rods in rod bundle slices with typical structures and neutronics. It was observed that a combination of numerical schemes in the CFD studies provided results comparable to those obtained from similar 1D models, enabling meaningful comparisons. The numerical discretisation and the internal iteration Courant number have been found to affect the convergence of the computations if not carefully selected.

Five different pseudo-subcooling values were adopted for the circular supercritical channel and the fuel bundle slices. The results obtained were used to construct stability maps which were compared with those obtained from 1D models adopted in the study. On the other hand, the single pseudo-subcooling number value adopted for the square assembly lattice subchannel slice was comparable to that corresponding to the operating conditions of some SCWR conceptual design.

Among the turbulence models adopted, it was observed that the k-ε and Reynolds stress models provided similar results, to be contrasted to some slightly different behaviour observed by the SST model. The standard k-ε model was adopted in the computations involving the circular channels and the fuel bundle slices while the Realizable k-ε model was adopted for the square lattice assembly

subchannel slice studies. The adoption of low Reynolds models with mesh refinement at the walls, checked for a few cases, provided stability results comparable to those with high y+ treatments, though the detailed effects on wall temperature predictions were not fully analysed.

In discussing the obtained results, some interesting physical effects were noted:

- in the addressed conditions, the flow direction was found to mostly affect the Ledinegg region of the stability maps; the vertical flow condition usually showed a larger region for the density wave form of instability, while the horizontal flow and then the downward flow show an increasingly larger extension of the Ledinegg instability region;
- the fluid-to-fluid comparison made in the case of the circular channel confirmed the similarity of the stability predictions among the four fluids at supercritical conditions already noted by 1D models;
- for the bare circular channel, the bottom-peaked power distribution resulted in a much more unstable behaviour as compared to the results of the uniform distribution; on the other hand, in the case of the subchannel slice with complete modelling of the fuel rod, the decay ratios were higher for the uniform distribution than for the bottom-peaked one, revealing the effects of the interaction between the time constants of the fuel rod and those of the fluid in the channel;
- the presence of a conductive wall has been found to stabilize the supercritical system as predicted by both 1D and CFD techniques; the similarities in the results obtained in this regard by the two computational methods call for further attention to be given to this subject;
- in the limits of the ranges considered in this work, roughness has been found to tend to destabilize the supercritical system.

The systematic comparison between CFD and 1D models provides confidence in the methodology adopted in the current study due to the similarities observed in the stability predictions for the various models of the supercritical system. Some differences were observed as was envisaged due to the detailed treatments made possible by the CFD code. However, there is the urgent need to

compare the computed results with those from experiments which are becoming available to the scientific community. This represents one of the most important tasks to be performed in the near future to provide better confidence in the predictions of the different models.

7.2 SPECIFIC RECOMMENDATIONS

It is recommended that the effects of wall surface roughness and wall thickness be further studied for the assembly subchannel slices and also for the slices with rod to ascertain the extent of the influence on stability of the supercritical channel.

Other power distributions than considered here, such as the sinusoidal one, can be assessed with the methodology proposed and tested in this work.

The higher frequency modes observed sometimes in the channel and slice studies require further attention to find out the causes and their effect on stability analysis with CFD.

The complete model which includes the fuel rod can be remodeled to include spacer grids to allow for a study on their effect on the stability predictions of the SCWR.

REFERENCES

[1] Pioro, R.B., Duffey, I.L., 2007, Heat transfer and hydraulic resistance at supercritical pressure in power-engineering applications. ASME Press.

[2] Oka, Y., Koshizuka, S., Ishiwatari, Y., Yamaji, A., 2010, Super Light Water Reactors and Super Fast Reactors, Supercritical-Pressure Light Water Cooled Reactors, Springer, ISBN 978-1-4419-6034-4.

[3] Schulenberg, T., Starflinger, J., (eds.), 2012, High Performance Light Water Reactor: Design and Analyses, Karlsruhe Institute of Technology Scientific Publishing, Karlsruhe.

[4] Xiong, T., Yan, X., Xiao, Z., Li, Y., Huang, Y., Yu, J., 2012, Experimental study on flow instability in parallel channels with supercritical water, Annals of Nuclear Energy, Volume 48, October 2012, Pages 60-67.

[5] Sharabi, M. B., 2008, CFD Analyses of Heat Transfer and Flow Instability Phenomena Relevant to Fuel Bundles in Supercritical Water Reactors, PhD thesis presented to Dipartimento di Ingegneria Meccanica, Nucleare e della Produzione, Università di Pisa, pp. 85-106.

[6] Bourè, J.A., Bergles, A.E., Tong, L.S., 1973, Review of Two-Phase Flow Instability, Nuclear Engineering and Design, 25, (1973), pp.165-192.

[7] March-Leuba, J., Rey, J.M., 1993, Coupled Thermohydraulic-Neutronic Instabilities in Boiling Water Nuclear Reactors: A Review of The State of the Art, Nuclear Engineering and Design, 145, pp. 97-111.

[8] D'Auria, F., Ambrosini, W., Anegawa, T., Blomstrand, J, In De Betou, J., Langenbuch, S., Lefvert, T., Valtonen, K., (Lead Authors), 1997, State of the Art Report on Boiling Water Reactor Stability,*OCDE/GD(97)13*, AEN/NEA, 1997.

[9] Kakaç, S., Bon, B., 2008, A Review of two-phase flow dynamic instabilities in tube boiling systems, International Journal of Heat and Mass Transfer 51 (2008) 399–433.

[10] Zuber, N., 1966, An analysis of thermally induced flow oscillation in the near-critical and supercritical thermal-dynamic region, Report no. NASA-CR-80609, General Electric Co., NY, USA.

[11] Zhao, J., Saha, P., Kazimi, M.S., 2005, Stability of supercritical water-cooled reactor during steady-state and sliding pressure start-up. The 11th International Topical Meeting on Nuclear Reactor Thermal-Hydraulics (NURETH-11), Paper: 106, Popes' Palace Conference Center, Avignon, France, October 2-6, 2005.

[12] Ortega Gómez, T., Class, A., Lahey, R. T., Jr., Schulenberg, T., 2008, Stability analysis of a uniformly heated channel with supercritical water, Nuclear Engineering and Design, 238, pp. 1930-1939.

[13] Ambrosini, W., 2007, On the analogies in the dynamic behaviour of heated channels with boiling and supercritical fluids, Nuclear Engineering and Design, Vol. 237/11, pp. 1164-1174.

[14] Ambrosini, W., Sharabi, M., 2008, Dimensionless parameters in stability analysis of heated channels with fluids at supercritical pressures, Nuclear Engineering and Design, Vol. 238, pp. 1917-1929.

[15] Sharabi, M., Ambrosini, W., He, S., Jiang, P.-X. and Zhao, C.-R., 2009, Transient Three-Dimensional Stability Analysis of Supercritical Water Reactor Rod Bundle Subchannels by a Computational Fluid Dynamics Code, J. Eng. Gas Turbines Power, March 2009, Volume 131, Issue 2, 022903, DOI:10.1115/1.3032437.

[16] Ambrosini, W., Damiani, G., Forgione, N., Ampomah-Amoako, E., 2012, Studies on the adoption of CFD codes in the analysis of stability in heated channels with supercritical fluids,

presented at 9th International Topical Meeting on Nuclear Thermal-Hydraulics, Operation and Safety (NUTHOS-9), N9P0281, Kaohsiung, Taiwan, September 9-13, 2012.

[17] Ampomah-Amoako, E., Ambrosini, W., 2013, Developing a CFD methodology for the analysis of flow stability in heated channels with fluids at supercritical pressures, Annals of Nuclear Energy 54, pp. 251–262.

[18] United States Department of Energy, 2006, The U. S. Generation IV Fast Reactor Strategy, A Report to U. S. Congress, DOE/NE-0130, pp. 7-9.

[19] Schenkel, R., Schulenberg, T., Renault, C., Haas, D., 2009, Advanced Supercritical Water and Molten Salt Reactors, GIF Symposium, Paris, France, 9 – 10 September 2009, pp. 35 – 44.

[20] LeBlanc, D., 2010, Molten salt reactors: A new beginning for an old idea, Nuclear Engineering and Design, Vol. 240, pp. 1644-1656.

[21] Moses, D. L., 2010, Very High-Temperature Reactor (VHTR) Proliferation Resistance and Physical Protection (PR&PP), Oak Ridge National Laboratory, ORNL/TM-2010/163, pp. 1,2.

[22] Yamada, K., Sakurai, S., Asanuma, Y., Hamazaki, R., Ishiwatari, Y., Kitoh, K., 2011, Overview of the Japanese SCWR Concept Developed under the GIF Collaboration, presented at 5th International Symposium on SCWR (ISSCWR-5), Vancouver, British Columbia, Canada, P031, pp. 1-14.

[23] Jiang, P. X., Zhao, C.- R., Shi, R.- F., Chen, Y., Ambrosini, W., 2009, Experimental and numerical study of convection heat transfer of CO_2 at Super-critical pressures during cooling in small vertical tube, International Journal of Heat and Mass Transfer, Vol 52, pp. 4748-4756.

[24] Mokry, S., Naidin, M., Baig, F., Gospodinov, Y., Zirn, U., Bakan, K., Pioro, I., Naterer, G., 2008, Conceptual Thermal-Design Options for Pressure-Tube SCWRs with Thermochemical Co-generation of Hydrogen, Proceedings of the International

Conference On Nuclear Engineering (ICONE-16, Paper-48313), Orlando, Florida, USA, 2008 May 11-15.

[25] U.S. DOE Nuclear Energy Research Advisory Committee and Generation IV International Forum, 2002, A Technology Roadmap for Generation IV Nuclear Energy System (GIF-002-00).

[26] Koehly, C., Schulenberg, T., Starflinger, J., 2009, HPLWR Reactor Design Concept, 4th International Symposium on Supercritical Water-Cooled Reactors, March 8-11, 2009, Heidelberg, Germany, Paper No. 37.

[27] Squarer, D., Schulenberg, T., Struwe, D., Oka, Y., Bitterman, D., Aksan, N., Maraczy, C., Kyrki-Rajamäki, R., Souryri, A., Dumaz, P., 2003, High performance light water reactor, Nuclear Engineering and Design 221, pp. 167-180.

[28] Brandauer, M., Schlagenhaufer, M., Schulenberg, T., 2009, Steam cycle optimization for the HPLWR, 4th Int. Symposium on SCWR, Paper No. 36, Heidelberg, Germany, March 8-11, 2009.

[29] Torgerson, D.F., Shalaby B.A., Pang, S., 2006, CANDU technology for generation III+ and IV reactors, Nuclear Engineering and Design, Vol. 236, No. 14-6, 2006, pp. 1565-1572.

[30] Naidin, M., Pioro, I., Zirn, U., Mokry, S., Naterer, G., 2009, Supercritical water-cooled NPPs with co-generation of hydrogen: general layout and thermodynamic cycle options, 4th Intern. Symp.on SCWR, Heidelberg, Germany, March 8-11, 2009.

[31] Yi, T.T., Koshizuka, S., Oka, Y., 2004, A linear stability analysis of supercritical water reactors, (II) coupled neutronic thermal–hydraulic stability. Journal of Nuclear Science and Technology 41, No. 12, pp. 1176–1186.

[32] Ishiwatari, Y., Oka, Y., Yamada, K., 2009, Japanese R&D project on pressure vessel type SCWR, 4th Intern. Symp.on SCWR, Heidelberg, Germany, March 8-11, 2009.

[33] Bae, Y.Y., Kim, H. Y., Kwon, J. H., Bae, S. M., Kwangho, L., Kim, Y. B., Hong, S. Y., 2009, Update on the SCWR research in Korea, 4th Intern. Symp.on SCWR, Heidelberg, Germany, March 8-11, 2009.

[34] Bae, Y. Y., Jang, J., Kim, H. Y., Yoon, H. Y., Kang, H. O., Bae, K. M., 2007, Research activities on a Supercritical Pressure Water Reactor in Korea, Nuclear Engineering and Technology, Vol. 39, No. 4, p. 278.

[35] Cheng, X., 2009, R&D activities on SCWR in China, 4th Intern. Symp.on SCWR, Heidelberg, Germany, March 8-11, 2009.

[36] Viktorov, A., 2011, Projecting Regulatory Expectations for Advanced Reactor Designs, presented at 5th International Symposium on SCWR (ISSCWR-5), Vancouver, British Columbia, Canada, P13, p. 11.

[37] Starflinger, J., Schulenberg, T., Bittermann, D., Andreani, M., Maraczy, C., 2011, Assessment of the High Performance Light Water Reactor Concept, presented at 5th International Symposium on SCWR (ISSCWR-5), Vancouver, British Columbia, Canada, P056, p. 1.

[38] Yi, T.T., Koshizuka, S., Oka, Y., 2004, A linear stability analysis of supercritical water reactors, (I) thermal–hydraulic stability. Journal of Nuclear Science and Technology 41, No. 12, pp. 1166–1175.

[39] Ikeda, H., Fukahori, T., Kubo, Y., Soneda, H., Mizokami, S., 2008, BWR Stability Issues in Japan, Hindawi Publishing Corporation, Science and Technology of Nuclear Installation, Volume 2008, Article ID 358616, pp. 1-11.

[40] Pis'menny, E.N., Razumovskiy, V.G., Maevskiy, A.E., Pioro, I.L., 2006, Heat Transfer to Supercritical Water in Gaseous State or Affected by Mixed Convection in Vertical Tubes, Proc. of the ICONE14-89483, Miami, USA.

[41] Mochizuki, H., 1994, Flow instabilities in boiling channels of pressure tube type reactor, Nuclear Engineering Design, 149, pp. 269-277.

[42] Vijayan, P. K., Nayak, A. K., 2005, Introduction to Instabilities in Natural Circulation Systems, in Natural Circulation in water cooled nuclear power plants, IAEA-TECDOC-1474, Annex 7, pp. 173-201.

[43] Lahey Jr., R. T., Moody, F. J., 1993,*The Thermal-Hydraulics of a Boiling Water Nuclear Reactor*, American Nuclear Society, Chicago, Illinois, USA, 2nd edition.

[44] March-Leuba, J., 1992, Density wave instabilities in boiling water reactors, Tech. Rep. NUREG/CR- 6003 ORNL/TM-12130, Oak Ridge National Laboratory, 1992.

[45] Carmichael, L. A., 1978, Transient and stability tests at peach bottom atomic power station unit 2 at end of cycle 2, *Electr Power Res Inst Rep EPRI NP 564*, 1978.

[46] Bergdahl, B. G., Oguma, R., 1990, BWR stability investigation in RINGHALS 1 measurement data from October 26, 1989, in *Proceedings of International Workshop on Boiling Water Reactor Stability*, vol. 142, New York, NY, USA, 1990.

[47] March-Leuba, J., Blakeman, E. D., 1991, "Mechanism for out-of-phase power instabilities in boiling water reactors," *Nuclear Science and Engineering*, vol. 107, no. 2, pp. 173–179.

[48] Hashimoto, K., 1993, "Linear modal analysis of out-of-phase instability in boiling water reactor cores," *Annals of Nuclear Energy*, vol. 20, no. 12, pp. 789–797.

[49] Takeuchi, Y., Takigawa, Y., and Uematsu, H., 1994, Study on boiling water reactor regional stability from the viewpoint of higher harmonics, *Nuclear Technology*, vol. 106, no. 3, pp. 300–314.

[50] Sun, P., 2012, Dynamic Model Construction and control System Design for Canadian Supercritical Water-cooled Reactors, A thesis submitted to Graduate Program in Electrical and

Computer Engineering, The School of Graduate and Postdoctoral Studies, University of Western Ontario, pp. 36-43.

[51] Buongiorno, J., MacDonald, P. E., 2003, Supercritcal Water Reactor: Progress Report for the FY-03 Generation-IV R&D Activities for the Development of the SCWR in the U.S., INEEL/EXT-03-01210.

[52] Nakatsuka, T., Oka, Y., Koshizuka, S., 1998, Control of a fast reactor cooled by supercritical light water, Nuclear Technology, Vol. 121, pp. 81-92.

[53] Ishiwatari, Y., Oka, Y., Koshizuka, S., 2003, Control of a High Temperature Supercritical Pressure Light Water Cooled and Moderated Reactor with Water Rods, Journal of Nuclear Science and Technology, Vol. 40, No. 5, pp. 298-306.

[54] Ishiwatari, Y., Peng, C. H., Ikejiri, S., Oka, Y., 2010, Improvements of feedwater controller for super fast reactor, Journal of Nuclear Science and Technology, Vol. 47, pp. 1155-1164.

[55] Schlagenhaufer, M., Starflinger, J., Schulenberg, T., 2009, Steam cycle analyses and control of the HPLWR plant, 4th Int. Symp. on SCWR, Paper 76, Heidelberg, Germany, March 8-11, 2009.

[56] APROS Version 5.08, 2012, VTT and Fortum, http://apros.vtt.fi

[57] Schlagenhaufer, M., Starflinger, J., Schulenberg, T., 2009, Plant control of the High Performance Light Water Reactor, Proc. GLOBAL 2009, Paper 9339, Paris, France, Sept. 6-11, 2009.

[58] Gòmez, T., O., 2009, Stability Analysis of the High Performance Light Water Reactor, Dissertation presented to Universität Karlsruhe (TH), pp. 1-129.

[59] Starflinger, J., Schulenberg, T., Marsault, P., Bittermann, D., Laurien, E., Maraczy, C., Anglart, H., Lycklama, J.-A., Andreani, M., Ruzickova, M., Vanttola, T., Kiss, A., Rohde, M., Novotny, R., 2010, High Performance Light Water Reactor Phase 2, Public Final Report –

Assessment of the HPLWR Concept, 6th Framework Programme, Contract No. FI60-036230, www.hplwr.eu

[60] Sanders, M., 2009, Thermo-Hydraulic Stability Analysis of the High Performance Light Water Reactor and a Scaled Experimental Facility, MSc thesis, Delft University of Technology, The Netherlands.

[61] Reiss, T., Fehér, S., Czifrus, Sz., 2009, Calculation of Xenon-Oscillations in the HPLWR, Proc. 4th International Symposium on Supercritical Water-Cooled Reactors, Heidelberg, Germany, March 8-11, 2009, Paper 47.

[62] Reiss, T., Fehér, S., Czifrus, Sz., 2011, Xenon oscillation in SCWRs, Progress in Nuclear Energy, 53, pp. 457-462.

[63] Csom Gy., 2005, Atomerőművek üzemtana (Operation of nuclear power plants), Műegyetemi kiadó, Budapest, 2005, in Hungarian.

[64] Cai, J., Ishiwatari, Y., Ikejiri, S., Oka, Y., 2009, Thermal and stability considerations for a supercritical water-cooled fast reactor with downward-flow channels during power-raising phase of plant startup". Nucl. Eng. Design, vol.239, pp. 665-679.

[65] Oka, Y., Morooka, S., Yamakawa, M., Ishiwatari, Y., Ikejiri, S., Katsumura, Y., Muroya, Y., Terai, T., Sasaki, K., Mori, H., Hamamoto, Y., Okumura, K., Kugo, T., Nakatsuka, T., Ezato, K., Akasaka, N., Hotta, A., 2011, Research and Development of Super Light Water Reactors and Super Fast Reactors in Japan, presented at 5th International Symposium on SCWR (ISSCWR-5), Vancouver, British Columbia, Canada, K002, p. 6.

[66] Ji, S., Shirahama, H., Koshizuka, S., Oka, Y., 2001, Stability analysis of Supercritical Pressure Light Water Cooled Reactor in constant pressure operation, Proc. Ninth Int. Conf. on Nuclear Engineering, Nice, France, April 8–12, 2001, ASME, ICONE-9306.

[67] Yi, T.T., Ishiwatari, Y., Koshizuka, S., Oka, Y., 2004, Startup thermal analysis of a high-temperature supercritical-pressure light water reactor. Journal of Nuclear Science and Technology 41, pp. 790–801.

[68] Yoo, J., 2006, Three-dimensional core design of large scale supercritical light water-cooled fast reactor. Ph.D. thesis, University of Tokyo, Japan.

[69] Ambrosini, W., Sharabi, M. B., 2007, Assessment of Stability Maps for Heated Channels with Supercritical Fluids versus the predictions of a System Code, Nuclear Engineering and Technology, Vol. 39, No. 5, pp. 627-636.

[70] Ambrosini, W., 2011, Assessment of flow stability boundaries in a heated channel with different fluids at supercritical pressure, Annals of Nuclear Energy, Vol. 38, pp. 615-627.

[71] De Rosa, M., Guetta, G., Ambrosini, W., Forgione, N., He, S., Jackson, J. D., 2011, Lessons learned from the application of CFD models in the prediction of heat transfer to fluids at supercritical pressure, In: The Fifth International Symposium on SCWR (ISSCWR-5), Vancouver, British Columbia, Canada, P060, pp. 1-13.

[72] FLUENT, 2005, FLUENT v.6.2.16, Users Guide.

[73] Cd-Adapco, 2012, User Guide, STAR-CCM+ Version 7.04.006.

[74] Ambrosini, W., 2010, Dimensionless Parameters in Stability Analysis of Heated Channels with Supercritical Fluids at Imposed Heating Flux and Wall Temperature Conditions, IAEA Technical Meeting on Heat Transfer, thermal-hydraulics and system design for supercritical pressure water cooled reactors, Pisa, Italy, TM-38683-20, pp. 1-15.

[75] Ambrosini, W., 2009, Continuing Assessment of System and CFD Codes for Heat Transfer and Stability in Supercritical Fluids, In: Fourth International Symposium on Supercritical Water-Cooled Reactors, Heidelberg, Germany, Paper No. 83, pp. 1-15.

[76] Sharabi, M.B., Ambrosini, W., He, S., 2008, Prediction of unstable behaviour in a heated channel with water at supercritical pressure by CFD models, Annals of Nuclear Energy, 35, pp. 767–782.

[77] Versteeg, H. K., Malalasekera, W., 2007, An Introduction to Computational Fluid Dynamics, The Finite Volume Method, Second edition, pp. 54-128.

[78] Launder, B. E., Spalding, D. B., 1974, The Numerical Computation of Turbulent Flows, *Comput. Methods Appl. Mech. Eng.*, Vol. 3, pp. 269-289.

[79] Jones, W.P. and Lander, B.E., 1972, The Prediction of Laminarization with a Two-Equation Model of Turbulence, *Int. J. Heat and Mass Transfer*, **15**, pp. 301-314.

[80] Launder, B.E. and Sharma, B.I., 1974, Application of the Energy Dissipation Model of Turbulence to the Calculation of Flow Near a Spinning Disc, Letter in Heat and Mass Transfer, vol. 1, no. 2, pp. 131-138.

[81] Spalart, P.R. and Rumsey, C.L., 2007, Effective Inflow Conditions for Turbulence Models in Aerodynamic Calculations, *AIAA Journal*, **45**(10), pp. 2544-2553.

[82] Henkes, R.A.W.M., van der Flugt, F.F., Hoohendoorn, C.J., 1991, Natural convection in a square cavity calculated with low-Reynolds number turbulence models, *Int. J. Heat Mass Transfer*, 34, pp. 1543-1557.

[83] Lien, F.S., Chen, W.L., and Leschziner, M.A., 1996, Low-Reynolds number eddy-viscosity modelling based on non-linear stress-strain/vorticity relations, Proc. 3rd Symp. on Engineering Turbulence Modelling and Measurements, 27-29 May, Crete, Greece.

[84] Wilcox, D.C., 1998, Turbulence Modeling for CFD, 2nd edition, DCW Industries, Inc.

[85] Durbin, P.A., 1996, On the k-e stagnation point anomaly, *Int. J. Heat and Fluid Flow*, vol. 17**,** pp. 89-90.

[86] Gibson, M.M., Launder, B.E., 1978, Ground effects on pressure fluctuations in the atmospheric boundary layer, *J. Fluid Mech.*,vol. 86(3), pp. 491-511.

[87] RELAP5 Code Development Team, 1995, RELAP5/MOD3 Code Manual, Volume I: Code Structure, System Models, and Solution Methods, NUREG/CR-5535, INEL-95/0174, pp. 1-414.

[88] Siefken, L. J., Allison, C. M., Bohn, M. P., Peck, S. O., 1981, FRAP-T6: A Computer Code for the Transient Analysis of Oxide Fuel Rods, EGG-CDAP-5410, pp. 1-66.

[89] Lamarsh, J. R., 1966, Introduction to Nuclear Reactor Theory, Addison-Wesley Publishing Company, Inc., p. 100.

[90] Reuss, P., 2008, Neutron Physics, EDP Sciences, p. 122.

[91] Ambrosini, W., 2011, Discussion of similarity principles for fluid-to-fluid scaling of heat transfer behaviour at supercritical pressures, *Nuclear Engineering and Design, Volume 241, Issue 12, December 2011, pp. 5149-5173.*

[92] NIST, 2002, Reference Fluid Thermodynamic and Transport Properties – REFPROP, Aug. (2002), Lemmon, E.W., McLinden, M.O., Hurber, M.L. (Eds.), NIST Standard Reference Database 23 (Software and Source), V. 7.0, U.S. Department of Commerce.

[93] SCIENTECH Inc., 1999, RELAP5/Mod3 Code Manual, vol. I: Code Structure, System Models and Solution Methods. The Thermal Hydraulics Group, Idaho, June 1999.

[94] Morresi, G., 2012, Analisi di stabilità del moto di un fluido supercritico con vari modelli di turbolenza, BSc Thesis, Università di Pisa, Dipartimento di Ingegneria Civile e Industriale, Anno Accademico 2011-2012, pp. 11-21.

[95] Yamaji A., Oka Y., Koshizuka S., 2001, Conceptual Core Design of a 1000MWe Supercritical Pressure Light Water Cooled and Moderated Reactor, ANS/HPS Student Conf. Texas, A&M University.

[96] Ammirabile L., 2010, Studies on supercritical water reactor fuel assemblies using the sub-channel code COBRA-EN, Nuclear Engineering and Design 240, pp. 3087-3094.

[97] Todreas, N.E., Kazimi, M.S, 1990, Nuclear Systems I, Thermal-hydraulic fundamentals, Taylor and Francis.

APPENDIX – FORTRAN PROGRAM FOR POINT KINETICS SENSITIVITY ANALYSES

```
!This application supports the implementation of analytic step change solution in
!STAR-CCM+ study on the stability of Supercritical Fuel Rod Bundles
PROGRAM crankdelayed
IMPLICIT NONE
INTEGER::i,m,n,p,q
REAL(KIND(0.d0))::beta,gent,tstep,dpower,sum1,sum2
REAL(KIND(0.d0))::rho0,power0,theta,pre,cpower,cconc1,dconc
REAL(KIND(0.d0)),DIMENSION(:),ALLOCATABLE::betai,lambda,cconc2
REAL(KIND(0.d0)),DIMENSION(:),ALLOCATABLE::thetai,gammai,fe,cpower1
n=6
p=1000
allocate(betai(n+10),lambda(n+10),thetai(n+10),cconc2(n+10))
allocate(gammai(n+10),fe(n+10),cpower1(p+10))
!gent represents lifetime which is a reserved word
open(UNIT=3,FILE='crankdelayedrhofinal.txt')
open(UNIT=4,FILE='inpdelayed2.txt')
!reading problem data
read(4,*)
read(4,*)gent,rho0
write(*,*)gent,rho0
read(4,*)
read(4,*)power0,tstep,theta
write(*,*)power0,tstep,theta
read(4,*)
read(4,*)betai(1),betai(2),betai(3),betai(4),betai(5),betai(6)
write(*,*)betai(1),betai(2),betai(3),betai(4),betai(5),betai(6)
read(4,*)
read(4,*)lambda(1),lambda(2),lambda(3),lambda(4)
write(*,*)lambda(1),lambda(2),lambda(3),lambda(4)
```

```
read(4,*)
read(4,*)lambda(5),lambda(6)
write(*,*)lambda(5),lambda(6)
close(4)
write(3,50)
50 format ("This solves Crank-Nicholson Approach-6 Delayed Neutron Groups")
write(3,*)
! Input Data
!rho0=cdens*dens+ctemp*temp
write(3,60)
60 format ("     Iteration              Initial Conc")
write(3,70)
70 format ("     ====================================")
!
beta = 0.d00
do m=1,n
  cconc1=betai(m)*power0/(lambda(m)*gent)
cconc2(m)=cconc1
  beta = beta + betai(m)
write(3,*)m,cconc2(m)
write(*,*)m,cconc2(m)
end do
write(3,*)"beta =",beta
write(*,*)"beta =",beta
cpower=power0
cpower1(1)=power0
write(3,90)
90 format ("      Iteration              Crank-Six-Grp-Power")
write(3,120)
120 format ("     ============================================")
```

```
write(3,100)cpower,(cconc2(i),i=1,n)
!
! Loop on time advancements
do q=1,p
! Loop on delayed groups
sum1=0
sum2=0
!
do i=1,n
fe(i)=1+lambda(i)*theta*tstep
thetai(i)=(1/fe(i))*((betai(i)*cpower/gent)-lambda(i)*cconc2(i))*tstep
gammai(i)=(betai(i)*theta*tstep/gent)/fe(i)
!
sum1 = sum1 + lambda(i) * ( cconc2(i)+theta*thetai(i) )
sum2=sum2+(lambda(i)*gammai(i))
!
!write(3,*)i,dconc,cconc2(i+1)
end do
! Advancing power
pre=1.d0 - (rho0-beta) * theta * tstep / gent
dpower=( (rho0-beta)*cpower*tstep/gent + sum1*tstep)/(pre-sum2*theta*tstep)
! Advancing concentrations
do i=1,n
dconc=thetai(i)+gammai(i)*dpower
cconc2(i)=cconc2(i)+dconc
end do
!write(3,*)"Sum 1 is",sum1
cpower=cpower+dpower
write(3,100)cpower,(cconc2(i),i=1,n)
end do
```

```
!
CLOSE(3,STATUS='KEEP')
write(*,*)"Computations completed and results stored in crankdelayedrho.txt"
PAUSE
!
100 FORMAT ('Power = ',1pe14.7,' Concs =',6(1x,1pe14.7))
END PROGRAM crankdelayed
```

INPUT DATA

```
lifetime   rho0
5.d-05     1.d-03
power0        timestep  theta
4.205442d08   0.1d00    0.5d00
beta1    beta2     beta3     beta4     beta5     beta6 !Reuss data
2.4d-04  1.23d-03  1.17d-03  2.62d-03  1.08d-03  4.5d-04
lambda1      lambda2       lambda3       lambda4
1.272265d-02 3.1746032d-02 1.16009281d-01 3.1055901d-01
lambda5         lambda6
1.4005602241d00 3.875968992d00
```